

**Confinement and Dynamics  
of Torus-Shaped Dust Clouds  
in Magnetized Anodic Plasmas**

Dissertation  
zur Erlangung des Doktorgrades  
der Mathematisch-Naturwissenschaftlichen Fakultät  
der Christian-Albrechts-Universität zu Kiel

vorgelegt von  
**Torben Reichstein**

Kiel  
2014

Erster Gutachter: Prof. Dr. Alexander Piel  
Zweiter Gutachter: Prof. Dr. Holger Kersten

Tag der mündlichen Prüfung: 25.07.2014  
Zum Druck genehmigt: Kiel, den 25.07.2014

gez. Prof. Dr. Wolfgang J. Duschl Dekan

## Zusammenfassung

In dieser Dissertation werden Struktur und Dynamik torusförmiger Staubwolken in schwach magnetisierten anodischen Plasmen untersucht. Der Staub ist im Plasma auf Grund eines Kraftgleichgewichts der radialen Komponenten von elektrischer Feldkraft und Ionenwindkraft eingeschlossen. Die Wolken weisen einen *Void* (einen staubfreien Raum) in ihrem Zentrum auf und die Partikel rotieren um die Hauptachse des Torus. Für eine detaillierte Untersuchung der Eigenschaften dieser Wolken werden zwei verschiedene Herangehensweisen verwendet: Auf der einen Seite werden die torusförmigen Staubwolken experimentell mittels Videomikroskopie untersucht. Auf der anderen Seite werden Molekulardynamik-Simulation von toroidalen Staubströmungen durchgeführt. Als Grundlage für die Simulationen dient ein auf Sondenmessungen basierendes hierarchisches Vielteilchenmodell. Experiment und Simulationen ergänzen sich dabei für ein umfassendes Verständnis der Strömung.

Hinsichtlich der Entstehung torusförmiger Staubwolken wurde die azimutale Hallkomponente des Ionenwindes als Antrieb für die Staubrotation identifiziert. Bedingt durch die Experimentgeometrie existiert ein durch die Gravitation gegebener Schwellwert für das Einsetzen der Staubrotation. Im Vergleich zu einem einzelnen Partikel senkt die kollektive Abstoßung der negativ geladenen Staubpartikel in großen Wolken den Schwellwert ab. Zusätzlich wird durch die Gravitation die Symmetrie des Systems gebrochen, was zu einer inhomogenen Strömung führt. Der Hauptfokus dieser Dissertation liegt auf der Erforschung der inhomogenen Strömung torusförmiger Staubwolken hinsichtlich dreier Zielsetzungen:

Erstens stellt sich die Frage, inwieweit eine hydrodynamische Beschreibung der toroidalen Staubströmung gegeben werden kann. Diesbezüglich ist herausgefunden worden, dass die inhomogene Strömung teilweise laminar und inkompressibel ist. Darüber hinaus führt die von der Gravitation verursachte Symmetriebrechung abhängig von der Reibung zu einer spontanen Ausbildung zweier verschiedener Strömungsinstabilitäten, einem stehenden Schock oder einer Kelvin-Helmholtz-Instabilität, die durch eine stark verscherte Strömung entsteht.

Zweitens wird der Einfluss starker Kopplung auf die Strömung untersucht. Da die Wechselwirkung von Partikeln untereinander in der Hydrodynamik nicht berücksichtigt wird, ist zu erwarten, dass neue, bislang für fluide Strömungen unbekannt Phänomene auftreten. Es ist beobachtet worden, dass durch starke Kopplung sowie Reibung die laminare Strömung in eine kristalline Schalenstruktur relaxiert. Im Gegensatz dazu verursacht die Anwesenheit von Strömungsinstabilitäten das Schmelzen der kristallinen Strömung.

Drittens sollen die mikroskopischen und makroskopischen Beobachtungen zu einer einheitlichen Beschreibung vereint werden, um ein verbessertes Verständnis für den Einfluss von mikroskopischen Bewegungen auf das makroskopische Strömungsverhalten zu gewinnen. Die Analyse eines strukturellen Phasenübergang innerhalb der inhomogenen Strömung zeigt, dass die Zeit- und Längenskalen für die individuelle Partikelbewegung viel kürzer sind als die, die das hydrodynamische Verhalten der Strömung beschreiben. Daraus lässt sich schlussfolgern, dass die durch starke Kopplung dominierte individuelle Partikelbewegung nur die lokale, kurzzeitige Entwicklung der Strömung beeinflusst. Somit kann die globale Strömung durch ihr hydrodynamisches Verhalten beschrieben werden.



## Abstract

In this thesis, the structure and dynamics of torus-shaped dust clouds in a weakly magnetized anodic plasma are investigated. The dust is confined in the plasma due to a force equilibrium of the radial components of electric field force and ion drag. The clouds exhibit a *void* (a dust-free region) in their center and the particles rotate about the major axis of the torus. For a detailed study of the properties of these clouds two different approaches are used: On the one hand, the torus-shaped dust clouds are analyzed experimentally by means of video microscopy. On the other hand, molecular dynamics simulations of toroidal dust flows are performed. For the simulations, a hierarchic many-particle model that is based on probe measurements is used as the physical basis. Experiment and simulations complement one another for a comprehensive understanding of the flow.

Regarding the formation of torus-shaped dust clouds, the azimuthal Hall component of the ion drag is identified as the driving mechanism for the dust rotation. Due to the geometry of the experiment, a threshold that is caused by gravity exists for the onset of torus rotation. Compared to a single particle, the collective electrostatic repulsion of the negatively charged dust particles lowers the threshold in large clouds. This threshold is lowered by the collective electrostatic repulsion of the negatively charged dust particles. In addition, gravity breaks the symmetry of the system, resulting in an inhomogeneous flow. The main focus of this thesis is on study of the inhomogeneous flow of torus-shaped dust clouds regarding three objectives:

First, the question arises to what extent a hydrodynamic description of the toroidal dust flow can be given. Concerning this matter, it is found out that the inhomogeneous flow is partially laminar and incompressible. Furthermore, depending on friction, the symmetry breaking caused by gravity leads to a spontaneous formation of two different flow instabilities, a standing shock or a Kelvin-Helmholtz instability caused by a strongly sheared flow.

Second, the influence of strong coupling on the flow is investigated. Since the interaction between particles is not considered in hydrodynamics, it is expected that new phenomena previously unknown to fluid flows develop. It is observed that due to strong coupling and frictional damping the laminar flow relaxes into a crystalline shell structure. In contrast, result in the crystallization of the laminar flow. In addition, the presence of flow instabilities induces melting of the crystalline flow.

Third, the microscopic and macroscopic observations shall be combined to a consistent description in order to gain a better understanding of the influence of microscopic motion on the macroscopic flow behavior. The analysis of a structural phase transition inside the inhomogeneous flow reveals that the time and length scales for individual particle motion are much shorter than those describing the hydrodynamical behavior of the flow. Hence, it is concluded that the individual particle motion dominated by strong coupling only affects the local short time evolution of the flow. Thus, the global flow can be described in terms of hydrodynamic behavior.



# Contents

<b>1</b>	<b>Introduction</b>	<b>1</b>
<b>2</b>	<b>Dust in Anodic Plasmas</b>	<b>3</b>
2.1	Basics of Dusty Plasmas . . . . .	3
2.1.1	Dust Charging . . . . .	4
2.1.2	Forces on Dust . . . . .	5
2.2	Anodic Plasmas . . . . .	8
2.2.1	Experimental Setup . . . . .	9
2.2.2	Properties of Anodic Plasmas . . . . .	10
2.2.3	Dust Confinement in Anodic Plasmas . . . . .	11
<b>3</b>	<b>Methodical Approach</b>	<b>13</b>
3.1	Experimental Diagnostics . . . . .	13
3.1.1	Probe Diagnostics . . . . .	14
3.1.2	Optical Diagnostics . . . . .	17
3.2	Langevin Dynamics Simulations of Dusty Plasmas . . . . .	19
3.2.1	Model of Dust Flows in a Toroidal Trap . . . . .	20
3.2.2	Langevin Dynamics Simulations on Graphics Processing Units . . . . .	22
<b>4</b>	<b>Toroidal Dust Streaming</b>	<b>25</b>
4.1	Torus Formation . . . . .	26
4.2	Stationary Flow Properties . . . . .	28
4.3	Local Evolution of the Flow . . . . .	30
4.4	Instabilities . . . . .	32
4.4.1	Shear Flow Instability . . . . .	32
4.4.2	Standing Shocks . . . . .	35
4.4.3	Dust-Density Waves . . . . .	38
4.5	Influence of a Sheared Force Field . . . . .	39
<b>5</b>	<b>Summary and Conclusions</b>	<b>43</b>
<b>A</b>	<b>Reprints of peer-reviewed articles</b>	<b>47</b>
A.1	Toroidal Dust Clouds and Voids in a Magnetized Anodic Plasma . . . . .	49
A.2	Toroidal dust motion in magnetized plasmas . . . . .	55
A.3	Simulation of dust streaming in toroidal traps: Stationary flows . . . . .	63

---

A.4 Experiments and Simulations of Particle Flows in a Magnetized Dust Torus	73
A.5 Dust Streaming in Toroidal Traps . . . . .	81
A.6 Spontaneous symmetry breaking in magnetized dust flows . . . . .	87
<b>Bibliography</b>	<b>95</b>



# 1 | Introduction

A plasma consists of ions, electrons and neutrals. If a fourth component, macroscopic solid particles (so-called dust particles) is immersed into the plasma, it is usually called a complex (or dusty) plasma. Complex plasmas are studied in the context of astrophysics [1, 2] and are of importance in technological plasma processes, e.g., see Refs. [3–6]. The properties of dust become increasingly important in fusion research [7–10]. Furthermore, dust particles can be used as probes [11, 12]. The discovery in 1994 of the Coulomb crystal [13–17] marks the beginning of basic research in complex plasmas. Since the particles obtain a large negative charge, they form crystal-like structures due to their electrostatic repulsion. Thus, these structures can be used as a model system for strongly coupled Coulomb systems which are known for ions in Paul traps [18–20] or in colloidal suspensions [21].

The main advantages of complex plasmas are: (i) the slow dust dynamics with typical frequencies in the range of tens to a few hundred Hertz, (ii) interparticle distances of the order of hundred microns, (iii) individually observable particles and (iv) a variety of manipulation possibilities, making complex plasmas an ideal model system for the study of coupled many-particle systems at the kinetic level [22–26]. In addition, depending on the coupling strength, dust particles can exhibit both solid and fluid behavior. Hence, a variety of investigations were conducted regarding the confinement and structure of two- [27, 28] and three-dimensional [29–31] finite systems, as well as dynamical behavior like phase transitions [28, 32–43], Mach cones [44–48] and waves [49–57] including nonlinear waves like solitons [58–60] and shock waves [61–63]. Furthermore, transport phenomena, e.g., heat transport [64, 65] or the determination of shear viscosity [66, 67] are investigated both experimentally and by means of numerical calculations.

The influence of streaming ions is another active topic and is studied regarding the ion drag force [68–77], ion wakes (e.g., see Refs. [78, 79] and references therein) or the formation of voids (dust-free regions) [80–94] that result from an excess of the ion drag force over other confining forces, usually the electric field force.

Magnetic field effects have also attracted substantial attention since they affect the dynamics of the light plasma species due to the Lorentz force. This in turn can influence the charging of dust as well as the forces that act on the dust. A direct influence of the magnetic field on dust for sufficiently strong magnetic field is one of the major objectives in this field [95]. However, already a weak magnetic field can cause a rotation of a dust cloud in  $\mathbf{E} \times \mathbf{B}$  direction [96–99] due to the Hall component of the ion flow. For stronger magnetic fields, the magnetization of ions can also alter the properties of ion wakes [100].

Another interesting subfield is the study of strongly coupled dust flows including vortex [80, 101–103] or shear flows [66, 101, 104–106]. Often, the dust flows are driven externally by laser manipulation [66, 101, 106] or a neutral gas flow due to thermal creep [80, 102, 103, 105]. In contrast to an external excitation, the ion drag can also drive a dust motion, e.g., dust rotation in a magnetic field.

In hydrodynamics, fluid flows can be divided into categories, e.g., incompressible flows, steady or unsteady flows, laminar or turbulent flows, to name a few. Furthermore, flow instabilities like shocks, Rayleigh-Taylor or Kelvin-Helmholtz instabilities are well known from fluid mechanics. Since complex plasmas allow an investigation of the dynamics on the kinetic level, the possible objectives can be formulated as follows: Is it possible to find similar categories for dust flows? What happens at small length scales when the discreteness of the system dominates and the assumption of a continuous fluid breaks down? And regarding the special properties of complex plasmas, how does strong coupling of the particles influence the flow properties? How is the individual particle motion connected to the overall flow?

In this thesis, these questions are tackled by investigating the structure and the dynamics of torus-shaped dust clouds in a magnetized anodic plasma, a DC discharge that is formed in front of a biased electrode. Barkan *et al.* [96] were the first to report on the confinement of a void-free dust cloud in an anodic plasma. However, Trottenberg *et al.* [107] reported on the observation of a torus-shaped dust cloud with a distinct hole in its center. It was later concluded that small void-free dust clouds are in fact part of a system that only fills a fraction of the toroidal dust trap. Iris Pilch studied the torus-shaped dust clouds in more detail in terms of optical investigations. Based on probe measurements I performed as a diploma student, we developed a single-particle model describing the confinement and formation of torus-shaped dust clouds in terms of a hierarchy of forces. The confinement was attributed to the radial components of ion drag and electric field force. The formation of dust tori was given by the interaction of the much weaker forces, i.e., gravity, friction and an azimuthal Hall component of the ion drag. This model is part of a joint publication [108] and serves as the basis for this thesis. For the study of toroidal dust flows, two complementary approaches are used: On the one hand, the experimental investigations of torus-shaped dust clouds are continued using a refined observation geometry [109]. On the other hand, the single-particle model is extended and is used as the physical basis for molecular dynamics simulations.

The present work is a cumulative thesis and led to several peer-reviewed publications [110–115] that can be found in the Appendix A. It is structured as follows: Chap. 2 gives a short survey of the fundamentals of complex plasmas together with a description of the experimental setup and the characteristic of anodic plasmas including the dust confinement. Chap. 3 is dedicated to the methods that are used for the study of torus-shaped dust clouds: For the experiments, the diagnostics for the analysis of the plasma and the dust dynamics are briefly introduced and for the numerical studies, the extended model together with the characteristics of the simulations are presented. Both experimental and numerical results are discussed in Chap. 4. A summary is given in Chap. 5.

# 2 | Dust in Anodic Plasmas

In order to study the dynamics of complex plasmas, the particles must be confined inside the plasma. For this purpose, it is important to study the forces acting on the dust for the understanding of the confinement and the dynamical behavior of the particles inside the plasma. This chapter gives a brief overview of the fundamentals of complex plasmas. Since a complete overview is beyond the scope of this work, the reader is referred to textbooks [25, 26, 116, 117] and review articles [22–24, 118, 119] for a more detailed description.

In Sec. 2.1, the basic properties of complex plasmas are discussed along with the charging mechanisms and the resulting forces acting on the dust. Then, in Sec. 2.2, the experimental setup, the properties of anodic plasmas and finally the dust confinement in anodic plasmas will be presented briefly.

## 2.1 Basics of Dusty Plasmas

In this section, the basic properties of complex plasmas are presented that are necessary for the understanding of the results discussed in this work.

A complex plasma consists of electrons, ions and neutrals along with small particles immersed into the plasma. Compared to the other plasma species, the so called *dust* particles are very large with radii  $r_d$  in the range of a few nanometer up to tens of microns. Since the particles become electrically charged, see Sec. 2.1.1, they alter the quasineutrality condition of the plasma:

$$n_e + Z_d n_d = n_i, \quad (2.1)$$

with  $n_e$  the electron number density,  $n_i$  the (singly positively charged) ion number density,  $n_d$  the dust number density and  $Z_d$  the number of elementary charges on a dust particle. For situations considered in this work, the dust density is orders of magnitude smaller than the ion density ( $n_d \ll n_i$ ) so that electron and ion density can be assumed to be equal here.

Due to Coulomb attraction of the positively charged ions and electron repulsion, the dust potential  $\phi_d$  will be shielded from the surrounding plasma as follows [116]:

$$\phi_d(r) = \frac{Q_d}{4\pi\epsilon_0 r} e^{-r/\lambda_D}, \quad (2.2)$$

with  $Q_d = Z_d e$  the dust charge, and  $r$  the distance from the dust grain. This shielded Coulomb potential is also called Debye-Hückel or Yukawa potential. The linearized Debye

length  $\lambda_D$  is given by

$$\frac{1}{\lambda_D^2} = \frac{1}{\lambda_{De}^2} + \frac{1}{\lambda_{Di}^2} \quad (2.3)$$

with the electron and ion Debye length, respectively,

$$\lambda_{De}^2 = \frac{\epsilon_0 k_B T_e}{n_e e^2}, \quad \lambda_{Di}^2 = \frac{\epsilon_0 k_B T_i}{n_i e^2}, \quad (2.4)$$

with the electron temperature  $T_e$  and the ion temperature  $T_i$ . For typical experimental parameters used in this work, the Debye length is  $\lambda_D \approx 250 \mu\text{m}$ .

When a system of  $N$  dust particles confined by external forces is considered, they will interact via their shielded Coulomb potentials, Eq. (2.2). Due to the contact with their surrounding environment, the dust particles will obtain a dust temperature  $T_d$ . Then, the system can be classified using the coupling parameter

$$\Gamma = \frac{Q_d^2}{4\pi\epsilon_0 a_{WS}} \frac{1}{k_B T_d}, \quad (2.5)$$

with  $a_{WS} = (4\pi n_d/3)^{-1/3}$  is the Wigner-Seitz radius.  $\Gamma$  denotes the ratio of Coulomb energy of neighboring particles to their thermal energy. For  $\Gamma < 1$  the system is weakly coupled and behaves like a gas, whereas for  $\Gamma > 1$ , the system is strongly coupled and exhibits fluid-like behavior. If  $\Gamma$  exceeds a critical value of  $\Gamma_{\text{crit}} = 170$ , the particles arrange themselves in crystalline structures [13].

In most experiments with particles of some  $\mu\text{m}$  radius, the interparticle distance is roughly given by the Debye length and is thus large compared to the particle size. Hence, the system is transparent which allows an easy observation of the whole system. The time scale for the dynamics of the plasma species is given by their plasma frequency  $\omega_{ps} = [n_s q_s^2 / (\epsilon_0 m_s)]^{1/2}$ . The subscript  $s=e,i,d$  denotes the different plasma species electrons, ions, and dust. Due to the small charge-to-mass ratio of the dust and its low density compared to electrons and ions, the dust dynamics is so slow that it is easily observable with standard video microscopy. Hence, complex plasmas are ideally suited for the study of many-particle systems on the kinetic level.

### 2.1.1 Dust Charging

Particles inside a plasma are subjected to several charging processes. For astrophysical plasmas [1, 120], photoemission [120] due to UV radiation plays a major role together with secondary electron emission [121, 122]. Both processes have the tendency to charge the dust positively which could be verified in laboratory experiments [123, 124].

For laboratory plasmas, charge collection due to electron and ion currents is the main charging process. The orbital motion limited (OML) model [125] is usually used to determine the surface potential  $\phi_d$  of an isolated particle in a collisionless plasma. Due to the higher mobility of the electrons the dust will obtain a negative charge, thus attracting positive ions and repelling electrons. The velocity dependent collection cross-section for attracted ions reads [125]:

$$\sigma_i(v) = \pi b_c^2 = \pi r_d^2 \left( 1 + 2 \frac{b_{90}}{r_d} \right) \quad (2.6)$$

with  $r_d$  the particle radius,  $b_c$  the radius for grazing incidence and  $b_{90} = r_d e |\phi_d| / (m_i v^2)$  the Coulomb radius for  $90^\circ$  scattering. The cross-section for the repelled electrons reads

$$\sigma_e = \pi r_d^2 \exp\left(\frac{e\phi_d}{k_B T_e}\right). \quad (2.7)$$

The floating potential  $\phi_{fl}$  is determined via an equilibrium of electron and ion current onto the particle:

$$\left(\frac{8k_B T_e}{\pi m_e}\right)^{1/2} \exp\left(\frac{e\phi_{fl}}{k_B T_e}\right) = \left(\frac{8k_B T_i}{\pi m_i}\right)^{1/2} \left[1 - \frac{e\phi_{fl}}{k_B T_i}\right]. \quad (2.8)$$

Solving this equation numerically and assuming that the particle is a spherical capacitor with a capacitance  $C = 4\pi\epsilon_0 r_d$ ,<sup>1</sup> the dust charge  $Q_d = C\phi_{fl} = Z_d e$  can be determined.

However, the presence of potential barriers [126, 127], streaming ions [120, 128, 129], collisions [130–132] or a dense packing of the dust particles [1, 133–135] can significantly alter the dust charge as predicted by the OML model.

Measurements of the particle charge have been performed by means of resonance methods [15, 136, 137], wave phenomena [54, 132, 138], particle collisions [139], a reduction in the electron saturation current [140] or by means of a controlled neutral gas rotation [141]. These experiments confirm that the OML theory estimates an upper limit for the dust charge.

### 2.1.2 Forces on Dust

Dust particles immersed into a plasma are subject to different forces which are briefly discussed here.

#### Gravity

In all Earth-bound experiments, the gravitational force on a spherical dust particle reads:

$$\mathbf{F}_g = m_d \mathbf{g} = \frac{4\pi}{3} \rho_d r_d^3 \mathbf{g}, \quad (2.9)$$

with  $m_d$  the particle mass,  $\rho_d$  the particle mass density and  $\mathbf{g}$  the gravitational acceleration. For  $\mu\text{m}$ -sized particles, this force can become dominant while for nanometer-sized dust, gravity can be neglected. In this work, melamine formaldehyde particles with  $\rho_d = 1514 \text{ kg/m}^3$  and diameter  $2r_d = 0.97 \pm 0.05 \mu\text{m}$  were used. For these particles, the force of gravity is  $F_g = 0.7 \times 10^{-14} \text{ N}$  and is more than one order of magnitude smaller than the total electric field force or the ion drag force as discussed later, cf. Fig 3.4(b).

#### Neutral gas drag

The neutral gas drag can be assumed to be a friction force in most experiments due to the collision of dust particles with the neutral gas background. For a dust particle with drift velocity  $\mathbf{v}_{d,d}$ , the neutral drag can be written as follows:

$$\mathbf{F}_N = -m_d \beta \mathbf{v}_{d,d}, \quad (2.10)$$

<sup>1</sup>The capacity of a spherical capacitor with inner radius  $r_d$  and outer radius  $\lambda_D$  is given by  $C = 4\pi\epsilon_0 r_d \lambda_D / (\lambda_D - r_d)$ . For  $r_d \ll \lambda_D$ , it reduces to  $C = 4\pi\epsilon_0 r_d$ .

<sup>2</sup>Throughout this work,  $\mathbf{A}$  denotes the vectorial quantity and  $A = |\mathbf{A}|$  denotes the absolute value.

with the Epstein friction coefficient  $\beta = \delta(8/\pi)p(r_d\rho_d v_{\text{th,n}})^{-1}$  [142], gas pressure  $p$  and the thermal velocity of the neutral gas  $v_{\text{th,n}} = [8k_B T_n/(\pi m_n)]^{1/2}$ . The parameter  $\delta$  lies in the range between 1 (for specular reflection) and 1.44 (for diffuse reflection). Recently, Carstensen *et al.* [143] confirmed experimentally the validity of Eq. (2.10) over a wide pressure range of  $p = (1 - 100)$  Pa for different noble gases (He, Ne, Ar, Kr) and found  $\delta \approx 1.44$ .

### Electric field force

Due to the electric charge of the particle, an electric field  $\mathbf{E}$  inside the plasma exerts an electric field force

$$\mathbf{F}_{\text{el}} = Q_d \mathbf{E} \quad (2.11)$$

onto the dust. Since the particles are negatively charged, the electric field force is directed antiparallel to the electric field. For electric field strengths of  $E = 1000$  V/m as observed in the experiment,  $F_{\text{el}} = 4 \times 10^{-13}$  N is considerably larger than gravity.

### Ion drag force

The ion drag force describes the momentum transfer of ions onto the dust. It has been studied analytically [68–70], in terms of simulations [71–73] and experimentally [74–77]. The influence of collisions on the ion drag is also an active topic of research [144]. Furthermore, the wake potential downstream of a particle immersed in an ion stream is studied extensively [145–149].

The ion drag force consists of a collection part due to ions directly hitting the dust and an orbital part because of Coulomb scattering of the ions. In general, the ion drag force can be calculated as follows [69]:

$$\mathbf{F}_i = \int \mathbf{v} m_i v f_i(\mathbf{v}) [\sigma_{\text{coll}}(v) + \sigma_{\text{orb}}(v)] d\mathbf{v}, \quad (2.12)$$

with the ion velocity distribution function  $f_i(\mathbf{v})$ , the collection cross-section  $\sigma_{\text{coll}}(v)$  and the orbital scattering cross-section  $\sigma_{\text{orb}}(v)$ . For a collisionless plasma, the collection cross-section  $\sigma_{\text{coll}}$  is given by the OML cross-section [Eq. (2.6)]. Barnes *et al.* [68] assumed a mean ion velocity  $v_{i,s} = (v_{i,d}^2 + v_{i,\text{th}}^2)^{1/2}$ , composed of ion drift velocity  $v_{i,d}$  and ion thermal velocity  $v_{i,\text{th}}$  to avoid the integration of Eq. (2.12). However, using  $v_{i,s}$  only gives exact results for very slow ( $v_{i,d} \ll v_{i,\text{th}}$ ) or very high ion drift velocities ( $v_{i,d} \gg v_{i,\text{th}}$ ). Better results for the collection force were obtained when the integration over a shifted Maxwellian distribution was conducted [72]:

$$F_{i,\text{coll}} = n_i r_d p^2 m_i v_{i,T}^2 \frac{\sqrt{\pi}}{2u^2} \left\{ u(2u^2 + 1 + 2\chi)e^{-u^2} + \left[ 4u^4 + 4u^2 - 1 - 2(1 - 2u^2)\chi \right] \frac{\sqrt{\pi}}{2} \text{erf}(u) \right\}, \quad (2.13)$$

with  $u = v_{i,d}/v_{i,T}$  the ion drift velocity normalized to the most probable ion velocity  $v_{i,T} = (2k_B T_i/m_i)^{1/2}$  and the normalized dust potential  $\chi = -Z_d e \phi_d / (k_B T_i)$ .

Ions that contribute to the orbital part of the ion drag have to come very close to the dust particle. Thus, an unshielded Coulomb potential is assumed. Then, the orbital

cross-section reads [69]:

$$\sigma_{\text{orb}}(v) = 4\pi \int_{b_{\text{min}}}^{b_{\text{max}}} \frac{b}{1 + (b/b_{90}(v))^2} db = 4\pi b_{90}^2 \ln \Lambda, \quad (2.14)$$

with the Coulomb logarithm  $\ln \Lambda$ :

$$\ln \Lambda(v) = \ln \left[ \frac{b_{90}^2(v) + b_{\text{max}}^2(v)}{b_{90}^2(v) + b_{\text{min}}^2(v)} \right]^{1/2}. \quad (2.15)$$

The integration limits of Eq. (2.14) are crucial for the value of the Coulomb logarithm. While the lower limit is given by  $b_c$ , the upper limit has been discussed extensively. Barnes *et al.* [68] chose the upper limit to be the Debye length  $\lambda_D$  which is only valid when  $b_{90} \ll \lambda_D$ . Khrapak *et al.* [69] argued that for large dust particles or slow ion drifts this upper limit underestimates the ion drag and thus proposed an upper limit that takes all ions into account which approach the dust particle closer than the Debye length. Then, the Coulomb logarithm [cf. Eq. (2.15)] reads:

$$\ln \Lambda(v) = \ln \left[ \frac{b_{90}(v) + \lambda_{\text{scr}}}{b_{90}(v) + r_d} \right]^{1/2}. \quad (2.16)$$

Zafiu *et al.* [74, 75] studied the ion drag experimentally. Their findings were subject to a debate on the correct interpretation of the experimental results [150, 151] and showed the importance of a correct choice of the screening length. Furthermore, the applicability of collisionless models to experiments at higher pressures was discussed.

In a different experimental setup, Hirt *et al.* [76, 77] performed ion drag investigations in a collisionless situation. They found that for high ion energies, the Barnes model [68] gives a good description of the experimental results while for slowly streaming ions the Khrapak model [152] was found to give a better description.

The influence of the ion drift on the Debye shielding has also been discussed. For an isotropic plasma, the linearized Debye length is the effective screening length, while for high ion drift velocities, the ions cannot participate in the screening so that the screening length is given by the electron Debye length [150, 153]. Therefore, Khrapak *et al.* [70] proposed a velocity dependent screening length  $\lambda_{\text{scr}}^2(v) = \lambda_{\text{De}}^2/[1 + k_B T_e/(k_B T_i + m_i v^2)]$  to account for the different asymptotic behavior for slow and fast ion drifts.

Recently, Hutchinson [73] studied the self-consistent collisionless ion drag onto a particle by means of particle-in-cell simulations and found that both models by Khrapak and Barnes underestimate the ion drag. He followed the calculation of Chandrasekhar [154] who calculated the momentum transfer of stars in the gravitational field of another star. Assuming that the Coulomb logarithm is not dependent on the ion velocity, the velocity integration of Eq. (2.12) yields [73]:

$$F_{\text{i,orb}} = n_i \frac{q_i^2 \phi_d^2}{m_i v_{i,t}^2} r_d^2 8\pi G(u) \ln \Lambda, \quad (2.17)$$

with the Chandrasekhar function  $G(u) \equiv [\text{erf}(u) - 2ue^{-u^2}/\sqrt{\pi}/(2u^2)]$  [154]. For the Coulomb logarithm, Hutchinson used the model by Khrapak [cf. Eq. (2.16)]. Then,

he proposed an approximate analytic expression for an effective ion energy that was fitted to the simulation results. With the effective ion velocity

$$m_i v_{\text{eff}}^2 = 2k_B T_i + m_i v_i^2 \times \left\{ 1 + \left[ \frac{v_i / \sqrt{k_B T_e / m_i}}{0.6 + 0.05 \ln(M) + (\lambda_{De} / 5r_d)(\sqrt{k_B T_i / k_B T_e} - 0.1)} \right]^3 \right\}, \quad (2.18)$$

with  $M$  being the ion mass in units of the mass of hydrogen, and using

$$b_{90} = r_d e \phi_d / (m_i v_{\text{eff}}^2), \quad \lambda_{\text{scr}}^2 = \lambda_{De}^2 / [1 + 2k_B T_e / (m_i v_{\text{eff}}^2)] + r_d^2 \quad (2.19)$$

as the parameters for the Coulomb logarithm, he found good agreement between this analytic expression and his simulation results.

With his simulations, Hutchinson covered the range where the dust radius is comparable to the electron Debye length ( $5 \leq \lambda_{De} / r_d \leq 20$ ). However, in the limit of very small particles, as used in the present work ( $\lambda_{De} / r_d \approx 800$ ), the different ion drag theories of Khrapak and Hutchinson coincide [155].

### Interparticle forces

Up to now, only an isolated dust particle was considered. In this thesis, extended dust clouds containing many particles  $N = \mathcal{O}(10^2 - 10^4)$  are studied. Thus, the particle interaction due to their shielded Coulomb (Yukawa) potentials [cf. Eq. (2.2)] has to be considered, too. Considering  $N$  particles, the  $i$ th particle moves in the electric field of the  $N - 1$  other particles, resulting in the Yukawa interaction force

$$\mathbf{F}_Y(\mathbf{r}_i) = Q_d \sum_{i \neq j}^N \mathbf{E}_i(\mathbf{r}_i) = \sum_{i \neq j}^N \frac{Q_d^2}{4\pi\epsilon_0 r_{ij}^3} \exp\left(-\frac{r_{ij}}{\lambda_D}\right) \left(1 + \frac{r_{ij}}{\lambda_D}\right) \mathbf{r}_{ij}. \quad (2.20)$$

Here,  $\mathbf{r}_i$  is the position of the  $i$ th particle and  $\mathbf{r}_{ij}$  is the distance vector between the  $i$ th and the  $j$ th particle.

### Influence of a magnetic field

In the presence of a magnetic field, the Lorentz force

$$\mathbf{F}_L = q(\mathbf{v} \times \mathbf{B}) \quad (2.21)$$

acts on all charged plasma species. The Lorentz force on a dust particle is usually negligible for all technically achievable magnetic field strengths  $B$ . The ion motion across  $\mathbf{B}$  due to the Lorentz force can have a significant influence on the dust dynamics, as discussed in Sec. 4.1.

## 2.2 Anodic Plasmas

In this section, the properties of anodic plasmas are briefly discussed. First, the experimental setup used in this work is presented. Then, the fundamentals of anodic plasmas are described. A brief description of the confinement of dust particles in anodic plasmas concludes this section.



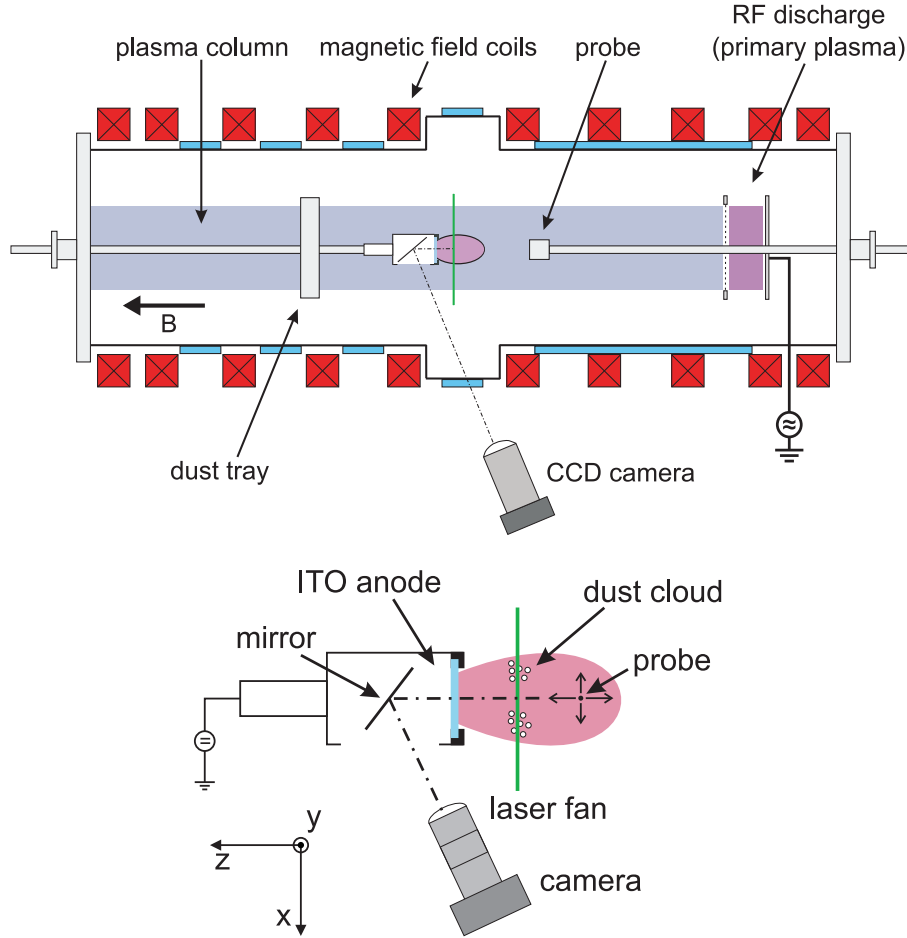


**Figure 2.1:** (Top) Top view sketch of the experimental setup. (Bottom) Detailed sketch of the observation geometry together with the used coordinate system. The indium-tin-oxide (ITO) coated anode is driven with a dc voltage. The dust particles are illuminated by a vertical laser fan ( $x - y$  plane) and the scattered light is deflected and recorded by a camera viewing through a side window.

### 2.2.1 Experimental Setup

The experiments presented in this thesis were conducted in the experiment Matilda-II, a cylindrical vacuum chamber 107 cm in length and 30 cm in diameter which is sketched in Fig. 2.1. As the primary plasma source, a capacitively coupled radio-frequency discharge ( $f = 27.12$  MHz) at low power of  $P_{\text{RF}} = (2 - 5)$  W is used. A secondary DC discharge is formed in front of a positively biased electrode. The electrode is referred to as anode and the DC discharge as anodic plasma. The anode is operated at voltages of  $U_A = (70 - 110)$  V and low currents of  $I_A = (8 - 20)$  mA. The experiments were performed in argon gas at pressures of  $p = (3 - 8)$  Pa. The external magnetic field has a strength of  $B = (5 - 20)$  mT.

Spherical monodisperse melamine formaldehyde dust particles with diameter  $2r_d = (0.97 \pm 0.05)$   $\mu\text{m}$  were used in the experiments. An indium-tin-oxide (ITO) coated glass substrate was taken as the anode, which is optically transparent and electrically conducting [109]. A vertical laser fan ( $\lambda = 532$  nm,  $P_\lambda = 2$  W) illuminates the dust particles in front

of the anode. The scattered light is then deflected by a mirror and recorded by a camera viewing through a side window. In Fig. 2.1, the experimental setup together with the coordinate system is sketched. The direction of gravity defines the negative  $y$ -axis, the horizontal axis of the vacuum chamber (and the direction of the magnetic field) defines the  $z$ -axis and the  $x$ -axis is tangential to the anode surface and completes the Cartesian coordinate system.

For the determination of the plasma parameters, a combination of a Langmuir and emissive probe is used. These probes are axially movable and radially rotatable to allow two-dimensional measurements in the  $x - z$  plane assuming rotational symmetry of the anodic plasma. Typical plasma parameters are ion density  $n_i = 10^{15} \text{ m}^{-3}$  and electron temperature  $T_e = 3 \text{ eV}$ . Due to a drift motion of the ions within an electric field that leads to ion heating [107, 156], the ion temperature  $T_i = 0.1 \text{ eV}$  exceeds the neutral gas temperature  $T_n$ .

### 2.2.2 Properties of Anodic Plasmas

Now, the basic properties of anodic plasmas are briefly presented. Malter, Johnson and Webster [157] carried out the first detailed study on low pressure arcs. They described the principle behavior and classified, depending on the anode voltage, the different observed discharge modes: the anode-glow mode at low voltages, the ball-of-fire mode and for high voltages the temperature-limited mode.

For the anode-glow mode, the plasma production is located in the Debye sheath in front of the anode where the electric field is sufficiently strong to accelerate electrons for ionization of the background gas to take place. Close to the anode surface, a faint glow can be observed [157–159].

With increasing voltage, the plasma production detaches from the anode surface and takes place in an expanded volume in front of the anode. Since the plasma has a spherical shape when no magnetic field is present [157, 160, 161], this mode is called ball-of-fire mode. When a uniform magnetic field is applied, the plasma becomes elongated along the magnetic field direction and is sometimes called *firerod* [162]. The experiments presented in this work were conducted in this mode.

In the temperature-limited mode, the anode current remains constant with increasing anode voltage. The name originates from thermionic discharges where the maximum current was limited by the temperature of the emitting material, e.g., tungsten filaments. In Matilda-II, the maximum current is given by the primary rf plasma, i.e., an increase in the rf power results in an increased anode current.

A common phenomenon observed in current-carrying plasmas is the formation of *double layers*. A double layer is characterized as a narrow region in a plasma which sustains a large potential jump. Double layers are located at the plasma boundary and occur due to counter-propagating flows of ions and electrons. These double layers were first observed in 1929 by Langmuir [163] and have since then been extensively studied [164–167]. Double layers were studied in detail in anodic plasmas [161, 162] and dust particles could be confined in an anodic plasma containing a double layer [96]. Although it is possible to obtain double layers in Matilda-II [107], the experiments presented in this work were performed in an anodic plasma without a distinct double layer.

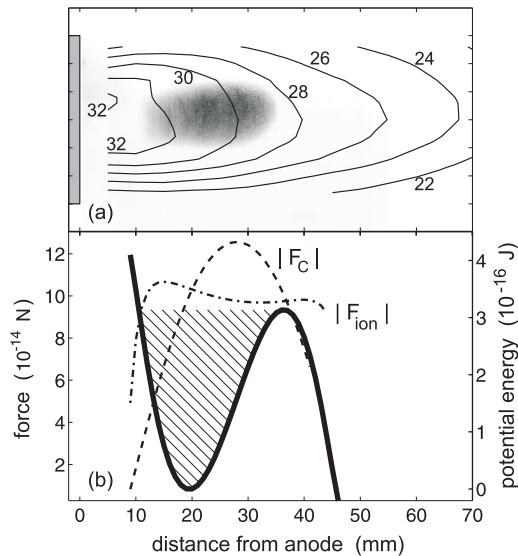


**Figure 2.2:** (a) Two-dimensional measurement of the plasma potential. The position of the anode to the left is indicated by the gray box, the dust position is also shown. (b) The axial dependency of the calculated forces of electric field force (dashed line) and ion drag force (dash-dotted line) together with the non-conservative confinement energy (thick solid line) estimated by the force balance. The hatched area indicates the position where the dust can be confined. (Adapted from [107])

### 2.2.3 Dust Confinement in Anodic Plasmas

The first observation of the confinement of a dust cloud in an anodic plasma was reported by Barkan and Merlino [96]. They studied a spherical dust cloud confined in the double layer of the anodic plasma and ascribed the dust confinement to a force equilibrium of electric field force and gravity. Furthermore, they observed a rotation in  $\mathbf{E} \times \mathbf{B}$  direction of the cloud and discussed the influence of a neutral drag and the ion drag onto the dust.

The confinement of dust clouds in Matilda-II in axial direction was examined in detail by Trottenberg *et al.* [107, 168]. Here, the confinement is given by a force equilibrium of electric field force and ion drag. By means of probe measurements, Trottenberg *et al.* found the plasma potential to have a convex structure [see Fig. 2.2(a)] with the electric field pointing away from the anode. Since the ion drag force is nearly aligned with the electric field, the particles will be pushed away from the anode. The electric field force, acting on the negatively charged dust, is directed in opposite direction of the electric field. Since the particles used here are smaller than those used by Barkan and Merlino, gravity is more than one order of magnitude smaller than the electric field force and ion drag and is thus negligible for the confinement here.

For the axial dust confinement [107, 168], the electric field force along the central axis was calculated from the plasma potential. For the determination of the ion drag, the approach by Daugherty and Graves [169] was used. Then, from the total force  $F = F_{\text{el}} + F_{\text{i}}$ , a non-conservative potential energy was calculated [see Fig. 2.2]. The resulting confinement region agreed well with the position where the dust was observed. The radial

confinement was ascribed to the strong electric field in radial direction at the boundary of the anodic plasma.

The radial confinement was studied by Pilch, Reichstein and Piel [108, 155]. Based on probe measurements, the ion drag and the electric field force were determined in radial direction from the two-dimensional plasma potential profile. The analysis of these force components revealed that for a sufficiently high ion density, a dust-free region (void) in the center of the weakly magnetized anodic plasma develops that allows the confinement of torus-shaped dust clouds. The radial confinement will be discussed in more detail in Sec. 3.2.1 since it is crucial for the understanding of the dynamics of torus-shaped dust clouds.

In this chapter, the fundamentals of complex plasmas as well as the experimental setup and the confinement of dust clouds in anodic plasmas were presented. The confinement was found to result from a force equilibrium of electric field force and ion drag while gravity could be neglected for the confinement. The methods used for the complementary approaches for the study of torus-shaped dust clouds are presented in the next chapter and the results are discussed in Chap. 4.

# 3 | Methodical Approach

After discussing the properties of dust particles in anodic plasmas and their confinement, this chapter is dedicated to the different methods used in this work for the analysis of the plasma parameters and the dust dynamics.

For a comprehensive understanding of dusty plasma experiments, the dynamics of the dust particles as well as the forces arising from the plasma environment that act on the dust have to be known as precisely as possible. For the determination of the forces, an accurate measurement of the plasma parameters is important. The use of electric probes for this purpose is a standard technique in plasma physics. For the analysis of the dust dynamics, particle tracking velocimetry (PTV) and particle image velocimetry (PIV) are adapted from fluid mechanics and are now common in complex plasma research.

On the other hand, numerical simulations are widely used as a complementary tool to experiments. In the context of dusty plasmas, molecular dynamics (MD) simulations are often used as they provide the possibility to study the dynamics of many body systems on the kinetic level. With the advent of CUDA developed by NVIDIA [170, 171], an architecture that allows an effective parallelization of calculations, MD simulations of complex plasmas are easily realized on personal computers.

In Sec. 3.1, the experimental diagnostics are presented with an emphasis on their working principles. For the simulation of these clouds, the hierarchic single-particle model [108, 155, 172] for the confinement and formation of torus-shaped dust clouds is extended to include many-particle interactions, inertia effects and the influence of the confinement on the dust dynamics. A description of the extended model is given in Sec. 3.2 together with the characteristics of the simulations. Both experimental and numerical methods were used for the study of torus-shaped dust clouds and the results will be presented in the following chapter.

## 3.1 Experimental Diagnostics

This section is dedicated to the experimental diagnostics. On the one hand, the plasma parameters like electron density  $n_e$ , electron temperature  $T_e$  and plasma potential  $\phi_{pl}$  are essential for the understanding of the plasma. For the determination of these properties electric probes are utilized and their principles are given in Sec. 3.1.1. On the other hand, the dust dynamics is analyzed by means of optical measurements. For this purpose, two techniques from fluid dynamics, the particle tracking velocimetry (PTV) and the particle image velocimetry (PIV) are adopted and their principles are presented in Sec. 3.1.2.

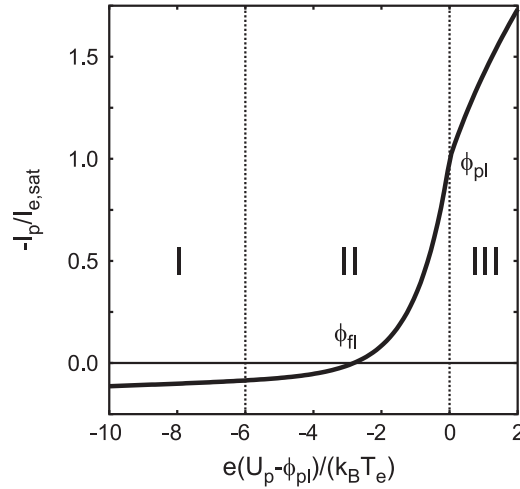


**Figure 3.1:** Schematic  $I_p - U_p$  characteristic of a cylindrical Langmuir probe. Depending on the bias voltage  $U_p$ , the different regimes are I: ion saturation regime, II: electron retardation regime and III: electron saturation regime. Two important values can be directly seen in the characteristics: the floating potential  $\phi_{fl}$  and the plasma potential  $\phi_{pl}$ . (Adapted with modifications from [26])

### 3.1.1 Probe Diagnostics

For the determination of the plasma parameters, a combination of a Langmuir probe and an emissive probe was used. Both techniques are widely known in plasma physics due to their simple setup. For a more complete overview on probe diagnostics, the reader is referred to textbooks [26, 173–176].

#### Langmuir probes

In 1926, Mott-Smith and Langmuir [125] studied the influence of additional electrodes immersed in a glow discharge and found a characteristic dependency of the probe current  $I_p$  on the applied voltage  $U_p$ . For cylindrical, spherical and planar electrodes they observed a similar behavior and assuming a collisionless plasma, they could describe the  $I_p - U_p$  characteristics in terms of the *orbital-motion-limited* (OML) theory [125, 177]. For a floating spherical probe, this description is equal to the charging of dust particles (cf. Sec. 2.1.1).

Now, the principles of a Langmuir probe are presented. First of all, the physical background of the  $I_p - U_p$  characteristics of a planar probe are presented. Then, the influence of the geometry of a cylindrical probe is analyzed and finally, the effect of a magnetic field onto the probe characteristic is discussed.

In Fig. 3.1, a typical characteristic of a cylindrical Langmuir probe is shown. Depending on the bias voltage  $U_p$ , one distinguishes between three regions:

**Ion saturation regime (Region I in Fig. 3.1)** For very negative bias voltages compared to the plasma potential ( $U_p \ll \phi_{pl}$ ), all electrons are repelled from the probe and only ions contribute to the probe current. Thus, it is called *ion saturation regime*. For a planar probe, the ion saturation current  $I_{i,sat}$  is independent of the probe voltage  $U_p$  [173].

**Electron saturation regime (Region III in Fig. 3.1)** The electron saturation regime is found for  $U_p > \phi_{pl}$ , because due to their low temperature all ions are repelled from the probe and the current is given only by the electrons. Due to the much higher mobility of the electrons, the electron saturation current  $I_{e,sat}$  is much higher than the ion saturation current  $I_{i,sat}$ . Again, for a planar probe,  $I_{e,sat}$  is independent of  $U_p$  [125].

**Electron retardation regime (Region II in Fig. 3.1)** For moderate negative bias voltages ( $U_p < \phi_{pl}$ ), all ions can reach the probe while low energetic electrons are repelled from the probe. This region is called electron retardation regime. Here, the electron current is reduced by a Boltzmann factor compared to the electron saturation current:

$$I_e(U_p) = I_{e,sat} \exp\left(\frac{e(U_p - \phi_{pl})}{k_B T_e}\right) \quad (3.1)$$

For the floating potential  $\phi_{fl}$ , the ion current is balanced by the electron current and so no net current is drawn by the probe. The electron retardation current can easily be used to determine the electron temperature from the slope of  $\ln(I_e)$ . At the plasma potential  $\phi_{pl}$ , the  $I_p - U_p$  characteristic has an inflection point for planar and cylindrical probes due to the change in the probe's behavior, i.e., the change from repelling to attracting electrons and accordingly from attracting to repelling ions. A common technique for the measurement of the plasma potential is thus to determine the position of the inflection point of the characteristic. However, in this work, the plasma potential was measured using an emissive probe as discussed later.

### Influence of the probe geometry

*Orbital-motion-limited theory:* For a cylindrical probe in a collisionless plasma, the ion (electron) saturation current increases with decreasing (increasing) probe voltage due to an orbital motion of the attracted species [125, 177] that results in an effectively larger collection surface of the probe. Thus, the saturation currents, as sketched in Fig. 3.1, are not constant.

*Alternative probe theories:* Under the assumption of cold ions ( $T_i = 0$ ) in a collisionless plasma, the ions will move radially onto the probe due to a lack of angular momentum. This so-called *radial motion theory* was first discussed by Allen, Boyd and Reynolds (ABR theory) in 1957 for a spherical probe [178] and was later presented for cylindrical probes by Chen [179]. Bernstein and Rabinowitz presented an extended theory for monoenergetic ions with  $T_i > 0$  which allows the ions to have a finite angular momentum, thus making the calculation of the ion current much more challenging due to the possibility of trapped ion orbits [180].

*Validity of OML theory:* A critical comparison of the different probe theories was performed by Chen [181]. He found that for probe radii that are small compared to the Debye length ( $r_p \ll \lambda_D$ ), the OML theory is valid, while for large probes ( $r_p \gg \lambda_D$ ) the ABR theory must be considered since the orbital motions of ions in the sheath do not contribute significantly to the ion current. In addition, the effect of collisions onto the ion current was studied as well [60, 182]. For weak collisionality, the orbital motion is inhibited without hindering the ion current to the probe too much. When the angular momentum of the ions given by the mean free path  $\lambda_{mfp}$  is smaller than the one required for a grazing

incident onto the probe [cf.  $b_c$  in Eq. (2.6)], orbital motion of the ions can be significantly be reduced [183]. In the present setup (see Fig. 2.1), this situation would occur when the mean free path is smaller than  $\lambda_{\text{mfp}} \approx 300 \mu\text{m}$  [155]. For the conducted experiments, the pressure is in the range (3 – 8) Pa, which corresponds to  $\lambda_{\text{mfp}} = (800 - 300) \mu\text{m}$ , so that in the present situation the use of the OML theory is justified.

### Influence of a magnetic field

In the presence of a magnetic field, the dynamics of electrons and ions is affected and with it the probe currents. The Hall parameter  $H_s = \omega_{cs}/\nu_{sn}$ <sup>1</sup> gives the ratio of the cyclotron frequency  $\omega_{cs}$  and the collision frequency  $\nu_{sn}$ . For  $H_s > 1$ , the plasma species is magnetized and thus the dynamics is mostly restricted to a motion along the magnetic field lines. In the present setup, the electron Hall parameter is  $H_e \approx 20$  and the ion Hall parameter is  $H_i \approx 0.05$ . Thus, the electron dynamics is strongly affected by the magnetic field. For the repelled species of a probe, however, the unmagnetized OML theory is still applicable, when the Larmor radius  $r_{L,s} = v_{s,\text{th}}/\omega_{cs}$  is larger than the probe radius ( $r_{L,s} \gg r_p$ ) [184]. Thus, in the present setup ( $r_{L,e} = 340 \mu\text{m}$ ,  $r_p = 25 \mu\text{m}$ ), the electron temperature can be determined from the electron retardation current. In addition, since the ion dynamics is only weakly affected by the magnetic field, the ion saturation current is used to determine the ion density.

### Emissive probes

The measurement of the plasma potential by means of determining the inflection point of the  $I_p - U_p$  characteristic of a Langmuir probe can become erroneous when, as in the present situation, the magnetic field alters the electron dynamics. Therefore, the use of an emissive probe is favored here. For a more comprehensive overview on emissive probes the reader is referred to a review article by Sheehan and Hershkowitz [185].

Emissive probes were first discussed in 1929 by Langmuir [163]. Kemp and Sellen proposed a technique for the determination of the plasma potential by using the floating potential of a strongly emitting probe in 1966 [186]. The basic idea of an emissive probe is as follows: The probe wire is heated to a sufficiently high temperature  $T_{\text{wire}}$  to emit thermal electrons. For probe bias voltages  $U_p < \phi_{\text{pl}}$ , these electrons are repelled and leave the probe. For  $U_p > \phi_{\text{pl}}$ , the thermal energy of the emitted electrons is so low that they all return to the probe, so that the total probe current is only affected for  $U_p < \phi_{\text{pl}}$ . Therefore, the electron emission current can be understood as a net ion current onto the probe.

An additional ion current must be balanced by a higher electron current at the floating potential. This results in a shift of  $\phi_{\text{fl}}$  to higher voltages. If space charge effects are neglected, the floating potential coincides with the plasma potential, when electron and ion currents become equally large.

Thus, measuring the floating potential of a strongly emitting probe is a convenient method to determine the plasma potential, especially since this procedure works well even in strong magnetic fields [187]. Moreover, a floating probe does not disturb the plasma as much as a biased probe would do.

---

<sup>1</sup>The subscript s=e,i,d stands for the different plasma species electrons, ions and dust, the subscript n denotes the neutrals.



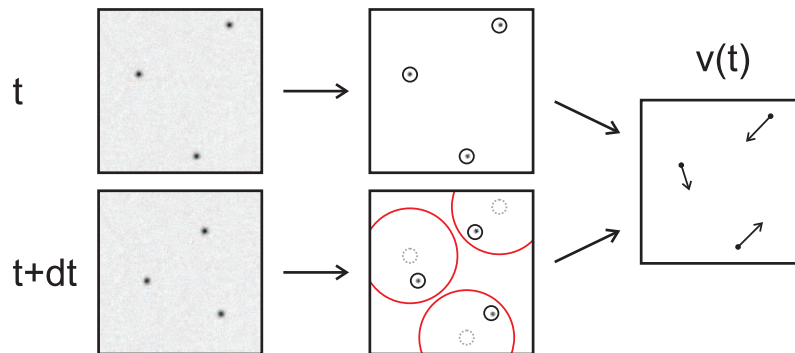


**Figure 3.2:** Principle of particle tracking velocimetry (PTV): After subtracting an offset from two successive frames (left), the particle positions are determined (center) and from the displacement, the velocities for each particle are determined (right).

However, Langmuir derived the potential around an emissive probe [163] and showed that a double layer forms around the probe and that therefore the emission current is space charge limited. Thus, the floating potential deviates from the plasma potential by  $\Delta\phi_{\text{pl}} \sim k_{\text{B}}T_{\text{wire}}/e \approx 0.2 \text{ V}$  in the present case, which is small compared to errors arising from the determination of the inflection point of a Langmuir probe characteristic.

In conclusion, electric probes are useful tools for determining ion density, electron temperature and plasma potential. Due to the invasive nature of probe diagnostics, it is not readily possible to measure inside a dust cloud since the particles are repelled due to the probe's electric field [89]. Although the presence of dust can alter the plasma parameters, e.g., a reduction of ion and electron density through recombination [188], the measurements without dust can be taken as an estimate for the plasma parameters inside the dust cloud.

### 3.1.2 Optical Diagnostics

While the probe diagnostics is essential for the determination of the plasma parameters, the dust dynamics has to be analyzed in detail as well. Since the main aspect of this work is the study of dust flows in toroidal traps, the flow profile of the dust particles is of great interest. For the determination of the flow properties of the dust cloud, two different optical diagnostics were used, the particle tracking velocimetry (PTV) and the particle image velocimetry (PIV).

#### Particle Tracking Velocimetry (PTV)

The first experiments concerning the visualization of flow properties were carried out by Prandtl in 1905 [189]. He studied the flow past obstacles by using mica particles in water as tracer particles. Other visualization techniques include, e.g., dye lines in water depicting von Kármán vortex streets [190] or smoke lines in wind tunnels to study the streamlines around an airfoil [191] and besides giving a better understanding of the fluid properties have also an artistic value [192].

These techniques are restricted to qualitative flow visualizations. For quantitative non-invasive measurements, the particle tracking velocimetry (PTV) is an advancement

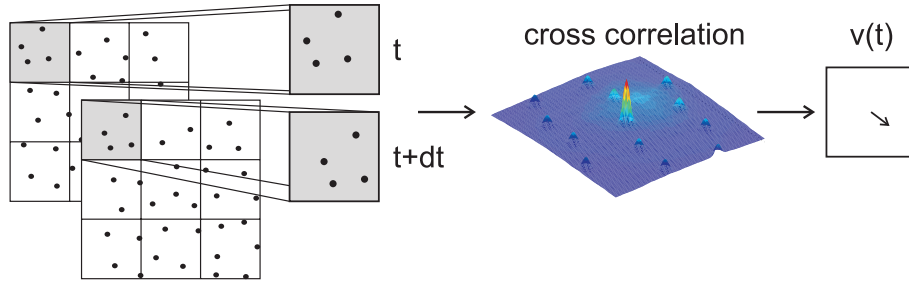


**Figure 3.3:** Principle of particle image velocimetry (PIV): Two successive images are divided into bins (left). Then, from a cross correlation between the bins with the second image (center) the mean displacement of the image information inside the bin gives the mean velocity (right).

of using tracer particles. Historically, the tracer particles were illuminated by two bursts of light and produced two images on the same piece of film, see e.g., Ref. [193]. From their displacement and the time delay between the bursts, the particle velocities were determined. In the field of dusty plasmas, the particles are illuminated by a laser and the scattered light is recorded by high-speed cameras.

The principle of the PTV analysis is sketched in Fig. 3.2. First, to minimize the noise, an offset is subtracted from each image. Then, the particle positions are determined for each frame. From the displacement of the particle positions in two successive images, the particle velocities are obtained.

Although this method is suitable for determining the properties of each particle, the maximum displacement of one particle has to be smaller than half of the minimum inter-particle distance in order to accurately identify the particles. Hence, PTV is restricted to a low particle density and small displacements resulting in the need for high-speed cameras. Furthermore, since PTV uses directly the particle positions, PTV might produce erroneous results when particles enter or leave the illuminated volume.

### Particle Image Velocimetry (PIV)

In contrast to PTV, particle image velocimetry (PIV) does not require the matching of images to a particle pair. The correlation based PIV determines the average motion of a group of particles within a small region of the image. Known for 30 years [193], this method has been established as a standard technique in fluid mechanics and several review articles [194–196] and textbooks [197–199] are devoted to the technique. Here, only the basic ideas of PIV are presented.

The working principle of PIV is sketched in Fig. 3.3. For the analysis, the images are divided into (square-shaped) interrogation regions. Then, for successive images, the spatial cross correlation of each region from the first image with the second image is computed. From the maximum of the correlation function the displacement vector for each region is obtained, thus resulting in a velocity field on a uniform grid. In this work, the MatPIV [200] routine was used.

Averaging over a group of particles makes PIV more noise-tolerant in comparison to PTV. Furthermore, since the velocity profile is directly estimated on a grid post-processing of the data, e.g., calculating the time-averaged velocity profile, is straightforward. These advantages come for the cost of losing spatial resolution compared to PTV due to the size of

the interrogation regions. In addition, since PIV only analyzes the translation of a particle group, errors may arise when the particle trajectories are curved or when the particles have significantly different velocities. Furthermore, an inhomogeneous illumination of the flow may result in erroneous velocities due to the correlation of light intensities. In these cases, the PIV technique tends to underestimate the flow velocities.

The restriction to the analysis of the in-plane velocities of the flow can be overcome by using more sophisticated PIV methods. The stereoscopic PIV technique uses two cameras at an angle to analyze the out-of-plane velocity component of a 2D-plane of the flow [201–203]. Furthermore, both holographic PIV [204] and tomographic PIV [205] offer the possibility to obtain the full three-dimensional velocity field of the studied flow.

In the context of dusty plasmas, Ed Thomas conducted the first PIV measurements in 1999 [206] and since then PIV was used extensively to study dusty plasmas, including e.g., transport phenomena [207], dust acoustic waves [208, 209] or phase transitions [210]. Also, stereoscopic [211, 212] and tomographic PIV [213] were used in the analysis of dusty plasma dynamics.

In this work, both PTV and PIV are used to study the two-dimensional flow pattern of torus-shaped dust clouds in an anodic plasma.

## 3.2 Langevin Dynamics Simulations of Dusty Plasmas

The diagnostics presented in the previous section are used to obtain experimental insights into the dynamics of dust in anodic plasmas. Numerical simulations allow a complementary approach to gain a deeper understanding of the dynamics of complex plasmas and can be used to study aspects that are experimentally challenging [214, 215] or even beyond current experimental possibilities [216, 217]. Therefore, this section is dedicated to the use of simulations for the study of torus-shaped dust clouds.

First, a general overview of the techniques of numerical simulations is given. Then, the physical model for the simulations is presented in Sec. 3.2.1 before the characteristics of Langevin dynamics simulations on graphic cards are discussed in Sec. 3.2.2.

### Simulation techniques

Based on carefully conducted experiments, the development of a theoretical model is important for the understanding of the physical processes inside the plasma. Numerical simulations have shown to be an important tool to test those theoretical models and predict new observations which in turn can be verified by further experiments. For the simulations, three main approaches exist that have both advantages and disadvantages over the other approaches. For a more complete overview, the reader is referred to textbooks on this topic [25, 218, 219].

The *first* approach is modeling the plasma as a fluid with the dust particles as an additional fluid, see e.g., [94, 220, 221]. Although fluid simulations give self-consistent solutions, due to the different time scales of the plasma species and the dust particles they are very time-consuming and the simulations typically switch between moving the plasma fluid and the microparticle fluid [221]. Both fluids are coupled via the Poisson equation and the forces acting on the particles.

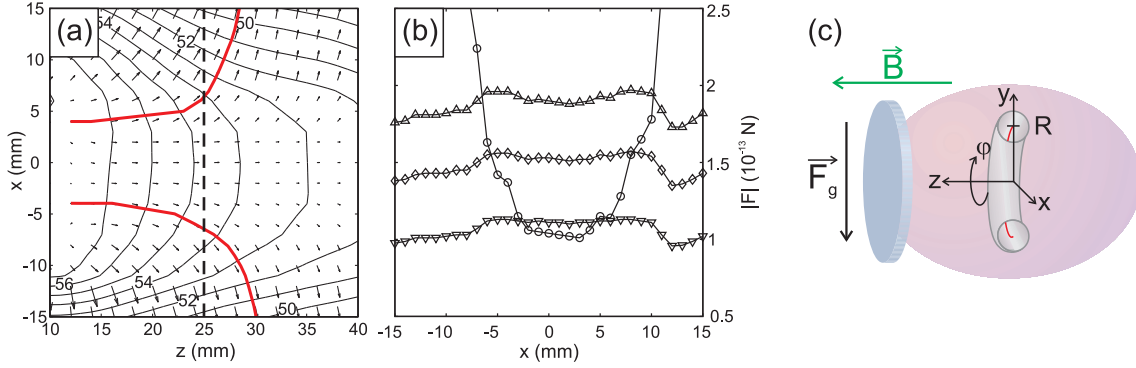


**Figure 3.4:** On the physical model of dust flows in toroidal traps: (a) Two-dimensional contours of the plasma potential together with the electric field. Two exemplary field lines are indicated by red lines. At  $z = 25$  mm (dashed line), the radial distribution of ion drag and electric field force is analyzed. (b) Radial distribution of the absolute values of the electric field force ( $\circ$ ) and the ion drag force for  $n_i = 4 \cdot 10^{15} \text{ m}^{-3}$  ( $\nabla$ ),  $n_i = 6 \cdot 10^{15} \text{ m}^{-3}$  ( $\diamond$ ) and  $n_i = 8 \cdot 10^{15} \text{ m}^{-3}$  ( $\triangle$ ). (c) Sketch of coordinate system used for the simulations. (Adapted from Appendices [A.1] and [A.4])

The *second* approach is the use of particle-in-cell (PIC) methods, often combined with Monte Carlo simulations to study the flow of ions and electrons near microparticles. The investigations include, e.g., the charging of dust particles [72, 222], ion drag [73] or the ion wake behind a dust particle [146, 148]. The electrons are either treated kinetically [222] or are assumed to be Boltzmann distributed [73, 146]. PIC simulations are also very time-consuming and thus mostly restricted to stationary dust grains.

The *third* approach is to use molecular dynamics (MD) or Langevin dynamics (LD) simulations, see Sec. 3.2.2. Here, the influence of the plasma onto the dust is introduced via the analytical expressions of the dust interaction potential [see Eq. (2.2)] and external forces like, e.g., electric field force [see Eq. (2.11)] and ion drag [see Eq. (2.17)]. Since electrons and ions only indirectly contribute to the dust dynamics, these systems are called one-component plasma (OCP). Furthermore, MD simulations study the dynamical behavior of complex plasmas on the dust time scale and are therefore computationally not as demanding as PIC or fluid simulations. However, since electrons and ions are only considered by their influence on the dust, MD simulations depend critically on the assumptions made for the plasma-dust interactions.

Hybrid approaches also exist, e.g., the particle-particle-particle-mesh (P<sup>3</sup>M) code by Matyash [145, 223, 224], a combination of PIC and MD simulations in order to study the dust charge of multiple particles immersed in a plasma.

### 3.2.1 Model of Dust Flows in a Toroidal Trap

In this work, Langevin dynamics simulations of dust flows in a toroidal trap are presented. Therefore, the physical background of the used model is presented in this section.

By means of probe measurements, the two-dimensional plasma potential profile together with the ion density in front of the anode was determined in the  $x-z$  plane. Then, the electric field  $\mathbf{E} = -\nabla\phi_{\text{pl}}$  was calculated as shown in Fig. 3.4(a). Due to the symmetric shape of the potential profile, it is justified to assume that the anodic plasma is rotational

symmetric. Hence, the electric field has no component in azimuthal direction. From the stationary equation of motion for the ions

$$m_i(\mathbf{v}_i \cdot \nabla)\mathbf{v}_i + m_i\nu_{in}\mathbf{v}_i = e(\mathbf{E} + \mathbf{v}_i \times \mathbf{B}), \quad (3.2)$$

the ion flow in the anodic plasma is determined.  $\nu_{in}$  denotes the ion-neutral collision frequency. The convective term in Eq. (3.2) is small compared to the friction term and is therefore neglected here. For the present situation with  $\mathbf{E} = (E_x, 0, E_z)$  and  $\mathbf{B} = (0, 0, B)$ , Eq. (3.2) now reads:

$$\mathbf{v}_i = \begin{pmatrix} \frac{1}{1+\mu^2 B^2} & \frac{\mu B}{1+\mu^2 B^2} & 0 \\ -\frac{\mu B}{1+\mu^2 B^2} & \frac{1}{1+\mu^2 B^2} & 0 \\ 0 & 0 & 1 \end{pmatrix} \mu \mathbf{E}, \quad (3.3)$$

with  $\mu = e/m_i\nu_{in}$  the ion mobility. The ion mobility was determined using the formula proposed by Frost [225]:

$$\mu(E, p) = \frac{\mu_0 p_0}{p} \left( 1 + \frac{AE}{p} \right)^{-1/2}, \quad (3.4)$$

with  $\mu_0 = 0.146 \text{ m}^2/\text{Vs}$ ,  $p_0 = 133 \text{ Pa}$  and  $A = 0.035 \text{ Pa m/V}$  for Ar gas.

It can easily be seen from Eq. (3.3) that due to the weak magnetic field ( $\mu B \sim 0.05$ ), the ion drift is mainly acting along the electric field direction, but has also a small Hall component in  $y$ -direction:

$$v_{i,x} = \frac{1}{1 + \mu^2 B^2} \mu E_x, \quad (3.5a)$$

$$v_{i,y} = -\frac{\mu B}{1 + \mu^2 B^2} \mu E_x, \quad (3.5b)$$

$$v_{i,z} = \mu E_z. \quad (3.5c)$$

Due to rotational symmetry, the  $x$  component acts in radial direction, while the  $y$  component can be seen as an azimuthal component of the ion drift.

Then, using the ion drag model by Hutchinson [73], see Sec. 2.1.2, the ion drag force  $\mathbf{F}_i$  [cf. Eq. (2.17)] and the electric field force  $\mathbf{F}_{el}$  [cf. Eq. (2.11)] acting on the dust are obtained.

For the radial confinement of the dust particles, the radial components of ion drag  $\mathbf{F}_{i,r}$  and electric field  $\mathbf{F}_{el,r}$  are considered. The ion drag acts in direction of the electric field while the electric field force is directed opposite to the electric field direction due to the negative dust charge. Thus, the dust confinement is given by a force equilibrium of these components as indicated by the intersection of the absolute values of these forces in Fig. 3.4(b). Since gravity is more than one order of magnitude smaller than the radial components of ion drag and electric field force, it can be neglected for the dust confinement.

For small excursions from the equilibrium position the total radial force acting on the dust varies linearly with distance from the equilibrium position. Hence, it is justified to assume a harmonic confinement potential in radial direction. For the axial confinement, Trottenberg *et al.* [107] also confirmed a harmonic confinement potential [cf. Fig. 2.2(b)].

As a result, the dust confinement potential is given by:

$$U_C(\rho, z) = \frac{m_d}{2} \omega_0^2 \left[ (\rho - R)^2 + z^2 \right] \quad (3.6)$$

with  $\omega_0$  the confinement strength in both axial and radial direction,  $\rho = (x^2 + y^2)^{1/2}$  the radial distance from the center of the anode ( $\{x,y\}=\{0,0\}$ ),  $R$  the radial distance of the potential minimum from the central axis ( $\rho = 0$ ) and  $z$  the axial distance from the potential minimum located at  $z = 0$ . The confinement force is given by  $\mathbf{F}_C = -\nabla U_C$ . The coordinate system used for the simulations is sketched in Fig. 3.4(c). The angle  $\varphi$  indicates the angular position along the confinement as ticks on a clock-dial.  $\varphi = 0$  corresponds to the 9 h and increases in clockwise direction.

The particles are under the influence of gravity  $\mathbf{F}_g$  [see Eq. (2.9)]. While neglected for the confinement, it is essential for the dynamics of torus-shaped dust clouds. Furthermore, due to the plasma environment, the particles obtain a dust charge of about  $Q_d = -2500e$  [125], which results in a shielded Coulomb (Yukawa) repulsion  $\mathbf{F}_Y$  between the particles [see Eq. (2.20)].

In addition, the Hall component of the ion drag  $\mathbf{F}_{i,\varphi}$  exerts a driving force onto the dust in azimuthal direction. It is on the order of a few percent of the radial ion drag component and roughly on the same order of magnitude as gravity. The absolute value is assumed to be constant:  $\mathbf{F}_{i,\varphi} = F_{i,\varphi} \mathbf{e}_\varphi$ . The magnitude  $F_{i,\varphi}$  is a free parameter for the simulations. Then, the sum of external forces acting on the dust is given by  $\mathbf{F}_S = \mathbf{F}_C + \mathbf{F}_g + \mathbf{F}_Y + \mathbf{F}_{i,\varphi}$ , as used in the simulation, see Sec. 3.2.2.

In order to study the influence of many-particle interactions, inertia effects and the strength of friction on the dynamics of torus-shaped dust clouds, several aspects were neglected in the simulations that may be relevant for the experiment: Due to the neutral gas background, the moving particles experience a friction force  $\mathbf{F}_N$  due to collisions with neutral gas atoms [see Eq. (2.10)]. Recently, Carstensen *et al.* [99] observed a neutral gas rotation due to crossed electric and magnetic fields. However, a possible rotation of the neutral gas column is neglected in the simulations. Furthermore, complex anodic plasmas are known to exhibit dust-density waves [107, 226–229] due to streaming ions [230]. A mechanism for the formation of dust-density waves was also not implemented in the simulations in order to keep the model simple.

### 3.2.2 Langevin Dynamics Simulations on Graphics Processing Units

After presenting the physical background of the simulations, this section aims at giving a short overview of the principles of Langevin dynamics (LD) simulations and the benefits of using graphic cards for the execution of the numerical simulations.

#### Molecular Dynamics Simulations

If a system of  $N$  particles is considered, molecular dynamics (MD) simulations solve the equations of motion for each particle for discrete times separated by a time step  $\Delta t$ . The equation of motion for the  $i$ th particle read:

$$\dot{\mathbf{r}}_i = \mathbf{v}_i \quad (3.7a)$$

$$m_d \dot{\mathbf{v}}_i = \mathbf{F}_S, \quad (3.7b)$$

with  $\mathbf{F}_S$  the sum of external forces acting on the  $i$ th particle, see Sec. 3.2.1. The integration of Eq. (3.7) can be done by, e.g., a Runge-Kutta scheme [231] or the Verlet algorithm [232, 233]. In MD simulations, though widely used, friction is not included. However,

Eq. (3.7) can be easily extended to include friction as well as heating. This extension is known as Langevin dynamics (LD) simulations.

### Langevin Dynamics Simulations

In experiments, the particles are confined in a partially ionized plasma and are thus in contact with the neutral gas background. Hence, they experience damping as well as random heating due to collisions with neutrals. In LD simulations, both effects are accounted for in a stochastic approach. A friction term accounts for the damping effect and a stochastic force  $\mathbf{F}^G$  emulates the random heating effect.<sup>1</sup> The neutral gas background can thus be seen as a heat bath for the dust particles [25].

Then, the Langevin equations of motion for the  $i$ th particle read [219]:

$$\dot{\mathbf{r}}_i = \mathbf{v}_i \quad (3.8a)$$

$$m_d \dot{\mathbf{v}}_i = \mathbf{F}_S - m_d \beta \mathbf{v}_i + \mathbf{F}^G. \quad (3.8b)$$

The fluctuation-dissipation theorem relates the random force  $\mathbf{F}^G$  to the friction term:

$$\left\langle F_{\alpha,i}^G(t_0) F_{\gamma,j}^G(t_0 + t) \right\rangle = 2m_d \beta k_B T \delta(t) \delta_{ij} \delta_{\alpha\gamma}, \quad \alpha, \gamma \in \{x, y, z\}, \quad (3.9)$$

with the temperature  $T$  of the heat bath and the Epstein collision frequency  $\beta$  [142], see Eq. (2.10). The time evolution can then be calculated using a Verlet-like algorithm [219]:

$$\mathbf{r}_i(t + \Delta t) = \mathbf{r}_i(t) + c_1 \Delta t \mathbf{v}_i(t) + c_2 (\Delta t)^2 \mathbf{a}_i(t) + \delta \mathbf{r}_i^G \quad (3.10a)$$

$$\mathbf{v}_i(t + \Delta t) = c_0 \mathbf{v}_i(t) + (c_1 - c_2) \Delta t \mathbf{a}_i(t) + c_2 \Delta t \mathbf{a}_i(t + \Delta t) + \delta \mathbf{v}_i^G. \quad (3.10b)$$

Here,  $\mathbf{a}_i = \mathbf{F}_S/m_d$  is the acceleration due to the external forces and  $\delta \mathbf{r}^G, \delta \mathbf{v}^G$  are random variables due to the random force. In the limit  $\beta \rightarrow 0$  Eq. (3.10) reduces to the velocity Verlet scheme [233].

Each pair of components of the random components is sampled from a bivariate Gaussian distribution with average zero and the following variances  $\sigma_r, \sigma_v$  and correlation coefficient  $c_{rv}$  [219, 234]:

$$\sigma_r^2 = (\Delta t)^2 \frac{k_B T}{m_d} (\beta \Delta t)^{-1} \left[ 2 - (\beta \Delta t)^{-1} \left( 3 - 4e^{-\beta \Delta t} + e^{-2\beta \Delta t} \right) \right], \quad (3.11a)$$

$$\sigma_v^2 = \frac{k_B T}{m_d} \left( 1 - e^{-2\beta \Delta t} \right), \quad (3.11b)$$

$$c_{rv} = \frac{k_B T}{m_d \beta} \left( 1 - e^{-\beta \Delta t} \right)^2. \quad (3.11c)$$

The numerical coefficients in Eq. (3.10) read:

$$c_0 = e^{-\beta \Delta t}, \quad (3.12a)$$

$$c_1 = \frac{1 - c_0}{\beta \Delta t}, \quad (3.12b)$$

$$c_2 = \frac{1 - c_1}{\beta \Delta t}. \quad (3.12c)$$

<sup>1</sup>The superscript G denotes components of a random process.

LD simulations are commonly used in the field of complex plasmas to study, e.g., diffusion properties of a 2D liquid [235, 236] or the build-up of correlations in Yukawa balls [214, 215]. In the overdamped limit where inertia effects are negligible, the resulting Brownian motion is studied extensively in the context of colloidal suspensions, see e.g., [237, 238].

### Implementation on graphic cards

During a simulation run, the sum of forces  $F_S$  acting on the dust have to be calculated for each time step. The most time-consuming calculation is the Yukawa interaction  $F_Y$  [cf. Eq. (2.20)], since for each of the  $N$  particles the interaction with every other particle has to be carried out, requiring  $N(N - 1)/2$  separate calculations. The Yukawa interaction is very similar to the *N-body problem* of  $N$  particles interacting via gravity which is very common in astrophysics and has been tackled by means of simulations for over seventy years [239].

Since the Yukawa force calculation for each particle is independent of the calculation of every other particle, a parallelization of the calculation reduces the simulation time significantly. Hence, graphic processing units (GPUs) are ideally suited for this task due to their architecture, offering a large number of processing units that can be used for parallelization.

With the advent of the *Compute Unified Device Architecture* (CUDA) developed by NVIDIA [170, 171], the use of GPUs for scientific applications increased rapidly and is now widespread used, e.g., in astrophysics [240, 241], in condensed matter physics [242], or in plasma physics [243–245].

A detailed description of the implementation of the *N-body problem* can be found in Ref. [246], that was closely adapted for the present work. The Yukawa interaction was carried out on a NVIDIA GTS 250 GPU, while the integration of Eq. (3.8) was performed on the host computer. As a benchmark, simulations with  $N = 4096$  particles were performed with the interaction being calculated both on the GPU and the CPU. Using the GPU, a reduction of the simulation time up to a factor of 50 was obtained.

### Simulation parameters

For a critical comparison with the experiment, the simulation parameters were chosen to be similar to the experiment. From the derivative of the total radial force, see Fig. 3.4(b), the confinement strength  $\omega_0$  [Eq. (3.6)] was estimated to be  $\omega_0 = 250 \text{ s}^{-1}$  and the Debye length, using Eq. (2.19), to be  $\lambda_D = 250 \text{ }\mu\text{m}$ . From optical measurements as well as from the force equilibrium [Fig. 3.4(b)], the major radius of the toroidal confinement was taken as  $R = 7 \text{ mm}$ .

A system of  $N = 4096$  particles with  $r_d = 0.5 \text{ }\mu\text{m}$  was considered. Using the OML model, the dust charge is  $Q_d = -2500e$ . Corresponding to neutral gas pressures in the range  $p = (3 - 8) \text{ Pa}$ , the Epstein friction coefficient is  $\beta = (30 - 100) \text{ s}^{-1}$ . The Hall component of the ion drag force is about the same strength as gravity. Thus, the azimuthal ion drag, normalized to gravity  $f_i = F_{i,\varphi}/F_g$  is varied in the range  $f_i = 0.5 - 2$ .

The methods presented in this chapter allow a comprehensive study of torus-shaped dust clouds in anodic plasmas both experimentally and by means of simulations, thus allowing a critical comparison between both approaches. The results concerning dust flows in toroidal traps are presented in the next chapter.



# 4 | Toroidal Dust Streaming

Since the discovery of the 2D plasma crystal [14–17], the confinement of extended dust clouds is also an active topic of research. The main task is to compensate gravity which is realized on parabolic flights [80, 89], by applying a temperature gradient [29, 30, 82, 83] or using *in situ* grown nano dust [87]. Another possibility is the use of a special electric field configuration which is found in anodic plasmas [96, 107, 227] as discussed in Sec. 2.2.3. In anodic plasmas, a variety of different dynamical properties are studied like dust-density waves [107, 226–229], shock formation [247–250] or vortex flows [251].

If a magnetic field is present, electrons, ions and dust particles are affected in their motion resulting in new dynamical effects. A measure for the influence of the magnetic field on the dynamics is the Hall parameter  $H_s$ , see Sec. 3.1.1. In the Matilda-II experiment, typical magnetic field strengths of  $B = 20$  mT result in strongly magnetized electrons ( $H_e \gg 1$ ) and weakly magnetized ions ( $H_i < 1$ ) while the dust particles are unmagnetized ( $H_d \ll 1$ ). Thus, the electrons move only along the magnetic field direction, while the ions follow mainly the electric field. But due to the magnetic field, the ion flow has a small Hall component which exerts a torque on the dust particles.

In two dimensions, the rotation of dust clusters in a magnetic field was studied by Konopka *et al.* [97] and the driving mechanism was attributed to the Hall component of the ion drag in  $\mathbf{E} \times \mathbf{B}$  direction. Recently, Carstensen *et al.* [99] observed a cluster rotation in opposite direction of the local  $\mathbf{E} \times \mathbf{B}$  direction and could identify a rotation of the neutral gas as the driving mechanism. The gas is set into motion by the global Hall ion drag via ion-neutral collisions. For very strong magnetic fields, Amatucci *et al.* [252] could directly observe the gyromotion of dust particles. The rotation of extended dust clouds in magnetized anodic plasmas was also studied experimentally [96, 253, 254].

In unmagnetized plasmas, a dust-free region (void) occurs in extended dust clouds when the outwards directed ion drag force exceeds the inwards directed electric field force in the center of the discharge. This phenomenon is well known under microgravity conditions [80, 81, 91], in laboratory plasmas where particles are grown *in-situ* [86, 87] or when gravity is compensated by thermophoresis [82]. Furthermore, voids around Langmuir probes were also observed [88–90]. Voids were also studied theoretically [91–93, 255] and by means of simulations [94, 220, 256]. The void closure could also be observed under microgravity conditions [84] and in the laboratory with a temperature gradient [83].

In magnetized anodic plasmas, the confined dust clouds are apparently void-free [96]. However, Trottenberg *et al.* [107] reported on the observation of a torus-shaped dust cloud with a distinct hole in its center. Iris Pilch and I [108, 155, 172] studied these clouds in more detail and could identify the force balance of ion drag and electric field force also as

the mechanism for the void formation in magnetized plasmas. Furthermore, they proposed a hierarchic single-particle model for the formation of torus-shaped dust clouds.

This thesis extends the study of torus-shaped dust clouds and the main results are presented in this chapter, which is based on my publications [110–115]. They can be found as the Appendices [A.1]–[A.6] of this thesis. In Sec. 4.1, the mechanism for the formation of torus-shaped dust clouds is presented with emphasis on the role of many-particle effects compared to the single-particle model [108, 155, 172]. Then, the stationary flow properties of these clouds are discussed in Sec. 4.2 and the influence of external parameters like magnetic field strength or friction onto the flow are analyzed. In addition, a critical comparison between the experimental findings and numerical simulation results is given. Sec. 4.3 is dedicated to the local evolution of the flow at the particle level. Sec. 4.4 addresses the transient dynamical phenomena that are present in the dust flows. Then, the influence of a sheared driving force onto the flow dynamics is discussed in Sec. 4.5.

## 4.1 Torus Formation

In this section, the mechanism for the formation of torus-shaped dust clouds is described in detail.

Anodic plasmas have a pronounced potential distribution [107, 108, 227]. This results in an electric field configuration that allows to confine dust [96, 107, 227], see Sec. 2.2.3 and Sec. 3.2.1. Iris Pilch and I showed by means of probe measurements [108, 155] that for a sufficiently large ion density, the radial ion drag force exceeds the radial electric field force in the central region of the anodic plasma, pushing the dust out of the center and thus forming a void in the central region of the anodic plasma, see Fig. 3.4. Due to rotational symmetry, an annular confinement potential in radial direction is formed as sketched in Fig. 4.1(a). Since gravity is more than one order of magnitude smaller than the radial components of ion drag and electric field force, gravity can be neglected for the confinement of dust. However, the particles accumulate at the lowest point of the confinement caused by gravity.

The magnetic field results in a small Hall component of the ion drag in azimuthal direction<sup>1</sup> that is roughly of the same order of magnitude as gravity. The ion drag pushes the dust against gravity upwards along the upright confinement, cf. Sec. 3.2.1, as sketched in Fig. 4.1(b). Because of the geometry of the experiment a threshold for the formation of torus-shaped dust clouds exists since the particles have to overcome gravity in order to form a torus. The critical point for the onset of torus rotation is located at the 9 h position of the torus since there gravity is directed in opposite direction to the ion drag. If the ion drag does not exceed this threshold only sickle-shaped dust clouds are observed, see Fig. 4.1(c). By increasing the ion drag, first the sickle-shaped cloud moves further up along the confinement, see Fig. 4.1(d), then single particles are able to overcome gravity and move along the confinement path, see Fig. 4.1(e) and Fig. 2(d) in [A.2]. If the ion drag is further increased, a fully established torus-shaped dust cloud is obtained, see Fig. 4.2(a).

---

<sup>1</sup>From here on, the term “ion drag” always refers to the azimuthal ion drag component unless otherwise stated, since this component is the driving force for the dust rotation.

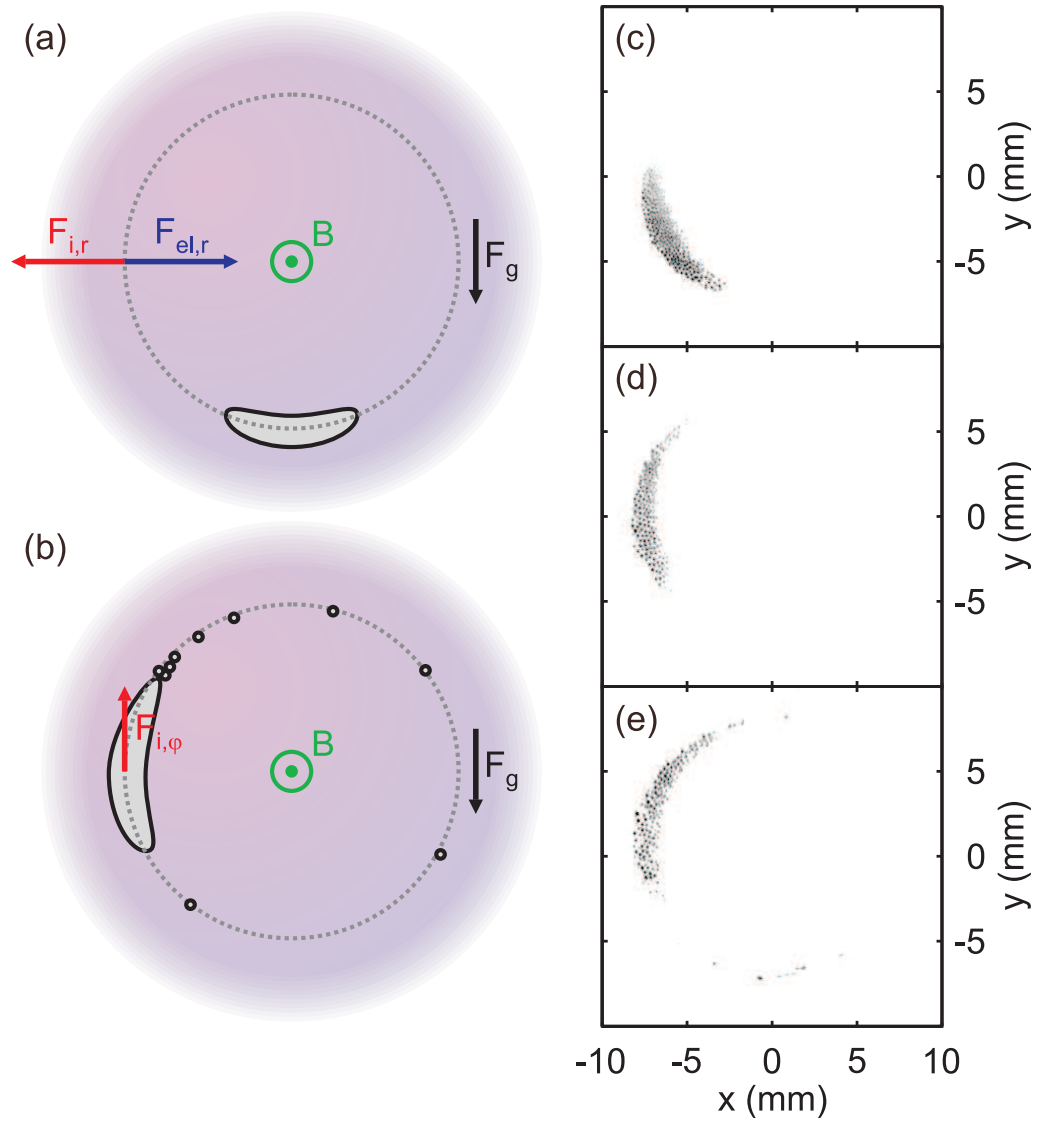


**Figure 4.1:** On the formation of torus-shaped dust clouds: (a) Sketch of the confinement given by the radial components of electric field force and ion drag. Due to gravity, the dust settles at the lowest point of the confinement. The lengths of the arrows are not to scale. (b) The Hall component of the ion drag drives the dust rotation along the confinement. **Experimental results (c)-(e):** Snapshots of a displaced dust cloud for (c)  $p = 3.83$  Pa, (d)  $p = 4.43$  Pa, and (e)  $p = 4.59$  Pa. (Adapted from Appendix A.2)

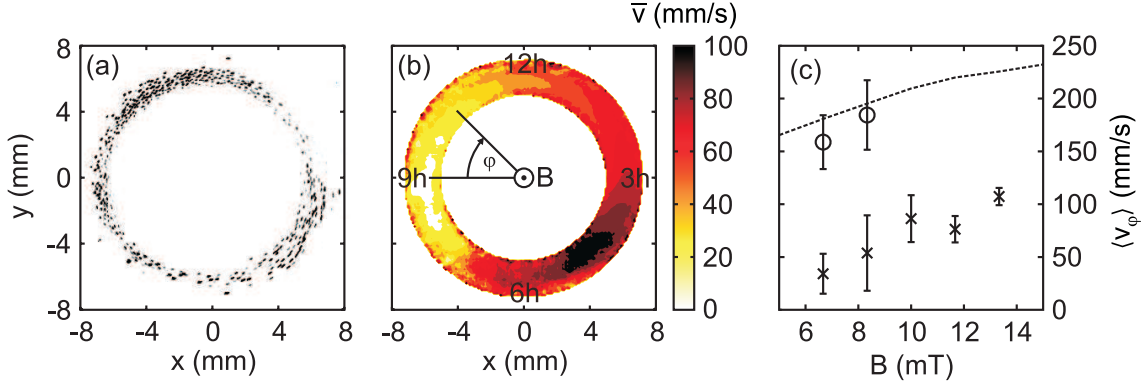


**Figure 4.2:** Stationary flow pattern of a torus-shaped dust cloud (**Experimental results**): (a) Snapshot of a torus-shaped dust cloud, (b) time averaged velocity profile obtained by means of PIV. (c) The maximum azimuthal velocity  $v_\varphi$  as a function of the magnetic field strength  $B$ , obtained by PIV ( $\times$ ) and PTV ( $\circ$ ). The dashed line corresponds to velocities obtained by MD simulations corresponding to the experimental conditions, cf. Fig. 4.3(c). (Adapted from Appendices A.1, A.2 and A.6)

## 4.2 Stationary Flow Properties

Now, the stationary flow properties of a fully established torus-shaped dust cloud are analyzed in detail. First, the experimental results are presented. Then, the findings of the numerical simulations are discussed. Afterwards, a critical comparison between both experiment and simulations is given.

### Experiment

If the ion drag exceeds a threshold given by gravity, a fully established torus-shaped dust cloud is found in the experiment [108], [A.1], see Fig. 4.2(a). When the particles are able to overcome gravity in the ascending branch of the torus, gravity will accelerate them in the descending branch of the torus. Thus, torus-shaped dust clouds only exist in a rotating state.

Hence, the stationary flow pattern of the dust flow is studied by means of PIV and is shown in Fig. 4.2(b). An overall clockwise motion of the dust is obtained. Positions along the annular confinement are indicated by an angle  $\varphi$  that is increasing in clockwise direction and  $\varphi = 0$  corresponds to the 9 h position on a clock dial. An inhomogeneous flow pattern is observed with the lowest velocities in the ascending torus branch around  $\varphi \hat{=} 9$  h and highest velocities in the descending branch around  $\varphi \hat{=} 5$  h due to gravity.

The influence of the magnetic field strength on the maximum rotation velocity in azimuthal direction  $v_\varphi$  is shown in Fig. 4.2(c). There, the velocities were obtained using the PIV ( $\times$ ) and the PTV technique ( $\circ$ ) from the same data set. The dashed line gives the rotation velocities obtained by MD simulations corresponding to the experimental conditions, cf. Fig. 4.3(c). For both PIV and PTV, an increase in the rotation velocity with increasing magnetic field strength is observed. But the PIV velocities are significantly smaller than those obtained by PTV caused by the curved trajectories of the particles and light intensity fluctuations of the particles.

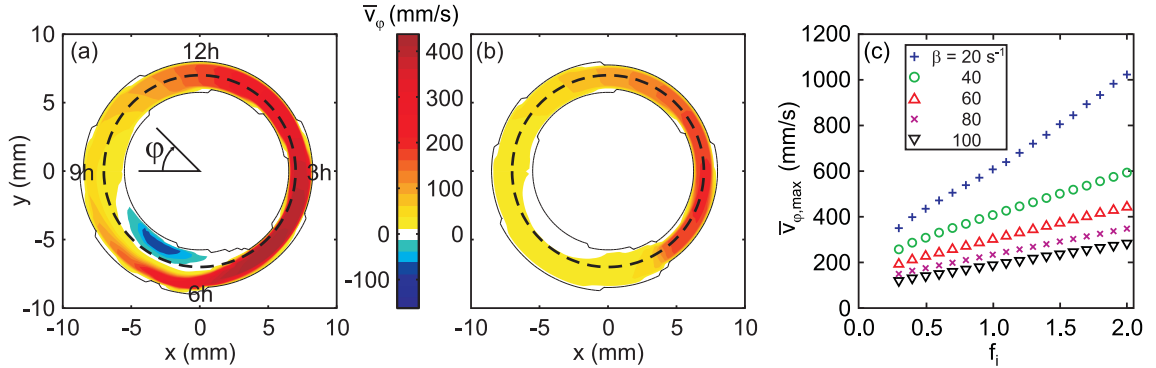


**Figure 4.3:** Dust streaming in a toroidal trap (**Simulation results**): For a normalized ion drag  $f_i = F_{i,\varphi}/F_g = 0.8$ , the time-averaged azimuthal velocity component  $v_\varphi$  is shown for (a) weak friction ( $\beta = 30 \text{ s}^{-1}$ ) and (b) strong friction ( $\beta = 90 \text{ s}^{-1}$ ). In (c), the maximum azimuthal velocity  $v_{\varphi,\text{max}}$  is plotted as a function of the normalized driving force  $f_i$  for different friction strengths as indicated by the inset. (Adapted from Appendices A.3 and A.5)

### Simulation

In addition to the experimental findings, the toroidal dust flow is also studied in terms of MD simulations, see Sec. 3.2. Since in the simulations the position and velocity of each particle is known for every time step, their properties are interpolated onto a polar grid [218] and averaged over time. Only particles with distance  $|z| < 0.2 \text{ mm}$  from the axial potential minimum are considered, corresponding to the experimental method of illuminating the midsection of the torus with a laser fan.

In Fig. 4.3, for a normalized Hall ion drag force  $f_i = F_{i,\varphi}/F_g = 0.8$  the time-averaged azimuthal velocity component  $v_\varphi$  is shown for weak friction with  $\beta = 30 \text{ s}^{-1}$  [Fig. 4.3(a)] and strong friction with  $\beta = 90 \text{ s}^{-1}$  [Fig. 4.3(b)]. A clockwise motion is indicated by positive velocities and the confinement potential minimum is indicated by a dashed line. For both friction strengths, an overall clockwise rotation is obtained. Starting from  $\varphi \hat{=} 9 \text{ h}$ ,  $v_\varphi$  increases and around 4-5 h it reaches its maximum before decreasing again.

For weak friction, the particles in the descending branch obtain high velocities. Thus, the particle flow is shifted radially outwards due to the centrifugal force acting on the dust. In the lower region of the torus, a spatial bifurcation of the flow into a fast particle population at the outer torus boundary and a slow particle population at the inner boundary that also inherits a back flow, see Fig. 4.3(a). Although this populations are spatially separated, a migration of particles from one population to another is observed [A.3] and is caused by a shear flow instability, see Sec. 4.4.1.

For strong friction, the overall velocities are slower. In addition, no spatial bifurcation of the flow is observed. Instead, a sudden decrease in velocity is found at  $\varphi \hat{=} 5 \text{ h}$  together with a broadening of the flow cross-section.

The maximum velocity as a function of the driving force  $f_i$  and the friction strength  $\beta$  is displayed in Fig. 4.3(c). For each friction coefficient, the velocity increases almost linearly with the driving force  $f_i$ , while for a fixed driving force an increase in the friction strength leads to a decrease of the velocity. Furthermore, torus rotation is observed down to values of  $f_i = 0.3$ .

It is noteworthy, that fully established torus-shaped dust clouds are obtained for  $f_i < 1$ . The single-particle model [108, 155, 172] states that if a single particle is considered, the ion drag has to exceed gravity, i.e.,  $f_i > 1$ , for the particle to overcome gravity at  $\varphi \hat{=} 9$  h. However, due to the Yukawa interaction the uppermost particles are repelled from the cloud resulting in an effective driving force allowing them to overcome gravity even for smaller values of the ion drag. Hence, the Yukawa interaction lowers the threshold for the onset of torus rotation.

### Comparison between experiment and simulation

The rotation velocities obtained by the simulations depend on the driving force  $f_i$  and the friction strength  $\beta$ . For a critical comparison, the ion drag force was determined by means of probe measurements and  $\beta$  was calculated from the pressure. Then, the rotation velocities were calculated [A.6] and are plotted as a dashed line in Fig. 4.2(c). Good agreement is found between the velocities obtained by PTV and the simulation results. PIV underestimates the velocities but shows qualitatively the same trend.

The angular velocity distribution is also similar in both experiment and simulation with lower velocities obtained by PIV. Furthermore, the experimental flow pattern shown in Fig. 4.2(b) exhibits neither a back flow nor a sudden velocity drop. A more detailed analysis of the special dynamical behavior in the lower torus region is given in Sec. 4.4.

## 4.3 Local Evolution of the Flow

With the knowledge of the particle positions and velocities for each time step, the simulations allow a much more precise analysis of the flow properties as it is possible by means of PIV or PTV. In this section, the local evolution of the flow is studied on the particle level.

For this purpose, the transit points of the particles through planes at constant angles  $\varphi$  are presented in Fig. 4.4 for a driving force  $f_i = 0.8$  and weak [ $\beta = 30 \text{ s}^{-1}$ , 4.4(a)] and strong friction [ $\beta = 90 \text{ s}^{-1}$ , 4.4(b)]. Particles transiting in clockwise direction are given by blue dots while counter-clockwise transiting particles are indicated by red dots. The same data sets are used for Fig. 4.3.

The transit points are not randomly distributed but arranged on nested shells. Starting at  $\varphi \hat{=} 10$ h, with increasing  $\varphi$  the number of shells decreases together with a shrinking of the flow cross-section. For weak friction, the shift to larger values of  $\rho$  due to the centrifugal force is seen while the shell structure remains intact. At  $\varphi \hat{=} 6$  h, the shell structure is lost, hinting at a phase transition. In addition, particles transiting in counter-clockwise direction are observed that are spatially separated from the main particle flow in clockwise direction. For strong friction, [Fig. 4.4(b)], the number of shells increases between  $\varphi \hat{=} 4$  h and  $\varphi \hat{=} 6$  h, while the shell structure remains intact.

For a more complete understanding, the shell-averaged azimuthal velocity  $v_\varphi$  for each shell in the range  $\varphi \hat{=} (10 - 3)$  h is shown in Fig. 4.4(c) as a function of the shell radius  $r = [(\rho - R)^2 + z^2]^{1/2}$ . Here, simulation parameters are  $f_i = 1.2$  and  $\beta = 100 \text{ s}^{-1}$ . With increasing  $\varphi$ , an increase in velocity together with a decrease of the shell radii is observed. Furthermore, the vanishing of the innermost shell is easily observable. In addition, it is

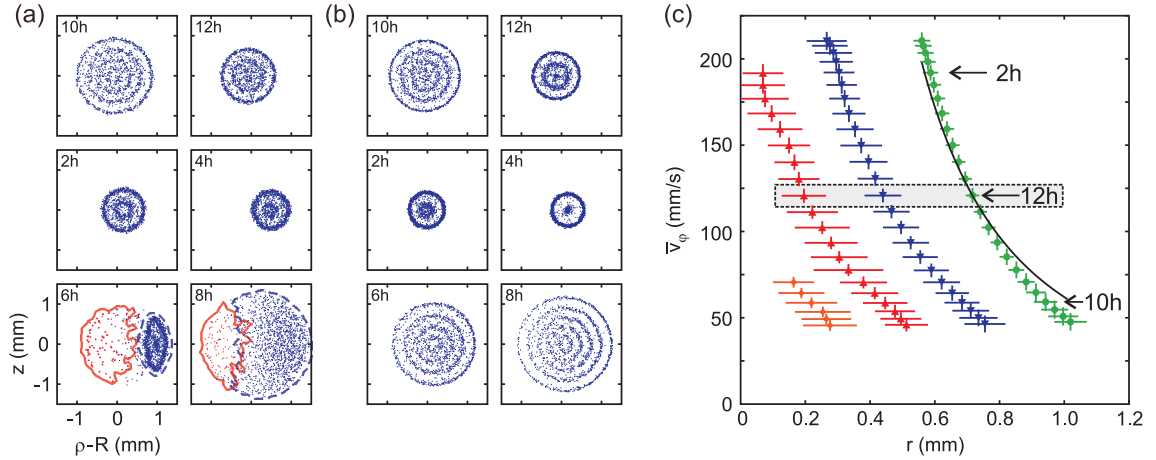


**Figure 4.4:** Local evolution of the dust flow (**Simulation results**): Transit points of dust particles through planes at constant angle  $\varphi$  for  $f_i = 0.8$  and (a) weak friction ( $\beta = 30 \text{ s}^{-1}$ ) and (b) strong friction ( $\beta = 90 \text{ s}^{-1}$ ). Blue indicates a transition in clockwise direction, red indicates a counter-clockwise transition through the plane. The contour lines indicate the region in which 90% of all transit points are located. (c) Shell-averaged azimuthal velocity  $v_\phi(r)$  as a function of the shell radius for  $\varphi \hat{=} (10 - 3) \text{ h}$ . Here, the simulation parameters are  $f_i = 1.2$  and  $\beta = 100 \text{ s}^{-1}$ . (Adapted from Appendices A.3 and A.4)

found that adjacent shells exhibit no sheared azimuthal motion,  $\Delta v_\phi / v_\phi = 0.2\%$ , as can be seen for  $\varphi \hat{=} 12 \text{ h}$  indicated by the gray box.

The formation of nested shells is accompanied by high values of the coupling parameter  $\Gamma \approx 400$  [A.3] due to the rapid cooling of the dust particles caused by neutral friction. Kählert *et al.* [214, 215] showed by means of LD simulations for a spherically confined Yukawa system that an initially disordered configuration becomes strongly coupled within  $\tau = 2.5\beta^{-1}$  for the conditions of the present situation. Taking the flow velocity into account the particles are strongly coupled after a relaxation "length"  $\Delta\varphi \hat{=} 1/4 \text{ h}$ . Hence, the flow can be considered as strongly coupled throughout the laminar region of the flow.

Since adjacent shells exhibit no shear, the particles can be regarded as being at rest in a comoving reference frame. For static strongly coupled systems, the crystallization into nested shells is well known, e.g., for finite two-dimensional systems [257, 258], Coulomb balls in a spherical trap [29–31] or ion crystals in Paul traps [18, 20, 259–261] where the crystallization is achieved by laser cooling of the system. While for ion crystals temperatures in the mK regime are required, the large particle charge in complex plasmas allows crystallization at room temperature.

For Coulomb balls, the spherical shape of the confinement results in concentric spheres of particles. When the parabolic confinement strength is weakened in one direction, e.g., for linear Paul traps, nested ellipsoids are obtained [20]. When the particles are allowed to move freely along one axis of the system while maintaining the biharmonic confinement potential perpendicular to that axis, interlaced tubes of particles are found. These so called Yukawa tubes are studied extensively by means of MD simulations [262] or Monte Carlo simulations [263]. In the context of complex plasmas, Totsuji *et al.* [264] presented first indications of the formation of nested dust particle tubes under microgravity conditions. Birkl *et al.* [260] observed ion crystals forming concentric tubes in a ring-shaped Paul

trap. Neglecting the local curvature of the trap, these systems can be seen as infinite Coulomb tubes. For both simulations [263] and experiment [260] it was found, that the linear particle density, i.e. the number of particles per unit length, has a crucial influence on the number of shells.

The influence of the external confinement on the structure of a dusty plasma was studied by Teng *et al.* [265]. They confined particles in a narrow channel between two vertical walls put on top of the lower electrode of a rf plasma. They observed a layered structure parallel to the channel walls. Decreasing the channel width resulted in a decrease of the number of layers. Köppl *et al.* [266, 267] studied the dynamical behavior of a colloidal suspension in a narrow channel. First, they let the particles settle in the narrow channel and also found a layered structure parallel to the walls. When a particle flow was induced by tilting the apparatus, they observed that the moving particle layers adapted to the external potential resulting in a decrease of the number of layers along the flow which they confirmed by means of Brownian dynamics simulations.

For the toroidal dust streaming, the absence of shear favors the relaxation of the flow into nested shells. Since the relaxation length is short the evolution of the flow can be understood as a sequence of nearly equilibrium situations: An increase of the flow velocity results in a decrease of the linear particle density along the flow direction. Hence, the flow cross-section shrinks as the particles rearrange themselves according to the altered situation. If it is energetically favorable, the innermost shell vanishes. This adaptation of the flow to the changing external conditions can be regarded as a structural phase transition along the flow.

The spontaneous formation of instabilities, which will be discussed in the subsequent section, has the tendency to destroy the shell structure, thus causing solid-liquid phase transitions inside the flow.

## 4.4 Instabilities

Besides the investigation of structures in complex plasmas, many experiments and simulations are dedicated to the analysis of dynamical phenomena since complex plasmas offer the opportunity to observe the dynamics of many-particle systems on the kinetic level. These studies include dust flows [265, 268, 269], phase transitions [28, 32–43, 63, 66, 106, 214, 215, 270–275], shear flows [104, 105, 274–276] that can form a Kelvin-Helmholtz [277, 278] or a Taylor-like instability [276] and waves, including shock waves [47, 48, 62, 63, 247–250, 279], and dust-density waves [54–57, 107, 226–229, 247, 280–282].

The analysis of the dynamics of torus-shaped dust clouds revealed that the toroidal flow also exhibits interesting dynamical behavior that deviates from a quiescent flow. In this section, these phenomena are analyzed in detail. First, the spontaneous formation of a shear flow is discussed in Sec. 4.4.1. Then, the formation of standing shocks in the toroidal flow is presented in Sec. 4.4.2. Finally, Sec. 4.4.3 is dedicated to dust-density waves that are common in complex anodic plasmas.

### 4.4.1 Shear Flow Instability

In the lower region of the torus, the flow is not quiescent but exhibits interesting dynamical behavior in both experiment and simulations. In the experiment, particle trajectories were



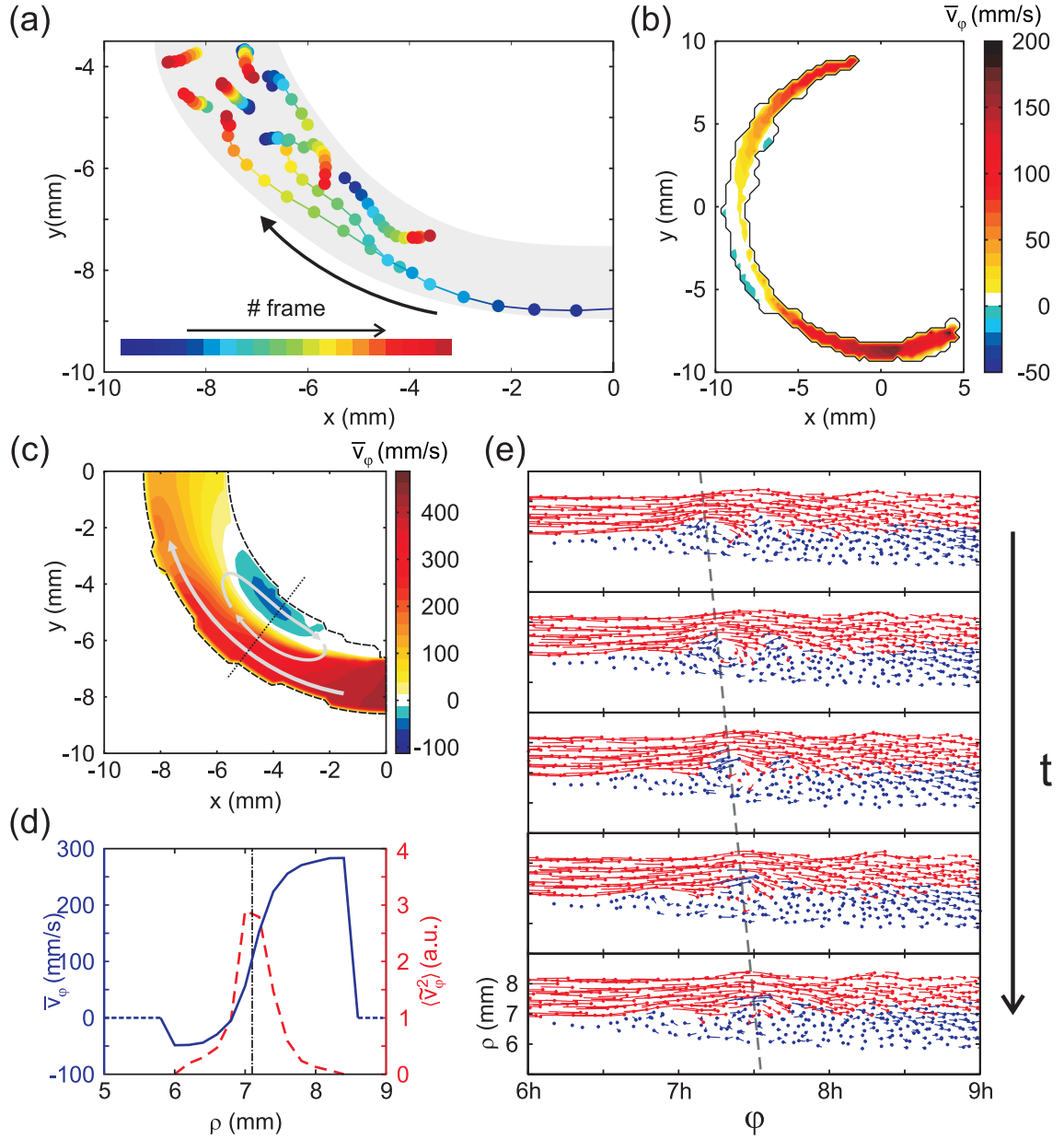


**Figure 4.5:** On the shear flow instability: **Experimental results (a)-(b):** (a) Particle trajectories inside a torus-shaped dust cloud obtained by PTV. Both clockwise and counter-clockwise motion is observed. (b) Sheared flow pattern in the ascending branch of a torus obtained by PIV; **Simulation results (c)-(e):** (c) Sheared flow pattern for  $f_i = 1.2$  and  $\beta = 40 \text{ s}^{-1}$ . (d) Radial flow profile (solid line) and velocity fluctuations (dashed line) of the flow at the angular position marked by the dotted line in Fig. 4.5(c). (e) Visualization of toroidal streamlines at the interface between positive (red) and negative (blue) flow velocities with respect to the flow velocity of maximum shear  $v_\phi = 100$  mm/s. (Adapted from Appendices A.4 and A.6)

obtained using PTV and examples are shown in Fig. 4.5(a). The majority of particles move in clockwise direction but a group of particles that move in counter-clockwise direction is also observed, hinting at the existence of a back flow. By means of PIV, the existence of a back flow could be verified in the experiment which is shown in Fig. 4.5(b). The back flow is located at the outer boundary of the ascending branch resulting in a radially sheared flow pattern.

In the simulations, a back flow was found for weak friction, too, cf. Fig. 4.3(a). In Fig. 4.5(c), the mean rotation velocity in the ascending branch is displayed for  $f_i = 1.2$  and  $\beta = 40 \text{ s}^{-1}$ . A well pronounced vortex-like back flow region is observed at the inner boundary of the torus. The radial flow profile is analyzed in more detail in Fig. 4.5(d). Therefore, the mean rotation velocity  $v_\varphi$  (solid blue line) along a radial cross-section, indicated by the dashed line in Fig. 4.5(c), is shown together with the velocity fluctuation amplitude  $\tilde{v}_\varphi^2$  (red dashed line), taken as  $\langle \tilde{v}_\varphi^2 \rangle = \langle (v_\varphi(t) - \langle v_\varphi \rangle)^2 \rangle$ . The flow is strongly sheared and the velocity fluctuation is peaked around the position of maximum shear at  $\rho = 7.2 \text{ mm}$ .

As could be seen in Fig. 4.4(a), in the sheared flow region the shell structure inside the flow is no longer present. In addition, the dynamical coupling parameter decreases to values well below  $\Gamma = 50$  in the sheared flow region [A.3]. Both findings indicate that the flow undergoes a solid-liquid phase transition, i.e., a melting process.

Phase transitions are an active topic of research in complex plasmas, both experimentally and theoretically. The liquid-solid phase transition is usually obtained by cooling the system. The build-up of correlations leading to crystallization was studied in detail by Kählert *et al.* [214, 215] by means of LD simulations. Experimentally, Rubin-Zuzic *et al.* [43] could directly observe the crystallization fronts in a three-dimensional complex plasma. Recently, Schella *et al.* [270] could experimentally observe the recrystallization of finite three-dimensional dust clouds after laser heating and their cooling rate was found to agree with the simulations by Kählert *et al.* [214, 215].

The reverse phase transition, i.e., the melting of a complex plasma was studied extensively using different methods, e.g., by changing the plasma power or neutral gas pressure for multilayered 2D crystals [28, 32–35], finite 3D systems [271] or extended dust clouds under microgravity conditions [272, 273]. Couëdel *et al.* [35] found that the melting front propagates through the crystal due to a mode-coupling instability of in-plane and out-of-plane modes. The propagation of the melting front was analyzed by Williams *et al.* [210] by means of PIV and PTV. For multilayered 2D crystals, Schweigert *et al.* [36, 37] could identify an instability in the ion wake that can lead to the melting of the system.

Other melting mechanisms include laser heating [38–41, 274] or exerting shear onto the crystal by either laser manipulation [66, 106] or a sheared neutral gas rotation [274, 275]. Samsonov *et al.* [63] studied the melting of a 2D crystal caused by the propagation of a shock wave through the system. In colloidal suspensions, shear-induced melting is also studied widely, see, e.g., [283, 284]. In the context of torus-shaped dust clouds, gravity leads to a spontaneous symmetry breaking in the flow resulting in a sheared flow profile which in turn induces the melting process.

The two particle populations, the fast streaming and the slow counter-rotating particles, are spatially separated but some particles are able to migrate from one population to the other [A.3]. In order to study the migration process on the kinetic level, the particle trajectories were studied in the polar  $\varphi - \rho$  plane in which a rotation about the major

axis corresponds to a straight trajectory. As a result, deviations from an azimuthal flow become easily visible. In Fig. 4.5(e), a sequence of particle trajectories is shown at the interface between positive (red) and negative (blue) velocities with respect to the flow velocity of maximum shear  $v_\varphi \approx 100$  mm/s, see Fig. 4.5(d). A wave-like perturbation at the interface with growing amplitude is observed that develops into a set of small eddies which are convected with the flow as indicated by the dashed line corresponding to  $v_\varphi = 150$  mm/s. This finding is a clear indication of a Kelvin-Helmholtz (KH) instability.

KH instabilities are known to occur at the interface of two sheared flows and are, e.g., proposed to be responsible for the transport of the solar wind through the Earth's magnetosphere [285] leading to magnetic storms or aurorae [286]. D'Angelo [287] proposed the existence of a KH instability in a magnetized plasma with a density gradient perpendicular to the magnetic field direction which could later be observed in a Q machine [288]. The stabilizing effect of immobile dust particles onto the ion KH instability was proposed by D'Angelo and Song [289] and was also experimentally verified in a Q machine by Luo *et al.* [290]. In terms of a multi-fluid model, Birk [291] and Wiechen [292] studied the influence of charge number and density of mobile dust onto the KH instability including neutral gas effects. The influence of strong coupling onto the growth rate of the KH instability in a two-dimensional Yukawa liquid with periodic boundary conditions was studied in terms of MD simulations by Ashwin and Ganesh [277]. Their MD results were in good qualitative agreement with their generalized hydrodynamic model [293].

Following Ref. [277] and using values for the shear viscosity of a 3D Yukawa liquid [294], a growth rate for the KH instability of  $\gamma_{\text{KH}} = 80 \text{ s}^{-1}$  would be obtained [A.4] for the parameters considered in this thesis. Instabilities are usually quenched when the collision rate  $\beta$  becomes comparable to the growth rate  $\gamma$  of the instability. Since  $\gamma_{\text{KH}}$  is significantly higher than  $\beta = 40 \text{ s}^{-1}$  in the present situation, the formation of a KH instability is in reasonable agreement with Ref. [277]. The long-time behavior of the KH instability in Ref. [277] showed the transition into a turbulent flow. Due to the geometry of the toroidal trap, the shear decreases along the flow. Accordingly, the growth rate decreases and therefore damping can effectively prevent the transition into a turbulent flow.

In hydrodynamics, the formation of KH instabilities is described in a fluid approach. Here, the KH instability forms on length scales that are comparable to the interparticle distance, e.g. the diameter of the eddies is of the order of ten  $a_{\text{WS}}$ . Hence, the observation of KH instabilities when the discreteness of the system is not negligible any more offers the opportunity to study the lower limits of their hydrodynamic description.

#### 4.4.2 Standing Shocks

When the neutral collision frequency  $\beta$  increases while the driving force  $f_i$  is kept constant, stronger damping leads to an overall reduction of the rotation velocity, see Fig. 4.3. Furthermore, the formation of a shear flow instability is suppressed due to the strong collisionality. However, another instability emerges. In Fig. 4.3(b), a sudden decrease of the rotation velocity is observed around  $\varphi \hat{=} 5$  h together with a broadening of the flow cross-section, cf. Fig. 4.4(b). For a more comprehensive analysis, the mean rotation velocity was radially averaged and is shown in Fig. 4.6(a) as a function of the angular position  $\varphi$ . Besides the overall velocity modulation due to gravity, the sudden velocity drop is

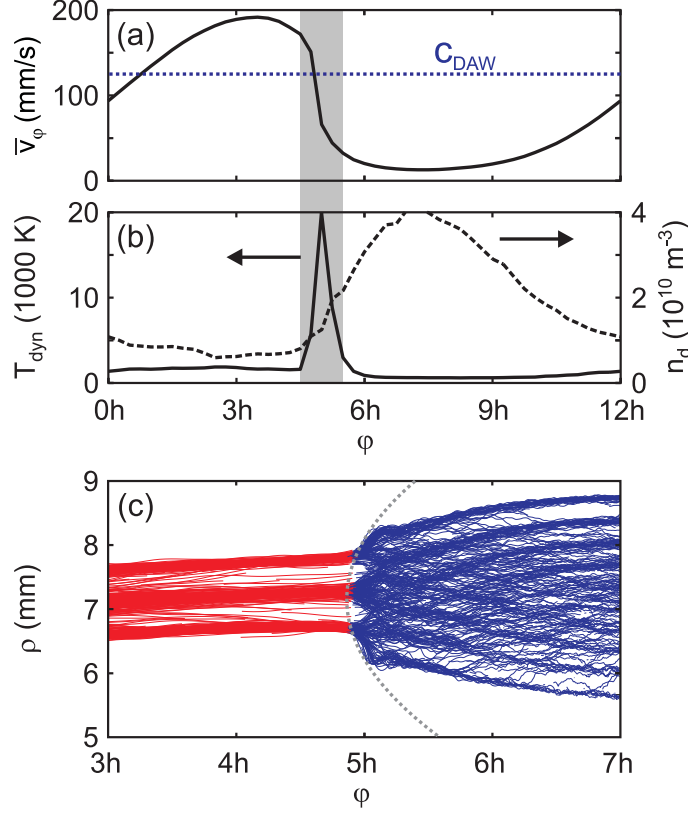


**Figure 4.6:** On the formation of standing shocks (**Simulation results**): For  $f_i = 0.8$  and  $\beta = 90 \text{ s}^{-1}$ , cf. Fig. 4.3(b), the angular distribution of (a) the mean azimuthal velocity  $v_\phi$  and (b) the dynamical temperature  $T_{dyn}$  and particle density  $n_d$  are displayed. The region of the shock is highlighted by a gray box. For comparison, in (a), the sound speed for compressional (dust acoustic) waves  $c_{DAW} = 125 \text{ mm/s}$  is indicated by a dotted line. (c) Visualization of the standing shock: Shown are the trajectories in the  $\phi$ - $\rho$  plane of all particles with  $|z| < 0.2 \text{ mm}$ . Particles with velocities  $v_\phi > c_{DAW}$  ( $v_\phi < c_{DAW}$ ) are colored red (blue). Around  $\phi \hat{=} 5 \text{ h}$ , a sudden broadening is observed. The gray dotted line illustrates the form of a bow shock. (Adapted from Appendix A.3)

clearly visible around  $\phi \hat{=} 5 \text{ h}$ . For comparison, the sound speed for compressional (dust acoustic) waves is in the present situation  $c_{DAW} = \omega_{pd} \lambda_D = 125 \text{ mm/s}$ . It is obvious that the dust flow is decelerated from supersonic to subsonic velocities hinting at the formation of a standing shock.

Bond *et al.* [295] define a shock wave as “a propagating disturbance characterized by an extremely rapid rise in pressure, temperature and density”.<sup>1</sup> Thus, the particle density  $n_d$  was estimated by calculating the 2D Voronoi cells of the particles on the outermost shell and taking the inter-shell distance as a measure for the radial extension of the Voronoi cell. The particle density is then taken as the reciprocal of the Voronoi cell volume and its angular dependency is shown in Fig. 4.6(b) together with a measure for the dust

<sup>1</sup>Bond, Watson, Welch, *Atomic Theory of Gas Dynamics*, Addison-Wesley Publishing Company, Inc., © 1965, Ch. 2, p. 14

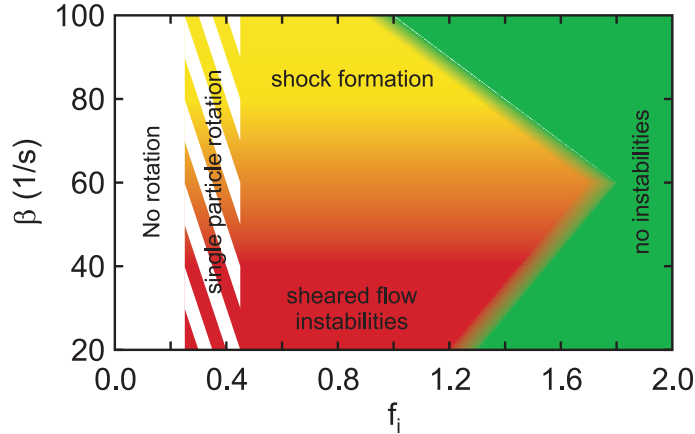


**Figure 4.7: (Simulation results):** Map of the different flow regimes depending on ion drag  $f_i$  and friction strength  $\beta$ . (From Appendix A.5)

temperature  $T_{\text{dyn}}$ . The dynamical temperature,

$$k_B T_{\text{dyn}} = \frac{1}{2} m_d \langle (\mathbf{v}_d(t) - \bar{\mathbf{v}}_d)^2 \rangle, \quad (4.1)$$

is taken as the kinetic energy of the dust flow velocity fluctuations with  $\bar{\mathbf{v}}_d$  the time averaged flow velocity and  $\langle \dots \rangle$  denotes averaging over all considered particles. While  $T_{\text{dyn}}$  remains nearly constant along the quiescent region of the flow, a very localized increase in temperature is observed around  $\varphi \hat{=} 5$  h. An increase around  $\varphi \hat{=} 5$  h in the particle density  $n_d$  is also obtained. These findings indicate the formation of a standing shock.

Shock waves or shocks are common in nature, e.g., the steepening of shallow water waves or mach cones around supersonic planes, and occur when an object moves faster than the information propagation velocity in the surrounding medium, e.g., the sound speed in air. In the context of plasma physics, shocks are also widely studied. Ion-acoustic shock waves were first studied by Taylor *et al.* [296] in a double-plasma device. The influence of dust onto ion-acoustic shocks was also analyzed experimentally [297–300]. Dust shocks were investigated under microgravity conditions [62] or in laboratory plasmas focusing on mach cones [47, 48], shock melting [63], steepening of dust-acoustic waves into shocks [247, 248] or the formation of a bow shock on the upstream side of an obstacle [249, 250, 279].

A bow shock is formed in a supersonic flow around an obstacle that deflects the flow so that the flow velocity reduces to subsonic values. Saitou *et al.* [279] used a vertical wire as an obstacle and created a supersonic particle flow by tilting their experiment. Meyer *et al.* [249, 250] could observe the formation of a bow shock around a wire placed inside an anodic plasma with an additional mesh grid in order to create a supersonic particle flow.

In this thesis, gravity accelerates the dust flow in the descending branch of the torus to supersonic velocities. Here, the electrostatic repulsion of the large group of slow particles in the lower region of the torus acts as an obstacle that deflects the supersonic particle flow as can be clearly seen in Fig. 4.6(c). The dotted line illustrates the form of a bow shock. Since the confinement in the simulations is stronger than in the experiments by Saitou and Meyer no extended bow shock is observed.

### Parameter dependency

For a more complete overview of the different flow instabilities, a map of the different flow regimes as a function of driving force and collision frequency is shown in Fig. 4.7. For  $f_i < 0.3$ , only a displaced sickle-shaped cloud is obtained, cf. Fig. 4.1(c). With further increasing  $f_i$ , single particles are able to rotate about the major axis of the torus, cf. Fig. 4.1(e) and Fig. 2(d) in A.2. For  $f_i > 0.5$ , all particles are in general able to participate in the overall rotation motion. For weak friction, shear flow instabilities are present, while for strong friction standing shocks develop. For intermediate friction strengths, hybrids of both instabilities are found. With further increasing driving force [ $f_i = (1.2 - 1.8)$ ], a continuous transition to an overall quiescent flow pattern without any instabilities is observed [A.5].

### 4.4.3 Dust-Density Waves

Besides the shear flow instability and the shock which both originate from the symmetry breaking of the flow due to gravity, a third instability occurs in torus-shaped dust clouds, the dust-density wave (DDW).

In complex plasmas, dust-density waves (or dust-acoustic waves) emerge spontaneously due to streaming ions [230]. The existence of the dust-acoustic wave was predicted by Rao *et al.* [49] and first observed in an rf discharge [280]. In anodic plasmas, dust-acoustic waves were first observed by Barkan *et al.* [226] and the dispersion relation was measured by Thompson *et al.* [227] by synchronizing the wave to an external force. Dust-acoustic waves are characterized by a linear dispersion, i.e., at low wave numbers group and phase velocity coincide, while for a dust-density wave this restriction is omitted [172]. Dust-density waves are also studied under microgravity conditions [54–57]. In anodic plasmas, many experiments are dedicated to the measurement of the dispersion relation [107, 227–229], the diffraction of waves behind obstacles [281], the transition of dust-density waves into shocks [247] or the temporal growth of dust-density waves [282]. In addition, PIV was used to study the properties of dust-density waves in anodic plasmas [208, 209, 301].

In torus-shaped dust clouds, self-excited dust-density waves are also observed. Fig. 4.8(a) shows a snapshot of a large torus-shaped dust cloud exhibiting self-excited dust-density waves. Following Ref. [229] for the analysis of the waves, a region of interest centered around  $\varphi \hat{=} 6$  h, indicated by the gray area, was chosen. First, for each frame the azimuthal sum of the light intensity

$$I(\rho, t) = \sum_{\varphi=\varphi_1}^{\varphi_2} I(\varphi, \rho, t) \quad (4.2)$$

was calculated. After averaging over the entire time series, the mean light intensity

$$\bar{I}(\rho) = \frac{1}{N} \sum_{i=1}^N I(\rho, t) \quad (4.3)$$

is obtained. Since the dust density is proportional to the scattered light intensity, the density fluctuation is given by

$$\tilde{n}_d(\rho, t) = I(\rho, t) - \bar{I}(\rho) \quad (4.4)$$

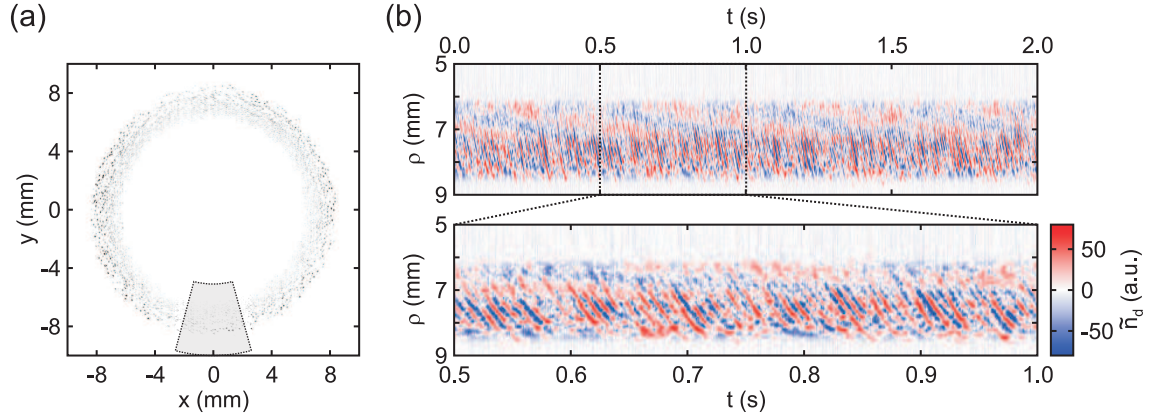


**Figure 4.8:** On dust-density waves (**Experimental results**): (a) Snapshot of a torus-shaped dust cloud with a large radial cross-section (inverted color). The shaded region around  $\varphi \hat{=} 6$  h was used for the analysis of the DDWs. (b) Space-time diagram of the dust density: A long time series is shown on the top. For  $\rho = (6-7)$  mm, slow propagating DDWs ( $v_{\text{ph}} \approx 1.8$  mm/s) are observed, while for  $\rho = (7-9)$  mm, the phase velocity of the DDW is increased. At the bottom, an enlarged time scale allows a more detailed view of the fast DDWs ( $v_{\text{ph}} \approx 42$  mm/s).

and is shown in Fig. 4.8(b) in terms of a space-time diagram. The obtained wave field can be divided into two spatially separated regions: For  $\rho = (6-7)$  mm, a slow propagating wave with a phase velocity of  $v_{\text{ph}} \approx 1.8$  mm/s is found, while for  $\rho = 7-9$  mm, a fast propagating dust-density wave with a phase velocity of  $v_{\text{ph}} \approx 42$  mm/s is obtained. Self-excited dust-density waves exhibit a broad frequency spectrum [229] with no dominant frequency. Here, for  $\rho > 7$  mm, the frequencies contributing most to the power spectrum lie in the range  $f = 40-120$  Hz. Comparing these frequencies with the time scale calculated by Kählert *et al.* for the build-up of correlations in a strongly-coupled system [214, 215] which for the present experiment would be  $\tau = 2.5\beta^{-1} \approx 40$  ms, see Sec. 4.4.1, it is obvious that the relaxation of the flow into nested shells is suppressed in the presence of dust-density waves.

Pilch *et al.* [228] also studied the influence of the size of the dust cloud on the formation of dust-density waves in anodic plasmas and found that the cloud diameter has to exceed the wave length for the wave to be excited. Furthermore, Pilch *et al.* [172, 228] could show that the propagation direction of the dust-density wave is aligned with the electric field direction. Since the electric field is mostly radially outwards directed at the confinement position of the dust torus [108, 155], the radial extent of the torus is crucial for the onset of dust-density waves.

## 4.5 Influence of a Sheared Force Field

As discussed in the preceding section, dust-density waves have a strong influence on the torus dynamics in the experiment. Since the simulations are not designed for the study of dust-density waves, the suppression of waves in the experiment is inevitable for a critical comparison between experiment and simulations. This can be achieved by either increasing the neutral gas pressure or by reducing the radial extent of the torus. For the latter, only a few particles were confined in the anodic plasma and their dynamics were studied by

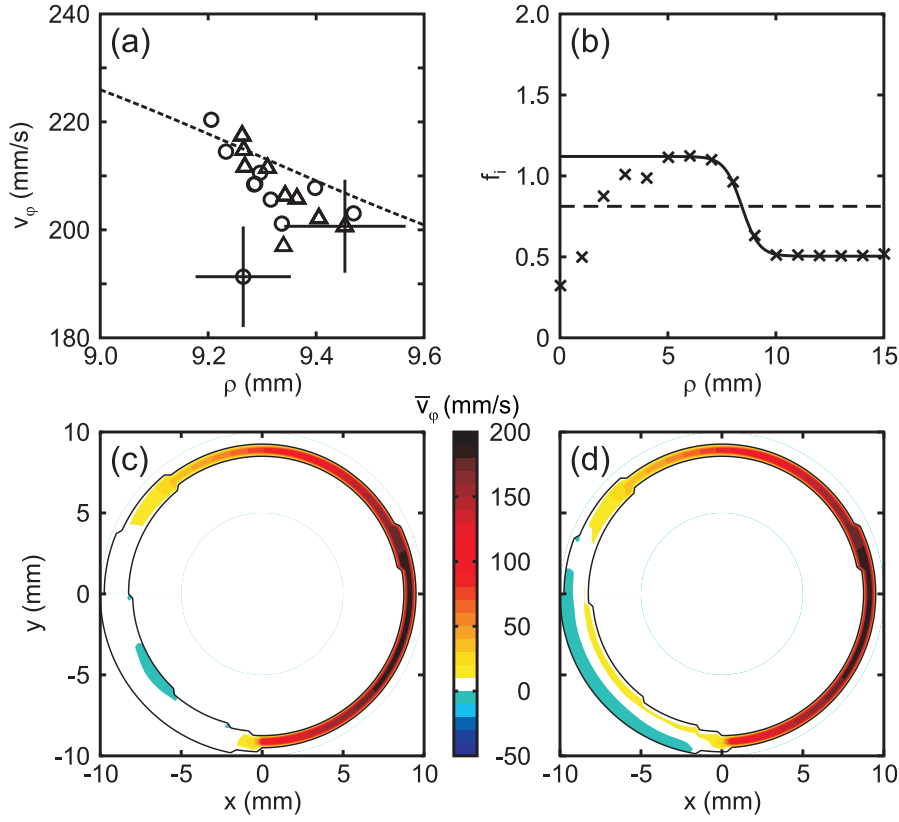


**Figure 4.9:** On the influence of a sheared ion drag: **Experimental results (a)-(b):** (a) Radial dependency of particle velocities obtained by PTV ( $\circ$  and  $\triangle$ ). The dashed line gives the velocities obtained by MD simulations corresponding to a sheared ion drag [solid line in Fig. 4.9(b)]. (b) radial distribution of the Hall ion drag ( $\times$ ) based on probe measurements. For  $\rho > 5$  mm, a tanh-type function was fitted onto the data points (solid line). For comparison, the dashed line gives a radially constant ion drag. **Simulation results (c)-(d):** Flow topology for simulations with  $N = 512$  particles and (c) a constant driving force  $f_i = 0.8$  [cf. dashed line in Fig. 4.9(a)] and (d) a radially dependent driving force  $f_i(\rho)$ , cf. solid line in Fig. 4.9(a). (Adapted from Appendix A.6)

means of PTV. In Fig. 4.9(a), the rotation velocity of two separate particles ( $\circ$  and  $\triangle$ ) at  $\varphi \cong 3$  h is shown as a function of their radial position  $\rho$ . For both particles an increase in radial position results in a decrease in velocity.

This finding is not reproduced by the simulations where a constant rotation velocity over a radial cross-section was observed in the quiescent region of the flow, cf. Figs. 4.3 and 4.4(c). Hence, the assumptions used in the simulations have been critically revised. For this purpose, the electric field of the anodic plasma was measured with an emissive probe. Then, using the model described in Sec. 3.2.1, the driving force  $f_i$  was calculated. In Fig. 4.9(b), the driving force  $f_i$  is plotted ( $\times$ ) over the radial displacement  $\rho$  from the anode center. For  $\rho < 5$  mm, an increase is observed, followed by constant values for  $f_i$ . Then, for  $\rho > 7$  mm, a decrease in  $f_i$ , again followed by constant values for  $\rho > 10$  mm. Since no dust is observed for  $\rho < 5$  mm, the ion drag in this region has no influence on the dust dynamics. In contrast to the assumption of a radially constant driving force in



the simulation, indicated by the dashed line,  $f_i$  is radially sheared and can be described by a tanh-type model function (Eq. (2) in A.6), indicated by the solid line.

From the simulations with constant driving force, a linear relationship between  $f_i$  and maximum rotation velocity was found, see Fig. 4.3(c) and Eq. (3) in A.6. Then, a radially dependent rotation velocity can be estimated from the simulation results which is shown as a dashed line in Fig. 4.9(a). One immediately sees that the radial shear of the driving force results in a decrease in rotation velocity with increasing radius. Although the slope of the experimental velocity distribution is steeper than the slope of the numerical results, a good qualitative agreement is found.

Regarding the topology of the sheared flow pattern, the discrepancy between the experiment and the simulation is also addressed. In the experiment, the back flow region was situated at the outer boundary of the torus, see Fig. 4.5(b), while for simulations with a constant driving force, the back flow region was located at the inner torus boundary, see Fig. 4.5(c). Thus, the influence of a sheared ion drag onto the flow topology is of high interest. In order to address this task, simulations with a radially constant driving force [dashed line in Fig. 4.9(b)], and with a tanh-type driving force [solid line in Fig. 4.9(b)] were performed. The resulting stationary flow patterns are shown in Fig. 4.9(c) for constant  $f_i$  and in Fig. 4.9(d) for the radially sheared driving force. The quiescent flow region ( $\varphi \hat{=} (10 - 6) h$ ) is similar in both cases. However, the profile of the ion drag has a crucial influence on the topology of the sheared flow pattern. For constant  $f_i$ , the back flow is located at the inner boundary of the torus, as expected [cf. Figs. 4.3(a) and 4.5(c)] while the radially sheared ion drag results in the formation of back flow at the outer boundary of the flow, as observed in the experiment [cf. Fig. 4.5(b)]. These findings strongly indicate that the driving force in the experiment is not constant but radially sheared.

Both experiment and simulations revealed multifaceted results concerning the dust flow in a toroidal trap. Gravity was found to have a crucial influence on the formation of torus-shaped dust clouds as well as their structure. Furthermore, the dynamics and the spontaneous occurrence of instabilities in the flow are strongly influenced by gravity, friction and the driving force. In addition, a radially sheared ion drag could be identified to have a significant influence on both the particle rotation velocity and the flow topology. The relationship between these manifold findings are discussed in the next chapter.



# 5 | Summary and Conclusions

In this work, the formation and dynamics of torus-shaped dust clouds in magnetized anodic plasmas were studied. On the experimental side, a refined observation geometry for the end-on observation of these clouds was implemented [109], [A.1], which allowed a more detailed investigation of the flow properties of torus-shaped dust clouds. In addition, the hierarchic single-particle model [108, 155, 172], [A.1] was extended to include many-particle interactions [A.2], friction [A.2], [A.3] and allowed to study the influence of the confinement on the torus rotation [A.2], [A.3]. By means of LD simulations, the experimental findings could be reproduced. Furthermore, additional dynamical phenomena like the spontaneous formation of shear flows were obtained [A.3], [A.4] which in turn could be observed in the experiment as well [A.6]. By critically re-examining the assumptions used for the model deviations between simulations and experiments could be resolved [A.6]. The main findings of this work are listed below.

**In weakly magnetized plasmas, the mechanism for void formation is the same as for unmagnetized plasmas:** In complex plasmas with gravity compensation, the formation of voids in extended dust clouds is commonly known [80–83, 87, 89]. The dust confinement in these situations is given by a force equilibrium of ion drag and electric field force. Due to the electric field geometry, the ion drag force exceeds the electric field force in the center of the discharge and pushes the dust out of the central region until a force equilibrium is reached. By means of probe measurements, the analysis of the radial components of electric field force and ion drag revealed that the same mechanism is responsible for the void formation in weakly magnetized anodic plasmas [A.1].

**In magnetized anodic plasmas with a void partially filled or fully established torus-shaped dust clouds are present:** When the ion density is sufficiently high, a void will form in the central region of an anodic plasma with an annular confinement region at its boundary [A.1]. In contrast to most complex plasma experiments with gravity compensation exhibiting a void, in magnetized anodic plasmas the dust does not always enclose the void. It could be demonstrated that the azimuthal Hall component of the ion drag as the driving force for the dust rotation has to overcome a threshold given by gravity so that a torus-shaped dust cloud is formed. For a driving force smaller than this threshold displaced sickle-shaped are obtained which can be regarded as a partially filled torus [A.2].

**Torus-shaped dust clouds only exist in a rotating state:** The critical point for the formation of torus-shaped dust clouds could be determined to be located at the 9 h position in the ascending torus branch since there, gravity is opposite to the driving force. If the particles are able to pass this position they will move along the confinement. In the descending branch, gravity will further accelerate the particles against the neutral gas friction. Thus, in magnetized plasmas, the torus clouds are always in motion [A.2], [A.3].

**Gravity breaks the symmetry of the flow leading to an inhomogeneous flow pattern:** Due to the confinement geometry, gravity not only causes a threshold for the torus rotation but also results in a periodic modulation of the dust acceleration along the confinement which in turn leads to a stationary inhomogeneous flow pattern [A.2], [A.3]. The flow patterns obtained by the numerical simulations were in good agreement with the flow pattern observed in the experiment. Furthermore, it was shown that influence of the magnetic field strength onto the rotation velocity as observed in the experiment can be well reproduced by the simulations [A.6]. Hence, the extended model used for the simulations is well suited for the description of the dynamics of torus-shaped dust clouds.

**Collective interparticle forces lower the threshold for torus formation:** In the single-particle model [108, 155, 172], [A.1], the condition for the onset of torus formation is that the azimuthal ion drag has to exceed gravity. In this work, it was shown that the mutual repulsion of the particles due to the Yukawa interaction acts as an effective additional driving force for the uppermost particles in the cloud. Thus, an ion drag force that is weaker than gravity is sufficient to drive the dust rotation [A.2], [A.3].

**Due to frictional damping the laminar flow relaxes into nested shells:** The simulations revealed that the particles in the quiescent flow are not randomly distributed but arrange themselves in nested shells [A.3]. Due to frictional damping, the particles are strongly coupled throughout the quiescent flow which in turn alleviates the establishment of an unshered flow [A.4]. If the particles are regarded as being at rest in a comoving reference system, a relaxation into shells is commonly known in strongly coupled complex plasmas. However, the observation of a crystallization process in a streaming strongly coupled system is not commonly observed.

**Due to the gravitational acceleration the laminar flow undergoes a structural phase transition:** The periodic modulation of the gravitational acceleration results in a continuous increase of the flow velocity in the quiescent flow region [A.4] which in turn leads to a increase in the interparticle distance in flow direction, thus decreasing the Yukawa repulsion in this direction. Hence, the force balance of Yukawa repulsion and external confinement leads to a decrease of the shell radii. Due to the strong frictional damping, the adaptation of the particles takes place on very short time scales so that this process can be understood as a sequence of local equilibria along the flow [A.4].

**The symmetry breaking of the flow results in the spontaneous formation of instabilities inside the flow:** The asymmetry in the flow velocities caused by gravity leads to an accumulation of particles in the lower region of the torus, that acts upon the

approaching particle flow in the descending torus branch as an obstacle [A.3]. Depending on the friction strength, two different instabilities were found: For weak friction, the main flow is radially shifted outwards from the confinement minimum due to its high velocity and evades radially the accumulation of particles at the bottom of the torus [A.3]. This spatial bifurcation of the flow into a fast flow and a slow back flow results in a strongly sheared flow profile which exhibits a Kelvin-Helmholtz instability [A.4]. For strong friction, the supersonic flow in the descending branch does not radially evade the obstacle but is deflected due to the electrostatic repulsion of the particles resulting in the formation of a standing shock [A.3]. Between these limiting cases a continuous transition with hybrids of these flow instabilities exists. When the driving force is increased, the gravitational modulation of the particle acceleration diminishes which results in a gradual transition into a quiescent flow for strong driving forces [A.5].

**Dust-density waves in torus-shaped dust clouds suppress the relaxation of the particles into nested shells:** Pilch *et al.* [172, 228] studied self-excited dust-density waves in magnetized anodic plasmas and found that the waves propagate in the electric field direction. Furthermore, they showed that if the length of the dust cloud does not exceed the wave length, self-excited dust-density waves are suppressed. At the confinement position of torus-shaped dust clouds, the electric field is mainly pointing in radial direction [A.1]. Thus, for radially extended tori, self-excited dust-density waves could be observed experimentally. Since the observed frequencies in the wave spectrum are significantly higher than the relaxation rate [214, 215], the formation of nested shells is efficiently suppressed.

**A strong radial gradient of the azimuthal ion drag results in a flow topology with the back flow located at the outer boundary of the torus:** A detailed examination of the electric field led to the insight that the driving force is radially sheared [A.6] in contrast to the assumption of a constant force in the simulations. The observation that the rotation velocity of the particles depend on their radial position supports this finding. Furthermore, the existence of a sheared flow pattern with a back flow at the outer boundary could be verified experimentally. Taking into account the radial gradient of the driving force, the simulations confirmed the experimentally observed flow pattern [A.6].

In conclusion, in this thesis it was shown that in magnetized anodic plasmas the dust flow is driven by the Hall component of the the ion drag. This driving mechanism is inherent to the system, in contrast to the external excitation of dust flows, e.g., by laser manipulation. The flow properties can be distinguished regarding their length scales: The crystallization due to strong coupling of the particles is a microscopic process governed by the inter-particle distance. On larger length scales, the flow shows hydrodynamical behavior, e.g., the formation of instabilities or the change in velocity due to gravity. Furthermore, the stability of the crystalline structure in the inhomogeneous flow demonstrates the different time scales of (i) the individual particle motion and (ii) the hydrodynamic change of the flow. Hence, torus-shaped dust clouds interlink the microscopic behavior of a strongly coupled Coulomb system with the macroscopic properties of a hydrodynamic flow and are therefore an ideally suited model system for the study of strongly coupled flows at the kinetic level.



# **A** | Reprints of peer-reviewed articles





## A.1

# TOROIDAL DUST CLOUDS AND VOIDS IN A MAGNETIZED ANODIC PLASMA

Torben Reichstein, Iris Pilch, Robert Große-Ahlert, and  
Alexander Piel

Reprinted with permission from  
Torben Reichstein, Iris Pilch, Robert Große-Ahlert, and Alexander Piel,  
IEEE Transactions on Plasma Science, Vol. 38, 814 (2010).  
Copyright 2010, IEEE.

# Toroidal Dust Clouds and Voids in a Magnetized Anodic Plasma

Torben Reichstein, Iris Pilch, Robert Große-Ahlert, and Alexander Piel

**Abstract**—Dust particles confined in a magnetized anodic plasma can form different cloud shapes. In a certain parameter regime, torus-shaped dust clouds with a dust-free region (void) in the center are found. One can observe that most of the particles perform a rotational motion about the major axis of the torus. In order to understand the responsible mechanism, a model was developed to describe the confinement of dust particles by means of a force balance of electric field force and ion drag force derived from electric measurements of the plasma potential and the plasma density. Furthermore, a condition for the onset of the particle rotation and, with it, the formation of a torus-shaped cloud is developed. It is also possible to estimate the rotation velocity of the particles. The resulting values are compared with the data observed by particle image velocimetry.

**Index Terms**—Anodic plasma, dusty plasma, probe diagnostics, void formation.

## I. INTRODUCTION

IN COMPLEX plasmas, a dust-free region (void) can develop when the ion drag force exceeds the electric field force. This phenomenon is well known from RF discharges under microgravity [1], [2], where dust is injected into the discharge. Here, the ion production rate is highest in the center of the discharge, and the ambipolar drift of the ions to the outer regions of the discharge exerts an ion drag force on the dust particles [3]–[6], pushing them out of the central region of the discharge. A sharp boundary between the void and the dust-containing area will form at the equilibrium position, where the outward-directed ion drag force is balanced by the inward-directed electric field force.

The confinement of void-free dust clouds in an “anodic plasma”, i.e., a secondary plasma in front of a positively biased disk electrode, could be achieved under different conditions, e.g., in an unmagnetized dc discharge [7], in a Q-machine with a strong magnetic field [8], or in a dc discharge with a weak magnetic field [9]. Trottenberg *et al.* [10] studied the confinement of a dust cloud in a magnetized anodic plasma in more detail. In the experiments of Barkan and Merlino [8], a rigid-body rotation of a dust ball in the  $(E \times B)$ -direction of the ions was observed, which indicates that a magnetic field can influence the dynamics of dust particles.

Manuscript received June 30, 2009; revised September 25, 2009. First published February 2, 2010; current version published April 9, 2010. This work was supported by DFG in the frame of SFB-TR 24 Greifswald-Kiel, Project A2.

The authors are with the Institut für Experimentelle und Angewandte Physik, Christian-Albrechts-Universität, 24098 Kiel, Germany (e-mail: reichstein@physik.uni-kiel.de; pilch@physik.uni-kiel.de; grosse@physik.uni-kiel.de; piel@physik.uni-kiel.de).

Digital Object Identifier 10.1109/TPS.2009.2038700

Recently, Pilch *et al.* [11] have reported on the formation of a torus-shaped dust cloud with a distinct dust-free region in the center. Moreover, the particles confined in the torus performed a rotation in the  $(E \times B)$ -direction of the ions. In a later work, Pilch *et al.* [12] analyzed these torus-shaped dust clouds in more detail, focusing on the behavior of the cloud while varying the external parameters pressure, magnetic field strength, and bias voltage of the anode. They could confirm the particle rotation and were able to measure the horizontal particle velocity at the top and at the bottom of the cloud. Furthermore, a model was briefly discussed, which describes the confinement and the formation of torus-shaped dust clouds.

In this paper, we focus in more detail on the confinement of particles in a magnetized anodic plasma and the particle rotation in torus-shaped dust clouds which is observed in an improved geometry. In Section II, a brief description of the experimental setup is given. The confinement of dust derived from electric measurements is described in Section III. In Section IV, a condition for the existence of torus-shaped dust clouds is proposed, and an estimate of the spatial-dependent rotation velocity of the particles is given, which is compared with particle image velocimetry (PIV) measurements.

## II. EXPERIMENTAL SETUP

The experiments presented in this paper are performed in the device MATILDA-II, which consists of a primary RF source plasma ( $f = 27.12$  MHz) at a low power of 3 W. By positively biasing a disk electrode, a secondary anodic plasma is generated. A detailed description of the experiment can be found in [10] or [11]. The anode (diameter  $d = 24$  mm) is operated at voltages of 65–75 V and low currents of 8–14 mA. The experiments are performed in argon gas at pressures of 5–8 Pa. The magnetic field has a strength of about 20 mT. Typical plasma parameters are density  $n_e \approx 10^{15} \text{ m}^{-3}$  and electron temperature  $T_e = 3$  eV. Because of the scattering of ions by ion–neutral collisions, the ion temperature is higher than the neutral temperature and reaches  $T_i \approx 0.1$  eV [10]. Spherical monodisperse dust particles (melamine formaldehyde) of  $(0.97 \pm 0.05) \mu\text{m}$  diameter were used for the experiments.

In order to observe a vertical plane of the torus-shaped dust cloud, our observation geometry was modified with respect to prior experiments [12]. The dust cloud is illuminated by a vertical laser fan ( $\lambda = 532$  nm, 200 mW), and the scattered light is recorded by a camera viewing through a transparent anode disk. For this purpose, an indium-tin-oxide-coated glass was used, and a mirror was mounted to fold the optical path through a side window. A sketch (top view) of this geometry is

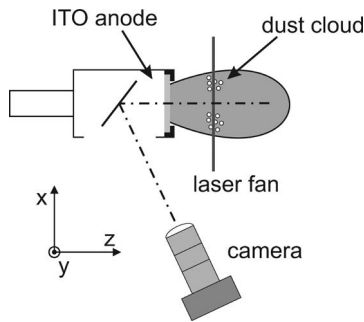


Fig. 1. Top view of a dust cloud trapped in the anodic plasma. It is observed through the indium-tin-oxide-coated anode with a combination of a vertical laser fan and a camera. A sketch of the used coordinate system is shown.

shown in Fig. 1. The coordinate system used here is defined in Fig. 1. The  $z$ -axis is aligned with the magnetic field direction, the  $x$ -axis lies in the horizontal plane, and the  $y$ -axis defines the vertical direction.

With an axially movable and rotatable emissive probe or a Langmuir probe, we are able to record 2-D scans of the plasma potential and the plasma density in the horizontal midplane in front of the anode, denoted  $xz$  plane.

### III. CONFINEMENT OF DUST PARTICLES

#### A. Derivation of Forces

In order to understand the behavior of dust particles immersed in a plasma, it is essential to know the plasma parameters like plasma density and plasma potential. Therefore, 2-D measurements of the plasma potential and the plasma density were performed using an emissive probe and a Langmuir probe, respectively. In Fig. 2(a), a 2-D scan of the plasma potential is shown. The potential is given in volts, and the magnetic field is directed toward the anode. It can be seen that the potential contours are convex and elongated and that they have a nearly symmetric shape about the midsection at  $x = 0$  mm. Therefore, it is justified to assume the plasma potential being rotationally symmetric about the axis of the anode. Then, the electric field  $\vec{E} = -\nabla\Phi$  lies in the  $xz$  plane and has no component perpendicular to this plane. The electric field vectors are shown in Fig. 2(a) as arrows, along with two electric field lines (gray lines) to illustrate their shape. One can see that the electric field has a divergent conical form.

While the plasma potential has a strong spatial dependence, no pronounced variations in the plasma density could be observed.

In order to evaluate the forces acting on the dust particles, one first has to determine the ion velocity defined by the equation of motion for the ions

$$m_i \dot{\vec{v}}_i + m_i \nu_{in} \vec{v}_i = e(\vec{E} + \vec{v}_i \times \vec{B}) \quad (1)$$

with  $\nu_{in}$  being the ion-neutral collision frequency,  $m_i$  the ion mass, and  $\vec{v}_i$  the ion drift velocity. Solving (1), one can see that the ion flow is mainly directed along the electric field lines, but due to the magnetic field, the ions are forced to describe a curved trajectory, resulting in a small azimuthal Hall component of the ion velocity of a few percent of the drift

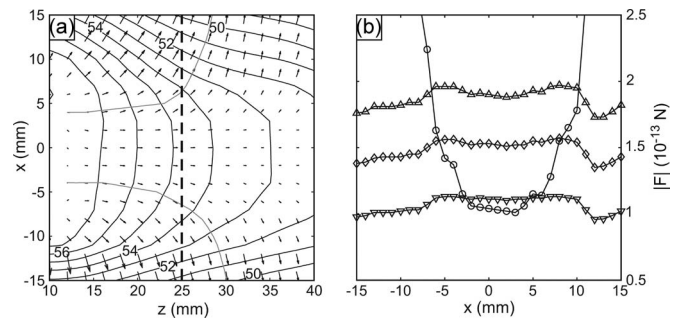


Fig. 2. Confinement of dust particles: (a) Two-dimensional scan of the plasma potential at a magnetic field strength of 20 mT in front of the anode is shown together with the (arrows) derived electric field and (gray lines) two exemplary electric field lines. (b) (Circles) Total electric field force and total ion drag force along the electric field line are plotted versus  $x$  at  $z = 25$  mm [indicated by the thick dashed line in (a)] for different ion densities of (downward-oriented triangles)  $n_i = 4 \times 10^{14} \text{ m}^{-3}$ , (diamonds)  $6 \times 10^{14} \text{ m}^{-3}$ , and (upward-directed triangles)  $8 \times 10^{14} \text{ m}^{-3}$ .

velocity. The charge of the dust particles was calculated using the capacitance model  $q_d = 4\pi\epsilon_0 r_d \Phi_d$ , with  $r_d$  being the dust particle radius and  $\Phi_d$  the surface potential of the dust grain, estimated using the floating condition for a dust grain in the OML approximation. To include the effect of drifting ions, the ion flow on the dust is described by a shifted Maxwellian distribution [13]. Next, the ion drag force of the drifting ions was calculated using the model of Hutchinson [6]. Using  $\vec{F}_{el} = q_d \vec{E}$ , the electric field force was also obtained. The ion drag force is aligned with the ion flow and therefore mainly directed along the electric field lines. Due to a negative dust charge, the electric field force is oriented opposite to the electric field. A more detailed description of the approach can be found in [12].

Now, the confinement of the dust particles in the axial and the radial direction is maintained by the balance of the axial and radial components of the electric field force and the ion drag force, respectively. For a detailed discussion of the axial confinement, see [10].

#### B. Void Criterion

In Fig. 2(b), the total electric field force (circles) and the total ion drag force for different ion densities of  $n_i = 4 \times 10^{14} \text{ m}^{-3}$  (downward-oriented triangles),  $6 \times 10^{14} \text{ m}^{-3}$  (diamonds), and  $8 \times 10^{14} \text{ m}^{-3}$  (upward-oriented triangles) are plotted versus  $x$  at  $z = 25$  mm. One can see that, with increasing ion density, the ion drag force increases almost linearly. As can be seen from Fig. 2(b), the electric field force  $F_{el}$  and the ion drag force  $F_i$  are of the order of  $\sim 10^{-13}$  N. The gravitational force is of the order of  $F_g \approx 0.7 \times 10^{-14}$  N. Therefore, the gravitational force can be neglected for the dust confinement. The intersection of the electric field force and the ion drag force defines a force equilibrium and, therewith, the radial equilibrium position of the dust cloud. Due to the rotational symmetry about  $x = 0$  mm, the two positions shown in Fig. 2(b) represent the same equilibrium position on the left and the right side of the anode axis. Due to the fact that the electric field force shows a very steep gradient, the equilibrium position depends only weakly on the ion density. The inward-directed electric field force pushes the dust particles into the center of the anodic plasma, while

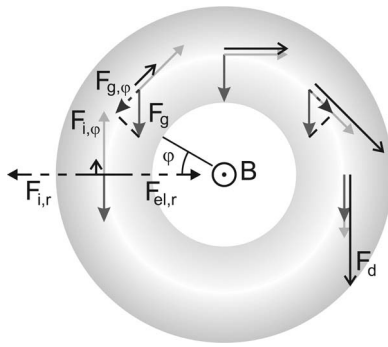


Fig. 3. Sketch of the acting forces. The radial components of the ion drag  $F_{i,r}$  and the electric field force  $F_{el,r}$  are accountable for the confinement. The balance of the weaker forces, i.e., the azimuthal components of the gravitational force  $F_{g,\varphi}$  and the ion drag force  $F_{i,\varphi}$ , determines the force  $F_d$  responsible for the particle rotation.

the outward-directed ion drag force pushes them out of the central region. Hence, a dust-free region will form when the ion drag force exceeds the electric field force. However, if the ion density decreases below a critical value, the ion drag force cannot exceed the electric field force, and no void will form.

#### IV. TORUS-SHAPED DUST CLOUDS

Pilch *et al.* [11] could observe small dust clouds in anodic plasmas, which were not positioned directly in front of the center of the anode but shifted downward to negative  $y$  values. This can be understood by the fact that a void was formed in the central region of the anodic plasma, pushing the dust cloud into a vertically shifted equilibrium position. In a later work, Pilch *et al.* [12] could observe the transformation of such displaced dust clouds into torus-shaped dust clouds.

Due to the rotational symmetry, the electric field has no azimuthal component. However, since the ions are forced onto curved trajectories by the magnetic field, there is an azimuthal component of the ion drag force  $F_{i,\varphi}$ , which is of the same order of magnitude as the gravitational force. Since the radial components of the electric field force and the ion drag force are more than one magnitude larger than the gravitational force, only the azimuthal component  $F_{g,\varphi}$  of the gravitational force can act on the dust, resulting in an angular-dependent gravitational force  $F_{g,\varphi} = -m_d g \cos \varphi$ , with  $g$  being the acceleration of gravity and  $\varphi = 0^\circ$  (9 h) increasing clockwise. This component has to be balanced by the azimuthal component of the ion drag force. A centrifugal force acting on the dust due to the circular path of the equilibrium position only results in a small shift of the equilibrium position to bigger radii and is otherwise negligible for the dust dynamics.

In Fig. 3, the forces are sketched, which are acting on the dust in the  $xy$  plane. It is obvious that, on the left-hand side,  $F_{i,\varphi}$  and  $F_{g,\varphi}$  are acting in opposite directions. A particle will be able to rotate about the torus when the azimuthal component of the ion drag force exceeds the gravitational force

$$F_{i,\varphi} > F_g. \quad (2)$$

In order to get an estimate of the particle rotation velocity, we assume that the acting force on the dust  $F_d = F_{i,\varphi} + F_{g,\varphi}$

is balanced by a neutral friction  $F_n = -m_d \beta v_d$ , with  $m_d$  being the particle mass,  $v_d$  the rotation velocity of the dust, and  $\beta = \delta(8/\pi)p(r_d \rho_d v_{th,n})^{-1}$  the Epstein coefficient [14], with  $p$  being the pressure,  $\rho_d$  the particle mass density,  $v_{th,n}$  the thermal velocity of the neutrals, and  $\delta$  a coefficient of the order of unity. This yields for the rotation velocity of the dust

$$|v_d| = \frac{F_{i,\varphi} - m_d g \cos \varphi}{m_d \beta}. \quad (3)$$

If one assumes that the azimuthal component of the ion drag force only marginally exceeds the gravitational force, the acting force on the dust in the ascending branch at the left-hand side of Fig. 3 is nearly zero, resulting in a very low dust velocity, while on the top and on the bottom, the acting force is about  $F_g$ , giving a velocity  $v_d = g/\beta = 180$  mm/s. On the descending branch, the acting force will be about  $2 \cdot F_g$ , corresponding to a velocity of  $v_d = 360$  mm/s.

In order to test these predictions, optical measurements of the  $xy$  plane of a torus-shaped dust cloud were performed. An image of the end-on view of a torus-shaped dust cloud is shown in Fig. 4(a). Here, an exposure time of  $t = 2$  ms of the camera was chosen, and one can see that the particles on the left-hand side are pointlike, while on the right-hand side, they form streaks, indicating a higher velocity on the right-hand side. Velocity measurements were made with PIV [15]. In Fig. 4(b), the corresponding velocity plot for the rotation velocity of the particles is shown. It can be seen that the velocities at the position 9 h are very low, increasing clockwise until 3 h, where the velocity reaches its maximum value before decreasing clockwise again. This tendency is in good agreement with the simple model proposed here.

In Fig. 4(c), the measured rotation velocity (circles) is plotted versus the angle  $\varphi$  along with the theoretical angular velocity distribution (line), obtained from (3). The reader should note that the velocities are normalized to the maximum value of the velocity. One can see that the measured velocities are well represented by the presented model. However, the measured velocities here are about a factor three smaller than the predicted one.

#### V. DISCUSSION

The difference between the measured and the predicted velocities can have several explanations. It could be observed that particles can stick together forming bigger particles which are not able to rotate along the equilibrium line and accumulate in the bottom part of the torus. Hence, the obtained particle velocities in this region might be smaller. However, since the particles have only a small velocity there, the resulting error should only be small and should only occur in the bottom part of the torus.

Since the distribution of the velocity can be well described by the model, it may be possible that the Epstein friction is not valid in our pressure regime, resulting in an erroneous scaling of the velocities. Therefore, experiments with particles falling through the chamber in neutral gas were performed. However, these experiments showed no velocity deviations from the Epstein formula, which are large enough to explain

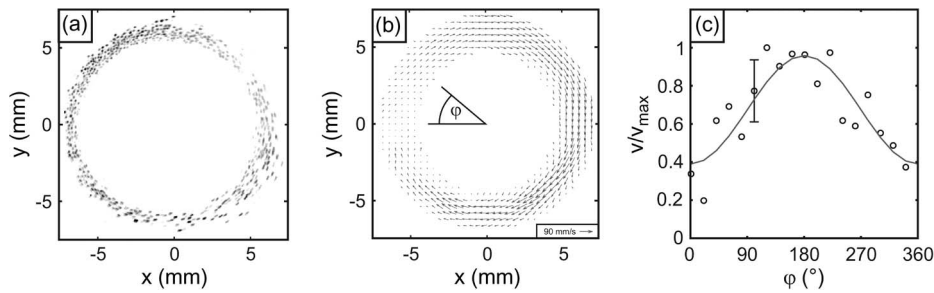


Fig. 4. Results of the end-on observations of a torus-shaped dust cloud: (a) Image of the torus (with exposure time  $t = 2$  ms). (b) Velocity plot of the rotation velocity of the dust particles, obtained with PIV. (c) (Circles) Measured rotation velocity is plotted versus the angle  $\varphi$ ;  $\varphi = 0^\circ$  corresponds to 9 h, increasing clockwise. Furthermore, the (line) theoretical angular velocity distribution, obtained from (3), is shown. The reader should note that the velocities are normalized to the maximum value of the velocity.

the difference between the predicted dust velocities and the observed velocities of the dust particles.

Another and more likely explanation is the fact that the single particle model proposed here neglects interparticle forces. The Coulomb interaction force between two isolated particles in these experiments is of the order of  $10^{-16}$ – $10^{-15}$  N and therefore smaller than the gravitational force. However, if the dust particles are in a dense cloud, the interaction force between neighboring particles might be of a substantial fraction or even exceed the external forces, which then could change the overall particle motion dramatically from the single particle motion. While this simple model can well describe the basic mechanism of torus formation, the model is still incomplete and has to be extended, e.g., to include interparticle forces.

#### REFERENCES

- [1] G. E. Morfill, H. M. Thomas, U. Konopka, H. Rothermel, M. Zuzic, A. Ivlev, and J. Goree, "Condensed plasmas under microgravity," *Phys. Rev. Lett.*, vol. 83, no. 8, pp. 1598–1601, Aug. 1999.
- [2] M. Klindworth, O. Arp, and A. Piel, "Langmuir probe diagnostics in the IMPF device and comparison with simulations and tracer particle experiments," *J. Phys. D, Appl. Phys.*, vol. 39, no. 6, pp. 1095–1104, Mar. 2006.
- [3] M. S. Barnes, J. H. Keller, J. C. Forster, J. A. O'Neill, and D. K. Coultas, "Transport of dust particles in glow-discharge plasmas," *Phys. Rev. Lett.*, vol. 68, no. 3, pp. 313–316, Jan. 1992.
- [4] S. A. Khrapak, A. V. Ivlev, G. E. Morfill, and H. M. Thomas, "Ion drag force in complex plasmas," *Phys. Rev. E, Stat. Phys. Plasmas Fluids Relat. Interdiscip. Top.*, vol. 66, no. 4, p. 046414, Oct. 2002.
- [5] S. A. Khrapak, A. V. Ivlev, S. K. Zhdanov, and G. E. Morfill, "Hybrid approach to the ion drag force," *Phys. Plasmas*, vol. 12, no. 4, p. 042308, Apr. 2005.
- [6] I. H. Hutchinson, "Collisionless ion drag force on a spherical grain," *Plasma Phys. Control. Fusion*, vol. 48, no. 2, pp. 185–202, Feb. 2006.
- [7] E. Thomas, Jr. and M. Watson, "First experiments in the dusty plasma experiment device," *Phys. Plasmas*, vol. 6, no. 10, pp. 4111–4117, Oct. 1999.
- [8] A. Barkan and R. L. Merlino, "Confinement of dust particles in a double layer," *Phys. Plasmas*, vol. 2, no. 9, pp. 3261–3265, Sep. 1995.
- [9] C. Thompson, A. Barkan, N. D'Angelo, and R. L. Merlino, "Dust acoustic waves in a direct current glow discharge," *Phys. Plasmas*, vol. 4, no. 7, pp. 2331–2335, Jul. 1997.
- [10] T. Trottenberg, D. Block, and A. Piel, "Dust confinement and dust-acoustic waves in weakly magnetized anodic plasmas," *Phys. Plasmas*, vol. 13, no. 4, p. 042105, Apr. 2006.
- [11] I. Pilch, T. Trottenberg, A. Piel, and M. E. Koepke, "Dynamics of small dust clouds trapped in a magnetized anodic plasma," *Phys. Plasmas*, vol. 14, no. 12, p. 123704, Dec. 2007.
- [12] I. Pilch, T. Reichstein, and A. Piel, "Torus-shaped dust clouds in a magnetized anodic plasma," *Phys. Plasmas*, vol. 15, no. 10, p. 103706, Oct. 2008.
- [13] E. C. Whipple, "Potentials of surfaces in space," *Rep. Prog. Phys.*, vol. 44, no. 11, pp. 1197–1250, Nov. 1981.
- [14] P. S. Epstein, "On the resistance experienced by spheres in their motion through gases," *Phys. Rev.*, vol. 23, no. 6, pp. 710–733, Jun. 1924.
- [15] J. Kristian Sween, MatPIV v. 1.6.1. [Online]. Available: <http://www.math.uio.no/~jks/matpiv/>



**Torben Reichstein** was born in 1984. He received the Diploma degree in physics from Christian-Albrechts-Universität, Kiel, Germany, in 2008, where he is currently working toward the Ph.D. degree in the group of A. Piel.

His research interests include dusty plasmas.



**Iris Pilch** was born in 1981. She received the Diploma degree in physics from Christian-Albrechts-Universität, Kiel, Germany, in 2006, where she is currently working toward the Ph.D. degree in the group of A. Piel.

Her research interests include dusty plasmas.



**Robert Große-Ahlert** was born in 1983. He received the Diploma degree from Christian-Albrechts-Universität (CAU), Kiel, Germany, in 2009 in the group of A. Piel.

His research interests include dusty plasmas.



**Alexander Piel** was born in 1950. He received the Ph.D. and Habilitation degrees from Ruhr University Bochum, Bochum, Germany, in 1977 and 1986, respectively.

Since 1989, he has been a Full Professor with Christian-Albrechts-Universität, Kiel, Germany. His research interests cover dusty plasmas, plasma waves, and ionospheric research.

Dr. Piel is a Fellow of the APS.



## A.2

# TOROIDAL DUST MOTION IN MAGNETIZED PLASMAS

Torben Reichstein, Iris Pilch, and Alexander Piel

Reprinted with permission from  
Torben Reichstein, Iris Pilch, and Alexander Piel,  
Physics of Plasmas, Vol. 17, 093701 (2010).  
Copyright 2010, American Institute of Physics.

## Toroidal dust motion in magnetized plasmas

Torben Reichstein,<sup>a)</sup> Iris Pilch, and Alexander Piel  
 IEAP, Christian-Albrechts-Universität, D-24098 Kiel, Germany

(Received 18 June 2010; accepted 19 July 2010; published online 17 September 2010)

In a magnetized anodic plasma, dust particles can be confined in a torus-shaped cloud with a distinct dust-free region (void) in its center. The formation of these clouds and their dynamical behavior are experimentally studied with a new observation geometry. The particles rotate about the major axis of the torus. A refined model for the description of the particle dynamics is presented that accounts for inertia and many-body effects. © 2010 American Institute of Physics. [doi:10.1063/1.3476279]

### I. INTRODUCTION

Dust particles immersed in a plasma are subjected to an ion drag force from drifting ions. Due to the negative charge of the dust particles, ion drag force and electric field force are usually directed in opposite directions. A dust-free region (void) can occur when the ion drag force exceeds the electric field force. This phenomenon is well known for dust clouds in rf-discharges under microgravity conditions,<sup>1,2</sup> in laboratory plasmas,<sup>3,4</sup> where particles are grown *in situ*,<sup>3</sup> or when the weight force is compensated by a vertical temperature gradient.<sup>4</sup> The closure of the void was found under microgravity conditions<sup>5</sup> and could be described in terms of simulations.<sup>6</sup> The boundary of a void under microgravity conditions was studied by Wolter *et al.*<sup>7</sup> by means of laser manipulation. There, dust particles were pushed into the void by a focused laser. From the observed particle trajectories, the acting forces at the boundary of a void could be derived.

The rotation of two-dimensional dust clusters in a horizontal plane caused by a magnetic field perpendicular to the cluster was studied experimentally<sup>8,9</sup> and by means of simulations.<sup>10</sup> Konopka *et al.*<sup>8</sup> found that, depending on the discharge parameters, a rigid-body rotation or a sheared rotation could be observed. Carstensen *et al.*<sup>9</sup> studied the influence of a neutral gas rotation on the cluster rotation in a magnetic field.

The confinement of void-free dust clouds can be realized in anodic plasmas.<sup>11,12</sup> Barkan and Merlino<sup>11</sup> reported on a rotation of such a dust cloud in the  $E \times B$ -direction in a magnetized plasma. In a similar setup, the formation of a torus-shaped dust cloud with a distinct dust-free region in its center was found in a magnetized anodic plasma.<sup>13,14</sup> It was found that the particles rotate about the major axis of the torus. Based on electric measurements, a simple single-particle model was proposed to describe the particle confinement as a force balance of ion drag force and electric field force. The formation of the torus-shaped dust clouds and their dynamics were ascribed to a force balance of the azimuthal Hall component of the ion drag force, gravity, and neutral friction. The resulting confinement condition and the basic mechanisms for the dynamics of the clouds were in general agreement with the observations.

<sup>a)</sup>Electronic mail: reichstein@physik.uni-kiel.de.

In the present paper, we present experiments in a new observation geometry that allows a study of these torus-shaped dust clouds in more detail. The new experimental results cannot be fully described by the single-particle model. Therefore, the model was extended to account for additional effects. The paper is organized as follows. In Sec. II, the new experimental findings are presented. The improved model is described in Sec. III and the model results are given in Sec. IV. A discussion concludes the paper in Sec. V.

### II. EXPERIMENTAL FINDINGS

The experiments were performed in the MATILDA-II experiment, which consists of a primary source plasma that is generated by a rf-plasma ( $f=27.12$  MHz) at low power of 2–5 W, and a secondary anodic plasma that is generated in front of a positively biased disk anode. A detailed description of the experiment was given in Refs. 12 and 13. The anode is biased at voltages of 70–90 V and low currents of 9–14 mA. The experiments are performed in argon gas at pressures of 3–7 Pa. The magnetic field has a strength of about 20–40 mT. Typical plasma parameters are density  $n_e \approx 10^{15} \text{ m}^{-3}$  and electron temperature  $T_e=3$  eV.

For our experiments, spherical monodisperse dust particles (melamine formaldehyde) of  $(0.97 \pm 0.05) \mu\text{m}$  diameter were used. The dust is confined in the anodic plasma by a force balance of the electric field and ion drag force. Trottenberg *et al.*<sup>12</sup> studied the axial confinement of dust clouds in front of an anode disk in detail. Pilch *et al.*<sup>14</sup> examined the radial confinement in the same setup.

A top-view sketch of the new observation geometry<sup>15</sup> is shown in Fig. 1(a). For the anode, an indium-tin-oxide coated glass substrate was used, which is optically transparent and electrically conducting. The dust cloud is illuminated by a vertical laser fan ( $\lambda=532$  nm, 200 mW) and the optical path of the scattered light is folded by a mirror and recorded by a camera viewing through a side window. The charge-coupled-device (CCD) camera has a maximum frame rate of 150 frames per second at a maximum resolution of  $480 \times 640$  pixels. By choosing a region of interest, the frame rate can be further increased.



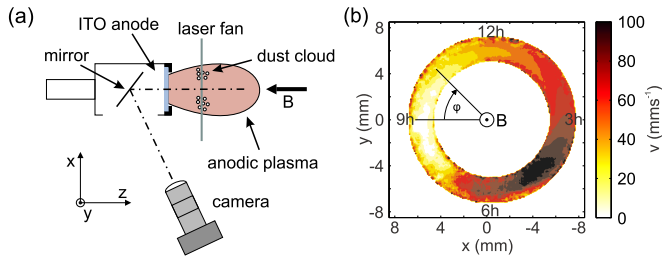


FIG. 1. (Color online) (a) Top-view sketch of the anodic plasma with the new observation geometry and (b) particle image velocimetry measurement of dust streaming velocity in a vertical section.

## A. Rotation

The new observation geometry allows a view along the major axis of the torus-shaped dust clouds, which makes it possible to study the rotational motion of these clouds in more detail. In Fig. 1(b) a measurement of the particle streaming velocity by the method of particle image velocimetry<sup>16</sup> is shown in a torus-shaped dust cloud. In this measurement, the particles performed a rotation in clockwise direction. Therefore, we use an angle  $\varphi$  to indicate a position along the circular path of the torus that is increasing clockwise and  $\varphi=0$  corresponds to the 9 h position on a clock dial. The rotation velocity is lowest around 9 h, and increases for larger  $\varphi$  until, around 5 h, a maximum velocity of about  $100 \text{ mm s}^{-1}$  is reached. Then, the velocity decreases again.

In a previous work,<sup>14</sup> a single-particle model was proposed to describe the confinement and the dynamical behavior of torus-shaped dust clouds. Based on electric measurements of the electric field of the anodic plasma, the radial dust confinement was calculated in terms of a force equilibrium of the electric field force and the ion drag force.<sup>17</sup> For sufficiently large ion densities, the ion drag force exceeds the electric field force in the center of the discharge, resulting in the formation of a void. Due to the rotational symmetry of the discharge, the equilibrium position has an annular shape. The radial components of ion drag force and electric field force were found more than one order of magnitude larger than the weight force acting on the particles.

As a first approach to understanding the dust dynamics, the forces acting on a single particle were examined. Due to the magnetic field, the ion drag force exhibits an azimuthal component that is of the same order of magnitude as the weight force. Because of the strong radial confinement, only the azimuthal component of the weight force was considered. As soon as the azimuthal component of the ion drag force exceeds the weight force, the particle is able to rotate about the major axis of the annular confinement. The excess of the ion drag force over the weight force is balanced by neutral friction, which is proportional to the instantaneous dust velocity.

This model predicted that the lowest velocity would be found at 9 h, while the highest velocity should occur at 3 h. Additionally, the maximum velocity was estimated to be  $\approx 400 \text{ mm s}^{-1}$  at 3 h. While the confinement of the dust clouds and the overall dust motion can be well described,

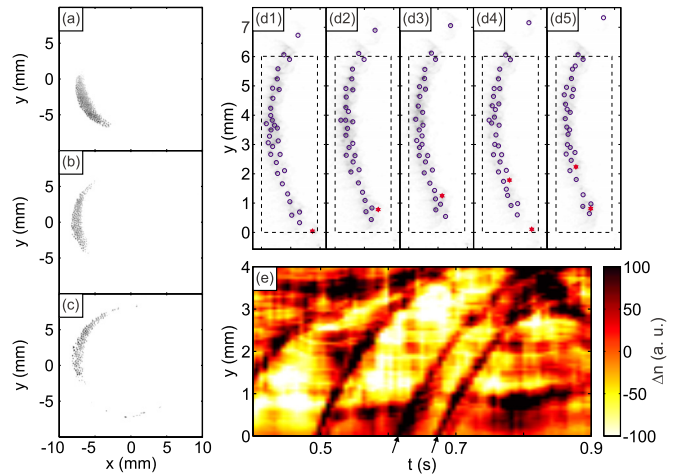


FIG. 2. (Color online) Sickle-shaped dust clouds: position of a displaced dust cloud for (a)  $p=3.83 \text{ Pa}$ , (b)  $p=4.43 \text{ Pa}$ , and (c)  $p=4.59 \text{ Pa}$ . (d) Snapshots of particle movement in a sickle-shaped cloud and (e) the associated time-space diagram of the dust density. The arrows denote the instants, when the red star-marked particles enter the region of interest in (d).

some experimental findings such as the absolute value of the dust velocity or the position of the maximum velocity cannot be described by the single-particle model.

## B. Sickle-shaped dust clouds

While the measurement in Fig. 1(b) shows the rotation of a complete torus-shaped dust cloud, the formation of these tori was studied in another measurement. In Figs. 2(a)–2(c) snapshots of a displaced dust cloud are shown for different pressures: (a)  $p=3.83 \text{ Pa}$ , (b)  $p=4.43 \text{ Pa}$ , and (c)  $p=4.59 \text{ Pa}$ . The observed cloud at  $p=3.83 \text{ Pa}$  is sickle-shaped and remains below the center of the anode. Because of the azimuthal ion drag force, the cloud is also slightly shifted in  $\varphi$ -direction to an equilibrium position around 8 h. No rotating particles are observed, the cloud is *trapped* in an annular confinement well.

For  $p=4.43 \text{ Pa}$ , the equilibrium position of the cloud is around 9 h with particles at positions larger than 9 h. Still, no rotating particles were observed, the state of the cloud is *critical*. If the pressure is further increased ( $p=4.59 \text{ Pa}$ ) an onset of particle rotation is observed.

This behavior can be understood by the fact that, with rising pressure, the ion density increases. Then, the ion drag force also increases and the dust particles are able to reach positions at larger values of  $\varphi$ . When the ion drag force exceeds a threshold value, the particles are able to rotate about the major axis of the annular confinement, which results in the formation of a torus-shaped dust cloud.

In Fig. 2(d) several snapshots of a detailed observation of the particle motion in such a sickle-shaped dust cloud are shown. It should be noted that  $y=0 \text{ mm}$  does not coincide with the vertical position of the center of the anode disk. The stationary particles inside the cloud are marked with circles (blue online), while two particles that enter the cloud from the lower part of the cloud, which can be seen in the first and fourth snapshot (from left to right), respectively, are marked

by stars (red online). When these particles reach the boundary of the cloud, they perform elastic collisions due to short range repulsion. While after the collision the cloud particles mainly move in radial direction, the star-marked particles maintain most of their velocity in azimuthal direction and penetrate deep into the cloud until they have lost their momentum. Furthermore, it can be seen that the uppermost particle moves slowly away from the cloud on a circular path resulting in a rotation about the major axis of the torus.

In order to study the penetration motion of the particles in Fig. 2(c), a time-space diagram of the density variation in the cloud is shown. For this purpose, a region of interest (ROI) is taken [indicated by the dashed box in Fig. 2(b)] and the pixel intensity is summed up along the  $x$ -axis. To get the intensity variation, the mean-intensity of each column was subtracted. Then, the variation of the intensity can be taken as a measurement for the dust density variation. A detailed description of this approach can be found elsewhere.<sup>18</sup>

The instants when the two star-marked particles in Fig. 2(b) enter the ROI are indicated by arrows. One can see areas of increased intensity propagating into the cloud, which can be attributed to the particles that penetrate the cloud as seen in Fig. 2(d). The decreasing slope of these density peaks confirms that the particles are decelerated due to collisions inside the cloud. Although this diagram looks similar to those of dust density waves, it should be noted that these density fluctuations are caused by the motion of one additional dust particle so that the term wave is not justified. However, this is a simple method to trace the motion of a single particle.

### III. MODEL

In the experiments with this new observation geometry, several new aspects of the dynamical behavior of torus-shaped dust clouds were observed that cannot be explained by the single-particle model. The confinement of the dust clouds can still be attributed to a force equilibrium of the radial components of electric field force and ion drag force, respectively. However, the assumption of a mobility-limited dust flow, in which the sum of ion drag and gravity is balanced by the friction force, is too simplistic.

The extended model starts with the observation that the radial components of electric field force and ion drag force are more than one order of magnitude larger than the azimuthal component of the ion drag force or the weight force. They form a very steep radial confinement so that the particles will mainly move in azimuthal direction. Hence, the aim of the model is the description of the dust dynamics in azimuthal direction. Therefore, the radial motion of the particles is neglected by the use of a one-dimensional model with the angle  $\varphi$  [as indicated in Fig. 1(b)] as the space-dependent variable.

Further, the model now takes collective effects and inertia effects into account. A system of  $N$  particles arranged on a ring with radius  $R$  is considered. The equation of motion for the  $i$ th particle at position  $\varphi_i$  and with the azimuthal particle velocity  $v_i$  then reads

$$m\dot{v}_i = F_{g,\varphi}(\varphi_i) + F_N(v_i, \beta) + F_{i,\varphi} + F_Y(\varphi_i, \varphi_j, \kappa, N) \quad (1)$$

with the acting forces  $F_{g,\varphi}$  (weight force),  $F_N(v_i, \beta)$  (neutral friction),  $F_{i,\varphi}$  (ion drag force), and  $F_Y(\varphi_i, \varphi_j, \kappa, N)$  (interparticle force due to a Yukawa repulsion between the particles).

$F_{g,\varphi} = -mg \cos \varphi$  is the azimuthal component of the weight force, with the mass of the dust particles  $m$  and the gravitational acceleration  $g$ . The neutral drag force  $F_N(v_i, \beta)$  is caused by the friction of the neutral gas with the streaming particles. It reads  $F_N = -m\beta v_i$ ,  $\beta = \delta(8/\pi)p(r_p \rho_p v_{th,n})^{-1}$  is the Epstein coefficient<sup>19</sup> with  $p$  as the pressure,  $\rho_p$  is the mass density of the particles,  $v_{th,n}$  is the thermal velocity of the neutrals, and  $\delta$  is a parameter in the order of unity.

Due to the magnetic field, the ion drag force has an azimuthally directed Hall component  $F_{i,\varphi}$  that is of the same order of magnitude as the gravitational force. This force has a constant absolute value and is always directed along the circular path.

The dust particles have a charge of about  $Q = -3000e$ ,  $e$  being the elementary charge, which results in a Yukawa repulsion force between the particles. The force on the  $i$ th particle by  $N-1$  identical particles at the particle position  $\vec{r}_i$  is given by

$$\vec{F}_Y(\vec{r}_i) = \sum_{j \neq i}^N \frac{Q^2}{4\pi\epsilon_0 r_{ij}} \exp\left(-\frac{r_{ij}}{\lambda_D}\right) \left(\frac{1}{r_{ij}} + \frac{1}{\lambda_D}\right) \vec{e}_{ij}, \quad (2)$$

where  $r_{ij}$  is the distance between the particles  $i$  and  $j$ ,  $\lambda_D$  is the Debye length, and  $\vec{e}_{ij} = \vec{r}_{ij}/|\vec{r}_{ij}|$  is the unit vector describing the direction from particle  $j$  to  $i$ .

Since the particles move only along a circular path with radius  $R$ , two new dimensionless variables are introduced, the normalized particle distance  $\rho_{ij} = r_{ij}/R$ , which is only dependent on the angles  $\varphi_i$  and  $\varphi_j$ , and the normalized screening strength  $\kappa = R/\lambda_D$ . The interaction force acts in the direction of the distance vector. However, only the component in azimuthal direction is considered, which is given by the scalar product of the unit distance vector  $\vec{e}_{ij}$  and the unit vector in azimuthal direction  $\vec{e}_{\varphi_i}$  at the position of the  $i$ th particle

$$\vec{e}_{ij} \cdot \vec{e}_{\varphi_i} = \frac{1}{\rho_{ij}} \sin(\varphi_i - \varphi_j). \quad (3)$$

The interaction force acting on the  $i$ th particle at position  $\varphi_i$  then reads

$$\begin{aligned} F_Y(\varphi_i) &= F_C \sum_{j \neq i}^N \frac{1}{\rho_{ij}} \exp(-\kappa \rho_{ij}) \left(\frac{1}{\rho_{ij}} + \kappa\right) \sin(\varphi_i - \varphi_j) \\ &= F_C \cdot Y(\varphi_i, \varphi_j, \kappa, N). \end{aligned} \quad (4)$$

$F_C = Q^2/(4\pi\epsilon_0 R^2)$  is the Coulomb interaction force between two particles at distance  $R$ .

After normalizing the forces in Eq. (1) by  $F_g = mg$ , the differential equations for particle  $i$  read

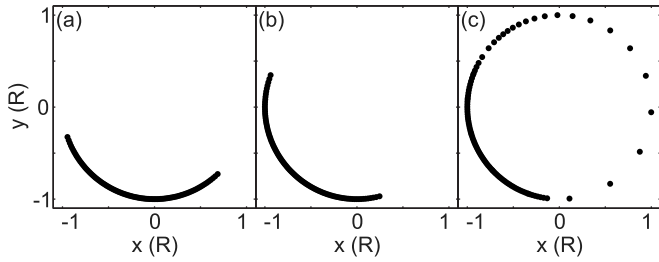


FIG. 3. Different kinds of particle behavior ( $N=100$ ): (a) *trapped* ( $f_i=0.2$ ), (b) *critical* ( $f_i=0.6$ ), and (c) *rotating* ( $f_i=0.8$ ).

$$\dot{\varphi}_i = \frac{v_i}{R},$$

(5)

$$\frac{1}{g}\dot{v}_i = -\cos \varphi_i - \frac{\beta}{g}v_i + f_i + f_C \cdot Y(\varphi_i, \varphi_j, \kappa, N),$$

$f_i = F_{i,\varphi}/F_g$  is the normalized azimuthal ion drag force and  $f_C = F_C/F_g$  is the normalized Coulomb interaction force.

In order to model the specific dynamics of the experiment, the model parameters were estimated from the experimental conditions under which the torus-shaped dust clouds were observed. With  $R \approx 6$  mm,  $n_i \approx 10^{15}$  m $^{-3}$  and  $p = 3-7$  Pa, the model parameters are  $\kappa = 100$ ,  $f_C = 0.01$ ,  $\beta = 40-80$  s $^{-1}$ , and  $f_i = \mathcal{O}(1)$ . The number of particles was varied in the range  $N = 10-600$ .

First, the relaxation of a system with  $N$  equally spaced particles on the circular path under the influence of gravity and Yukawa repulsion without an external driving force ( $f_i = 0$ ) was computed by solving Eq. (5) using a Runge–Kutta algorithm.<sup>20</sup> Then, starting from this relaxed particle configuration, the dynamics of the system were calculated by integrating Eq. (5) with an external driving force ( $f_i > 0$ ).

#### IV. RESULTS

In Fig. 3 snapshots of the particle positions ( $N=100$ ) of the steady-state are shown for three different values of  $f_i$ . The radius of the annular equilibrium position is  $R$ . The particles are represented as filled circles and magnified for a better visualization.

For small  $f_i = 0.2$  [Fig. 3(a)], the particles are nearly symmetrically arranged around the 7 h position. Because of the weak ion drag force, only a minor shift of the cloud toward higher values of  $\varphi$  is observed, and the particles come to rest in this state. This behavior can be described as *trapped*, since no rotation is observed.

With increasing ion drag force [ $f_i = 0.6$ , Fig. 3(b)], the cloud is shifted further up along the circular path. The uppermost particle reaches positions  $\varphi > 9$  h without being able to rotate about the torus axis. Again, the particles are at rest in this state. But, when  $f_i$  is only slightly increased, the uppermost particle overcomes the gravitational force, allowing a rotation motion along the annular path. Therefore, this state is called *critical*.

For an even higher ion drag force [ $f_i = 0.8$ , Fig. 3(c)] the particles are now able to move along the annular equilibrium path. While on the ascending branch (left hand side) the

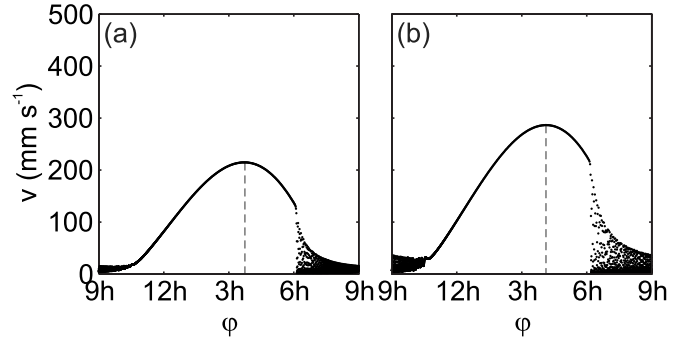


FIG. 4. Phase space diagram of one particle ( $N=100$ ,  $f_i=0.8$ ) for (a)  $\beta=80$  s $^{-1}$  and (b)  $\beta=60$  s $^{-1}$ .

interparticle distance is small, the interparticle distance on the descending branch (right hand side) is much larger.

Due to the repulsion of the particles, the cloud in the trapped and the critical state are elongated, pushing the upper particles of the cloud further up than expected by a force equilibrium of ion drag force and gravitational force. Moreover, the onset of particle rotation is found to occur for even lower values of the ion drag force  $f_i < 1$ , which could not be predicted by the single-particle model. There, it was required that the ion drag force has to overcome gravity for particle rotation ( $f_i > 1$ ). Here, the repulsive interaction between the particles leads to a lowering of the threshold for the onset of particle rotation.

For a better insight on the particle rotation, the case of  $N=100$  and  $f_i=0.8$  is studied in more detail. Therefore, in Fig. 4 phase space diagrams for different values of the Epstein friction coefficient are shown. Each dot in the phase space represents the position of a single particle for each time step in the simulation. It is seen that, for strong friction, the maximum velocity of the particles is significantly smaller than for weak friction and lies in the range of  $v_{\max} = 200-400$  mm s $^{-1}$ .

The angular position of the point of maximum speed is of interest, too. For a better visibility, they are indicated by the dotted lines in Fig. 4. The position is also dependent on  $\beta$  and increases with decreasing friction and lies in the range of  $\varphi(v_{\max}) = 3.5-4.5$  h.

Furthermore, two different types of particle motion can be distinguished. While the motion from 10 to 6 h is continuous, from 6 to 10 h the particles exhibit an oscillatory motion in terms of a dust lattice wave, which will be discussed later in more detail.

#### A. Variation of parameters

Now, the influence of the particle number  $N$ , friction  $\beta$ , and the normalized ion drag force  $f_i$  on the particle motion is studied in more detail. Therefore, the maximum (minimum) particle velocity  $v_{\max}$  ( $v_{\min}$ ) is plotted as filled (open) symbols as a function of the particle number  $N$  (Fig. 5), or as a function of the normalized ion drag force  $f_i$  [Fig. 6(a)]. Additionally, the influence of the normalized ion drag force  $f_i$  and friction  $\beta$  on the position of maximum velocity  $\varphi(v_{\max})$

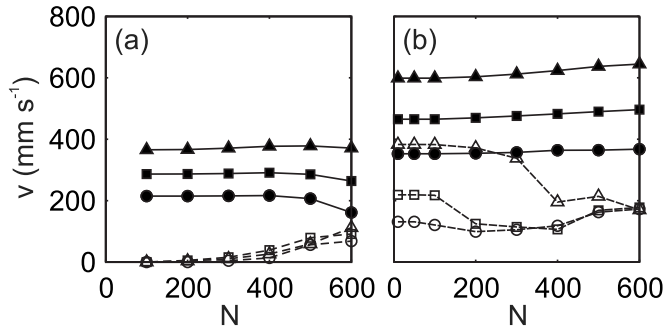


FIG. 5. Influence of particle number  $N$  and friction  $\beta$  on the rotation velocity  $v$  for (a)  $f_i=0.8$  and (b)  $f_i=2.0$ . The closed (open) symbols represent the maximum (minimum) particle velocity. Shown are the results for  $\beta=80 \text{ s}^{-1}$  (circles),  $\beta=60 \text{ s}^{-1}$  (squares), and  $\beta=40 \text{ s}^{-1}$  (triangles).

is presented in Fig. 6(b). The results are shown for  $\beta=80 \text{ s}^{-1}$  (circles),  $\beta=60 \text{ s}^{-1}$  (squares), and  $\beta=40 \text{ s}^{-1}$  (triangles).

The influence of  $N$  and  $\beta$  on the rotation velocities for small ion drag force ( $f_i=0.8$ ) and high ion drag force ( $f_i=2.0$ ) are shown in Figs. 5(a) and 5(b), respectively. In Fig. 5(a)  $v_{\max}$  ranges from 200 to 400  $\text{mm s}^{-1}$ . While  $v_{\max}$  is nearly independent on the particle number, an increase of friction (increasing  $\beta$ ) leads to smaller velocities. Simulations were also carried out for  $N < 100$ , however, for small particle numbers no rotation was obtained for  $f_i=0.8$ . This can be understood by the fact that for small  $N$ , the repulsive force is too weak to compensate the missing fraction of ion drag force to overcome gravity. The open symbols represent the minimum velocity  $v_{\min}$  of the particles. The very low values result from the oscillatory motion already seen in Fig. 4. However, with increasing particle number,  $v_{\min}$  also slightly increases and is nearly independent of the friction of the system.

In Fig. 5(b) the results for  $f_i=2.0$  are shown. While  $v_{\max}$  is still nearly independent of the particle number and shows the same behavior regarding the influence of friction as in the case of a smaller ion drag force, the absolute values of  $v_{\max}$  are significantly higher and are now in the range of  $v_{\max}=400\text{--}600 \text{ mm s}^{-1}$ . Furthermore, one can see that, for small particle numbers, a rotational motion was observed. For the minimum particle velocity, the behavior is different for high ion drag force. For small particle numbers,  $v_{\min}$  is nearly independent of  $N$  but varies much with  $\beta$ , similar to  $v_{\max}$ . With increasing  $N$ ,  $v_{\min}$  decreases and becomes more and more independent of  $\beta$  as seen for  $v_{\min}$  in Fig. 5(a).

This behavior can be explained by the different situations for low and high ion drag force. For small ion drag force and small particle number, the cloud is mainly shifted and only due to the repulsive force, several particles are able to rotate about the major axis while many particles remain in the shifted cloud. With increasing particle number, the interparticle distance decreases, leading to a stronger repulsive force between neighboring particles. In the limit of an extremely large particle number, the annular trap would be completely filled with particles and due to the strong Yukawa repulsion a rigid-body rotation would occur even for very small ion drag forces.

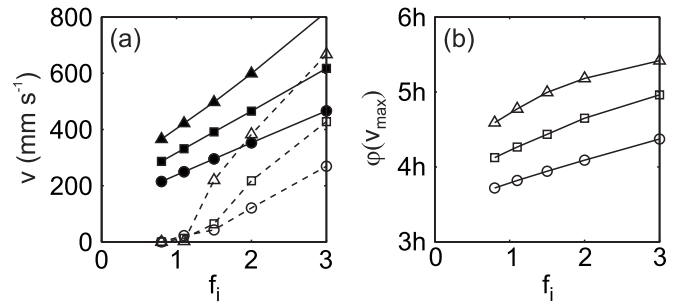


FIG. 6. Influence of the normalized ion drag force  $f_i$  and friction  $\beta$  ( $N=100$ ) on (a) the particle rotation velocity and (b) the position of maximum velocity. Shown are the results for  $\beta=80 \text{ s}^{-1}$  (circles),  $\beta=60 \text{ s}^{-1}$  (squares), and  $\beta=40 \text{ s}^{-1}$  (triangles).

For a high ion drag force and small particle numbers, the interparticle forces are small and the dynamic is mainly described by the modulation of the ion drag by gravity. However, for high particle numbers, the particles have to be considered as a ring of springs with high repulsive forces between each other. A small deviation of the interparticle distance will then lead to a significantly large additional force on a particle, which in return leads to a relaxation. Since the particles cannot pass each other, the relaxation will exhibit an oscillatory character.

For a better insight on the influence of the ion drag force on the particle motion, in Fig. 6(a)  $v_{\max}$  and  $v_{\min}$  are plotted over  $f_i$  (with  $N=100$ ). The used symbols are the same as in Fig. 5. It can be seen that  $v_{\max}$  increases almost linearly with increasing  $f_i$ . The same influence of the friction is found, as observed in Fig. 5. High friction leads to a smaller  $v_{\max}$ . For ion drag forces  $f_i < 0.8$ , only displaced clouds without particle rotation were found.

For ion drag forces around  $f_i=1$ ,  $v_{\min}$  is independent of friction and nearly zero, indicating that for these cases wave-like behavior is obtained. If  $f_i$  is further increased  $v_{\min}$  also increases almost linearly with increasing ion drag force and a strong dependence on the friction is observed. For high ion drag force,  $v_{\min}$  and  $v_{\max}$  approach each other more and more, leading to a more rigid-bodylike motion that is only little disturbed by the modulation of the weight force.

Figure 6(b) shows the influence of friction and ion drag force on the position of maximum speed  $\varphi(v_{\max})$ . Two trends can be observed,  $\varphi(v_{\max})$  increases slightly with increasing ion drag force and  $\varphi(v_{\max})$  decreases significantly with increasing friction. Furthermore,  $\varphi(v_{\max})$  is in every case  $> 3 \text{ h}$ . For high  $f_i$  and low  $\beta$ ,  $\varphi(v_{\max})$  reaches values larger than 5 h.

This behavior can be explained by the inertia of the particles that allows them to obtain higher velocities at  $\varphi > 3 \text{ h}$  although their highest acceleration is at 3 h. For strong friction this effect becomes less important resulting in a lower value of  $\varphi(v_{\max})$ .

## B. Dust lattice waves

Now, the aforementioned oscillatory motion of the particles is studied in more detail. A snapshot of the phase space of the ascending branch of the torus is shown in Fig. 7(a). Every circle represents one particle with a linear interpola-

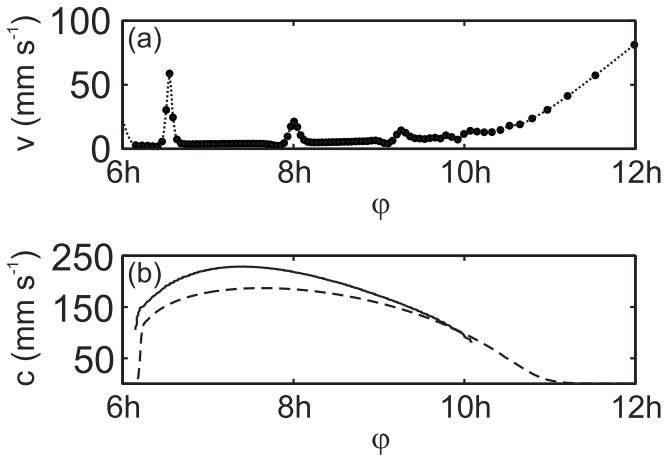


FIG. 7. On the oscillatory particle motion: (a) snapshot of the particle positions in the phase space (circles) with a linear interpolation onto an equally spaced grid (dotted line). Three peaks can be seen which propagate through the particle chain similar to a DLW. (b) Velocities of the DLW: Shown are the propagation velocity of a peak in (a) (solid line) and the theoretical DLW velocity (dashed line) calculated from the mean interparticle distance of the particles using Eq. (6).

tion of the particle velocity (dotted line). One can see that the particles in the range of  $\varphi=6-10$  h are arranged on a chain with small interparticle distances. Furthermore, most of the particles exhibit only a very low velocity  $v$ , which means that they are mainly at rest. But also very localized particles are found which have a significantly higher velocity than their surroundings at 6.5, 8, and 9 h. Additionally, for  $\varphi > 10$  h the interparticle distance increases as well as  $v$  with increasing  $\varphi$ .

The particles in the area of  $\varphi > 10$  h show a continuous motion as already seen in Fig. 4. For  $\varphi=6-10$  h the particles are arranged on a chain and fast particles, which rotate about the torus axis, hit the lower end of this chain. Then, a compressional wave propagates through the chain, which can be seen as a propagation of the peaks of enhanced dust velocity. The geometry of this system gives rise to the assumption that this motion can be described in terms of a one-dimensional dust lattice wave (DLW). For a DLW, the wave velocity is<sup>21</sup>

$$c = \sqrt{\frac{D}{m_d} \langle r_{ij} \rangle}, \quad \text{with } D = \left. \frac{\partial F_Y}{\partial r} \right|_{r=\langle r_{ij} \rangle} \quad (6)$$

with the “spring constant”  $D$  being the derivative of the interparticle force taken at the mean interparticle distance  $\langle r_{ij} \rangle$ .

In order to verify the assumption, the propagation velocity of one peak (solid line) is shown in Fig. 7(b) together with the theoretical wave velocity (dashed line) obtained from the mean interparticle distance, using Eqs. (6) and (4), taking only one nearest neighbor into account. A good agreement between both velocities is seen. However, the velocities obtained from Eq. (6) slightly underestimate the velocities obtained from the simulations when using the mean interparticle distance. When two particles are compressed by the wave, their interparticle distance is smaller. Taking the

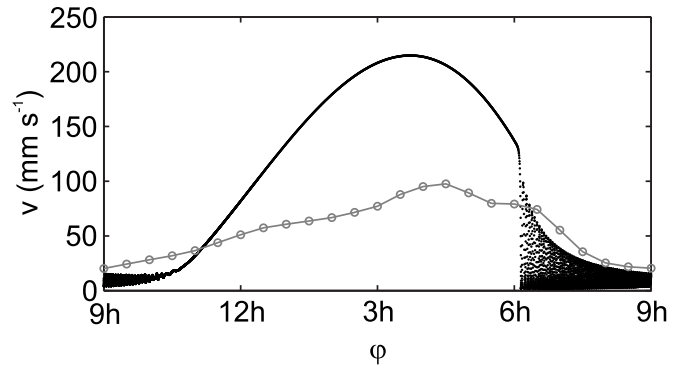


FIG. 8. Comparison of simulation and experiment. The simulation data [same as in Fig. 4(a)] are shown as black filled dots, the data obtained from the experiment [same as in Fig. 1(b)] are given by gray open circles with a solid line.

reduced interparticle distance of two compressed particles into account, the theoretical velocity obtained from Eq. (6) would be higher, resulting in an even better agreement with the velocities observed in the simulations.

In Fig. 8 a comparison of the phase space obtained from the experiment and the model is given. The phase space from the model is presented as filled black dots [same as in Fig. 4(a)]. For the phase space from the experiment (gray open circles with solid line) the same data set as for Fig. 1(b) was used. One can see that the model still overestimates the maximum velocity by a factor of 2 but the agreement of the position of the maximum velocity is much better than with the single-particle model.<sup>14</sup>

## V. DISCUSSION

Dust motion in a toroidal confinement region can be understood as follows: The essential force for the particle motion is the azimuthal component of the ion drag force. It determines the particle velocity as well as the onset of particle rotation. With increasing ion drag force, the velocity modulation by the weight force becomes less important, leading in the limit of very large ion drag forces to a rigid-body rotation.

For the critical ion drag force, i.e., the value of  $f_i$  for the onset of particle rotation, the repulsive Yukawa interaction of the particles is of particular interest. A single particle is able to rotate about the main torus axis only when the ion drag force overcomes gravity,  $f_i > 1$ . When many particles are trapped, the formation of a torus can be achieved for  $f_i < 1$  (see Fig. 3), i.e., the threshold is lowered by the collectivity caused by the particle repulsion. Moreover, this reduced threshold leads to an overall lower particle velocity.

Due to the particle inertia, ballistic effects occur on the descending branch of the torus, resulting in a shift of the position of maximum particle velocity  $\varphi(v_{\max})$  toward higher values of  $\varphi$ . Friction has a strong effect on this position, low friction leads to a larger shift, allowing the particles to obtain a very high velocity. At high friction, the shift of  $\varphi(v_{\max})$  is smaller so that  $v_{\max}$  becomes also smaller than for low friction.

In the transition region from a displaced sickle-shaped dust cloud into a torus-shaped dust cloud with rotating particles, the model predicts the occurrence of dust lattice wave-like particle motion due to the restriction of the model to one dimension, in which particles are not allowed to overtake each other. In experiments, however, single particles are able to penetrate into the cloud. Due to the three-dimensional shape of their confinement, they have the possibility to pass other particles and to lose momentum not in a single collision but by many collisions, as observed.

The restriction to one dimension has several limitations. If too many particles are taken into account in the simulation, the Yukawa repulsion leads to a completely filled ring so that even a very low ion drag force ( $f_i \ll 1$ ) would be sufficient to enable particle rotation. Furthermore, if the interparticle distance decreases below a critical value, the system would become unstable against a zigzag transition.<sup>22,23</sup> Therefore, the number of particles used in the simulations should not be too high.

The overestimation of the maximum particle velocities can also be attributed to the restriction to one dimension. Since the equation of continuity has to be satisfied, the product of particle velocity and particle density (here the inverse interparticle distance) has to be constant. Because of the small interparticle distance in the ascending branch of the torus, the velocity in the descending branch has to increase significantly because of the high increase of the interparticle distance there.

It is expected that an extension of the model to three dimensions will overcome these limitations. Then, particles will be able to evade radially as seen in the experiments. This should lead to an even better agreement between model and experiments. However, the enhancement of the single-particle model has shown a significant improvement in order to describe and understand the particle behavior in torus-shaped dust clouds.

## ACKNOWLEDGMENTS

Robert Große-Ahlert is gratefully acknowledged for the construction of the new observation geometry and first experiments.

The present investigations were financially supported by DFG within the Transregional Collaborative Research Center TR-24, project A2.

- <sup>1</sup>G. E. Morfill, H. M. Thomas, U. Konopka, H. Rothermel, M. Zuzic, A. Ivlev, and J. Goree, *Phys. Rev. Lett.* **83**, 1598 (1999).
- <sup>2</sup>M. Klindworth, O. Arp, and A. Piel, *J. Phys. D* **39**, 1095 (2006).
- <sup>3</sup>D. Samsonov and J. Goree, *Phys. Rev. E* **59**, 1047 (1999).
- <sup>4</sup>H. Rothermel, T. Hagl, G. E. Morfill, M. H. Thoma, and H. M. Thomas, *Phys. Rev. Lett.* **89**, 175001 (2002).
- <sup>5</sup>A. M. Lipaev, S. A. Khrapak, V. I. Molotkov, G. E. Morfill, V. E. Fortov, A. V. Ivlev, H. M. Thomas, A. G. Khrapak, V. N. Naumkin, A. I. Ivanov, S. E. Tretschnev, and G. I. Padalka, *Phys. Rev. Lett.* **98**, 265006 (2007).
- <sup>6</sup>V. Land and W. J. Goedheer, *New J. Phys.* **10**, 123028 (2008).
- <sup>7</sup>M. Wolter, A. Melzer, O. Arp, M. Klindworth, and A. Piel, *Phys. Plasmas* **14**, 123707 (2007).
- <sup>8</sup>U. Konopka, D. Samsonov, A. V. Ivlev, J. Goree, V. Steinberg, and G. E. Morfill, *Phys. Rev. E* **61**, 1890 (2000).
- <sup>9</sup>J. Carstensen, F. Greiner, L.-J. Hou, H. Maurer, and A. Piel, *Phys. Plasmas* **16**, 013702 (2009).
- <sup>10</sup>L.-J. Hou and Y. N. Wang, *Phys. Plasmas* **12**, 042104 (2005).
- <sup>11</sup>A. Barkan and R. L. Merlino, *Phys. Plasmas* **2**, 3261 (1995).
- <sup>12</sup>T. Trottenberg, D. Block, and A. Piel, *Phys. Plasmas* **13**, 042105 (2006).
- <sup>13</sup>I. Pilch, T. Trottenberg, A. Piel, and M. Koepke, *Phys. Plasmas* **14**, 123704 (2007).
- <sup>14</sup>I. Pilch, T. Reichstein, and A. Piel, *Phys. Plasmas* **15**, 103706 (2008).
- <sup>15</sup>T. Reichstein, I. Pilch, R. Grosse-Ahlert, and A. Piel, *IEEE Trans. Plasma Sci.* **38**, 814 (2010).
- <sup>16</sup>See <http://www.math.uio.no/~jks/matpiv/> for "An introduction to MATPIV v. 1.6.1."
- <sup>17</sup>I. H. Hutchinson, *Plasma Phys. Controlled Fusion* **48**, 185 (2006).
- <sup>18</sup>I. Pilch, T. Reichstein, and A. Piel, *Phys. Plasmas* **16**, 123709 (2009).
- <sup>19</sup>P. S. Epstein, *Phys. Rev.* **23**, 710 (1924).
- <sup>20</sup>W. H. Press, B. P. Flannery, S. A. Teukolsky, and W. T. Vetterling, *Numerical Recipes: The Art of Scientific Computing* (Cambridge University Press, Cambridge, 1992).
- <sup>21</sup>F. Melandsø, *Phys. Plasmas* **3**, 3890 (1996).
- <sup>22</sup>I. V. Schweigert, V. A. Schweigert, and F. M. Peeters, *Phys. Rev. B* **54**, 10827 (1996).
- <sup>23</sup>T. E. Sheridan, *Phys. Scr.* **80**, 065502 (2009).

## A.3

# SIMULATION OF DUST STREAMING IN TOROIDAL TRAPS: STATIONARY FLOWS

Torben Reichstein and Alexander Piel

Reprinted with permission from  
Torben Reichstein and Alexander Piel,  
Physics of Plasmas, Vol. 18, 083705 (2011).  
Copyright 2011, American Institute of Physics.

## Simulation of dust streaming in toroidal traps: Stationary flows

Torben Reichstein<sup>a)</sup> and Alexander Piel

IEAP, Christian-Albrechts-Universität, D-24098 Kiel, Germany

(Received 31 May 2011; accepted 21 June 2011; published online 9 August 2011)

Molecular-dynamic simulations were performed to study dust motion in a toroidal trap under the influence of the ion drag force driven by a Hall motion of the ions in  $E \times B$  direction, gravity, interparticle forces, and friction with the neutral gas. This article is focused on the inhomogeneous stationary streaming motion. Depending on the strength of friction, the spontaneous formation of a stationary shock or a spatial bifurcation into a fast flow and a slow vortex flow is observed. In the quiescent streaming region, the particle flow features a shell structure which undergoes a structural phase transition along the flow direction. © 2011 American Institute of Physics.  
[doi:10.1063/1.3610376]

### I. INTRODUCTION

In complex plasmas, micrometer-sized particles are subjected to the ion drag force and the electric field force. Due to the negative charge of the particles, these forces are usually directed in opposite directions. If the ion drag force exceeds the electric field force in the center of a discharge, a dust-free region (void) forms, which is well known for experiments under microgravity conditions<sup>1,2</sup> and in laboratory plasmas,<sup>3,4</sup> when particles are grown *in situ*<sup>3</sup> or when gravity is compensated by a temperature gradient.<sup>4</sup> The closure of the void was demonstrated under microgravity conditions<sup>5</sup> and recently in a laboratory plasma.<sup>6</sup>

The influence of a magnetic field on the motion of two-dimensional dust cloud in a horizontal plane was studied experimentally<sup>7,8</sup> and by means of simulations.<sup>9</sup> Depending on the discharge parameters, Konopka *et al.*<sup>7</sup> found that a rigid-body rotation or a sheared rotation of the clusters could be observed. Carstensen *et al.*<sup>8</sup> studied the influence of the rotation of the neutral gas on the dust motion in a magnetic field.

Moving particles in narrow channels form confinement-induced layers.<sup>10,11</sup> Teng *et al.*<sup>10</sup> found that the layering propagates from the boundary into the center of the channel. In colloidal systems, Henseler *et al.*<sup>11</sup> observed that a density gradient of the particles leads to a reduction of the number of layers, when it is energetically favorable. For laser-cooled ions in a quadrupole ring, Birkel *et al.*<sup>12</sup> reported the formation of helical and multiple-shell structures.

In magnetized anodic plasmas, void-free dust clouds can be confined.<sup>13,14</sup> Barkan and Merlino<sup>13</sup> had found a rigid-body rotation of a dust cloud in  $E \times B$  direction. In a similar setup, we had observed torus-shaped dust clouds with a distinct dust-free region in its center.<sup>15,16</sup> The particles perform a rotation about the major axis of the torus, which coincides with the magnetic field direction. Based on probe measurements, it was concluded that the radial components of ion drag force and electric field force lead to the formation of the void,<sup>16</sup> similar to the unmagnetized plasma. The Hall component of the ion drag force, which is directed in azimuthal direction, was identified as the driving mechanism for the

cloud rotation.<sup>16</sup> Motivated by new experimental findings,<sup>17,18</sup> a one-dimensional  $N$ -particle model with strong radial confinement was proposed to account for many-particle effects as well as inertia effects.<sup>18</sup> The reduction of the threshold for the onset of particle rotation due to the particle reduction was found and the influence of friction on the particle motion was studied. Furthermore, dust lattice waves could be observed.

In the present paper, this model is further extended to three dimensions to describe dust streaming in a toroidal trap with weak radial confinement by means of molecular-dynamics (MD) simulations. The paper is organized as follows. In Sec. II, the three-dimensional model is presented. In Sec. III, the stationary streaming is studied in detail and the local evolution of the flux is analyzed in Sec. IV. A discussion concludes the paper in Sec. V.

### II. MODEL

The main goal of the performed simulations is a detailed description of dust particle motion in a toroidal trap as observed in previous experiments.<sup>16,18</sup> Therefore, the geometry is chosen very similar to the experimental setup. In Fig. 1, a sketch of the anodic plasma with the used coordinate system is shown.

Based on the probe measurements, it is justified to assume the confinement potential to be harmonic in radial<sup>16</sup> and in axial<sup>14</sup> directions, given by

$$\begin{aligned} U_C(\tilde{\rho}) &= \frac{m_d}{2} \omega_0^2 (\tilde{\rho} - R)^2, \\ U_C(z) &= \frac{m_d}{2} \omega_0^2 z^2, \end{aligned} \quad (1)$$

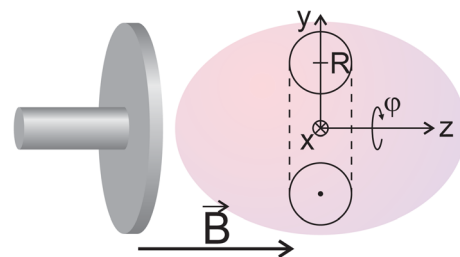


FIG. 1. (Color online) Sketch of the anodic plasma with the used coordinate system.

<sup>a)</sup>Electronic mail: reichstein@physik.uni-kiel.de.



with  $m_d$  being the particle mass,  $\omega_0$  the confinement strength in radial and axial directions,  $\tilde{\rho} = \sqrt{x^2 + y^2}$  the radial particle distance from the center of the anode ( $\{x, y\} = \{0, 0\}$ ), and  $R$  the radial distance of the potential minimum from the central axis ( $\tilde{\rho} = 0$ ). For the axial confinement,  $z$  denotes the axial distance from the potential minimum, which is here located at  $z=0$ . With  $\vec{F}_C = -\nabla(U_C(\rho) + U_C(z))$  the confinement force  $\vec{F}_C$  can be calculated. The particles are under the influence of gravity  $\vec{F}_g = -m_d g \vec{e}_y$ , where  $\vec{F}_g$  defines the  $y$ -direction.

Since the plasma is magnetized, the ion motion has a Hall component in  $\vec{E} \times \vec{B}$  direction, which in our setup is directed in azimuthal direction. This Hall component results in an azimuthal ion drag force, which is on the order of a few percent of the radial ion drag force for the considered case. The absolute value of the azimuthal ion drag force component is assumed to be constant and acts in azimuthal direction:  $\vec{F}_i = F_i \vec{e}_\phi$ . From here on, the term ‘‘ion drag force’’ always refers to the azimuthal component of the ion drag force, unless otherwise stated. It was found that the ion drag is of the same order of magnitude as the weight force.

Due to the plasma environment particles of  $a = 1 \mu\text{m}$  diameter obtain a charge of about  $Z_d = -2500$  elementary charges, which results in an electrostatic repulsion between the particles. The force acting on the  $i$ th particle by  $N - 1$  identical particles is given by the shielded Coulomb (Yukawa) force

$$\vec{F}_Y(\vec{r}_i) = \sum_{j \neq i}^N \frac{Q_d^2}{4\pi\epsilon_0 \Delta_{ij}^3} \exp(-\kappa \Delta_{ij}) (1 + \kappa \Delta_{ij}) \vec{r}_{ij}. \quad (2)$$

Here,  $\vec{r}_i$  is the particle position,  $\vec{r}_{ij}$  the distance vector between the  $i$ th and  $j$ th particles,  $\Delta_{ij} = |\vec{r}_{ij}|$ , and  $\kappa = 1/\lambda_D$ , the inverse of the Debye length.

The streaming particles experience friction by the neutral gas background  $\vec{F}_N = -m_d \beta \vec{v}$ , with  $\vec{v}$  being the velocity of a particle and  $\beta$  the Epstein friction coefficient.<sup>19</sup>

A Gaussian random force  $\vec{F}_R$ , which is assumed to be uncorrelated in time<sup>20</sup>  $\langle \vec{F}_R(t) \vec{F}_R(0) \rangle = 2m_d \beta k_B T \delta(t)$ , is introduced into the system as a heat bath to compensate for the energy dissipation by friction. Then, the Langevin equations of motion for the  $i$ th particle read<sup>21</sup>

$$\begin{aligned} \dot{\vec{r}}_i &= \vec{v}_i, \\ m_d \dot{\vec{v}}_i &= \vec{F}_S - m_d \beta \vec{v}_i + \vec{F}_R. \end{aligned} \quad (3)$$

$\vec{F}_S = \vec{F}_C + \vec{F}_g + \vec{F}_i + \vec{F}_Y$  denotes the sum of the external forces acting on the system. The time evolution is then calculated using a Verlet-like algorithm,<sup>21</sup>

$$\begin{aligned} \vec{r}_i(t + \delta t) &= \vec{r}_i(t) + c_1 \delta t \vec{v}_i(t) + c_2 \delta t^2 \vec{a}_i(t) + \delta \vec{r}_i^G \\ \vec{v}_i(t + \delta t) &= c_0 \vec{v}_i(t) + (c_1 - c_2) \delta t \vec{a}_i(t) + \dots \\ &\quad + c_2 \delta t \vec{a}_i(t + \delta t) + \delta \vec{v}_i^G. \end{aligned} \quad (4)$$

Here,  $\vec{a} = \vec{F}_S/m_d$  is the acceleration due to the external forces and  $\delta \vec{r}^G$ ,  $\delta \vec{v}^G$  are random displacements of the particles' position and velocity due to the random force. The numerical coefficients read  $c_0 = \exp(-\beta \delta t)$ ,  $c_1 = (\beta \delta t)^{-1} (1 - c_0)$ , and  $c_2 = (\beta \delta t)^{-1} (1 - c_1)$ .

Every simulation run starts from randomly distributed particles inside the trap. The time step  $\delta t$  is chosen sufficiently short so that the particle displacement in a single time step typically does not exceed 2% of the Wigner-Seitz radius from the random start distribution in order to fulfill the Courant-Friedrichs-Lewy-condition<sup>22</sup> even when the particles are strongly compressed during the simulation. A typical run consists of  $10^5$  time steps, a steady state is reached after 25 000 steps. The parameters that are typically varied are the ion drag force, normalized to gravity ( $f_i = F_i/F_g = 0.0 \dots 2.0$ ) and the friction coefficient ( $\beta = 10 \dots 100 \text{ s}^{-1}$ ). In order to describe a situation similar to the experiments, typical experimental values for confinement strength  $\omega_0 = 250 \text{ s}^{-1}$ , particle number  $N = 4096$ , and Debye length  $\lambda_D = 250 \mu\text{m}$  are chosen.

Our calculations make use of the high performance of graphical processing units (GPUs). Their architecture allows a very efficient parallelization of the calculation of the  $N$ -body problem. Our implementation closely follows the one given in Ref. 23, which describes the calculation of  $N$  bodies interacting via gravity. In our case, the interaction force is the shielded Coulomb force given by Eq. (2). The simulations were carried out on a NVIDIA<sup>®</sup> GPU (GTS 250) using CUDA<sup>™</sup>. One simulation run with 4096 particles and  $10^5$  time steps usually takes about 15 min including about 4 min for the calculation of the  $N$ -body interactions.

### III. STATIONARY STREAMING

In this section, the stationary streaming of the particles is presented. The velocity field is visualized by interpolating the particle velocities in the steady state onto a fixed grid in polar coordinates<sup>24</sup> and averaging over time. Only particles with distance  $|z| < 0.2 \text{ mm}$  from the axial potential minimum were considered, which corresponds to the experimental method of illuminating the midsection of a torus-shaped dust cloud by a laser fan.

In Fig. 2, the streaming velocities for the normalized ion drag force  $f_i = 0.8$  at weak friction [ $\beta = 30 \text{ s}^{-1}$ , Figs. 2(a) and 2(c)] and strong friction [ $\beta = 90 \text{ s}^{-1}$ , Figs. 2(b) and 2(d)] are displayed. Shown are the azimuthal [ $v_\phi$ , Figs. 2(a) and 2(b)] and radial [ $v_r$ , Figs. 2(c) and 2(d)] velocity components. Clockwise (counter-clockwise) rotation of the particles is indicated by a positive (negative) azimuthal velocity, a radially outwards directed velocity is called positive. The boundary of the cloud is marked by a thin black line in each figure. In Figs. 2(c) and 2(d), the position of the potential minimum is indicated by a dashed line. Additionally, the angle  $\phi$  is introduced to indicate the position along the circular path of the torus and angles are given as hours on a clock-dial.  $\phi$  is increasing clockwise and  $\phi = 0$  corresponds to the 9 h position.

Starting at  $\phi = 9 \text{ h}$  for weak friction [Fig. 2(a)], the azimuthal velocity increases with  $\phi$  until it reaches a maximum at about 5 h while maintaining a nearly constant velocity value along a radial cross-section. For  $\phi = 5 - 8 \text{ h}$ , two spatially separated streaming regions can be found. While at the outer boundary a fast clockwise rotation is found, the inner region of the torus shows a slow streaming motion in opposite direction.

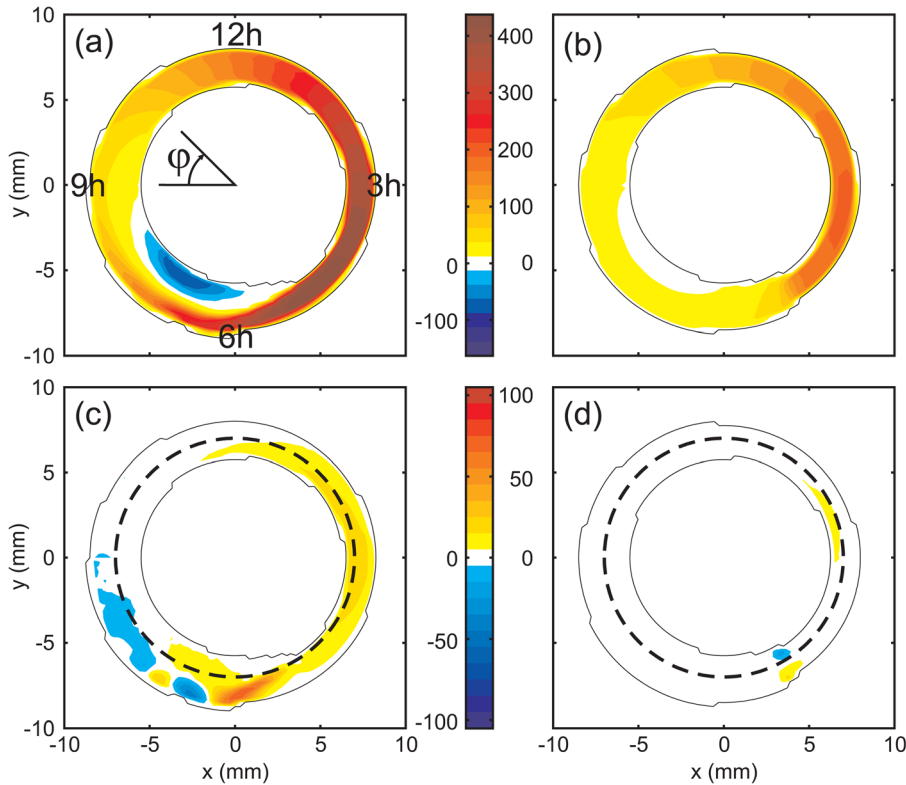


FIG. 2. (Color online) For normalized ion drag force  $f_i = 0.8$ , the azimuthal  $[v_\phi, (a), (b)]$  and radial  $[v_r, (c), (d)]$  velocity components are shown for weak friction  $[\beta = 30 \text{ s}^{-1}, (a), (c)]$  and strong friction  $[\beta = 90 \text{ s}^{-1}, (b), (d)]$ . The boundary of the cloud is given by thin solid lines and the potential minimum is indicated by a thick dashed line in (c) and (d).

The corresponding radial velocities [Fig. 2(c)] are about a factor of 5 smaller than the azimuthal velocities. Thus, the rotational motion is dominant. The radial velocity is nearly zero in the area  $\varphi = 9 - 12 \text{ h}$ . For  $\varphi = 12 - 5 \text{ h}$ , positive velocities are found. In addition, a shift of the cloud to larger radii with respect to the potential minimum can be observed. Around  $\varphi = 6 \text{ h}$ , a strong increase of  $v_r$  is found at the outer boundary of the cloud. With further increasing  $\varphi$ , areas with alternating sign of the velocity are found.

The streaming can be divided into two different types of flows. For  $\varphi = 9 - 5 \text{ h}$ , a steady flow is observed. Due to their rotation motion, the particles experience a centrifugal force that pushes the cloud radially away from the potential minimum, resulting in the positive radial velocities and an overall shift of the cloud. In the lower region of the cloud, particles that are not able to rotate about the torus are trapped in this region forming a barrier for the rotating particles. These fast particles evade radially while maintaining most of their rotation velocity. Due to the restoring confinement force, these particles perform a sloshing motion in radial direction. The trapped particles perform a slow rotation motion inside the lower region of the torus resulting in the formation of a large-scale vortex.

When friction is strong [Figs. 2(b) and 2(d)], the streaming motion is more quiescent. The azimuthal velocity increases from  $\varphi = 9 \text{ h}$  with increasing  $\varphi$  and reaches a maximum around  $\varphi = 4 \text{ h}$ . At  $\varphi = 5 \text{ h}$  a sudden decrease of the velocity is found but no vortex formation is observed. Also, the maximum velocity is about a factor of 2 smaller than that for weak friction.

The corresponding radial velocity is almost everywhere nearly zero. Only around  $\varphi = 3 \text{ h}$ , a small positive velocity is found. In addition, the cloud boundary is nearly symmetric

around the potential minimum. Around  $\varphi = 5 \text{ h}$ , an area with negative velocities is found for  $\tilde{\rho} < R$  while for  $\tilde{\rho} > R$ , a region with positive velocity is found.

In comparison with the streaming at weak friction, the position of maximum velocity is shifted to smaller values of  $\varphi$  as well as the maximum velocity is reduced, which is in agreement with our earlier investigations.<sup>18</sup> With lower rotation velocities, the particles experience no significantly strong centrifugal force, i.e., no radial shift of the cloud is observed. In contrast to weak friction, the formation of a vortex is not found, but a sudden decrease of the rotation velocity which coincides with a strong increase of the cross-section of the flux.

In Fig. 3, the azimuthal velocity component is studied in more detail. Therefore, the torus was divided into 24 equal segments centered around  $\varphi = [9.5; 10.0; \dots 9.0] \text{ h}$ . For every segment, a time-averaged histogram of the azimuthal velocity component of every particle inside the segment was calculated and is displayed in terms of a waterfall diagram. Shown are the same simulation results as in Fig. 2. For better visibility, a dashed line indicates  $v_\phi = 0 \text{ mm/s}$ .

For weak friction  $[\beta = 30 \text{ s}^{-1}, \text{ Fig. 3(a)}]$ , starting from  $\varphi = 9.5 \text{ h}$ , one can see a nearly Gaussian velocity distribution centered around  $v_\phi \approx 80 \text{ mm/s}$ . With increasing  $\varphi$ , the azimuthal velocity increases, too, and reaches a maximum of  $v_\phi \approx 450 \text{ mm/s}$  at  $\varphi = 5 \text{ h}$ . There, a secondary velocity population occurs with zero mean value. While this population becomes dominant for values  $\varphi \geq 6 \text{ h}$ , the mean velocity of the fast particle population decreases rapidly. Furthermore, the distribution of the fast population can no longer be described as Gaussian, and for  $\varphi \geq 7 \text{ h}$ , the fast population cannot be distinguished at all. At the same time, negative velocity values of the slow population can be

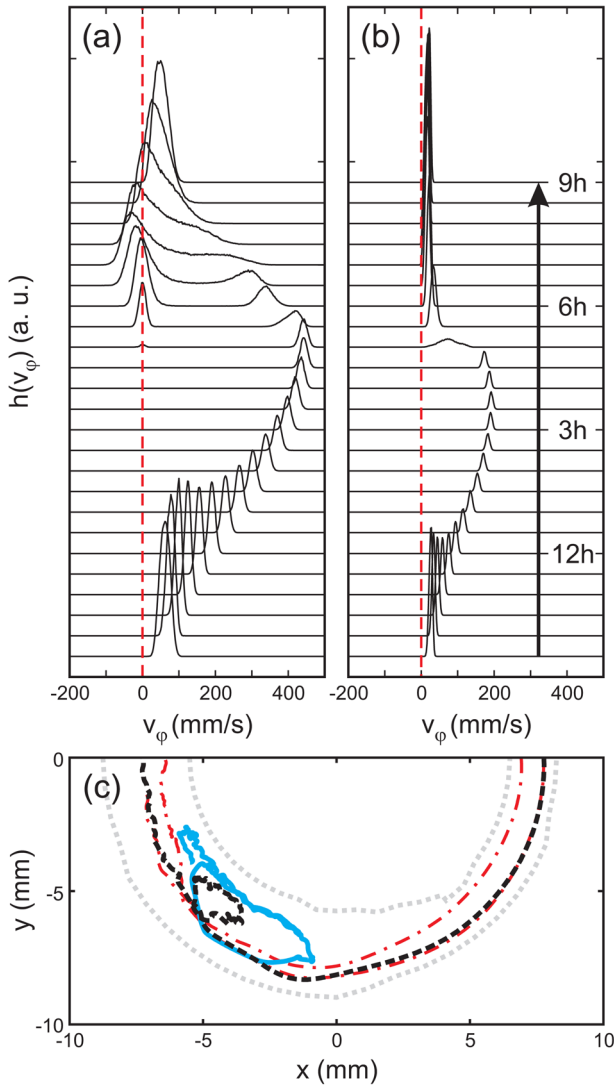


FIG. 3. (Color online) Waterfall plots for the velocity distribution of the azimuthal velocity component for (a)  $\beta = 30 \text{ s}^{-1}$  and (b)  $\beta = 90 \text{ s}^{-1}$ . (c) Typical trajectories of particles in the vortex structure are shown ( $f_i = 0.8$ ,  $\beta = 30 \text{ s}^{-1}$ ): a *trapped* particle (solid line), a *partially trapped* particle (dashed line), and a *free* particle (point-dashed line). The boundary of the cloud is indicated by two dotted lines.

observed, corresponding to a counter-clockwise particle rotation. When  $\phi$  approaches 9 h, the velocity distribution becomes more Gaussian again.

Here, the two different occurring types of flows can easily be separated. A fast particle population that rotates about the major axis of the torus is influenced by gravity resulting in a modulation of the rotation velocity. A slow particle population is situated in the lower region of the torus and exhibits both positive and negative velocities, resulting in the formation of a vortex. Furthermore, the fast particles penetrate deep into the region of the slow population before they lose their kinetic energy through momentum transfer to the slow particles.

In Fig. 3(c), examples for the different particle populations inside the stream with a large-scale vortex [ $f_i = 0.8$ ,  $\beta = 30 \text{ s}^{-1}$ , and cf. Figs. 2(a) and 3(a)] are displayed. The cloud boundaries are given by two dotted lines. The trajectory of a *trapped* particle, i.e., a particle that does not leave

the vortex region, is indicated by a solid line. The rotational motion inside the vortex is easily observed. This particle belongs to the slow particle population.

An example for a fast particle is given by a dashed-dotted line. This particle rotates about the major axis of the torus without interacting with the particles inside the vortex. Therefore, this particle can be seen as *free*.

Although the fast flow and the slow vortex flow are mostly spatially separated from each other, it is possible for particles to migrate from one population to the other. The trajectory of such a particle, which can be regarded as *partially trapped*, is given by a dashed line. In addition, the vortex structure leads to a distinct asymmetry of the cloud shape, which was observed in earlier experiments.<sup>16</sup>

For strong friction [ $\beta = 90 \text{ s}^{-1}$ , Fig. 3(b)], compared to weak friction, the velocities are smaller with a maximum of  $v_\phi \approx 200 \text{ mm/s}$  at  $\phi = 3.5 \text{ h}$ . In addition, the width of the distribution is much narrower. At  $\phi = 5 \text{ h}$ , a sudden decrease of the velocity is found, combined with a large broadening of the velocity distribution. With further increasing  $\phi$ , very small but positive velocities are observed.

Since for weak friction, the inhomogeneous streaming led to the spontaneous formation of a vortex, it is expected that for strong friction an instability will occur as well. The sudden decrease of the velocity hints at the formation of a stationary shock. A shock is a disturbance characterized by a rapid rise in pressure, temperature, and density.<sup>25</sup> Therefore, the properties of the particle flow are analyzed in more detail. In Fig. 4(a), the angular distribution of the mean rotation velocity of the flow is shown. Besides the overall modulation of the velocity due to gravity, the sudden decrease of  $v_\phi$  around  $\phi = 5 \text{ h}$  is obtained. The area  $\phi = 4.5 - 5.5 \text{ h}$  is colored gray.

The dynamical temperature,

$$k_B T_{\text{dyn}} = \frac{1}{2} m_d \langle (\vec{v} - \vec{v}_m)^2 \rangle, \quad (5)$$

is taken as the kinetic energy of the fluctuations of the particles.  $\vec{v}_m$  is the time-averaged particle velocity field and  $\langle \dots \rangle$  denotes averaging over all considered particles.

Since the particles are arranged on shells, which will be discussed in detail in Sec. IV, the particle density  $\rho_d$  was

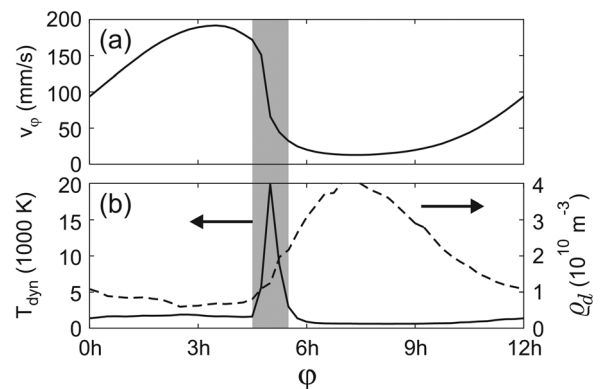


FIG. 4. On the formation of a stationary shock: displayed are for  $f_i = 0.8$  and  $\beta = 90 \text{ s}^{-1}$ , the angular distribution of (a) the mean rotation velocity  $v_\phi$ , (b) the dynamical temperature  $T_{\text{dyn}}$  and particle density  $\rho_d$ .

estimated by calculating the two-dimensional Voronoi cells of the particles in the outermost shell. The intershell distance was taken as a measure for the radial dimension of the Voronoi cell and the particle density as the reciprocal of the three-dimensional Voronoi cell.

The angular distributions of  $T_{\text{dyn}}$  (solid line) and  $\varrho_d$  (dashed line) are shown in Fig. 4(b).  $T_{\text{dyn}}$  is nearly constant for a wide range of  $\varphi$  but shows a very localized increase around  $\varphi = 5$  h with values one order of magnitude larger than in the regions of the quiescent flow.  $\varrho_d$  also shows an increase around  $\varphi = 5$  h.

These findings, a strong decrease in velocity combined with a very localized increase in temperature and density, led to the conclusion that the flow forms a stationary shock in this case. The radial extension of the stream is determined by a force equilibrium of confinement force and Yukawa repulsion between the particles. With increasing particle density, the electrostatic repulsion between particles also increases, resulting in a radial broadening of the cross-section of the flow as observed.

#### IV. LOCAL EVOLUTION OF THE STREAM

##### A. Shell structure

In this section, the local evolution of the flow along the annular confinement is studied in more detail. Therefore, the transit points of the particles through areas with constant  $\varphi$  are shown in Fig. 5 for normalized ion drag force  $f_i = 0.8$  and weak friction [ $\beta = 30 \text{ s}^{-1}$ , Fig. 5(a)] and strong friction [ $\beta = 90 \text{ s}^{-1}$ , Fig. 5(b)], respectively.  $\rho = \tilde{\rho} - R$  denotes the radial displacement from the potential minimum at  $\{\rho, z\} = \{0, 0\}$  mm. For a better visibility of the structure of the flow, the particle transits for  $10^4$  time steps are displayed.

In areas where particles with both positive and negative azimuthal velocities are observed, contour lines are displayed inside which 90% of all particles are found. The contour line for particles with negative (positive) azimuthal velocity is given by a solid (dashed) line.

For weak friction [Fig. 5(a)], the transit points are not randomly distributed over the cross-section of the flux but are arranged on shells over a wide range of  $\varphi$ . At  $\varphi = 10$  h, four separate shells are distinguishable. With increasing  $\varphi$ , the number of shells decreases as well as the cross-section. It can be seen that the innermost shell disappears while the radii of the outer shells decrease, e.g., the transition from three shells at  $\varphi = 1$  h to two shells at  $\varphi = 2$  h. In addition, an overall shift of the cross-section to higher values of  $\rho$  is found for  $\varphi = 2 - 5$  h that is caused by a centrifugal force due to their rotation. For  $\varphi = 6$  h, an ellipsoidal structure can be observed which is created by the fast particles which avoid the slow particle population. In the region where the vortex is found ( $\varphi = 6 - 8$  h), the transit points are mostly randomly distributed. Note that the overlap between the contour lines is very small, indicating that the regions of clockwise and counter-clockwise rotation are spatially separated. For  $\varphi = 9$  h, the formation of an outer shell can be seen, while the particles in the center of the cross-section are still randomly distributed.

In the case of strong friction [Fig. 5(b)], the observed structure is very similar to the case for weak friction. For most values of  $\varphi$ , the number of shells is the same as in Fig. 5(a) and a decrease of shell numbers and cross-section with increasing  $\varphi$  can be observed, too. For strong friction, the shell structure is observed for all values of  $\varphi$ . The rapid increase in the cross-section between  $\varphi = 5$  h and  $\varphi = 6$  h results from the stationary shock.

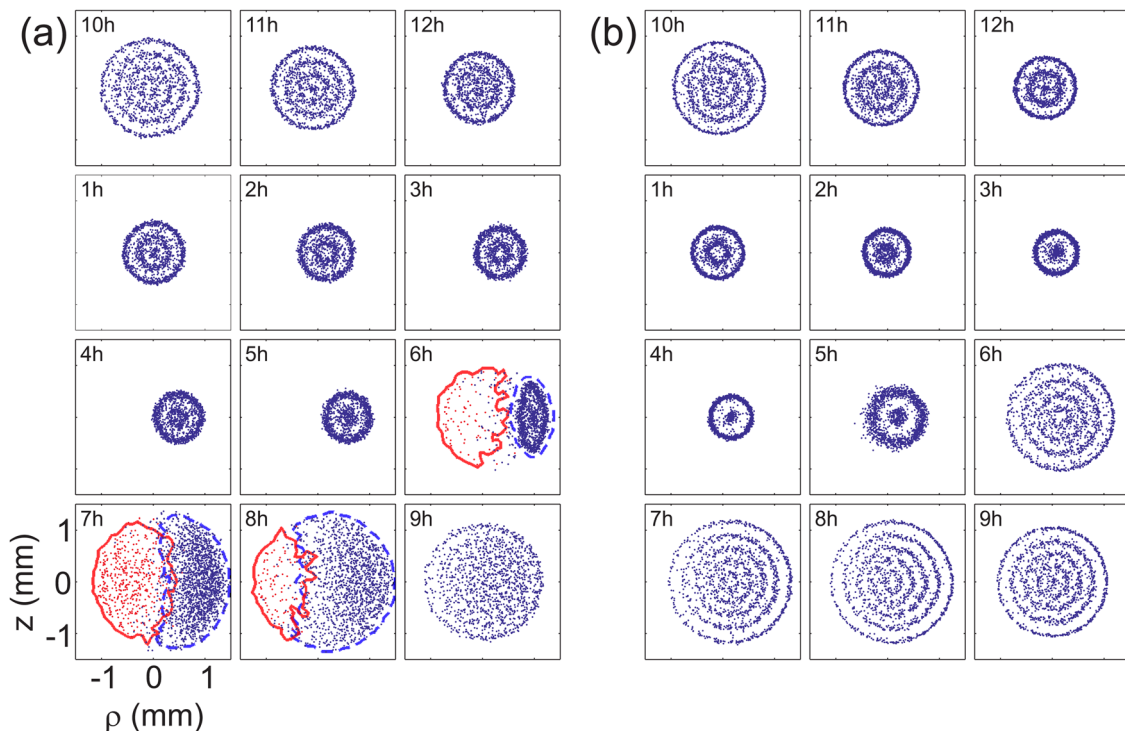


FIG. 5. (Color online) Time-averaged transit points of the particle flux for  $f_i = 0.8$  with (a)  $\beta = 30 \text{ s}^{-1}$  and (b)  $\beta = 90 \text{ s}^{-1}$ .

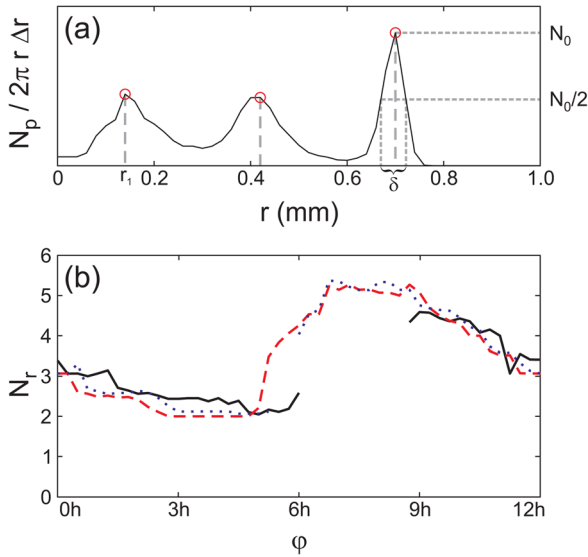


FIG. 6. (Color online) (a) Radial distribution of transit points ( $f_i=0.8$ ,  $\beta=90\text{ s}^{-1}$ ,  $\varphi=11\text{ h}$ ), (b) angular distribution of  $N_r$  for  $\beta=30\text{ s}^{-1}$  (solid line),  $\beta=60\text{ s}^{-1}$  (dotted line), and  $\beta=90\text{ s}^{-1}$  (dashed line).

The rotation velocity of the particles increases with increasing  $\varphi$  in the upper region of the torus ( $\varphi=9-3\text{ h}$ ). Since the number of particles is constant, the equation of continuity demands that the product of velocity, density, and cross-section of the flux has to be constant. Since the increase of velocity is compensated here by a decrease of the cross-section, one can assume that the flux is approximately incompressible. Therefore, the particles have to adapt to the changing conditions. Since neighboring particles have nearly the same rotation velocity, they can be regarded as being at rest in a comoving reference frame. Simulations had shown that particles in a Yukawa tube, i.e., a system of Yukawa particles trapped in a cylinder with a radial harmonic confinement and periodic boundary conditions in axial directions, arrange themselves on shells with high symmetry in the ground state.<sup>26</sup> The present situation is more complex in that the shell structure varies along the flow according to the stream velocity.

The shell structure is analyzed by calculating the particle distribution of the flow in radial direction. First, the center of mass of the transit points was determined. Then, the number of particles  $N_p$  inside a ring with radius  $r$  and thickness  $\Delta r$  concentric about the center of mass was calculated and normalized to the area of the ring  $2\pi r \Delta r$ . In Fig. 6(a), an example for the particle distribution is displayed [ $f_i=0.8$ ,  $\beta=90\text{ s}^{-1}$ ,  $\varphi=11\text{ h}$ , and see Fig. 5(b)]. Three maxima indicated by open circles can be seen. They represent the radial position of the shells.  $\delta$  is the full width at half maximum (FWHM) of the outermost shell and is taken as an indicator for the thickness of the shells and  $r_1$  denotes the radius of the innermost shell.

In order to study the number of shells along the torus, a continuous shell number  $N_r$  is introduced as  $N_r=N+r_1/\delta$  in order to account for the fact, that when the innermost shell disappears, the radius of the new inner shell stays nearly the same so that  $N_r$  shows a more continuous trend than the shell number  $N$ . In Fig. 6(b), the angular distribution of  $N_r$  is dis-

played for weak ( $\beta=30\text{ s}^{-1}$ , solid line), medium ( $\beta=60\text{ s}^{-1}$ , dotted line), and strong friction ( $\beta=90\text{ s}^{-1}$ , dashed line). Note that the gap for weak and medium friction results from the absence of a shell structure due to the appearance of a vortex. For all values of  $\beta$ , the same trend is observed. At  $\varphi=9\text{ h}$ , about five shells were determined. Then, a continuous decrease of  $N_r$  with increasing  $\varphi$  is found while  $N_r$  is nearly independent of friction over a large span of  $\varphi$ . Only for  $\varphi=5-6\text{ h}$ , a strong deviation of  $N_r$  for weak and strong friction is found.

With increasing particle velocity, the number of particles inside a torus segment with constant volume decreases. The simulations on Yukawa tubes<sup>26</sup> showed that if the ratio of particles per unit length is decreased, the number of shells in the ground state also decreases. The same behavior is observed here, too.

For strong friction, the stationary shock at  $\varphi=5\text{ h}$  decelerates the particles so that the number of particles inside the segment rapidly increases resulting in the formation of a larger number of shells. For  $\varphi=6-9\text{ h}$ , the particle velocity is nearly constant so that  $N_r$  does not significantly change in this region. For weak friction, the interaction of the two different particle populations destroys the structure in the vortex region ( $\varphi=6-8.5\text{ h}$ ).

## B. Dynamical coupling parameter

These findings allow the conjecture that the particles inside the flow might be in a solid phase. In complex plasmas, the coupling parameter  $\Gamma=Q_d^2/(4\pi\epsilon_0 a_{\text{WS}})(k_B T)^{-1}$  is often used to describe the structural properties of a system.  $a_{\text{WS}}=(4q_d\pi/3)^{-1/3}$  is the Wigner-Seitz radius with  $q_d$  being the particle number density.  $\Gamma$  gives the ratio of the Coulomb energy of neighboring particles to their thermal energy. If  $\Gamma>170$ , particles arrange themselves in crystalline structures.<sup>27</sup> Here, a dynamical coupling parameter  $\Gamma_{\text{dyn}}=Q_d^2/(4\pi\epsilon_0 a_{\text{WS}})(k_B T_{\text{dyn}})^{-1}$  is introduced, which describes the Coulomb energy of neighboring particles in terms of the dynamical temperature  $k_B T_{\text{dyn}}$  [Eq. (5)]. For the calculation of  $\Gamma_{\text{dyn}}$ , all particles inside a segment centered about a value of  $\varphi$  were taken into account. In Fig. 7, the angular distribution of  $\Gamma_{\text{dyn}}$  is shown for weak ( $\beta=30\text{ s}^{-1}$ , solid line), medium ( $\beta=60\text{ s}^{-1}$ , dotted line), and strong friction ( $\beta=90\text{ s}^{-1}$ , dashed line).

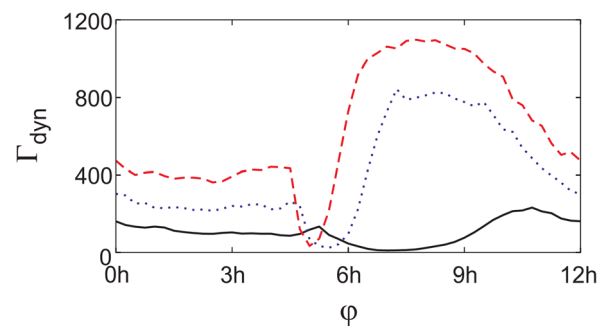


FIG. 7. (Color online)  $\Gamma_{\text{dyn}}$  over  $\varphi$  for (black solid line)  $\beta=30\text{ s}^{-1}$ , (blue dotted line)  $\beta=60\text{ s}^{-1}$ , and (red dashed line)  $\beta=90\text{ s}^{-1}$ .

One can see that the friction has a crucial influence on  $\Gamma_{\text{dyn}}$ , i.e., for strong friction,  $\Gamma_{\text{dyn}}$  reaches values up to  $\Gamma_{\text{dyn}} = 1100$ , while for medium friction  $\Gamma_{\text{dyn}} \leq 800$  and for weak friction we find  $\Gamma_{\text{dyn}} < 250$ . The angular development is similar for all cases considered. From  $\varphi = 0$  h to  $\varphi = 5$  h,  $\Gamma_{\text{dyn}}$  remains nearly constant. Around  $\varphi = 5$  h, a sudden decrease of  $\Gamma_{\text{dyn}}$  is found, which is shifted towards higher values of  $\varphi$  with decreasing friction. For weak friction, very low values of  $\Gamma_{\text{dyn}}$  are found over a wider range of  $\varphi$ .

It was found that  $a_{\text{WS}}$  is constant within 10% for all values of  $\varphi$  and  $\beta$  considered. Therefore, the different characteristics of  $\Gamma_{\text{dyn}}$  are attributed to a change of the dynamical temperature  $T_{\text{dyn}}$ . As seen in Fig. 4(b),  $T_{\text{dyn}}$  increases rapidly in the vicinity of instabilities inside the flow, leading to a decline of  $\Gamma_{\text{dyn}}$ . Thus, the position of low values of  $\Gamma_{\text{dyn}}$  coincides with the position of the instabilities. Since for weak friction, a large-scale vortex is formed,  $\Gamma_{\text{dyn}}$  remains small over a wide range of  $\varphi$ .

Another measure for the degree of order of a dusty plasma is the pair correlation function  $g(r)$ , which gives the probability of finding a particle at a distance  $r$  from another particle.  $g(r)$  was calculated for every segment of the torus. In Fig. 8(a),  $g(r)$  is shown for  $\beta = 30 \text{ s}^{-1}$  (solid line) and  $\beta = 90 \text{ s}^{-1}$  (dashed line) at position  $\varphi = 7$  h, cf. Fig. 5. For both curves, the inter-particle distance  $r_{\text{ip}}$ , given by the first maximum of  $g(r)$ , is found to be  $r_{\text{ip}} \approx 0.3$  mm but the shape of  $g(r)$  differs. For weak friction, one peak without any additional structure is observed, while for strong friction, a steep increase towards the first peak can be seen as well as several further peaks. The continuous decline of  $g(r)$  for larger values of  $r$  follows from the finite size of the segment.

The shape of  $g(r)$  for weak friction is typical for a fluid since there is a non-zero probability to find a particle for values  $r < r_{\text{ip}}$ . In addition, no long-range order is found. For strong friction,  $g(r)$  exhibits the characteristics of a solid with a well-defined excluded volume around each particle and a pronounced long-range order.

It was observed that the shape of  $g(r)$  inside the disturbed flow shows the characteristics of a fluid, while with increasing  $\varphi$ ,  $g(r)$  shows more characteristics of a solid, indicating that the flow undergoes a fluid-solid phase transition along its path. The instabilities inside the flow destroy any structure leading to a fluid phase. A typical time scale on which the system relaxes is given by  $\tau = 1/\beta$ . During this time, the particles cover the distance  $s_{\text{rel}} = v_{\varphi}\tau$ . Thus, it is

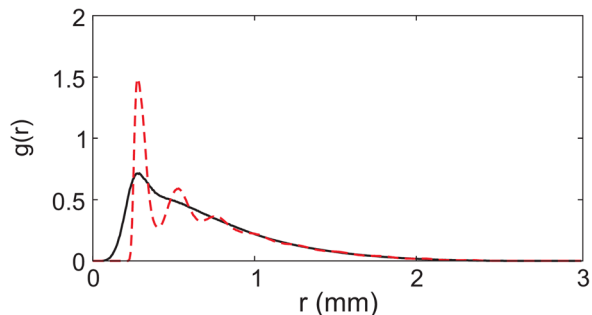


FIG. 8. (Color online) Pair correlation function  $g(r)$  at  $\varphi = 7$  h for (solid line)  $\beta = 30 \text{ s}^{-1}$  and (dashed line)  $\beta = 90 \text{ s}^{-1}$ .

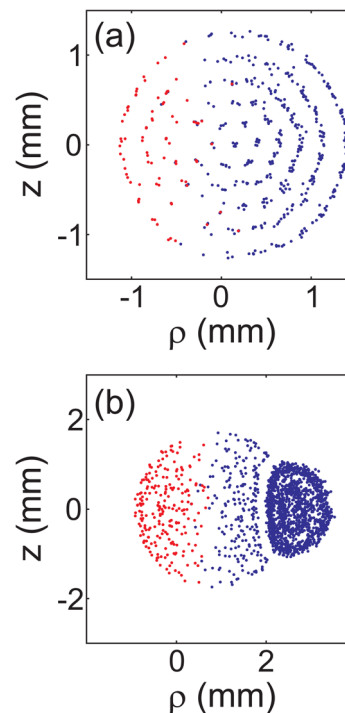


FIG. 9. (Color online) Shell structure inside vortex region, found at  $\varphi = 7$  h for (a)  $f_i = 0.5$ ,  $\beta = 100 \text{ s}^{-1}$ ,  $\omega_0 = 250 \text{ s}^{-1}$  and (b)  $f_i = 0.9$ ,  $\beta = 30 \text{ s}^{-1}$ ,  $\omega_0 = 100 \text{ s}^{-1}$ .

expected to find equilibrium configurations of the particles well behind the position of the instability.

The previous analysis was restricted to a narrow set of parameters that are considered to be in agreement with the parameters found in the experiments.<sup>16,18</sup> In Fig. 9, two examples for a different behavior of the flow are given. In Fig. 9(a), the transit points of the particles are displayed at position  $\varphi = 7$  h for low ion drag force  $f_i = 0.5$ , strong friction  $\beta = 100 \text{ s}^{-1}$ , and  $\omega_0 = 250 \text{ s}^{-1}$ . Particles with positive (negative) rotation velocity are marked by (color online) blue (red) dots, cf. Fig. 5. Independent of their velocity direction, all particles are arranged on distinct shells, i.e., the shell structure is maintained inside this vortex.

In Fig. 9(b), the transit points at  $\varphi = 7$  h for  $f_i = 0.9$ , low friction  $\beta = 30 \text{ s}^{-1}$ , and weak confinement strength  $\omega_0 = 100 \text{ s}^{-1}$  are shown. Note the different scale of the axes compared to Fig. 9(a). A vortex structure can be recognized together with the transit points of a fast particle population for  $\rho > 2$  mm, similar to the case of  $\varphi = 6$  h in Fig. 5(a). Here, not only the fast particles exhibit a shell structure but also the vortex.

## V. DISCUSSION

In this paper, we have presented a three-dimensional model for the description of particle motion in a toroidal trap. A similar model for the description of two-dimensional Coulomb clusters in a ring-shaped confinement potential was proposed by Schweigert *et al.*<sup>28</sup> There, gravity determines the vertical confinement of the particles. In our setup, the confinement is determined by ion drag and electric field force and the resulting principal confinement plane is aligned

with gravity. Thus, gravity breaks the symmetry of the confinement, resulting in an inhomogeneous streaming since the direction of gravity is aligned with the flow direction on the down-streaming branch of the torus but is antiparallel to the flow on the up-streaming branch.

In our 1D-model,<sup>18</sup> several properties of the particle motion were found. Due to the mutual repulsion of the particles, the threshold for the onset of particle rotation was lowered compared to a single-particle model. In addition, ballistic effects like a shift of the position of maximum rotation velocity to higher values of  $\varphi$  were observed. It was found that friction has a crucial influence on the rotation characteristics. In our 3D-model all of these basic findings were reproduced.

The restriction to one dimension led to the formation of dust lattice waves because the particles could not pass each other. In the 3D-simulations, dust lattice waves were not found. Instead, for strong friction, the spontaneous formation of a stationary shock with a distinct broadening of the cross-section of the flow was observed. For weak friction, the stream spontaneously develops a spatial bifurcation into a slow vortex flow and a fast stream which radially evades the vortex flow. Both shock and vortex formation result from the asymmetry of the flow due to gravity and not from an external barrier placed inside the stream.

In the regions of a quiescent flow, the formation of a shell structure was observed. It was found that the particles inside a small volume arrange themselves in their ground state configuration, resulting in the formation of shells, as could be found for Yukawa tubes.<sup>26</sup> Since the relaxation time of the system is short, the particles can be considered as being in a local equilibrium. But due to the changing rotation velocity, the particles undergo a structural phase transition along the path of the flow.

Normally, instabilities lead to a disarrangement of the particles. But for some parameter sets, highly ordered structures inside a vortex structure were observed, indicating that the mechanisms responsible for the ordered arrangements of particles may become dominant.

The simulations showed an asymmetric shape of the torus-shaped dust clouds with an overall thickening in the lower region of the cloud. This shape could also be observed in experiments.<sup>16</sup> The angular velocity distribution was studied experimentally,<sup>18</sup> and is in general agreement with the simulations. In summary, the performed simulations support the experimental findings and motivate a refined experimental study of toroidal dust motion in order to experimentally

confirm the spontaneous formation of vortices or shocks or an ordered particle arrangement inside the flow.

## ACKNOWLEDGMENTS

Fruitful discussions with O. Arp are gratefully acknowledged. The present investigations were financially supported by Deutsche Forschungsgemeinschaft (DFG) within the Transregional Collaborative Research Center TR-24, project A2.

- <sup>1</sup>G. E. Morfill, H. M. Thomas, U. Konopka, H. Rothermel, M. Zuzic, A. Ivlev, and J. Goree, *Phys. Rev. Lett.* **83**, 1598 (1999).
- <sup>2</sup>M. Klindworth, O. Arp, and A. Piel, *J. Phys. D* **39**, 1095 (2006).
- <sup>3</sup>D. Samsonov and J. Goree, *Phys. Rev. E* **59**, 1047 (1999).
- <sup>4</sup>H. Rothermel, T. Hagl, G. E. Morfill, M. H. Thoma, and H. M. Thomas, *Phys. Rev. Lett.* **89**, 175001 (2002).
- <sup>5</sup>A. M. Lipaev, S. A. Khrapak, V. I. Molotkov, G. E. Morfill, V. E. Fortov, A. V. Ivlev, H. M. Thomas, A. G. Khrapak, V. N. Naumkin, A. I. Ivanov, S. E. Tretschnev, and G. I. Padalka, *Phys. Rev. Lett.* **98**, 265006 (2007).
- <sup>6</sup>C. Schmidt, O. Arp, and A. Piel, *Phys. Plasmas* **18**, 013704 (2011).
- <sup>7</sup>U. Konopka, D. Samsonov, A. V. Ivlev, J. Goree, V. Steinberg, and G. E. Morfill, *Phys. Rev. E* **61**, 1890 (2000).
- <sup>8</sup>J. Carstensen, F. Greiner, L.-J. Hou, H. Maurer, and A. Piel, *Phys. Plasmas* **16**, 013702 (2009).
- <sup>9</sup>L.-J. Hou, Y.-N. Wang, and Z. L. Mišković, *Phys. Plasmas* **12**, 042104 (2005).
- <sup>10</sup>L.-W. Teng, P.-S. Tu, and L. I. *Phys. Rev. Lett.* **90**, 245004 (2003).
- <sup>11</sup>P. Henseler, A. Erbe, M. Köppl, P. Leiderer, and P. Nielaba, *Phys. Rev. E* **81**, 041402 (2010).
- <sup>12</sup>G. Birkel, S. Kassner, and H. Walther, *Nature* **357**, 310 (1992).
- <sup>13</sup>A. Barkan and R. L. Merlino, *Phys. Plasmas* **2**, 3261 (1995).
- <sup>14</sup>T. Trottenberg, D. Block, and A. Piel, *Phys. Plasmas* **13**, 042105 (2006).
- <sup>15</sup>I. Pilch, T. Trottenberg, A. Piel, and M. Koepke, *Phys. Plasmas* **14**, 123704 (2007).
- <sup>16</sup>I. Pilch, T. Reichstein, and A. Piel, *Phys. Plasmas* **15**, 103706 (2008).
- <sup>17</sup>T. Reichstein, I. Pilch, R. Grosse-Ahlert, and A. Piel, *IEEE Trans. Plasma Sci.* **38**, 814 (2010a).
- <sup>18</sup>T. Reichstein, I. Pilch, and A. Piel, *Phys. Plasmas* **17**, 093701 (2010b).
- <sup>19</sup>P. S. Epstein, *Phys. Rev.* **23**, 710 (1924).
- <sup>20</sup>S. Chandrasekhar, *Rev. Mod. Phys.* **15**, 1 (1943).
- <sup>21</sup>M. P. Allen and D. J. Tildesley, *Computer Simulation of Liquids* (Oxford Science Publications, Oxford, 1994).
- <sup>22</sup>R. Courant, K. Friedrichs, and H. Lewy, *Math. Ann.* **100**, 32 (1928).
- <sup>23</sup>L. Nyland, M. Harris, and J. Prins, "Fast N-body simulation with CUDA," in *GPU Gems 3*, edited by H. Nguyen (Pearson Education, Inc., Upper Saddle River, NJ, 2008).
- <sup>24</sup>C. K. Birdsall and A. B. Langdon, *Plasma Physics Via Computer Simulation* (IOP Publishing Ltd, Philadelphia, 1991).
- <sup>25</sup>J. W. Bond, K. M. Watson, and J. A. J. Welch, *Atomic Theory of Gas Dynamics* (Addison-Wesley, Reading, MA, 1965).
- <sup>26</sup>H. Baumgartner, "Structure and dynamics of Yukawa balls," Ph.D. thesis (University Kiel, 2009).
- <sup>27</sup>S. Ichimaru, *Rev. Mod. Phys.* **54**, 1017 (1982).
- <sup>28</sup>I. V. Schweigert, V. A. Schweigert, and F. M. Peeters, *Phys. Rev. B* **54**, 10827 (1996).





## A.4

# EXPERIMENTS AND SIMULATIONS OF PARTICLE FLOWS IN A MAGNETIZED DUST TORUS

Torben Reichstein, Jochen Wilms, Franko Greiner,  
Alexander Piel, and André Melzer

Reprinted with permission from  
Torben Reichstein, Jochen Wilms, Franko Greiner, Alexander Piel, and  
André Melzer,  
Contributions to Plasma Physics, Vol. 52, 813 (2012).  
Copyright 2012, WILEY-VCH Verlag GmbH & Co. KGaA, Weinheim.

# Experiments and Simulations of Particle Flows in a Magnetized Dust Torus

T. Reichstein<sup>1\*</sup>, J. Wilms<sup>1</sup>, F. Greiner<sup>1</sup>, A. Piel<sup>1</sup>, and A. Melzer<sup>2</sup>

<sup>1</sup> IEAP, Christian-Albrechts-Universität, D-24098 Kiel, Germany

<sup>2</sup> Institut für Physik, Universität Greifswald, D-17487 Greifswald, Germany

Received 24 April 2012, accepted 29 May 2012

Published online 08 November 2012

**Key words** Dusty plasma, molecular dynamics, transport processes, instabilities.

An overview is given of the confinement and dynamical phenomena observed in experiments and simulations of magnetized dust tori. Due to the presence of gravity, a strongly inhomogeneous velocity field is found along the circumference of the torus. The simulations show that the dust flow, which is unshaped and nearly incompressible, exhibits a distinct shell structure, which can be understood by rapid frictional cooling and strong Coulomb coupling. At lower frictional damping, the symmetry of the flow can be spontaneously broken, leading to a region of strong velocity shear and excitation of Kelvin-Helmholtz instabilities. New experimental evidence of counterflows is found.

## 1 Introduction

Dusty plasmas are suitable model systems to study the influence of strong coupling on the structure and dynamics of many-particle systems. In this issue, the competition of ordering phenomena is discussed by Block et al. [1] and phase transitions by Melzer et al. [2]. The present article extends the field of investigations by studying strongly coupled dust flows. In earlier experiments, the dust flow around obstacles [3] or shear flow instabilities [4] at the boundary of two streams of different velocity were studied. Recently, a Taylor-type instability was found in an experiment with a sheared dust flow [5]. Sheared dust flows can also be studied by molecular dynamics (MD) simulations of dusty plasmas, from which a Kelvin-Helmholtz instability [6] was recently reported, and the simulation results were found in general agreement with a generalized hydrodynamic model [7].

The investigations described in this article concern dust clouds that are confined in a magnetized anodic plasma [8, 9] and attain a toroidal shape [10]. The dust is set into rotation by the Hall component of the ion flow across a magnetic field, which exerts an ion drag force on the dust particles. Steady dust rotation about the major torus axis requires a minimum drag force that overcomes the weight force of the dust particles, otherwise a small eccentric dust cloud is formed [10]. Above this threshold a stationary dust flow is established with a flow speed that is smaller on the rising side of the dust flow than on the descent. The main features of this stationary flow were described in Refs. [11, 12]. In the present article, an overview of the phenomena in toroidal dust flows is given and the aspects of shell formation and non-stationary flows are studied in more detail. Here, we are interested in the role of velocity gradients on the structure of the flow pattern and the onset of instabilities in sheared flows. Refined experimental studies are focused on individual particle motions in the flow.

## 2 Dust tori in magnetized anodic plasmas

The dust torus is trapped in a secondary “anodic” plasma [8, 9], which forms in front of a positively biased ( $U_a \approx +80 V_{DC}$ ) electrode that is embedded in a larger radio-frequency discharge plasma with an axial magnetic field of  $B = (10\text{--}40)$  mT. The transparent anode is a 30 mm diameter quartz disk with a conducting indium-tin-oxide (ITO) coating and the dust torus is observed end-on with a fast charge-coupled-device video camera

\* Corresponding author. E-mail: reichstein@physik.uni-kiel.de, Phone: +49 431 880 3871, Fax: +49 431 880 3809

[Fig. 1(a)]. The average dust streaming velocity is determined by particle-image velocimetry (PIV) [Fig. 1(b)] and shows a clockwise rotation with an inhomogeneous velocity field. In the following, angular positions are given as readings on a clock dial. The minimum of the flow velocity is found at  $\varphi \hat{=} 9$  h and the maximum at the 5 h position.

Emissive probe measurements [9, 10] had shown that the radial and axial confinement of the dust cloud is achieved by a force equilibrium of ion drag and electric field force. In the center of the anodic plasma the ion drag force exceeds the electric field force, which leads to the formation of a dust-free region (void) in the center. Dust accumulates in a torus with a major radius that is determined by the force equilibrium. In the crossed radial electric and axial magnetic fields of our experiment and in the presence of ion-neutral collisions, the ion flow has a dominant radial component that provides the confinement of the torus and a smaller toroidal (“Hall”) component that exerts a toroidal ion-drag force on the dust particles. The typical ion Hall parameter is 0.05.

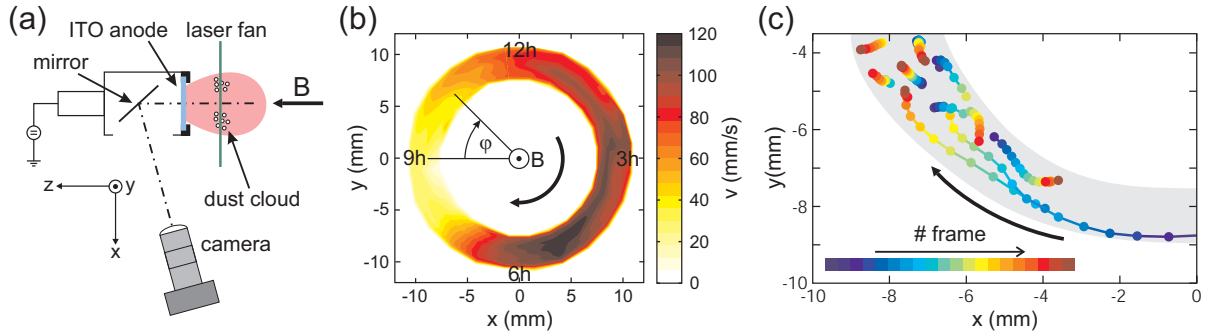


**Fig. 1** (a) Observation geometry for dust tori in a magnetized anodic plasma. (b) Toroidal dust streaming velocity obtained by PIV. (c) Examples of particle trajectories inside a torus-shaped dust cloud. Both clockwise and retroflow motion is observed. The main flow direction is indicated by an arrow.

### 3 MD-Simulation of dust flows

The geometry used for the Langevin MD-simulations [12] is similar to the experimental situation and the coordinates are defined in Fig. 2(a). We assume the confinement potential to be bi-harmonic  $U_c(\rho, z) = \frac{1}{2}m_d\omega_0^2(\rho^2 + z^2)$ , with  $m_d$  being the particle mass,  $\omega_0$  the confinement strength in radial and axial direction, and  $\rho = (x^2 + y^2)^{1/2} - R$  with  $x = y = 0$  at the center of the anode and  $R$  is the position of the torus axis. The confinement force is given by  $\vec{F}_c = -\nabla U_c$ . The particles are under the influence of gravity  $\vec{F}_g = -m_d g \vec{e}_y$ . The absolute value of the azimuthal ion drag force component is assumed to be constant and acts in azimuthal direction:  $\vec{F}_i = F_i \vec{e}_\varphi$ . A motion of the neutral gas, as observed in Ref. [13], is neglected here. Due to the plasma environment particles of diameter  $2a = 1 \mu\text{m}$  obtain a charge of about  $Q_d = -2500e$  [14], which results in an electrostatic repulsion between the particles. The force acting on the  $i$ th particle by  $N - 1$  identical particles is given by the shielded Coulomb (Yukawa) force

$$\vec{F}_Y(\vec{r}_i) = \sum_{j \neq i}^N \frac{Q_d^2}{4\pi\epsilon_0 \Delta_{ij}^3} \exp(-\kappa \Delta_{ij}) (1 + \kappa \Delta_{ij}) \vec{r}_{ij}. \quad (1)$$

Here,  $\vec{r}_i$  is the position of particle  $i$ ,  $\vec{r}_{ij} = \vec{r}_i - \vec{r}_j$ ,  $\Delta_{ij} = |\vec{r}_{ij}|$ , and  $\kappa = 1/\lambda_D$  the inverse of the Debye length. For the present calculations we use  $\lambda_D = 250 \mu\text{m}$  which corresponds to the experimental value of the shielding length and agrees with an effective Debye length in the presence of fast streaming ions [15]. The streaming particles experience friction by the neutral gas background  $\vec{F}_N = -m_d \beta \vec{v}$ , with  $\vec{v}$  the velocity of particle  $i$  and  $\beta$  the Epstein friction coefficient. The sum of the external forces is then  $\vec{F}_{ext} = \vec{F}_c + \vec{F}_g + \vec{F}_i + \vec{F}_Y$ .

Starting at  $\varphi \hat{=} 9$  h for weak friction [Fig. 2(b)], the azimuthal velocity increases with  $\varphi$  until it reaches a maximum at about 5 h while maintaining a nearly constant velocity value along a radial cross section. For  $\varphi \hat{=} 6$ –8 h, two spatially separated streaming regions can be found. While at the outer boundary a fast clockwise rotation is found, the inner region of the torus shows a slow streaming motion in opposite direction.

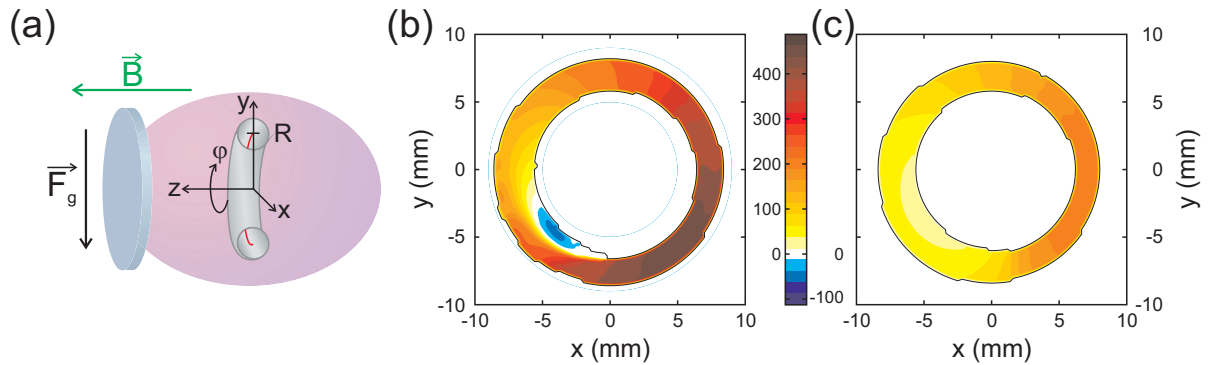


**Fig. 2** (a) Coordinates used for the MD-simulation. (b) Distribution of the toroidal velocity component at weak friction ( $\beta = 40 \text{ s}^{-1}$ ) and (c) strong friction ( $\beta = 100 \text{ s}^{-1}$ ).

When friction is strong [Fig. 2(c)], the streaming motion is more quiescent. The azimuthal velocity increases from  $\varphi \hat{=} 9 \text{ h}$  with increasing  $\varphi$  and reaches a maximum around  $\varphi \hat{=} 4 \text{ h}$ . Between  $\varphi \hat{=} 5 \text{ h}$  and  $6 \text{ h}$  a sudden decrease of the velocity is found but no vortex-like motion is observed. Also, the maximum velocity is about a factor of 2 smaller than for weak friction.

#### 4 Shell structures in stationary flows

Shell formation is an inherent feature of strongly coupled finite dust clusters [16, 17]. For spherical clusters, the build-up of correlations during a cooling process was studied in Refs. [18, 19]. The destruction of shell order by shear forces is demonstrated in Ref. [2]. Here, we investigate how a continuous change of the shell structure can be established in an inhomogeneous dust flow.

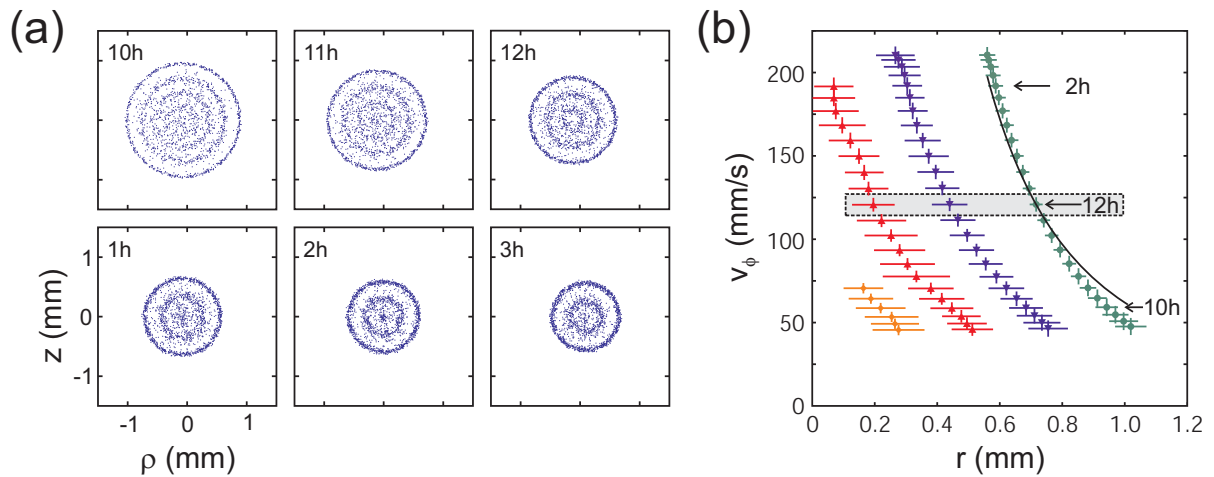


**Fig. 3** (a) Plot of the transit points of dust particles through selected planes at angular positions  $\varphi \hat{=} (10 \text{ h} - 3 \text{ h})$ . (b) The shell-averaged toroidal velocity  $v_\varphi(r)$  as a function of the shell radius  $r$ . Adjacent shells (highlighted at  $\varphi \hat{=} 12 \text{ h}$  by a box) exhibit no sheared toroidal motion,  $\Delta v_\varphi / v_\varphi = 0.2\%$ . A solid line represents the relationship between flow velocity and radius for an incompressible liquid.

The structure of the dust flow is resolved by plotting the transit points of the particles through  $\rho$ - $z$  planes of constant angular position  $\varphi$ , as shown in Fig. 3(a) for normalized ion drag force  $f_i = F_i / F_g = 1.2$  and strong friction ( $\beta = 100 \text{ s}^{-1}$ ). For a better visibility of the structure of the flow, the particle transits for 5000 time steps are displayed. With increasing  $\varphi$ , the number of shells decreases and the cross-section shrinks. It can be seen,

that the innermost shell disappears, see for example the transition from four shells at  $\varphi \hat{=} 11$  h to three shells at  $\varphi \hat{=} 12$  h.

This evolution can be seen more clearly in Fig. 3(b), where the toroidal velocity is averaged over each shell and plotted vs. the radius  $r = (\rho^2 + z^2)^{1/2}$  of that shell. One immediately recognizes the shrinking of the shell radius with the toroidal speed and the vanishing of the innermost shell. Furthermore, the toroidal speed of adjacent shells is practically the same as can be seen for  $\varphi \hat{=} 12$  h highlighted by a box. This means that there is no substantial velocity shear between adjacent shells. It is therefore justified to attribute the formation of nested shells to the absence of velocity shear. The dust flow behaves almost like an incompressible liquid, which would imply a unique relationship  $v_\varphi \propto r_{max}^{-2}$  between flow velocity and radius of the outermost shell. This relationship is represented by a solid line in Fig. 3(b) and shows fair agreement with the simulation data.

## 5 Sheared dust flows and flow instability

For weak frictional damping ( $\beta = 40 \text{ s}^{-1}$ ), the flow remains nearly unsheared for  $\varphi \hat{=} (10 \text{ h} - 3 \text{ h})$ . However, a strongly-sheared dust flow is found in the lower region of the torus, where an obstacle in the flow is spontaneously formed [12], as can be seen in Fig. 2(a) and magnified in Fig. 4(a) between  $\varphi \hat{=} (6 \text{ h} - 8 \text{ h})$ . The flow pattern consists of a fast passing flow in the outer half of the torus cross-section and an inner region with a slow flow in opposite direction. We call this region “vortex-like” because there are some particle trajectories that encircle this region. The majority of trajectories, however, is a mixture of free streaming particles and reflected particles, which have a turning point somewhere between  $\varphi \hat{=} 7:30$  h and 9 h.

The time-averaged flow profile in a poloidal section at  $\varphi \hat{=} 7:15$  h is shown as a solid line in Fig. 4(b). Here, it becomes evident that the time-averaged flow is highly sheared with a maximum velocity gradient at  $r = 7.2$  mm. This toroidal flow is not strictly stationary but exhibits velocity fluctuations. The radial distribution of the fluctuation amplitude (dashed line) is sharply peaked at the point of maximum velocity shear. The corresponding flow speed is  $\varphi \approx 100 \text{ mm s}^{-1}$ .

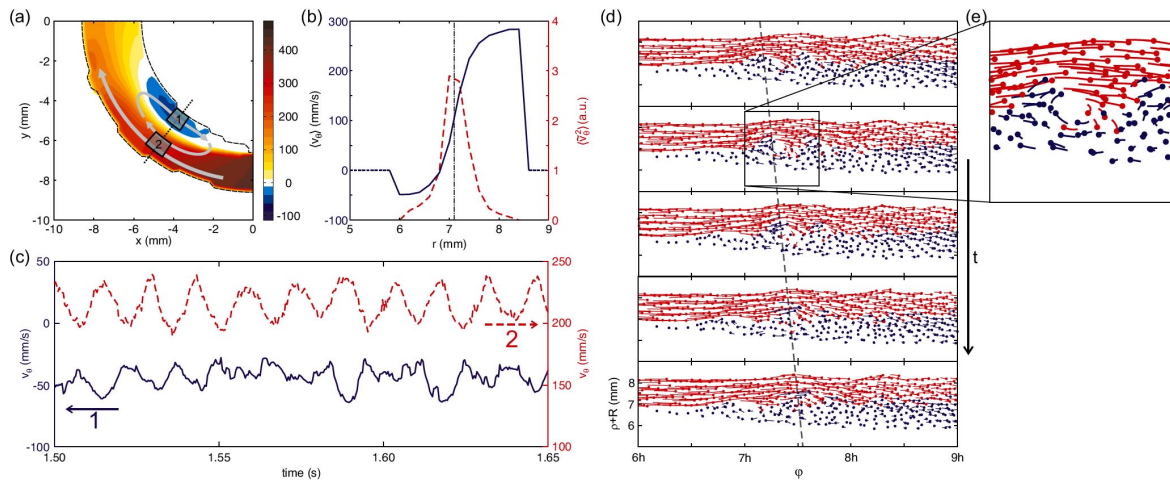


**Fig. 4** (a) Magnified region of sheared flow: The boxes 1 and 2 are used for determining the fluctuating flow velocities. (b) Velocity fluctuations (dashed line) and radial profile of flow speeds (solid line) at position marked by dotted line in Fig. 4(a). (c) Fluctuations of the toroidal velocity for the passing (positive) flow in box 2 and the (negative) retroflux of the vortex in box 1. (d) Visualization of toroidal streamlines at the interface between positive and negative flow velocities w.r.t. the flow velocity of maximum shear. (e) Magnified view of eddy formation.

The mean instantaneous flow speed is determined by averaging the particle velocities in the boxes 1 and 2 in Fig. 4(a) for each time step. The resulting toroidal flow speeds are compared in Fig. 4(c). The positive flow (2) has an average speed of  $v_\varphi = 270 \text{ mm s}^{-1}$  and the negative flow (1) has  $v_\varphi = -50 \text{ mm s}^{-1}$ . Both flow speeds show periodic oscillations at a frequency of  $\omega = 440 \text{ s}^{-1}$ . For comparison, the dust-plasma frequency is  $\omega_{pd} = [n_d Z_d^2 e^2 / (\epsilon_0 m_d)]^{1/2} = 820 \text{ s}^{-1}$ . It is also instructive to compare the dust speed with the sound speed for compressional (dust acoustic) waves,  $c_{DAW} = \omega_{pd} \lambda_D = 210 \text{ mm s}^{-1}$ .

The phase shift between the fluctuations in box 1 and 2 is  $180^\circ$ . This means that the angular velocity of the vortex is periodically modulated.

The spatio-temporal evolution of the flow pattern is shown in Fig. 4(d). Here, the coordinates are transformed into a cartesian  $\rho$ - $\varphi$  plane, where deviations from a straight flow become more easily visible. The streamlines of the flow are visualized by representing each dust particle by a line that represents the path of that particle during the last 100 simulation steps. The color of this line corresponds to the initial velocity of this particle, red representing particles with  $v_\varphi > 100 \text{ mm s}^{-1}$  and blue corresponds to  $v_\varphi < 100 \text{ mm s}^{-1}$ . In this way those particles become clearly visible which cross the interface between the positive and negative flow w.r.t. the flow velocity of maximum velocity shear. A wave-like perturbation of the interface with growing amplitude develops into a set of small eddies. A magnified view of such an eddy is shown in Fig. 4(e). The dashed line in Fig. 4(d) guides the eye in tracing the motion of such an eddy. The speed derived from the slope of the dashed line ( $150 \text{ mm s}^{-1}$ ) is in general agreement with the flow speed at the point of steepest velocity gradient. Therefore, the eddies are simply convected with the flow, rather than being a propagating nonlinear wave in the flowing dust medium.

## 6 Experimental evidence of counterflows

Refined experimental and data analysis techniques now make it possible to trace individual particle trajectories that lie in the cross section shown in Fig. 1(c). The motion of representative particles is shown by color-coding the particle positions in subsequent frames. Fast clockwise rotating particles are found at the outer torus edge while retrograde motion is seen at the inner edge. By implementing the stereoscopic methods that were used for studying phase transitions [2], we expect a deeper insight into the flow structure and the onset of instabilities.

## 7 Discussion

In a magnetized anodic plasma, we could identify a hierarchy of mechanisms: In zeroth order, the combination of electric field and ion drag force confines dust particles radially in a toroidal confinement. In first order, the small Hall component of the ion drag drives the dust rotation leading to an inhomogeneous dust flow in the competition with gravity. In MD simulations, several new aspects of this flow were obtained like the formation of shells, comparable to the layering of 2D dusty plasma liquids in narrow channels [20].

The formation of nested shells in the stationary dust flow is accompanied by large values of the Coulomb-coupling parameter  $\Gamma = Q_d^2 / (4\pi\epsilon_0 a_{WS} k T_d)$ , with the Wigner-Seitz radius  $a_{WS} = (4\pi n / 3)^{-1/3}$  and the dust temperature  $T_d$ . In Ref. [12] values of  $\Gamma = (400\text{--}800)$  were found for the region of  $\varphi = 10\text{ h--}3\text{ h}$ . Such high values of  $\Gamma$  are established by gas friction, which rapidly cools the dust particles to room temperature. The effectivity of cooling becomes evident from comparing the toroidal angular velocity  $\omega = v_\varphi / R \leq 29 \text{ s}^{-1}$  with the much higher momentum loss rate  $\beta = 100 \text{ s}^{-1}$ . It should be mentioned that shell formation persists even for  $\omega/\beta \approx 1$  [12]. It was found in Ref. [19] that for a normalized friction rate  $\beta/\omega_0 = 0.3$ , which corresponds to the present situation, the initially disordered system ( $\Gamma = 0.2$ ) reaches the regime of a strongly-coupled liquid ( $\Gamma > 10$ ) within  $t = 2.5 \beta^{-1}$ . Here, the flow would reach this regime within  $\Delta\varphi \hat{=} 1/4\text{ h}$ . Thus, the particles can be considered as strongly-coupled throughout the laminar region of the flow.

The second aspect of shell formation is the absence of velocity shear. The flow velocity in adjacent shells is practically constant within 0.2% at 12 h. Therefore, the relative position of particles in adjacent shells changes only slowly. Since the particles are strongly coupled, the roughness of the shells reduces the shear between the shells, which in turn favors the shell formation. Thus, the evolution of the flow can be understood as a sequence of nearly equilibrium situations: The flow velocity increases continuously from  $\varphi \hat{=} (10\text{ h--}3\text{ h})$  by a factor of 5 while the radius of the outer shell shrinks, but in such a way that the dust density remains approximately constant.

At low damping rates, we found pronounced shear-flow effects due to a spontaneously formed strongly sheared flow pattern. At the interface between the passing flow and the slow retrograde flow a transverse wave starts growing and evolves into a sequence of eddies with the same clockwise sense of rotation. The maximum of the fluctuation amplitudes is found at the point of steepest gradient of the mean flow velocity. These findings are clear indications of a Kelvin-Helmholtz instability (KHI).

Ashwin and Ganesh [6] have recently studied the KHI in subsonic (and frictionless) two-dimensional dust flows. The growth rate of the KHI was found to increase with  $\Gamma$  in the liquid regime  $1 < \Gamma < 100$ , which is also found in their generalized hydrodynamic model [7]. In our case, we have a three-dimensional system, the coupling parameter is  $\Gamma \approx 5$  [12] and the flow speed is subsonic in the sheared flow region. Using the values of Ref. [21] for the shear viscosity in a 3D Yukawa liquid, and  $d \approx 0.8$  mm as the characteristic shear length we obtain a Reynolds number  $Re \approx 13$ . Following Ref. [6], we would obtain a growth rate  $\gamma \approx 80 \text{ s}^{-1}$ . Instabilities are usually quenched when the collisional damping rate becomes comparable to the growth rate. Since our collision rate  $\beta = 40 \text{ s}^{-1}$  is smaller, the appearance of a KHI is in reasonable agreement with Ref. [6].

The main features of the particle flow observed in the experiment are in good agreement with the simulations, showing an inhomogeneous distribution of the mean speed along its angular position. Furthermore, a retroflux particle flow could be observed experimentally, which may be a precursor of the KHI that is observed in other experiments with a similar setup [5].

## 8 Conclusion

In summary, we have obtained a detailed picture of dust dynamics in magnetized plasmas. For a single particle, a hierarchy of processes could be identified: The radial components of electric field force and ion drag determine the toroidal confinement while the combination of gravity and the small Hall component of the ion drag drives the particle rotation. For an extended dust cloud, the driving mechanism remains the same but many-particle interactions alter the flow characteristics. It is an important finding that the same mechanism that governs the establishment of order in spherical dust clouds [18, 19] is also responsible for the formation of nested shells in dust flows. Moreover, the system was found to behave almost like an incompressible liquid in which the shell radii and number of shells adapt themselves adiabatically to the changing flow velocity. In other words, the system undergoes a sequence of configuration changes, in which the number of particles in a given cross-section varies. This observation links the dynamic phenomena with the thermodynamic investigations described in Ref. [2]. In systems with low damping rates, kinetic effects can become dominant, resulting in a spontaneously emerging strongly sheared flow pattern which develops a Kelvin-Helmholtz instability.

**Acknowledgements** The authors acknowledge fruitful discussions with M. Bonitz, H. Kählert, K. Pacha and R.-L. Merlino. This work was financially supported by DFG SFB-TR24 projects A2 and A3.

## References

- [1] D. Block et al., *Contrib. Plasma Phys.* **52**, 804–812 (2012).
- [2] A. Melzer et al., *Contrib. Plasma Phys.* **52**, 795–803 (2012).
- [3] G.E. Morfill, S.A. Khrapak, A.V. Ivlev, B.A. Klumov, M. Rubin-Zuzic, and H.M. Thomas, *Phys. Scr.* **2004**, 59 (2004).
- [4] R. Heidemann, S. Zhdanov, K. R. Sütterlin, H.M. Thomas, and G.E. Morfill, *EPL* **96**, 15001 (2011).
- [5] K.A. Pacha, J.R. Heinrich, S.H. Kim, and R.L. Merlino, *Phys. Plasmas* **19**, 014501 (2012).
- [6] A. J. and R. Ganesh, *Phys. Rev. Lett.* **104**, 215003 (2010).
- [7] A. J. and R. Ganesh, *Phys. Plasmas* **17**, 103706 (2010).
- [8] A. Barkan and R. L. Merlino, *Phys. Plasmas* **2**, 3261 (1995).
- [9] T. Trottenberg, D. Block, and A. Piel, *Phys. Plasmas* **13**, 042105 (2006).
- [10] I. Pilch, T. Reichstein, and A. Piel, *Phys. Plasmas* **15**, 103706 (2008).
- [11] T. Reichstein, I. Pilch, and A. Piel, *Phys. Plasmas* **17**, 093701 (2010).
- [12] T. Reichstein and A. Piel, *Phys. Plasmas* **18**, 083705 (2011).
- [13] J. Carstensen, F. Greiner, L. J. Hou, H. Maurer, and A. Piel, *Phys. Plasmas* **16**, 013702 (2009).
- [14] H. Mott-Smith and I. Langmuir, *Phys. Rev.* **28**, 727–763 (1926).
- [15] I. Hutchinson, *Plasma Phys. Control. Fusion* **48**, 185–202 (2006).
- [16] O. Arp, D. Block, and A. Piel, *Phys. Rev. Lett.* **93**, 165004 (2004).
- [17] M. Bonitz, D. Block, O. Arp, V. Golubnychiy, H. Baumgartner, P. Ludwig, A. Piel, and A. Filinov, *Phys. Rev. Lett.* **96**, 075001 (2006).
- [18] H. Kählert and M. Bonitz, *Phys. Rev. Lett.* **104**, 015001 (2010).
- [19] H. Kählert and M. Bonitz, *Contrib. Plasma Phys.* **51**, 519–523 (2011).
- [20] L.W. Teng, P.S. Tu, and L. I, *Phys. Rev. Lett.* **90**, 245004 (2003).
- [21] Z. Donkó and P. Hartmann, *Phys. Rev. E* **78**, 026408 (2008).





## A.5

### DUST STREAMING IN TOROIDAL TRAPS

Torben Reichstein, Jochen Wilms, and Alexander Piel

Reprinted with permission from  
Torben Reichstein, Jochen Wilms, and Alexander Piel,  
IEEE Transactions on Plasma Science, Vol. 41, 759 (2013).  
Copyright 2012, IEEE.

# Dust Streaming in Toroidal Traps

Torben Reichstein, Jochen Wilms, and Alexander Piel

**Abstract**—Molecular dynamic simulations were performed to study the characteristics of particle flows in a toroidal trap driven by the ion drag under the influence of gravity, interparticle forces, and friction with a neutral gas background. This paper is focused on the influence of the driving force and the strength of friction on the dynamics of the dust flow and its different regimes. For small values of the ion drag, the particle flow exhibits instabilities with strong velocity fluctuations, while for high values of the ion drag, a quiescent particle flow is obtained. The transition from unstable flows to quiescent flows is studied in detail.

**Index Terms**—Dusty plasma, instabilities, molecular dynamics (MD), transport processes.

## I. INTRODUCTION

**D**USTY plasmas offer the opportunity to study the influence of strong coupling on the structure and dynamics of many-particle systems. An interesting subfield is the study of strongly coupled dust flows. Earlier experiments were focused, e.g., on the dust flow around obstacles [1] or shear flow instabilities [2] driven by two dust streams of different velocities. Recently, Pacha *et al.* [3] reported on a Taylor-type instability in an experiment with a sheared dust flow. Molecular dynamics (MD) simulations of dusty plasmas also focus on sheared dust flows [4] from which a Kelvin–Helmholtz instability was reported, and the simulation results were found in general agreement with a generalized hydrodynamic model [5].

This paper extends the investigations of dust flows in a toroidal trap by means of MD simulations. In a magnetized anodic plasma [6], [7], torus-shaped dust clouds can be confined [8]. The Hall component of the ion flow across a magnetic field exerts an ion drag force on the particles setting the cloud into rotation. A minimum drag force is required for steady dust rotation about the major torus axis. Then, a stationary dust flow is established with flow speeds that are, because of gravity, larger on the descending torus branch than on the ascending. The main features of this stationary flow were investigated experimentally [9]–[11] and by means of MD simulations [11], [12]. The simulated dust flow exhibits, depending on the strength of friction, different types of instabilities like the formation of a standing shock or a Kelvin–Helmholtz instability due to a spontaneously emerging and strongly sheared dust

flow [12]. In this paper, we analyze the influence of ion drag force and friction strength on these instabilities in more detail. In Section II, a brief overview of our model is given. The properties of the flow are presented in Section III, and the influence of ion drag and friction are analyzed in Section IV. A discussion concludes this paper in Section V.

## II. MD SIMULATION OF DUST FLOWS

The geometry used for the Langevin MD simulations [11], [12] is similar to the experimental situation [8]–[10] and is sketched in Fig. 1(a). We assume a biharmonic confinement potential  $U_c(\rho, z) = (1/2)m_d\omega_0^2(\rho^2 + z^2)$ , with  $m_d$  being the particle mass,  $\omega_0$  being the confinement strength in both the radial and axial directions, and  $\rho = (x^2 + y^2)^{1/2} - R$  with  $x = y = 0$  at the center of the anode and  $R$  as the position of the torus axis. The confinement force is then given by  $\vec{F}_c = -\nabla U_c$ . The particles are under the influence of gravity  $\vec{F}_g = -m_d g \vec{e}_y$ . Since the plasma is magnetized, the ion motion has a small component in the  $E \times B$  direction. Due to the radial symmetry of the electric field of the anodic plasma [8], the Hall component of the ion motion is directed in azimuthal direction and acts as the ion drag force on the particles. The absolute value of this ion drag force component is assumed to be constant:  $\vec{F}_i = F_i \vec{e}_\varphi$ . A motion of the neutral gas, as observed in [13], is neglected in the simulations.

Particles of diameter  $2a = 1 \mu\text{m}$  obtain a charge of about  $Q_d = -2500$  elementary charges [14] due to the plasma environment. This results in an electrostatic repulsion between the particles. The corresponding force between the  $i$ th particle and  $N - 1$  identical particles is given by the shielded Coulomb force

$$\vec{F}_Y(\vec{r}_i) = \sum_{j \neq i}^N \frac{Q_d^2}{4\pi\epsilon_0 \Delta_{ij}^3} \exp(-\kappa \Delta_{ij})(1 + \kappa \Delta_{ij}) \vec{r}_{ij}. \quad (1)$$

Here,  $\vec{r}_i$  is the position of particle  $i$ ,  $\vec{r}_{ij} = \vec{r}_i - \vec{r}_j$ ,  $\Delta_{ij} = |\vec{r}_{ij}|$ , and  $\kappa = 1/\lambda_D$  is the inverse of the Debye length. Here,  $\lambda_D = 250 \mu\text{m}$  is used, which corresponds to the experimental shielding length and agrees with simulations for an effective Debye length in the presence of fast ions [15]. The neutral gas background damps the motion of the particles as neutral friction  $\vec{F}_N = -m_d \beta \vec{v}$ , with  $\vec{v}$  as the velocity of particle  $i$  and  $\beta$  as the Epstein friction coefficient. The sum of the external forces is then  $\vec{F}_{\text{ext}} = \vec{F}_c + \vec{F}_g + \vec{F}_i + \vec{F}_Y$ . A random force  $\vec{F}_R$  is introduced as a heat bath to compensate for energy dissipation by friction. The resulting equation of motion is then integrated using a Verlet-like algorithm [16]. More details of the simulations can be found in [11].

Manuscript received July 10, 2012; accepted September 25, 2012. Date of publication October 18, 2012; date of current version April 6, 2013. This work was supported by DFG in the frame of SFB-TR24 Greifswald–Kiel, Project A2.

The authors are with the Institut für Experimentelle und Angewandte Physik, Christian-Albrechts-Universität, D-24098 Kiel, Germany (e-mail: reichstein@physik.uni-kiel.de; wilms@physik.uni-kiel.de; piel@physik.uni-kiel.de).

Color versions of one or more of the figures in this paper are available online at <http://ieeexplore.ieee.org>.

Digital Object Identifier 10.1109/TPS.2012.2222052

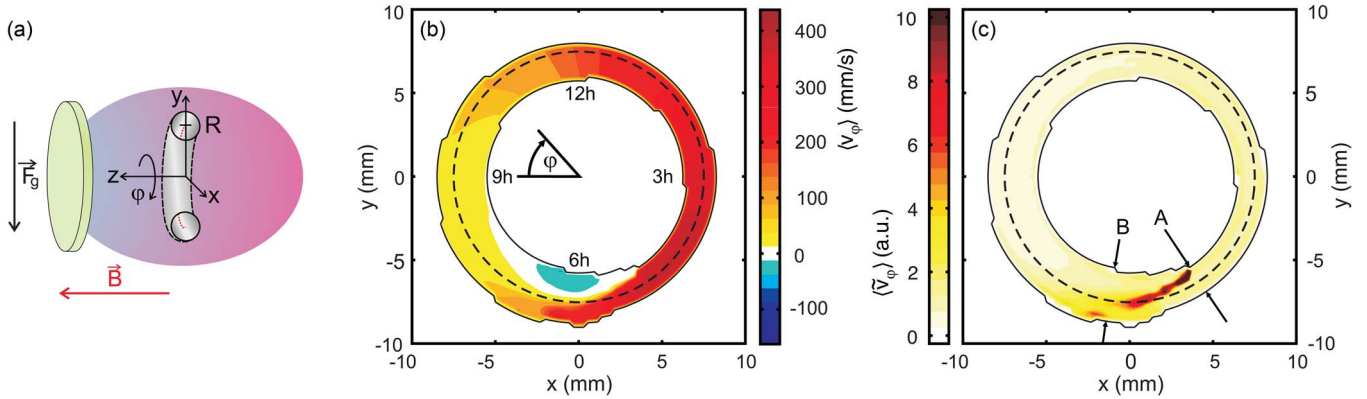


Fig. 1. (Color online) (a) Sketch of the geometry used in the simulations. (b) Distribution of the mean toroidal velocity component for  $F_i = 0.8F_g$  and  $\beta = 40\text{ s}^{-1}$  and (c) the distribution of the corresponding mean velocity fluctuation amplitude.

### III. FLOW PROPERTIES

In Fig. 1(b), the distribution of the mean toroidal flow velocity  $\langle v_\varphi \rangle$  is shown for driving force  $F_i = 0.8F_g$  and weak friction ( $\beta = 40\text{ s}^{-1}$ ). Therefore, the particle velocities were interpolated onto a grid in polar coordinates and averaged over time. Positions along the circular path of the flow are given by the angle  $\varphi$  and marked as hour ticks on a clock dial.  $\varphi$  is increasing clockwise, and  $\varphi = 0$  corresponds to the 9-h position. Positive velocities correspond to a clockwise motion.

Starting at  $\varphi \cong 9\text{ h}$ , the toroidal flow velocity increases with increasing  $\varphi$  until a maximum at about 4.5 h is reached. Up to this position, the flow maintains a nearly homogeneous velocity profile in a radial cross section. At 5 h, a sudden velocity decrease at the inner boundary of the torus is observed, leading to a strongly sheared velocity profile within a radial cross section. Around 6 h, a retrograde flow is observed with particles moving in a direction opposite to the main flow direction. Up to 8 h, a sheared flow pattern is observed, but the velocity gradient in radial direction decreases along the main flow direction with increasing  $\varphi$ .

In Fig. 1(c), the amplitude of velocity fluctuations in toroidal direction is presented. For this purpose, the rms deviation of the velocity from the mean velocity was taken at every time step:  $\langle \tilde{v}_\varphi \rangle = \langle (v_\varphi(t) - \langle v_\varphi \rangle)^2 \rangle^{1/2}$ . While, for most values of  $\varphi$ , the fluctuations are very small, strong fluctuations are found at  $\varphi \cong 5\text{--}7\text{ h}$  in a radially narrow region corresponding to the region of maximum velocity shear [Fig. 1(b)]. These strongly sheared dust flows lead to the formation of Kelvin–Helmholtz instabilities [12]. The angular position of the onset of strong velocity fluctuations is indicated as position A; the disappearance is indicated as position B. The definition for these positions will be given later.

For a better insight, in Fig. 2(a), the angular distribution of the mean toroidal speed (black dashed line) and the corresponding velocity fluctuation amplitude (red solid line) are displayed. Here, the radial mean values of the same data set as in Fig. 1(b) and (c) were plotted as a function of  $\varphi$ .

In the range  $\varphi \cong 8\text{--}5\text{ h}$ , a continuous increase of  $\langle v_\varphi \rangle$  with increasing  $\varphi$  is seen, while  $\langle \tilde{v}_\varphi \rangle$  remains at very low values. The maximum velocity  $\langle v_\varphi \rangle_{\max}$  is found at  $\varphi(\langle v_\varphi \rangle_{\max}) \cong 4.5\text{ h}$ . At position A [the same as in Fig. 1(c)], a sudden decrease of  $\langle v_\varphi \rangle$  is observed together with an abrupt increase of  $\langle \tilde{v}_\varphi \rangle$ .

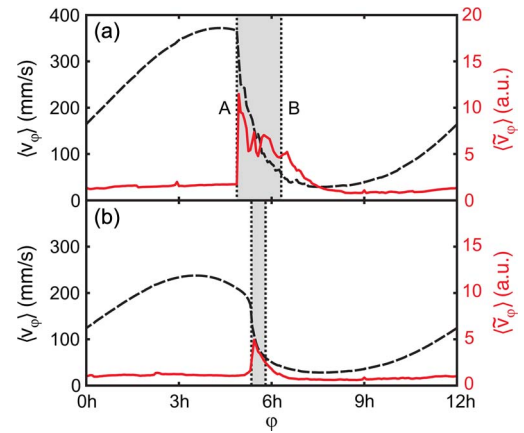


Fig. 2. (Color online) Angular distribution of mean rotation velocity (black dashed line) and corresponding fluctuation amplitude (red solid line) for (a)  $F_i = 0.8F_g$  and  $\beta = 40\text{ s}^{-1}$  and (b)  $F_i = 1.0F_g$  and  $\beta = 80\text{ s}^{-1}$ . For a better visualization, the region of increased velocity fluctuations is shaded gray.

While  $\langle v_\varphi \rangle$  decreases to very low values,  $\langle \tilde{v}_\varphi \rangle$  remains at high values over a wider range until decreasing again at position B. In order to determine the positions A and B, the maximum value of  $\langle \tilde{v}_\varphi \rangle$  is determined:  $\langle \tilde{v}_\varphi \rangle_{\max}$ . The area between A and B is then determined by  $\langle \tilde{v}_\varphi \rangle(\varphi) > \langle \tilde{v}_\varphi \rangle_{\max}/2$ . If no fluctuations are present in a simulation run, this condition holds for all values of  $\varphi$  (cf. Fig. 4).

Fig. 2(b) shows the angular distribution of  $\langle v_\varphi \rangle$  and  $\langle \tilde{v}_\varphi \rangle$  for a slightly higher ion drag force ( $F_i = 1.0F_g$ ) and strong friction ( $\beta = 80\text{ s}^{-1}$ ). Qualitatively, both curves show the same trend as in Fig. 2(a). However, the overall velocities are lower. In addition, the region of increased velocity fluctuations is much narrower.

The sudden decrease of  $\langle v_\varphi \rangle$  in Fig. 2(a) results from the strongly sheared flow pattern in this region. The velocity gradient across the cross section of the flow leads to the formation of Kelvin–Helmholtz instabilities [12], which, in turn, lead to a strong increase of velocity fluctuations. Since these instabilities exist over a wide angular range, the velocity fluctuations will also be significantly higher in this region. When friction is strong, the formation of standing shocks in the flow is favored [11]. Since these shocks are strongly localized, the corresponding region of high velocity fluctuations is very narrow as well.

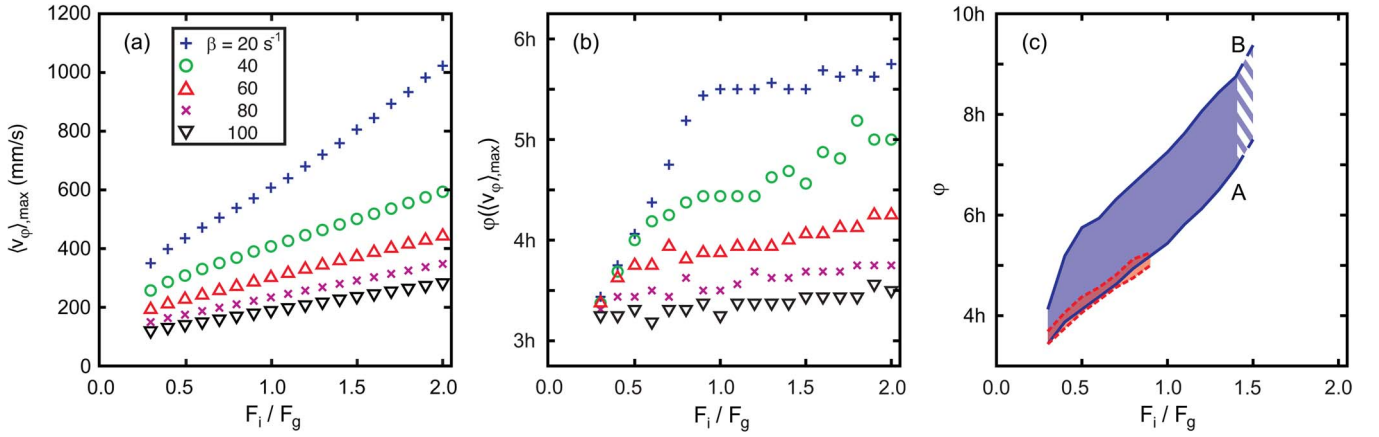


Fig. 3. (Color online) Influence of the normalized ion drag force  $F_i/F_g$  and friction strength  $\beta$  on (a) the maximum rotation velocity, (b) the position of maximum velocity, and (c) the position of the unstable flow region as the region between positions A and B (cf. Figs. 1(c) and 2). Shown are the results for the following:  $\beta = 20 \text{ s}^{-1}$  (+),  $40 \text{ s}^{-1}$  (O),  $60 \text{ s}^{-1}$  ( $\Delta$ ),  $80 \text{ s}^{-1}$  (x), and  $100 \text{ s}^{-1}$  ( $\nabla$ ). In (c), only results for (solid lines)  $\beta = 40 \text{ s}^{-1}$  and (dashed lines)  $\beta = 100 \text{ s}^{-1}$  are shown.

#### IV. INFLUENCE OF PARAMETERS

Now, the influence of driving force  $F_i$  and friction strength  $\beta$  on the dust flow characteristics is studied in more detail. In Fig. 3(a), the maximum rotation velocity is plotted as a function of the normalized ion drag force  $F_i/F_g$  for different values of  $\beta$  [ $\beta = 20 \text{ s}^{-1}$  (+),  $40 \text{ s}^{-1}$  (O),  $60 \text{ s}^{-1}$  ( $\Delta$ ),  $80 \text{ s}^{-1}$  (x), and  $100 \text{ s}^{-1}$  ( $\nabla$ )]. A linear increase of the velocity with  $F_i$  is seen for all values of  $\beta$ . With increasing  $\beta$ , the maximum velocity decreases for a given value of  $F_i$ . For  $F_i < 0.3F_g$ , no particle rotation was observed. However, the characteristics indicate a “velocity offset”  $\langle v_\varphi \rangle_{\max} > 0$  for  $F_i = 0$ .

Since the ion drag acts as an external driving force, an increase of maximum velocity with increasing  $F_i$  is expected. Collisional damping is proportional to the friction strength  $\beta$ , so that stronger friction results in lower velocities. Without a driving force, particles situated around  $\varphi \hat{=} 12 \text{ h}$  descend due to gravity, obtaining velocities in the order of a terminal velocity given by an equilibrium of gravity and friction  $v_t = g/\beta$ . Since this motion is independent of the ion drag but superimposed on the motion driven by the ion drag, a “velocity offset” is observed.

In Fig. 3(b), the influence of the driving force on the angular position of highest rotation velocity is shown for different friction strengths [the same as in Fig. 3(a)]. For small values of  $F_i$ , the position is independent of  $\beta$  and is located close to 3 h. For strong friction,  $\varphi$  remains nearly constant, while for lower values of  $\beta$ , there is a stronger increase of  $\varphi$  with increasing ion drag. For weak friction [ $\beta = 20 \text{ s}^{-1}$  (+)], a position around 5.5 h is reached for  $F_i = 0.9F_g$  and remains constant with further increasing ion drag.

In the strongly coupled case, dust rotation is possible even for  $F_i/F_g < 1$ . When the ion drag is small compared to gravity, the dust dynamics is mainly given by an equilibrium of the azimuthal component of gravity and friction. Due to the system geometry, the azimuthal component of gravity is strongest at  $\varphi \hat{=} 3 \text{ h}$  and then weakens with increasing  $\varphi$ . Thus, the position of maximum velocity is located close to the maximum of the azimuthal gravity component. With increasing ion drag, the driving force increases, and ballistic effects can become

important for weak friction, resulting in higher values of  $\varphi$ . The angular position cannot increase indefinitely due to the used geometry. On the ascending branch, the particles will be slower since gravity acts against the driving force. Therefore, a constant value for the position of highest velocity is expected to be around  $\varphi \hat{=} 6 \text{ h}$  as seen in Fig. 3(b).

The influence of driving force and friction on the position of the region of disturbed flow is shown in Fig. 3(c). There, the area of increased velocity fluctuations (area between positions A and B in Figs. 1(c) and 2) is plotted as a function of the ion drag force for weak ( $\beta = 40 \text{ s}^{-1}$ , solid lines) and strong friction ( $\beta = 100 \text{ s}^{-1}$ , dashed lines). One immediately sees that, with increasing  $F_i$ , the disturbed flow region is shifted to higher values of  $\varphi$ . For both friction strengths, the position of the onset of the fluctuations is nearly the same, but for strong friction, the region has a smaller angular extent than for weak friction. Furthermore, for strong friction, no fluctuations are observed for  $F_i > 0.9F_g$ . For weak friction, a quiescent flow throughout the entire system is obtained for  $F_i > 1.5F_g$ .

With increasing ion drag force, ballistic effects can become important, which, in turn, shift the disturbed region to higher values of  $\varphi$ . When friction is strong, strongly localized standing shocks occur, resulting in a very narrow disturbed flow region. In addition, strong friction results in smaller velocity deviations in the two different branches, which, in turn, leads to a more quiescent flow without instabilities. On the other hand, for weak friction, strongly sheared flow profiles occur, leading to large-scale Kelvin–Helmholtz instabilities. Furthermore, the value of the driving ion drag force has to become significantly larger than gravity in order to reduce the influence of gravity on the flow dynamics. Therefore, a quiescent flow is first found for weak friction at higher values of the ion drag.

An overview over the different flow regimes is given in Fig. 4. For  $F_i < 0.3F_g$ , no particle rotation was observed. For  $F_i < 0.5F_g$ , only single particles were able to rotate about the major axis of the torus. Up until  $F_i \approx 1.0F_g$ , only dust flows containing an instability were observed. For weak friction, instabilities driven by a sheared flow pattern were observed, while for strong friction, a shock formation was present.

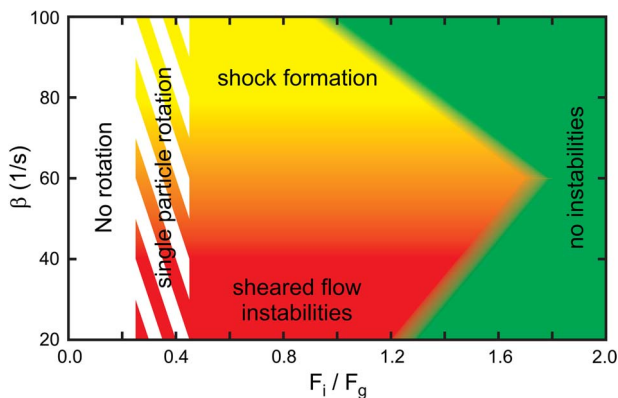


Fig. 4. (Color online) Map of different flow regimes depending on ion drag and friction.

For intermediate friction strengths, hybrids of both instabilities were observed. For even higher values of  $F_i$ , depending on friction, the transition to quiescent flow patterns without instabilities was found. For strong and weak friction, the transition begins for lower values of  $F_i$  compared to medium friction strengths which can be seen in Fig. 4 as a V-shaped transition line, indicating that there are two different mechanisms responsible for this transition.

Instabilities are effectively quenched if the collisional damping rate is on the order of the growth rate of the instability. Therefore, particle flows exhibit no large-scale instabilities for strong friction. The formation of a standing shock is due to the asymmetry of the flow caused by gravity. With increasing ion drag, the influence of gravity on the dynamics diminishes, and with it, the asymmetry of the flow diminishes.

For weak friction, this asymmetry results in a strongly sheared flow pattern with a distinct retrograde flow similar to granular flows in rotating drums [17], [18]. There, granular matter is set into motion via a rotating horizontal cylinder. While the lower part of the granular matters performs a rigid-body rotation in the same rotational direction as the cylinder, the upper particles move in a way that a sheared velocity profile emerges. Juarez *et al.* [18] showed, by means of experiments and simulations, that, with increasing angular velocity of the cylinder, centrifugal effects become dominant so that all particles perform a rigid-body rotation arranged in a ring-shaped structure. In our simulations, the strong velocity shear can result in the formation of Kelvin–Helmholtz instabilities. If the rotation velocities become high enough that centrifugal effects inhibit a retrograde flow, shear-driven instabilities can no longer develop. If the ion drag is increased, centrifugal effects become relevant even for higher friction strengths, which results in the observed characteristics of the transition.

## V. DISCUSSION

Particle flows in toroidal traps feature interesting dynamical properties like structural phase transitions [11] or the spontaneous development of instabilities in the stream due to the asymmetry of the flow caused by gravity. Here, friction has been found to play an important role whether a

very localized standing shock, an extended shear-flow-driven Kelvin–Helmholtz instability, or hybrids are emerging. With increasing ion drag force, a transition to quiescent dust flows was found, and two different mechanisms responsible for the transition could be identified.

In the experiment, the particle flows of a torus-shaped dust cloud were studied and agree well with our simulations [11], [12]. Also, the first experimental evidence of a retrograde flow was observed [12]. Experiments are in progress that aim at verifying the various instability scenarios described in this paper.

## ACKNOWLEDGMENT

The authors would like to thank O. Arp for the hint at the similarity to rotating granular matter.

## REFERENCES

- [1] G. E. Morfill, S. A. Khrapak, A. V. Ivlev, B. A. Klumov, M. Rubin-Zuzic, and H. M. Thomas, "From fluid flows to crystallization: New results from complex plasmas," *Phys. Scr.*, vol. 2004, no. T107, pp. 59–64, 2004.
- [2] R. Heidemann, S. Zhdanov, K. R. Sütterlin, H. M. Thomas, and G. E. Morfill, "Shear flow instability at the interface among two streams of a highly dissipative complex plasma," *Eur. Phys. Lett.*, vol. 96, no. 1, p. 15001, Oct. 2011.
- [3] K. A. Pacha, J. R. Heinrich, S.-H. Kim, and R. L. Merlino, "Observation of the Taylor instability in a dusty plasma," *Phys. Plasmas*, vol. 19, no. 1, p. 014501, Jan. 2012.
- [4] J. Ashwin and R. Ganesh, "Kelvin Helmholtz instability in strongly coupled Yukawa liquids," *Phys. Rev. Lett.*, vol. 104, no. 21, p. 215003, May 2010.
- [5] J. Ashwin and R. Ganesh, "Parallel shear flow instabilities in strongly coupled Yukawa liquids: A comparison of generalized hydrodynamic model and molecular dynamics results," *Phys. Plasmas*, vol. 17, no. 10, p. 103706, Oct. 2010.
- [6] A. Barkan and R. L. Merlino, "Confinement of dust particles in a double layer," *Phys. Plasmas*, vol. 2, no. 9, pp. 3261–3265, Sep. 1995.
- [7] T. Trottenberg, D. Block, and A. Piel, "Dust confinement and dust-acoustic waves in weakly magnetized anodic plasmas," *Phys. Plasmas*, vol. 13, no. 4, p. 042105, Apr. 2006.
- [8] I. Pilch, T. Reichstein, and A. Piel, "Torus-shaped dust clouds in magnetized anodic plasmas," *Phys. Plasmas*, vol. 15, no. 10, p. 103706, Oct. 2008.
- [9] T. Reichstein, I. Pilch, R. Grosse-Ahlert, and A. Piel, "Toroidal dust clouds and voids in a magnetized anodic plasma," *IEEE Trans. Plasma Sci.*, vol. 38, no. 4, pp. 814–817, Apr. 2010.
- [10] T. Reichstein, I. Pilch, and A. Piel, "Toroidal dust motion in magnetized plasmas," *Phys. Plasmas*, vol. 17, no. 9, p. 093701, Sep. 2010.
- [11] T. Reichstein and A. Piel, "Simulation of dust streaming in toroidal traps: Stationary flows," *Phys. Plasmas*, vol. 18, no. 8, p. 083705, Aug. 2011.
- [12] T. Reichstein, J. Wilms, F. Greiner, A. Piel, and A. Melzer, "Experiments and simulations of particle flows in a magnetized dust torus," *Contrib. Plasma Phys.*, 2012. doi:10.1002/ctpp.201200029, to be published.
- [13] J. Carstensen, F. Greiner, L.-J. Hou, H. Maurer, and A. Piel, "Effect of neutral gas motion on the rotation of dust clusters in an axial magnetic field," *Phys. Plasmas*, vol. 16, no. 1, p. 013702, Jan. 2009.
- [14] H. Mott-Smith and I. Langmuir, "The theory of collectors in gaseous discharges," *Phys. Rev.*, vol. 28, no. 4, pp. 727–763, Oct. 1926.
- [15] I. Hutchinson, "Collisionless ion drag force on a spherical grain," *Plasma Phys. Control. Fusion*, vol. 48, no. 2, pp. 185–202, Feb. 2006.
- [16] M. P. Allen and D. J. Tildesley, *Computer Simulation of Liquids*. Oxford, U.K.: Oxford Science, 1994.
- [17] J. Rajchenbach, "Flow in powders: From discrete avalanches to continuous regime," *Phys. Rev. Lett.*, vol. 65, no. 18, pp. 2221–2224, Oct. 1990.
- [18] G. Juarez, P. Chen, and R. M. Lueptow, "Transition to centrifuging granular flow in rotating tumblers: A modified Froude number," *New J. Phys.*, vol. 13, no. 5, p. 053055, May 2011.

**Torben Reichstein** was born in 1984. He received the Diploma degree in physics from Christian-Albrechts-Universität, Kiel, Germany, in 2008, where he is currently working toward the Ph.D. degree in the group of A. Piel.

His research interests include dusty plasmas.

**Jochen Wilms** was born in 1985. He received the Diploma degree in physics from Christian-Albrechts-Universität, Kiel, Germany, in 2012, where he is currently working toward the Ph.D. degree in the group of A. Piel.

His research interests include dusty plasmas.

**Alexander Piel** was born in 1950. He received the Ph.D. degree and the Habilitation degrees from Ruhr University Bochum, Bochum, Germany, in 1977 and 1986, respectively.

Since 1989, he has been a Full Professor with Christian-Albrechts-Universität, Kiel, Germany. His research interests cover dusty plasmas, plasma waves, and ionospheric research.

Dr. Piel is a Fellow of APS.

## A.6

# SPONTANEOUS SYMMETRY BREAKING IN MAGNETIZED DUST FLOWS

Torben Reichstein, Jochen Wilms, and Alexander Piel

Reprinted with permission from  
Torben Reichstein, Jochen Wilms, and Alexander Piel,  
Physics of Plasmas, Vol.21, 023705 (2014).  
Copyright 2014, American Institute of Physics.

## Spontaneous symmetry breaking in magnetized dust flows

Torben Reichstein,<sup>a)</sup> Jochen Wilms, and Alexander Piel  
 IEAP, Christian-Albrechts-Universität, D-24098 Kiel, Germany

(Received 20 December 2013; accepted 4 February 2014; published online 20 February 2014)

Toroidal dust flows in magnetized anodic plasmas are driven by an azimuthal Hall component of the ion drag. By means of Langmuir probe measurements, it was found that the ion drag has a strong radial gradient. This finding is supported by the rotation velocities obtained by particle tracking analysis. The topology of shear flows is also attributed to the radial gradient of the ion drag. Furthermore, from a critical comparison of particle image velocimetry and particle tracking, a much better agreement between the measured rotation velocity and simulations could be achieved. © 2014 AIP Publishing LLC. [<http://dx.doi.org/10.1063/1.4866018>]

### I. INTRODUCTION

Dusty (complex) plasmas are a suitable model system to study the influence of strong coupling on the structure and dynamics of a many-particle system on a kinetic level.<sup>1</sup> The study of strongly coupled dust flows is an interesting subfield.<sup>2–6</sup> Earlier experiments were dedicated to sheared flows driven by two dust streams of different velocities,<sup>3</sup> behind obstacles<sup>4</sup> or the formation of a Taylor-like instability due to a sheared dust flow.<sup>5</sup> Molecular dynamic (known hereafter as MD) simulations were also focused on sheared dust flows<sup>6</sup> from which a Kelvin-Helmholtz instability was reported, and the simulation results were found in general agreement with a generalized hydrodynamic model.<sup>7</sup>

In a laboratory plasma,  $\mu\text{m}$ -sized dust particles are subjected to the ion drag force and the electric field force. Due to the negative particle charge, these forces are usually directed in opposite directions. If the ion drag exceeds the (radial) electric field force in the center of the discharge, a dust-free region (void) forms, which is well known from experiments under microgravity conditions<sup>8,9</sup> and in laboratory plasmas,<sup>10,11</sup> when the particles are grown *in situ*,<sup>10</sup> or when a thermophoretic force compensates gravity.<sup>11</sup>

In an anodic dc plasma<sup>12</sup> with an superimposed magnetic field, void-free dust clouds can be confined.<sup>13,14</sup> Barkan and Merlino<sup>13</sup> reported a rigid-body cloud rotation in  $E \times B$ -direction. In a similar setup, torus-shaped dust clouds with a distinct void in the center were observed.<sup>15,16</sup> The formation, structure, and dynamics of these tori were investigated experimentally<sup>16–19</sup> and by means of MD simulations.<sup>19–21</sup> The toroidal flow of the dust particles can be ascribed to the Hall component of the ion flow across the magnetic field, which exerts an ion drag force in azimuthal direction and drives the dust rotation. Because the major torus axis is horizontal, this ion drag component has to exceed a threshold given by gravity to form a torus-shaped dust cloud. An inhomogeneous stationary flow pattern is observed with high rotation speed on the descending branch of the torus and low velocities on the ascending branch. In the simulations, an NVIDIA® GPU (GTS 250) using CUDA™ was used to calculate the N-body interactions.<sup>20,22</sup>

<sup>a)</sup>Electronic mail: reichstein@physik.uni-kiel.de

In the simulations, the obtained dust flows spontaneously developed—dependent on the friction strength—two different kinds of flow instabilities. For strong friction, a standing shock with a sudden decrease in the flow speed together with an increase in number density and kinetic temperature of the particles was observed. For weak friction, a strongly sheared flow pattern arised in the lower region of the torus with a retroflow at the inner boundary of the torus.<sup>20</sup> A more detailed analysis of the sheared flow indicated that a Kelvin-Helmholtz instability forms at the boundary between the fast particles and the slow particles in the retroflow.<sup>19</sup> In the upper region of the torus, a quiescent unsheread flow was observed, which allowed the particles to relax into nested shells. Furthermore, the influence of friction and driving force on the flow dynamics like the maximum rotation velocity has been studied in detail.<sup>21</sup>

This paper addresses the discrepancy arising from a comparison of simulations and experimental results. New experimental results showed a different topology than predicted by the simulations. Hence, a critical analysis of the driving mechanism was performed. Also, the overall rotation velocities obtained in the simulations were a factor of 2–3 higher than optical measurements by means of particle image velocimetry (known hereafter as PIV). Therefore, a comparison of PIV with a particle tracking analysis was conducted. Furthermore, self-excited dust-density waves are common in anodic plasmas which are not present in the simulation. Thus, systems of only a few particles were studied to suppress the formation of waves in the experiment.

The paper is organized as follows: In Sec. II, the experimental setup is presented. In Sec. III, the electric field of the anodic plasma is studied in detail by means of probe measurements, and experimental results are presented, which are compared with MD simulations in Sec. IV. A discussion concludes the paper in Sec. V.

### II. SETUP

The experiments were conducted in the experiment MATILDA-II, a cylindrical vacuum chamber with a primary radio-frequency discharge ( $f = 27.12$  MHz) at low power of 2–5 W and a secondary DC discharge that is formed in front of a positively biased anode. A detailed description of the



experimental setup is given in Refs. 14 and 15. The anode is biased at voltages of 70–110 V and low currents of 8–20 mA. The experiments were performed in argon gas at pressures of 3–8 Pa. The external magnetic field has a strength of 5–20 mT. The plasma parameters typically are ion density  $n_i \approx 10^{15} \text{ m}^{-3}$  and electron temperature  $T_e = 3 \text{ eV}$ . For the measurement of plasma density and plasma potential, an axially movable and radially rotatable combination of an emissive and Langmuir probe was used.

Spherical monodisperse dust particles (melamine formaldehyde) of  $2r_p = 0.97 \pm 0.05 \text{ }\mu\text{m}$  were used in the experiments. The particles are confined in the anodic plasma by a force equilibrium of the electric field force and the ion drag force. The axial confinement was studied in detail in Ref. 14 and the radial confinement was examined in Ref. 16 in the same setup.

In Fig. 1, a top-view sketch of the observation geometry is given. An indium-tin-oxide (ITO) coated glass substrate is used as the anode, which is optically transparent and electrically conducting. A vertical laser fan ( $\lambda = 532 \text{ nm}$ ,  $P = 2 \text{ W}$ ) illuminates the dust in front of the anode. The scattered light is deflected by a mirror and recorded by a camera viewing through a side window. The CMOS camera has a maximum frame rate of 506 frames per second at a maximum resolution of  $1280 \times 1024$  pixels. The frame rate can be further increased by using a smaller region of interest.

The direction of gravity defines the negative  $y$ -axis, the horizontal axis of the vacuum chamber defines the  $z$ -axis, and the  $x$ -axis is tangential to the surface of the anode. The radial displacement from the anode center is  $r = \sqrt{x^2 + y^2}$ .

### III. ELECTRICAL AND OPTICAL MEASUREMENTS

Charged dust particles are confined by a force equilibrium of the dominant forces inside a plasma. In MATILDA-II, the electric field force  $F_{el}$ , and the ion drag force  $F_i$ , are orders of magnitude larger than gravity. Due to the negative dust charge, the electric field force is antiparallel to the electric field direction while the ion drag acts along the flow direction of the positive ions which is nearly aligned with the electric field. Thus, these forces are responsible for the dust confinement. Hence, the analysis of these forces by means of probe measurements is of high interest.

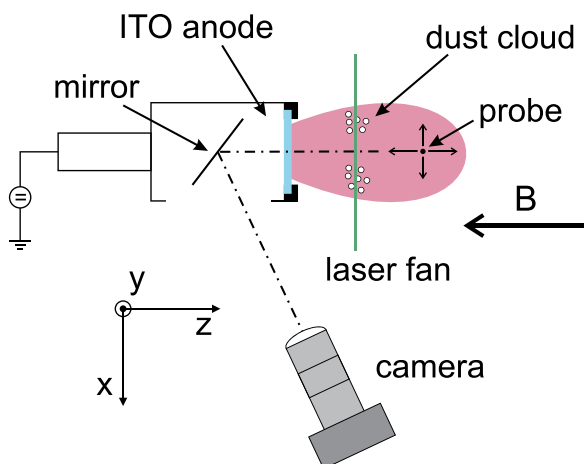


FIG. 1. Top-view sketch of the experimental setup.

### A. Probe measurements

In Fig. 2(a), the absolute values of electric field force (solid line) and ion drag (dashed line) are plotted as a function of the electric field strength for typical experiment parameters. For weak electric fields, the ion drag exceeds the electric field force, pushing the dust out of the weak-field region. For an intermediate field strength ( $V \approx 700 \text{ V/m}$ ), a stable force equilibrium is found.

Since torus-shaped dust clouds are the main topic of this work, the radial confinement is of high interest. Therefore, the electric field in both axial and radial direction was measured by an emissive probe at an axial displacement of  $z \approx 25 \text{ mm}$  from the anode center, where the torus-shaped dust cloud is usually located. In Fig. 2(b), the radial distribution of both radial (circles) and axial (squares) electric field component is displayed. While the axial field component is nearly independent of the radial displacement  $r$ , a strong increase in the radial field component towards the boundary of the anodic plasma is observed.

For ions under the influence of an electric field  $\vec{E} = (E_x, 0, E_z)$ , and a magnetic field  $\vec{B} = (0, 0, B)$ , the stationary equation of motion reads

$$m_i(\vec{v}_i \cdot \nabla)\vec{v}_i + m_i\nu_{in}\vec{v}_i = e(\vec{E} + \vec{v}_i \times \vec{B}) \quad (1)$$

with the ion mass  $m_i$ , ion-neutral collision frequency  $\nu_{in}$ , and ion drift velocity  $\vec{v}_i$ . The convective term is small compared with the friction term and can therefore be neglected here. Following the analysis described in Ref. 16, the electric field force  $F_{el}$ , and the ion drag force  $F_i$ , are calculated in radial direction. For the determination of the ion drag, the model of Hutchinson [Eqs. (1), (2), (4), (8), (10), (11) in Ref. 23] was used. For a detailed description of the calculation of the ion drag and the electric field force, please refer to the Appendix. Then, from the total force in radial direction,  $F_{el,r} + F_{i,r}$ , a non-conservative confinement potential energy has been calculated and is shown in Fig. 2(c) as circles. A minimum for the confinement energy is found around  $r = 9 \text{ mm}$ . For small excursions from the confinement minimum ( $7 \text{ mm} < r < 11 \text{ mm}$ ), a harmonic confinement potential was fitted to the data, which is shown in Fig. 2(c) as a dashed line. Its minimum is located at  $r_h = 8.7 \text{ mm}$ . Since the minor radii of the observed torus-shaped dust clouds are usually less than 2 mm [indicated as the shaded area in Fig. 2(c)], the assumption of a harmonic confinement potential is valid.

Due to the magnetic field, the ion drift velocity (and with it the ion drag force) has a small Hall component in azimuthal direction  $F_{i,\phi}$ . The ratio of  $F_{i,\phi}/F_{i,r}$  is constant. In Fig. 2(d), the radial distribution of  $F_{i,\phi}$ , normalized to gravity  $F_g$ , is shown as crosses. For small  $r$ , an increase in  $F_{i,\phi}$  is observed. For  $5 \text{ mm} < r < 7 \text{ mm}$ ,  $F_{i,\phi}$  remains constant at a value of  $F_{i,\phi} = 1.1F_g$ . For larger values of  $r$ , a decrease is observed and for  $r > 10 \text{ mm}$  constant values of  $F_{i,\phi}/F_g = 0.5$  are found.

The ion drag force  $F_{i,\phi}$  is strongly dependent on the electric field strength [see Fig. 2(a)]. For small values of  $r$ , the electric field is weak [see Fig. 2(b)] so that an increase in  $E_r$  leads to an increase in  $F_i$ . Around  $r = 7 \text{ mm}$ , the measured electric field strength corresponds to the maximum value of

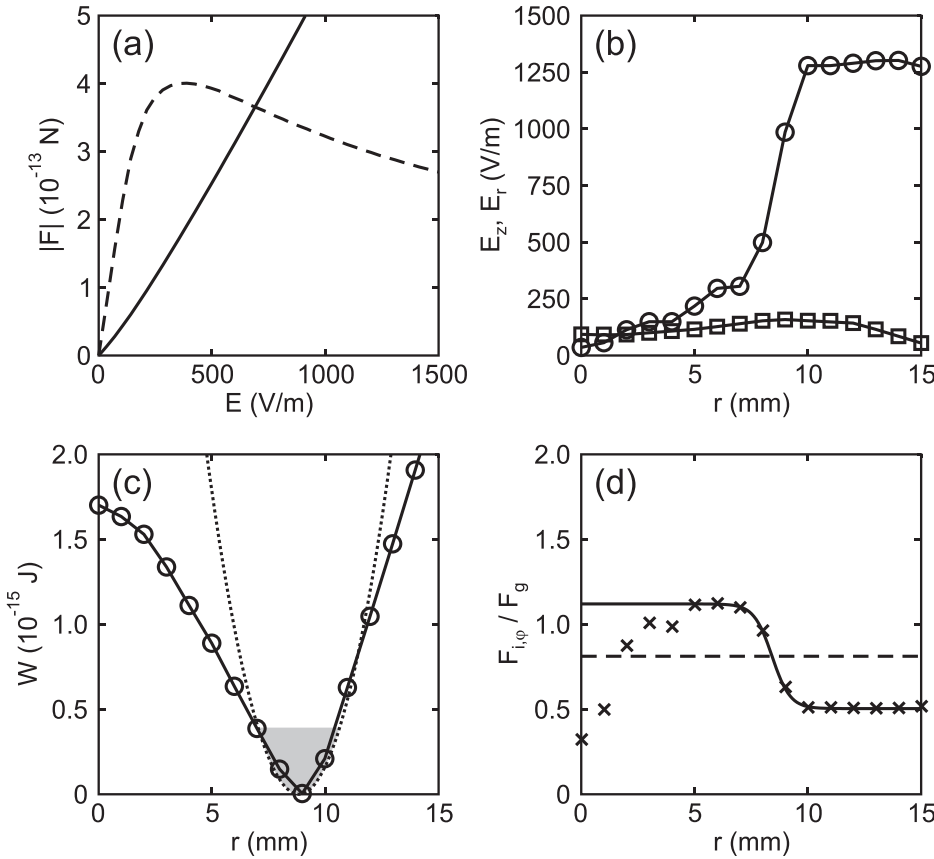


FIG. 2. (a) Absolute values of electric field force  $F_{el}$  (solid line), and ion drag force  $F_i$  (dashed line), as a function of the electric field strength  $E$ . (b) Radial distribution of radial electric field  $E_r$  (circles), and axial electric field  $E_z$  (squares), measured by an emissive probe at an axial distance  $z = 25$  mm from the anode center. (c) Radial potential energy (circles) derived from the total radial force  $F_{el,r} + F_{i,r}$  together with a harmonic confinement potential (dotted line) fitted to the potential energy around  $r = 9$  mm (shaded area). (d) Radial distribution of the azimuthal ion drag component  $F_{i,\phi}$ , normalized to gravity  $F_g$  (crosses), together with a fit (solid line) to the data for  $r > 5$  mm [cf. Eq. (2)] and a mean value of  $F_{i,\phi}/F_g = 0.8$  (dashed line) for comparison with simulations (cf. Sec. IV).

the ion drag, so that an increase in the electric field only has little influence on  $F_{i,\phi}$ . However, for the confinement region of the dust ( $r \approx 9$  mm), a strong increase in the electric field strength leads to a decrease in the ion drag in the vicinity of the equilibrium field strength. Thus,  $F_{i,\phi}$  is strongly sheared in radial direction. Since dust was not observed for  $r < 5$  mm, a model function of tanh-type

$$F_{i,\phi}/F_g = f_m - \Delta f \cdot \tanh\left(\frac{r-R}{\Delta r}\right) \quad (2)$$

was fitted to all values of  $F_{i,\phi}$  for  $r \geq 5$  mm and is shown as a solid line in Fig. 2(d). The mean value  $f_m = 0.8$  corresponding to an unsheared ion drag is given as a dashed line in Fig. 2(d) for comparison with simulations (see Sec. IV).  $R = 8.4$  mm corresponds to the inflection point of the curve and its value agrees with the position of the minimum of the harmonic confinement potential  $r_h$ . The parameter  $\Delta f = 0.308$  gives the magnitude of the force shear and  $\Delta r = 0.8$  mm corresponds to the shear length.

## B. Dust flow properties

Now, the implication of this radial gradient for the dust dynamics is studied in detail. Since the azimuthal ion drag component  $F_{i,\phi}$  is the driving force for the dynamics of torus-shaped dust clouds, the driving force is radially sheared. Thus, the rotation velocity of a dust particle should depend on its radial position for a fixed angular position along its annular path in the toroidal confinement. Therefore, an experiment was conducted with only a few particles

confined inside the anodic plasma in order to suppress many-particle effects like dust density waves.<sup>24</sup>

In Figs. 3(a)–3(c), snapshots of a clockwise rotating string with seven particles are shown. For the analysis of the dust dynamics, the particle positions were determined for each frame and the trajectories were calculated using a particle tracking algorithm.<sup>25</sup> The tracked particle positions are also marked by open circles. The snapshots are taken from consecutive cycles, when the foremost particle of the string reaches an angular position corresponding to  $\phi = 3$  h on a clock dial (see Fig. 4). An additional single particle can be seen, that precedes the string. Furthermore, a second string consisting of three particles could be observed, which is not shown here.

Since the distance between the single particle and the string decreases within one cycle, the single particle has an overall lower rotational frequency than the string. This could be due to slightly different particle masses. Taking the radius deviation of the particles into account, the ion drag can be different up to about 10%, gravity can vary up to 15%, resulting in different rotation velocities.

Now, for each cycle, the mean rotation velocity together with the mean radius of the particles was estimated in the range  $2.5 \text{ h} < \phi < 3.5 \text{ h}$ . In Fig. 3(d), the resulting rotation velocities were plotted as a function of the corresponding radii for the foremost particle of the 7-particle string (circles) and the foremost particle of the 3-particle string (triangles). Typical error bars are given at two exemplary values. It is evident that for both particles, the rotation velocity decreases with increasing radius.

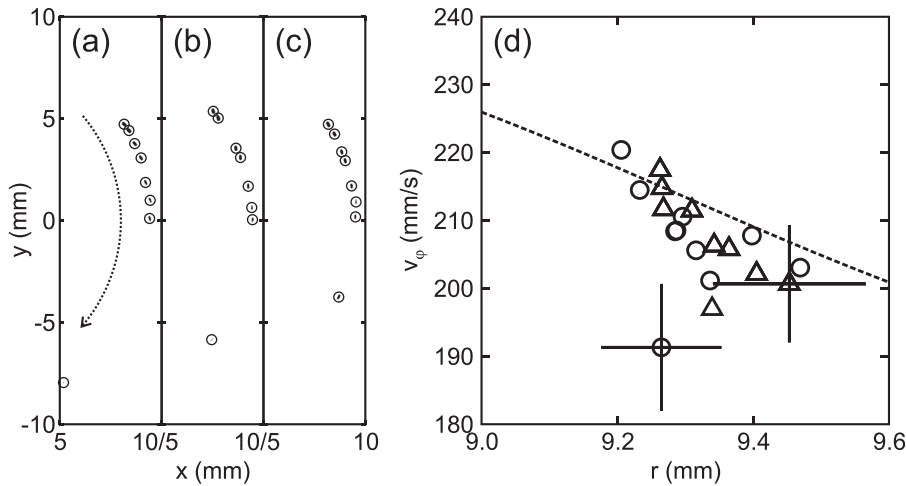


FIG. 3. (a)–(c) Snapshots of consecutive cycles of a 7-particle string together with a single particle. The flow direction is indicated by an arrow. (d) The mean rotation velocity of two particles around an angular position of  $\varphi = 3$  h as a function of the radius. Shown are data from the foremost particles of the 7-particle string (circles) and a 3-particle string (triangles) with typical error bars. The dashed line gives the dependency  $v_\varphi(r)$  using Eqs. (2) and (3).

In an earlier work, the dependency of the dust velocity on the ion drag was studied in detail [see Fig. 3(a) in Ref. 21]. From that, the following linear expression:

$$v_d(f_i) \approx 115 \frac{\text{mm}}{\text{s}} \cdot f_i + 120 \frac{\text{mm}}{\text{s}} \quad (3)$$

for the dust velocity  $v_d$  can be derived as a function of the normalized ion drag  $f_i$ . Combining Eqs. (2) and (3), we get a function  $v_d(r)$ , which is shown in Fig. 3(d) as a dashed line. Here, a decrease in velocity with increasing radius can also be observed.

Because the same particles are observed during one experimental run, this effect cannot be attributed to a change of external parameters. Since the azimuthal component of the ion drag decreases with increasing radius, particles at greater radii experience less ion drag. Hence, their rotation velocity will be lower. Furthermore, a good agreement between the empirical model [Eqs. (2) and (3)] and the measured velocities is found.

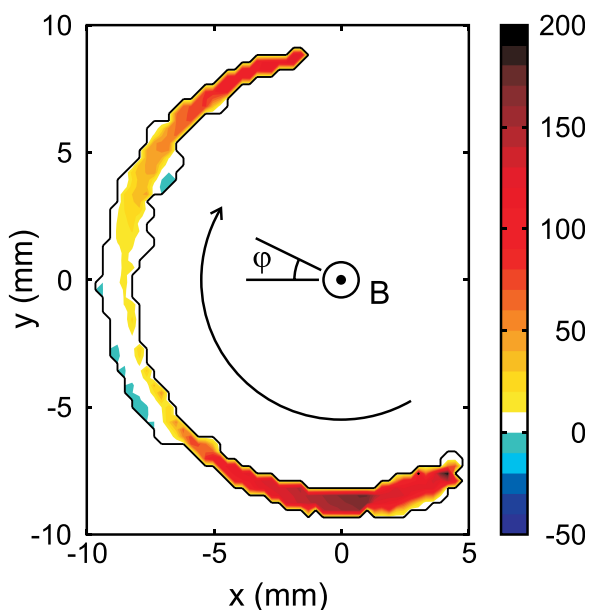


FIG. 4. Particle image velocimetry measurement of the toroidal velocity in the ascending branch of the torus-shaped dust cloud.

Besides the study of single particles inside the toroidal trap, torus-shaped dust clouds with many particles were also studied and their velocities were determined using PIV.<sup>26</sup> From the time-averaged velocities in the  $x$ - $y$  plane, the mean toroidal velocity  $v_\varphi$  was calculated and is shown in Fig. 4. Positive values of  $v_\varphi$  correspond to a clockwise motion about the main axis of the torus. The highest values of  $v_\varphi$  are found around  $\varphi = 6$  h. With increasing  $\varphi$ , the velocity first decreases and then increases again for  $\varphi > 9$  h. Furthermore, in the region of  $7 \text{ h} < \varphi < 9 \text{ h}$ , negative velocities are observed at the outer boundary.

The decrease in velocity in the ascending branch of a torus-shaped dust cloud was observed in earlier experiments<sup>17,20</sup> and is attributed to the reduction of the effective driving force due to gravity. The sheared flow pattern can be attributed to the radial gradient of the azimuthal ion drag. Since the ion drag is weaker than gravity for large radii, particles are unable to overcome gravity. Thus, they cannot participate in the global rotation of the cloud and are trapped at the outer boundary of the torus.

#### IV. COMPARISON OF EXPERIMENT AND SIMULATION

In MD simulations of toroidal dust streaming,<sup>19–21</sup> we had found, for weak friction, a sheared flow pattern with a retroflow in the ascending branch could be observed over a certain range of the driving force  $f_i$ . The simulations showed, in contrast to the experimental findings in Fig. 4, that the retroflow region was always located at the inner boundary of the torus.

##### A. Flow topology

In the simulation,<sup>20</sup> the azimuthal component of the ion drag,  $F_{i,\varphi}$ , was assumed independent of the radial position. Now, based on the experimental findings presented in Sec. III, a radially sheared  $F_{i,\varphi}$ , using Eq. (2) was implemented in the MD code. In Fig. 5(a), the time averaged velocity field of  $v_\varphi$  for a simulation run with  $N = 512$  particles is shown for a fixed normalized driving force  $f_i = 0.8$  as indicated by the dashed line in Fig. 2(d). Fig. 5(b) shows the velocity field for a simulation run with a radially sheared driving force  $f_i(r)$ , using Eq. (2) as shown by the solid line in Fig. 2(d). In order

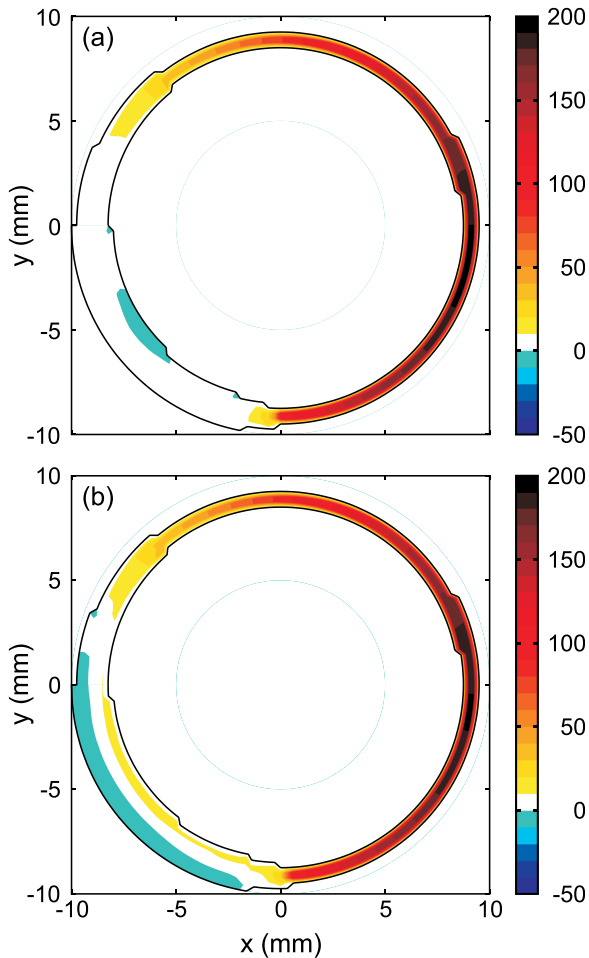


FIG. 5. Time averaged velocity field of  $v_\phi$  for a simulation run with  $N=512$  particles for (a) a constant driving force  $f_i=0.8$  [cf. dashed line in Fig. 2(d)] and (b) a radially dependent driving force  $f_i(r)$  using Eq. (2) [cf. solid line in Fig. 2(d)].

to study only the effect of the different driving forces, all other simulation parameters were kept constant.

For both simulation runs, an inhomogeneous stationary flow pattern with an overall clockwise rotation was found. The value and position of highest velocity ( $v_\phi \approx 200$  mm/s at  $\varphi \approx 4$  h) are the same as well as the shape of the cloud. Also, for  $\varphi = 6$  h, a decrease in velocity is observed and for  $7 \text{ h} < \varphi < 9$  h, a retroflow can be observed. For the radially constant driving force, the retroflow is again located at the inner boundary of the cloud as observed in earlier simulations.<sup>19,20</sup> For the radially dependent driving force, the retroflow region is now located at the outer boundary as observed in the experiment (see Fig. 4).

## B. Influence of external parameters

Besides giving a good description of the flow topology, the simulations should also predict the same trends as observed in the experiment when an external parameter like the magnetic field is varied. Therefore, by means of PIV measurements, the maximum rotation velocity of a torus-shaped dust cloud was determined as a function of the magnetic field strength with fixed pressure, power, and anode

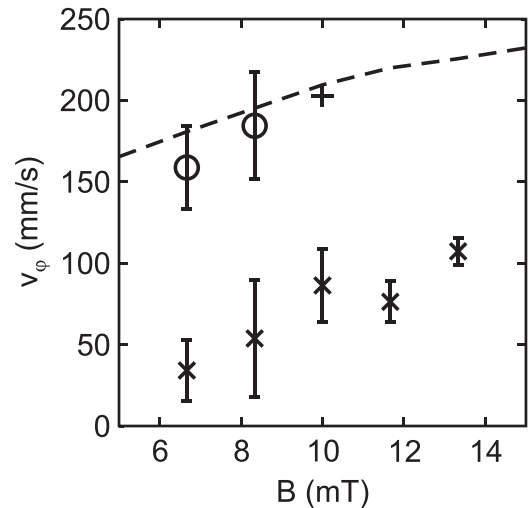


FIG. 6. Comparison of experiment and simulation of the maximum rotation velocity as a function of magnetic field. Experimental data obtained by PIV (crosses) and particle tracking (circles and plus sign) and data obtained by simulation (dashed line).

current. The results are displayed as crosses in Fig. 6. With rising magnetic field, the maximum velocity also increases.

For the comparison with the simulation, the ion density was measured by a Langmuir probe at the same discharge parameters. From that, the corresponding ion drag force was calculated as described in Ref. 16. Using Eq. (3), the corresponding velocities are determined and are shown in Fig. 6 as a dashed line. Again, with rising magnetic field, the velocity also increases. However, compared with the simulation results, the PIV measurements give smaller velocities by a factor 2–3.

This apparent contradiction can be resolved as follows: Since PIV only measures the translation of a group of particles, errors can occur when the particle trajectories are curved. Hence, the data for  $B = 6.6$  mT and  $B = 8.3$  mT were also analysed by means of particle tracking analysis in order to check for potential PIV errors arising from the experiment's geometry. The resulting velocities are shown in Fig. 6 as circles. The velocities are indeed much higher than those obtained by PIV and agree well with the simulation data. The plus sign in Fig. 6 indicates the mean maximum velocity of the particle strings shown in Fig. 3. Again, the velocities obtained by particle tracking agree well with the simulation.

## V. DISCUSSION

In this paper, we could resolve some discrepancies in the comparison of our earlier MD simulations with experimental results: The simulations predicted the existence of two particle populations: fast particles that contribute to the overall rotation motion of the cloud as well as a group of trapped particles that form a retroflow at the boundary of the torus. Now, we could verify the existence of these two particle populations experimentally.

In previous simulations,<sup>20</sup> the retroflow was located at the inner boundary of the torus, while in the experiment, the trapped particles are observed at the outer boundary. A detailed examination of the electric field led to the insight

that the azimuthal ion drag component, that drives the dust rotation, has a strong radial gradient. The flow topology of simulations with a radial gradient in the driving force are now in good agreement with the experiment.

Dust-density waves are common in magnetized anodic plasmas<sup>14,27</sup> but will not develop when the cloud size does not exceed the wave length.<sup>15</sup> Thus, tori with only a few particles were studied by means of particle tracking analysis. The result that particles at larger radii exhibit lower rotation velocities backs up the finding of the radial gradient of the ion drag.

Furthermore, particle tracking results of particle velocities were found in good agreement with the simulation results. Since the particle trajectories are curved due to the experiment's geometry, the PIV analysis underestimates the rotation velocities. However, the same velocity trend with rising magnetic field could be obtained from both particle tracking and PIV analysis.

In summary, the critical comparison between experiment and simulation led to deeper understanding of the underlying mechanisms of toroidal dust flows.

## ACKNOWLEDGMENTS

The present investigations were financially supported by Deutsche Forschungsgemeinschaft (DFG) within the Transregional Collaborative Research Center TR-24, project A2.

## APPENDIX: ION DRAG FORCE

The calculation of the ion drag described here closely follows the analysis given in Ref. 16 and is based on the ion drag model of Hutchinson [Eqs. (1), (2), (4), (8), (10), (11) in Ref. 23]:

The ion drag force consists of a collection part arising from direct momentum transfer of ions hitting the dust ( $F_c$ ) and an orbital part due to Coulomb scattering of the ions ( $F_o$ ). The orbital motion limited (OML) collection force for a shifted Maxwellian distribution with a flow velocity  $v_i$  in terms of  $u = v_i/v_{ti}$  normalized to the ion thermal velocity  $v_{ti} = \sqrt{2k_B T_i/m_i}$  reads

$$F_c = n_i r_p^2 m_i v_{ti}^2 \frac{\sqrt{\pi}}{2u^2} \left\{ u(2u^2 + 1 + 2\chi)e^{-u^2} + [4u^4 + 4u^2 - 1 - 2(1 - 2u^2)\chi] \frac{\sqrt{\pi}}{2} \operatorname{erf}(u) \right\} \quad (\text{A1})$$

with  $r_p$  the dust radius and  $\chi \equiv -e\phi_p/k_B T_i$  being the normalized potential of the particle. The orbital force reads as follows:

$$F_o = n_i \frac{q_i^2 \phi_p^2}{m_i v_{ti}^2} r_p^2 8\pi G(u) \ln \Lambda, \quad (\text{A2})$$

where  $G(u) \equiv [\operatorname{erf}(u) - 2ue^{-u^2}/\sqrt{\pi}]/(2u^2)$  is the Chandrasekhar function,<sup>28</sup>  $q_i$  the ion charge and  $\ln \Lambda$  the Coulomb logarithm. Using the floating condition for a dust grain in the OML approximation, the surface potential  $\phi_p$  is estimated

$$\bar{\Gamma}_e(\phi_p) = \frac{1}{4} n_{e\infty} \left( \frac{8k_B T_e}{\pi m_e} \right)^{1/2} \exp(e\phi_p/k_B T_e) = n_{e\infty} v_{ti} \frac{u}{4} \left\{ \left( 1 + \frac{1}{2u^2} + \frac{\chi}{u^2} \right) \operatorname{erf}(u) + \frac{1}{u\sqrt{\pi}} \exp(-u^2) \right\} = \bar{\Gamma}_i. \quad (\text{A3})$$

For the Coulomb logarithm  $\ln \Lambda$ , the expression from Khrapak *et al.*<sup>29</sup> is used:  $\ln \Lambda = \ln[(b_{90} + \lambda_s)/(b_{90} + r_p)]$ , where  $b_{90} = r_p e \phi_p / m_i v_{\text{eff}}^2$  is the 90° scattering impact parameter for Coulomb collisions and  $\lambda_s^2 = \lambda_{De}^2 / [1 + 2k_B T_e / m_i v_{\text{eff}}^2] + r_p^2$  the effective Debye length. Hutchinson<sup>23</sup> showed good agreement between this analytic expression and simulations if one takes the following expression for an effective drift velocity  $v_{\text{eff}}$ :

$$m_i v_{\text{eff}}^2 = 2k_B T_i + m_i v_i^2 \left\{ 1 + \left[ \frac{v_i / \sqrt{k_B T_e / m_i}}{0.6 + 0.05 \ln(M) + (\lambda_{De} / 5r_p) (\sqrt{k_B T_i / k_B T_e} - 0.1)} \right]^3 \right\}, \quad (\text{A4})$$

$M$  being the ion mass in units of hydrogen mass. Combining Eqs. (1), (A1)–(A4), the ion drag force is calculated along the drift direction of the ions. Using the capacitance model for the dust charge  $q_d = 4\pi\epsilon_0 r_p \phi_p$ , the electric field force  $\vec{F}_{el} = q_d \vec{E}$  is obtained.

<sup>4</sup>R. Heidemann, S. Zhdanov, K. R. Sütterlin, H. M. Thomas, and G. E. Morfill, *Europhys. Lett.* **96**, 15001 (2011).

<sup>5</sup>K. A. Pacha, J. R. Heinrich, S.-H. Kim, and R. L. Merlino, *Phys. Plasmas* **19**, 014501 (2012).

<sup>6</sup>J. Ashwin and R. Ganesh, *Phys. Rev. Lett.* **104**, 215003 (2010).

<sup>7</sup>J. Ashwin and R. Ganesh, *Phys. Plasmas* **17**, 103706 (2010).

<sup>8</sup>G. E. Morfill, H. M. Thomas, U. Konopka, H. Rothermel, M. Zuzic, A. Ivlev, and J. Goree, *Phys. Rev. Lett.* **83**, 1598 (1999).

<sup>9</sup>M. Klindworth, A. Piel, A. Melzer, U. Konopka, H. Rothermel, K. Tarantik, and G. E. Morfill, *Phys. Rev. Lett.* **93**, 195002 (2004).

<sup>10</sup>D. Samsonov and J. Goree, *Phys. Rev. E* **59**, 1047 (1999).

<sup>11</sup>H. Rothermel, T. Hagl, G. E. Morfill, M. H. Thoma, and H. M. Thomas, *Phys. Rev. Lett.* **89**, 175001 (2002).

<sup>1</sup>O. Ishihara, *J. Phys. D* **40**, R121 (2007).

<sup>2</sup>L.-W. Teng, P.-S. Tu, and I. Lin *Phys. Rev. Lett.* **90**, 245004 (2003).

<sup>3</sup>G. E. Morfill, S. A. Khrapak, A. V. Ivlev, B. A. Klumov, M. Rubin-Zuzic, and H. M. Thomas, *Phys. Scr.* **T107**, 59 (2004).

- <sup>12</sup>E. Thomas, *Contrib. Plasma Phys.* **49**, 316 (2009).
- <sup>13</sup>A. Barkan and R. L. Merlino, *Phys. Plasmas* **2**, 3261 (1995).
- <sup>14</sup>T. Trottenberg, D. Block, and A. Piel, *Phys. Plasmas* **13**, 042105 (2006).
- <sup>15</sup>I. Pilch, T. Trottenberg, A. Piel, and M. Koepke, *Phys. Plasmas* **14**, 123704 (2007).
- <sup>16</sup>I. Pilch, T. Reichstein, and A. Piel, *Phys. Plasmas* **15**, 103706 (2008).
- <sup>17</sup>T. Reichstein, I. Pilch, R. Grosse-Ahlert, and A. Piel, *IEEE Trans. Plasma Sci.* **38**, 814 (2010).
- <sup>18</sup>T. Reichstein, I. Pilch, and A. Piel, *Phys. Plasmas* **17**, 093701 (2010).
- <sup>19</sup>T. Reichstein, J. Wilms, F. Greiner, A. Piel, and A. Melzer, *Contrib. Plasma Phys.* **52**, 813 (2012).
- <sup>20</sup>T. Reichstein and A. Piel, *Phys. Plasmas* **18**, 083705 (2011).
- <sup>21</sup>T. Reichstein, J. Wilms, and A. Piel, *IEEE Trans. Plasma Sci.* **41**, 759 (2013).
- <sup>22</sup>L. Nyland, M. Harris, and J. Prins, in *GPU Gems 3*, edited by H. Nguyen (Pearson Education, Inc., 2008).
- <sup>23</sup>I. H. Hutchinson, *Plasma Phys. Controlled Fusion* **48**, 185 (2006).
- <sup>24</sup>I. Pilch, T. Reichstein, and A. Piel, *Phys. Plasmas* **16**, 123709 (2009).
- <sup>25</sup>O. Arp, private communication (2008).
- <sup>26</sup>J. Kristian Sveen, "An introduction to MatPIV v. 1.6.1," <http://folk.uio.no/jks/matpiv/index2.html>.
- <sup>27</sup>A. Barkan, R. L. Merlino, and N. D'Angelo, *Phys. Plasmas* **2**, 3563 (1995).
- <sup>28</sup>S. Chandrasekhar, *Astrophys. J.* **97**, 255 (1943).
- <sup>29</sup>S. A. Khrapak, A. V. Ivlev, G. E. Morfill, and H. M. Thomas, *Phys. Rev. E* **66**, 046414 (2002).

# Bibliography

- [1] C. K. GOERTZ. **Dusty plasmas in the solar system.** *Rev. Geophys.*, **27**, 271–292, (1989).
- [2] J. R. SMITH ET AL. **A New Look at the Saturn System: The Voyager 2 Images.** *Science*, **215**, 504–537, (1982).
- [3] G. S. SELWYN, J. E. HEIDENREICH, AND K. L. HALLER. **Particle trapping phenomena in radio frequency plasmas.** *Appl. Phys. Lett.*, **57**, 1876–1878, (1990).
- [4] A. BOUCHOULE. **Dusty Plasmas: Physics, Chemistry, and Technological Impact in Plasma Processing.** Wiley, Chichester, (1999).
- [5] P. ROCA I CABARROCAS, A. F. I MORRAL, AND Y. POISSANT. **Growth and optoelectronic properties of polymorphous silicon thin films.** *Thin Solid Films*, **403–404**, 39 – 46, (2002). Proceedings of Symposium P on Thin Film Materials for Photovoltaics.
- [6] R. HIPPLER AND H. KERSTEN. **Application of Dusty Plasmas.** in *Low Temperature plasmas (2nd Edn.)*, edited by R. HIPPLER, H. KERSTEN, M. SCHMIDT, AND K. H. SCHOENBACH, chapter 30, pages 797–802. WILEY-VCH Verlag GmbH & Co. KGaA, Weinheim, (2008).
- [7] J. WINTER. **Dust: A new challenge in nuclear fusion research?** *Phys. Plasmas*, **7**, 3862–3866, (2000).
- [8] G. FEDERICI, C. SKINNER, J. BROOKS, J. COAD, C. GRISOLIA, A. HAASZ, A. HASSANEIN, V. PHILIPPS, C. PITCHER, J. ROTH, W. WAMPLER, AND D. WHYTE. **Plasma-material interactions in current tokamaks and their implications for next step fusion reactors.** *Nucl. Fusion*, **41**, 1967, (2001).
- [9] M. RUBEL, M. CECCONELLO, J. MALMBERG, G. SERGIENKO, W. BIEL, J. DRAKE, A. HEDQVIST, A. HUBER, AND V. PHILIPPS. **Dust particles in controlled fusion devices: morphology, observations in the plasma and influence on the plasma performance.** *Nucl. Fusion*, **41**, 1087, (2001).

- 
- [10] J. WINTER. **Dust in fusion devices – a multi-faceted problem connecting high- and low-temperature plasma physics.** *Plasma Phys. Control. Fusion*, **46**, B583, (2004).
- [11] J. BECKERS, T. OCKENGA, M. WOLTER, W. W. STOFFELS, J. VAN DIJK, H. KERSTEN, AND G. M. W. KROESEN. **Microparticles in a Collisional Rf Plasma Sheath under Hypergravity Conditions as Probes for the Electric Field Strength and the Particle Charge.** *Phys. Rev. Lett.*, **106**, 115002, (2011).
- [12] H. MAURER, V. SCHNEIDER, M. WOLTER, R. BASNER, T. TROTTENBERG, AND H. KERSTEN. **Microparticles as Plasma Diagnostic Tools.** *Contrib. Plasma Phys.*, **51**, 218–227, (2011).
- [13] H. IKEZI. **Coulomb solid of small particles in plasmas.** *Phys. Fluids*, **29**, 1764–1766, (1986).
- [14] J. H. CHU AND L. I. **Direct observation of Coulomb crystals and liquids in strongly coupled rf dusty plasmas.** *Phys. Rev. Lett.*, **72**, 4009–4012, (1994).
- [15] A. MELZER, T. TROTTENBERG, AND A. PIEL. **Experimental determination of the charge on dust particles forming Coulomb lattices.** *Phys. Lett. A*, **191**, 301 – 308, (1994).
- [16] H. THOMAS, G. E. MORFILL, V. DEMMEL, J. GOREE, B. FEUERBACHER, AND D. MÖHLMANN. **Plasma Crystal: Coulomb Crystallization in a Dusty Plasma.** *Phys. Rev. Lett.*, **73**, 652–655, (1994).
- [17] Y. HAYASHI AND K. TACHIBANA. **Observation of Coulomb-Crystal Formation from Carbon Particles Grown in a Methane Plasma.** *Jpn. J. Appl. Phys.*, **33**, L804, (1994).
- [18] D. J. WINELAND, J. C. BERGQUIST, W. M. ITANO, J. J. BOLLINGER, AND C. H. MANNEY. **Atomic-Ion Coulomb Clusters in an Ion Trap.** *Phys. Rev. Lett.*, **59**, 2935–2938, (1987).
- [19] F. DIEDRICH, E. PEIK, J. M. CHEN, W. QUINT, AND H. WALTHER. **Observation of a Phase Transition of Stored Laser-Cooled Ions.** *Phys. Rev. Lett.*, **59**, 2931–2934, (1987).
- [20] M. DREWSSEN, C. BRODERSEN, L. HORNEKÆR, J. S. HANGST, AND J. P. SCHIFFFER. **Large Ion Crystals in a Linear Paul Trap.** *Phys. Rev. Lett.*, **81**, 2878–2881, (1998).
- [21] H. LÖWEN. **Twenty years of confined colloids: from confinement-induced freezing to giant breathing.** *J. Phys.: Condens. Matter*, **21**, 474203, (2009).



- [22] V. FORTOV, A. IVLEV, S. KHRAPAK, A. KHRAPAK, AND G. MORFILL. **Complex (dusty) plasmas: Current status, open issues, perspectives.** *Phys. Rep.*, **421**, 1 – 103, (2005).
- [23] O. ISHIHARA. **Complex plasma: dusts in plasma.** *J. Phys. D: Appl. Phys.*, **40**, R121, (2007).
- [24] G. E. MORFILL AND A. V. IVLEV. **Complex plasmas: An interdisciplinary research field.** *Rev. Mod. Phys.*, **81**, 1353–1404, (2009).
- [25] M. BONITZ, N. HORING, AND P. LUDWIG. **Introduction to Complex Plasmas.** Springer-Verlag Berlin Heidelberg, Cambridge, (2010).
- [26] A. PIEL. **Plasma Physics – An Introduction to Laboratory, Space, and Fusion Plasmas.** Springer Verlag Berlin Heidelberg, (2010).
- [27] A. MELZER, V. A. SCHWEIGERT, I. V. SCHWEIGERT, A. HOMANN, S. PETERS, AND A. PIEL. **Structure and stability of the plasma crystal.** *Phys. Rev. E*, **54**, R46–R49, (1996).
- [28] H. M. THOMAS AND G. E. MORFILL. **Melting dynamics of a plasma crystal.** *Nature*, **379**, 806–809, (1996).
- [29] O. ARP, D. BLOCK, A. PIEL, AND A. MELZER. **Dust Coulomb Balls: Three-Dimensional Plasma Crystals.** *Phys. Rev. Lett.*, **93**, 165004, (2004).
- [30] O. ARP, D. BLOCK, M. KLINDWORTH, AND A. PIEL. **Confinement of Coulomb balls.** *Phys. Plasmas*, **12**, 122102, (2005).
- [31] M. BONITZ, D. BLOCK, O. ARP, V. GOLUBNYCHIY, H. BAUMGARTNER, P. LUDWIG, A. PIEL, AND A. FILINOV. **Structural Properties of Screened Coulomb Balls.** *Phys. Rev. Lett.*, **96**, 075001, (2006).
- [32] A. MELZER, A. HOMANN, AND A. PIEL. **Experimental investigation of the melting transition of the plasma crystal.** *Phys. Rev. E*, **53**, 2757–2766, (1996).
- [33] R. ICHIKI, Y. IVANOV, M. WOLTER, Y. KAWAI, AND A. MELZER. **Melting and heating of two-dimensional Coulomb clusters in dusty plasmas.** *Phys. Rev. E*, **70**, 066404, (2004).
- [34] Y. IVANOV AND A. MELZER. **Melting dynamics of finite clusters in dusty plasmas.** *Phys. Plasmas*, **12**, 072110, (2005).
- [35] L. COUËDEL, V. NOSENKO, A. V. IVLEV, S. K. ZHDANOV, H. M. THOMAS, AND G. E. MORFILL. **Direct Observation of Mode-Coupling Instability in Two-Dimensional Plasma Crystals.** *Phys. Rev. Lett.*, **104**, 195001, (2010).

- 
- [36] V. A. SCHWEIGERT, I. V. SCHWEIGERT, A. MELZER, A. HOMANN, AND A. PIEL. **Alignment and instability of dust crystals in plasmas.** *Phys. Rev. E*, **54**, 4155–4166, (1996).
- [37] V. A. SCHWEIGERT, I. V. SCHWEIGERT, A. MELZER, A. HOMANN, AND A. PIEL. **Plasma Crystal Melting: A Nonequilibrium Phase Transition.** *Phys. Rev. Lett.*, **80**, 5345–5348, (1998).
- [38] V. NOSENKO, J. GOREE, AND A. PIEL. **Laser method of heating monolayer dusty plasmas.** *Phys. Plasmas*, **13**, 032106, (2006).
- [39] Y. FENG, J. GOREE, AND B. LIU. **Solid Superheating Observed in Two-Dimensional Strongly Coupled Dusty Plasma.** *Phys. Rev. Lett.*, **100**, 205007, (2008).
- [40] A. MELZER, A. SCHELLA, J. SCHABLINSKI, D. BLOCK, AND A. PIEL. **Instantaneous Normal Mode Analysis of Melting of Finite Dust Clusters.** *Phys. Rev. Lett.*, **108**, 225001, (2012).
- [41] J. SCHABLINSKI, D. BLOCK, A. PIEL, A. MELZER, H. THOMSEN, H. KÄHLERT, AND M. BONITZ. **Laser heating of finite two-dimensional dust clusters: A. Experiments.** *Phys. Plasmas*, **19**, 013705, (2012).
- [42] H. THOMSEN, H. KÄHLERT, M. BONITZ, J. SCHABLINSKI, D. BLOCK, A. PIEL, AND A. MELZER. **Laser heating of finite two-dimensional dust clusters: B. Simulations.** *Phys. Plasmas*, **19**, 023701, (2012).
- [43] M. RUBIN-ZUZIC, G. E. MORFILL, A. V. IVLEV, R. POMPL, B. A. KLUMOV, W. BUNK, H. M. THOMAS, H. ROTHERMEL, O. HAVNES, AND A. FOUQUET. **Kinetic development of crystallization fronts in complex plasmas.** *Nature Phys.*, **2**, 181–185, (2006).
- [44] D. H. E. DUBIN. **The phonon wake behind a charge moving relative to a two-dimensional plasma crystal.** *Phys. Plasmas*, **7**, 3895–3903, (2000).
- [45] O. HAVNES, F. LI, F. MELANDSØ, T. ASLAKSEN, T. W. HARTQUIST, G. E. MORFILL, T. NITTER, AND V. TSYTOVICH. **Diagnostic of dusty plasma conditions by the observation of Mach cones caused by dust acoustic waves.** *J. Vac. Sci. Technol. A*, **14**, 525–528, (1996).
- [46] A. MELZER, S. NUNOMURA, D. SAMSONOV, Z. W. MA, AND J. GOREE. **Laser-excited Mach cones in a dusty plasma crystal.** *Phys. Rev. E*, **62**, 4162–4176, (2000).
- [47] D. SAMSONOV, J. GOREE, Z. W. MA, A. BHATTACHARJEE, H. M. THOMAS, AND G. E. MORFILL. **Mach Cones in a Coulomb Lattice and a Dusty Plasma.** *Phys. Rev. Lett.*, **83**, 3649–3652, (1999).

- [48] D. SAMSONOV, J. GOREE, H. M. THOMAS, AND G. E. MORFILL. **Mach cone shocks in a two-dimensional Yukawa solid using a complex plasma.** *Phys. Rev. E*, **61**, 5557–5572, (2000).
- [49] N. RAO, P. SHUKLA, AND M. YU. **Dust-acoustic waves in dusty plasmas.** *Planet. Space Sci.*, **38**, 543 – 546, (1990).
- [50] F. MELANDSØ. **Lattice waves in dust plasma crystals.** *Phys. Plasmas*, **3**, 3890–3901, (1996).
- [51] S. PETERS, A. HOMANN, A. MELZER, AND A. PIEL. **Measurement of dust particle shielding in a plasma from oscillations of a linear chain.** *Phys. Lett. A*, **223**, 389 – 393, (1996).
- [52] A. HOMANN, A. MELZER, S. PETERS, R. MADANI, AND A. PIEL. **Laser-excited dust lattice waves in plasma crystals.** *Phys. Lett. A*, **242**, 173 – 180, (1998).
- [53] S. NUNOMURA, D. SAMSONOV, AND J. GOREE. **Transverse Waves in a Two-Dimensional Screened-Coulomb Crystal (Dusty Plasma).** *Phys. Rev. Lett.*, **84**, 5141–5144, (2000).
- [54] S. KHRAPAK, D. SAMSONOV, G. MORFILL, H. THOMAS, V. YAROSHENKO, H. ROTHERMEL, T. HAGL, V. FORTOV, A. NEFEDOV, V. MOLOTKOV, O. PETROV, A. LIPAIEV, A. IVANOV, AND Y. BATURIN. **Compressional waves in complex (dusty) plasmas under microgravity conditions.** *Phys. Plasmas*, **10**, 1–4, (2003).
- [55] A. PIEL, M. KLINDWORTH, O. ARP, A. MELZER, AND M. WOLTER. **Obliquely Propagating Dust-Density Plasma Waves in the Presence of an Ion Beam.** *Phys. Rev. Lett.*, **97**, 205009, (2006).
- [56] A. PIEL, M. KLINDWORTH, O. ARP, A. MELZER, AND M. WOLTER. **Erratum: Obliquely Propagating Dust-Density Plasma Waves in the Presence of an Ion Beam [Phys. Rev. Lett. 97, 205009 (2006)].** *Phys. Rev. Lett.*, **99**, 209903, (2007).
- [57] K. O. MENZEL, O. ARP, AND A. PIEL. **Spatial Frequency Clustering in Nonlinear Dust-Density Waves.** *Phys. Rev. Lett.*, **104**, 235002, (2010).
- [58] D. SAMSONOV, A. V. IVLEV, R. A. QUINN, G. MORFILL, AND S. ZHDANOV. **Dissipative Longitudinal Solitons in a Two-Dimensional Strongly Coupled Complex (Dusty) Plasma.** *Phys. Rev. Lett.*, **88**, 095004, (2002).
- [59] P. K. SHUKLA AND A. A. MAMUN. **Solitons, shocks and vortices in dusty plasmas.** *New J. Phys.*, **5**, 17, (2003).

- [60] S. K. SHARMA, A. BORUAH, AND H. BAILUNG. **Head-on collision of dust-acoustic solitons in a strongly coupled dusty plasma.** *Phys. Rev. E*, **89**, 013110, (2014).
- [61] F. LI AND O. HAVNES. **Shock waves in a dusty plasma.** *Phys. Rev. E*, **64**, 066407, (2001).
- [62] D. SAMSONOV, G. MORFILL, H. THOMAS, T. HAGL, H. ROTHERMEL, V. FORTOV, A. LIPAEV, V. MOLOTKOV, A. NEFEDOV, O. PETROV, A. IVANOV, AND S. KRIKALEV. **Kinetic measurements of shock wave propagation in a three-dimensional complex (dusty) plasma.** *Phys. Rev. E*, **67**, 036404, (2003).
- [63] D. SAMSONOV, S. K. ZHDANOV, R. A. QUINN, S. I. POPEL, AND G. E. MORFILL. **Shock Melting of a Two-Dimensional Complex (Dusty) Plasma.** *Phys. Rev. Lett.*, **92**, 255004, (2004).
- [64] V. E. FORTOV, O. S. VAULINA, O. F. PETROV, M. N. VASILIEV, A. V. GAVRIKOV, I. A. SHAKOVA, N. A. VORONA, Y. V. KHRUSTALYOV, A. A. MANOHIN, AND A. V. CHERNYSHEV. **Experimental study of the heat transport processes in dusty plasma fluid.** *Phys. Rev. E*, **75**, 026403, (2007).
- [65] V. NOSENKO, S. ZHDANOV, A. V. IVLEV, G. MORFILL, J. GOREE, AND A. PIEL. **Heat Transport in a Two-Dimensional Complex (Dusty) Plasma at Melting Conditions.** *Phys. Rev. Lett.*, **100**, 025003, (2008).
- [66] V. NOSENKO AND J. GOREE. **Shear Flows and Shear Viscosity in a Two-Dimensional Yukawa System (Dusty Plasma).** *Phys. Rev. Lett.*, **93**, 155004, (2004).
- [67] B. LIU AND J. GOREE. **Shear Viscosity of Two-Dimensional Yukawa Systems in the Liquid State.** *Phys. Rev. Lett.*, **94**, 185002, (2005).
- [68] M. S. BARNES, J. H. KELLER, J. C. FORSTER, J. A. O'NEILL, AND D. K. COULTAS. **Transport of dust particles in glow-discharge plasmas.** *Phys. Rev. Lett.*, **68**, 313–316, (1992).
- [69] S. A. KHRAPAK, A. V. IVLEV, G. E. MORFILL, AND H. M. THOMAS. **Ion drag force in complex plasmas.** *Phys. Rev. E*, **66**, 046414, (2002).
- [70] S. A. KHRAPAK, A. V. IVLEV, S. K. ZHDANOV, AND G. E. MORFILL. **Hybrid approach to the ion drag force.** *Phys. Plasmas*, **12**, 042308, (2005).
- [71] M. D. KILGORE, J. E. DAUGHERTY, R. K. PORTEOUS, AND D. B. GRAVES. **Ion drag on an isolated particulate in a low-pressure discharge.** *J. Appl. Phys.*, **73**, 7195–7202, (1993).

- [72] I. H. HUTCHINSON. **Ion collection by a sphere in a flowing plasma: 3. Floating potential and drag force.** *Plasma Phys. Control. Fusion*, **47**, 71, (2005).
- [73] I. H. HUTCHINSON. **Collisionless ion drag force on a spherical grain.** *Plasma Phys. Control. Fusion*, **48**, 185–202, (2006).
- [74] C. ZAFIU, A. MELZER, AND A. PIEL. **Ion drag and thermophoretic forces acting on free falling charged particles in an rf-driven complex plasma.** *Phys. Plasmas*, **9**, 4794–4803, (2002).
- [75] C. ZAFIU, A. MELZER, AND A. PIEL. **Measurement of the ion drag force on falling dust particles and its relation to the void formation in complex (dusty) plasmas.** *Phys. Plasmas*, **10**, 1278–1282, (2003).
- [76] M. HIRT, D. BLOCK, AND A. PIEL. **Measurement of the ion drag force on free falling microspheres in a plasma.** *Phys. Plasmas*, **11**, 5690–5696, (2004).
- [77] M. HIRT, D. BLOCK, AND A. PIEL. **Measurements of the ion drag force on micrometer sized particles in the double plasma device DODO.** *IEEE Trans. Plasma Phys.*, **32**, 582–585, (2004).
- [78] A. SCHELLA, A. MELZER, P. LUDWIG, H. THOMSEN, AND M. BONITZ. **Introduction to Streaming Complex Plasmas A: Attraction of Like-Charged Particles.** in *Complex Plasmas*, edited by M. BONITZ, J. LOPEZ, K. BECKER, AND H. THOMSEN, chapter 2, pages 51–72. Springer International Publishing Switzerland, (2014).
- [79] P. LUDWIG, C. ARRAN, AND M. BONITZ. **Introduction to Streaming Complex Plasmas B: Theoretical Description of Wake Effects.** in *Complex Plasmas*, edited by M. BONITZ, J. LOPEZ, K. BECKER, AND H. THOMSEN, chapter 3, pages 73–100. Springer International Publishing Switzerland, (2014).
- [80] G. E. MORFILL, H. M. THOMAS, U. KONOPKA, H. ROTHERMEL, M. ZUZIC, A. IVLEV, AND J. GOREE. **Condensed Plasmas under Microgravity.** *Phys. Rev. Lett.*, **83**, 1598–1601, (1999).
- [81] A. P. NEFEDOV, G. E. MORFILL, V. E. FORTOV, H. M. THOMAS, H. ROTHERMEL, T. HAGL, A. V. IVLEV, M. ZUZIC, B. A. KLUMOV, A. M. LIPAEV, V. I. MOLOTKOV, O. F. PETROV, Y. P. GIDZENKO, S. K. KRIKALEV, W. SHEPHERD, A. I. IVANOV, M. ROTH, H. BINNENBRUCK, J. A. GOREE, AND Y. P. SEMENOV. **PKE-Nefedov: plasma crystal experiments on the International Space Station.** *New J. Phys.*, **5**, 33, (2003).

- [82] H. ROTHERMEL, T. HAGL, G. E. MORFILL, M. H. THOMA, AND H. M. THOMAS. **Gravity compensation in complex plasmas by application of a temperature gradient.** *Phys. Rev. Lett.*, **89**, 175001–1–1, (2002).
- [83] C. SCHMIDT, O. ARP, AND A. PIEL. **Spatially extended void-free dusty plasmas in a laboratory radio-frequency discharge.** *Phys. Plasmas*, **18**, 013704, (2011).
- [84] A. M. LIPAEV, S. A. KHRAPAK, V. I. MOLOTKOV, G. E. MORFILL, V. E. FORTOV, A. V. IVLEV, H. M. THOMAS, A. G. KHRAPAK, V. N. NAUMKIN, A. I. IVANOV, S. E. TRETSCHEV, AND G. I. PADALKA. **Void Closure in Complex Plasmas under Microgravity Conditions.** *Phys. Rev. Lett.*, **98**, 265006, (2007).
- [85] V. LAND AND W. J. GOEDHEER. **How to make large, void-free dust clusters in dusty plasma under micro-gravity.** *New J. Phys.*, **10**, 123028, (2008).
- [86] G. PRABURAM AND J. GOREE. **Experimental observation of very low-frequency macroscopic modes in a dusty plasma.** *Phys. Plasmas*, **3**, 1212–1219, (1996).
- [87] D. SAMSONOV AND J. GOREE. **Instabilities in a dusty plasma with ion drag and ionization.** *Phys. Rev. E*, **59**, 1047–1057, (1999).
- [88] C. O. THOMPSON, N. D’ANGELO, AND R. L. MERLINO. **The interaction of stationary and moving objects with dusty plasmas.** *Phys. Plasmas*, **6**, 1421–1426, (1999).
- [89] M. KLINDWORTH, A. PIEL, A. MELZER, U. KONOPKA, H. ROTHERMEL, K. TARANTIK, AND G. E. MORFILL. **Dust-Free Regions around Langmuir Probes in Complex Plasmas under Microgravity.** *Phys. Rev. Lett.*, **93**, 195002, (2004).
- [90] E. THOMAS, JR., K. AVINASH, AND R. L. MERLINO. **Probe induced voids in a dusty plasma.** *Phys. Plasmas*, **11**, 1770–1774, (2004).
- [91] J. GOREE, G. E. MORFILL, V. N. TSYTOVICH, AND S. V. VLADIMIROV. **Theory of dust voids in plasmas.** *Phys. Rev. E*, **59**, 7055–7067, (1999).
- [92] K. AVINASH. **“Voids” and phase separation in complex (dusty) plasmas.** *Phys. Plasmas*, **8**, 2601–2604, (2001).
- [93] K. AVINASH, A. BHATTACHARJEE, AND S. HU. **Nonlinear Theory of Void Formation in Colloidal Plasmas.** *Phys. Rev. Lett.*, **90**, 075001, (2003).
- [94] M. R. AKDIM AND W. J. GOEDHEER. **Modeling of voids in colloidal plasmas.** *Phys. Rev. E*, **65**, 015401, (2001).

- [95] E. THOMAS, JR., R. L. MERLINO, AND M. ROSENBERG. **Magnetized dusty plasmas: the next frontier for complex plasma research.** *Plasma Phys. Control. Fusion*, **54**, 124034, (2012).
- [96] A. BARKAN AND R. L. MERLINO. **Confinement of dust particles in a double layer.** *Phys. Plasmas*, **2**, 3261, (1995).
- [97] U. KONOPKA, D. SAMSONOV, A. V. IVLEV, J. GOREE, V. STEINBERG, AND G. E. MORFILL. **Rigid and differential plasma crystal rotation induced by magnetic fields.** *Phys. Rev. E*, **61**, 1890–1898, (2000).
- [98] K. MATYASH, M. FRÖHLICH, H. KERSTEN, G. THIEME, R. SCHNEIDER, M. HANNEMANN, AND R. HIPPLER. **Rotating dust ring in an RF discharge coupled with a dc-magnetron sputter source. Experiment and simulation.** *J. Phys. D: Appl. Phys.*, **37**, 2703, (2004).
- [99] J. CARSTENSEN, F. GREINER, L.-J. HOU, H. MAURER, AND A. PIEL. **Effect of neutral gas motion on the rotation of dust clusters in an axial magnetic field.** *Phys. Plasmas*, **16**, 013702, (2009).
- [100] J. CARSTENSEN, F. GREINER, AND A. PIEL. **Ion-Wake-Mediated Particle Interaction in a Magnetized-Plasma Flow.** *Phys. Rev. Lett.*, **109**, 135001, (2012).
- [101] W.-T. JUAN, M.-H. CHEN, AND L. I. **Nonlinear transports and microvortex excitations in sheared quasi-two-dimensional dust Coulomb liquids.** *Phys. Rev. E*, **64**, 016402, (2001).
- [102] S. MITIC, R. SÜTTERLIN, A. V. I. H. HÖFNER, M. H. THOMA, S. ZHDANOV, AND G. E. MORFILL. **Convective Dust Clouds Driven by Thermal Creep in a Complex Plasma.** *Phys. Rev. Lett.*, **101**, 235001, (2008).
- [103] T. M. FLANAGAN AND J. GOREE. **Gas flow driven by thermal creep in dusty plasma.** *Phys. Rev. E*, **80**, 046402, (2009).
- [104] G. E. MORFILL, S. A. KHRAPAK, A. V. IVLEV, B. A. KLUMOV, M. RUBIN-ZUZIC, AND H. M. THOMAS. **From Fluid Flows to Crystallization: New Results from Complex Plasmas.** *Phys. Scr.*, **T107**, 59, (2004).
- [105] R. HEIDEMANN, S. ZHDANOV, K. R. SÜTTERLIN, H. M. THOMAS, AND G. E. MORFILL. **Shear flow instability at the interface among two streams of a highly dissipative complex plasma.** *Europhys. Lett.*, **96**, 15001, (2011).
- [106] Y. FENG, J. GOREE, AND B. LIU. **Evolution of Shear-Induced Melting in a Dusty Plasma.** *Phys. Rev. Lett.*, **104**, 165003, (2010).

- 
- [107] T. TROTTENBERG, D. BLOCK, AND A. PIEL. **Dust confinement and dust-acoustic waves in weakly magnetized anodic plasmas.** *Phys. Plasmas*, **13**, 042105, (2006).
- [108] I. PILCH, T. REICHSTEIN, AND A. PIEL. **Torus-shaped dust clouds in a magnetized anodic plasmas.** *Phys. Plasmas*, **15**, 103706, (2008).
- [109] R. GROSSE-AHLERT. **Struktur und Bewegungsvorgnge in magnetisierten staubigen Plasmen.** Diplomarbeit, Christian-Albrechts-Universität zu Kiel, (2009).
- [110] T. REICHSTEIN, I. PILCH, R. GROSSE-AHLERT, AND A. PIEL. **Toroidal Dust Clouds and Voids in a Magnetized Anodic Plasma.** *IEEE Trans. Plasma Sci.*, **38**, 814–817, (2010). (see Appendix A.1).
- [111] T. REICHSTEIN, I. PILCH, AND A. PIEL. **Toroidal dust motion in magnetized plasmas.** *Phys. Plasmas*, **17**, 093701, (2010). (see Appendix A.2).
- [112] T. REICHSTEIN AND A. PIEL. **Simulation of dust streaming in toroidal traps: Stationary flows.** *Phys. Plasmas*, **18**, 083705, (2011). (see Appendix A.3).
- [113] T. REICHSTEIN, J. WILMS, F. GREINER, A. PIEL, AND A. MELZER. **Experiments and Simulations of Particle Flows in a Magnetized Dust Torus.** *Contrib. Plasma Phys.*, **52**, 813–818, (2012). (see Appendix A.4).
- [114] T. REICHSTEIN, J. WILMS, AND A. PIEL. **Dust Streaming in Toroidal Traps.** *IEEE Trans. Plasma Sci.*, **41**, 759–763, (2013). (see Appendix A.5).
- [115] T. REICHSTEIN, J. WILMS, AND A. PIEL. **Spontaneous symmetry breaking in magnetized dust flows.** *Phys. Plasmas*, **21**, 023705, (2014). (see Appendix A.6).
- [116] F. F. CHEN. **Introduction to plasma physics and controlled fusion.** Plenum Press, New York, 2nd edition, (1990).
- [117] A. M. P. SHUKLA. **Introduction to dusty plasma physics.** Inst. of Physics Publ., Bristol, (2002).
- [118] P. K. SHUKLA AND B. ELIASSON. **Colloquium: Fundamentals of dust-plasma interactions.** *Rev. Mod. Phys.*, **81**, 25–44, (2009).
- [119] M. BONITZ, C. HENNING, AND D. BLOCK. **Complex plasmas: a laboratory for strong correlations.** *Rep. Prog. Phys.*, **73**, 066501, (2010).
- [120] E. C. WHIPPLE. **Potentials of surfaces in space.** *Rep. Prog. Phys.*, **44**, 1197, (1981).
- [121] E. J. STERNGLASS. **Theory of Secondary Electron Emission by High-Speed Ions.** *Phys. Rev.*, **108**, 1–12, (1957).



- [122] B. T. DRAINE AND E. E. SALPETER. **On the physics of dust grains in hot gas.** *Astrophys. J.*, **231**, 77–94, (1979).
- [123] A. A. SICKAFOOSE, J. E. COLWELL, M. HORÁNYI, AND S. ROBERTSON. **Photoelectric Charging of Dust Particles in Vacuum.** *Phys. Rev. Lett.*, **84**, 6034–6037, (2000).
- [124] B. WALCH, M. HORANYI, AND S. ROBERTSON. **Measurement of the charging of individual dust grains in a plasma.** *IEEE Trans. Plasma Phys.*, **22**, 97–102, (1994).
- [125] H. M. MOTT-SMITH AND I. LANGMUIR. **The Theory of Collectors in Gaseous Discharges.** *Phys. Rev.*, **28**, 727–763, (1926).
- [126] J. E. ALLEN, B. M. ANNARATONE, AND U. DE ANGELIS. **On the orbital motion limited theory for a small body at floating potential in a Maxwellian plasma.** *J. Plasma Phys.*, **63**, 299–309, (2000).
- [127] M. LAMPE. **Limits of validity for orbital-motion-limited theory for a small floating collector.** *J. Plasma Phys.*, **65**, 171–180, (2001).
- [128] T. G. NORTHROP AND T. J. BIRMINGHAM. **Equilibrium electric potential of spherical, cylindrical, and planar dust grains moving through a plasma.** *J. Geophys. Res. - Space*, **101**, 10793–10796, (1996).
- [129] A. V. IVLEV, G. MORFILL, AND V. E. FORTOV. **Potential of a dielectric particle in a flow of a collisionless plasma.** *Phys. Plasmas*, **6**, 1415–1420, (1999).
- [130] M. LAMPE, V. GAVRISHCHAKA, G. GANGULI, AND G. JOYCE. **Effect of Trapped Ions on Shielding of a Charged Spherical Object in a Plasma.** *Phys. Rev. Lett.*, **86**, 5278–5281, (2001).
- [131] P. BRYANT. **Floating potential of spherical probes and dust grains in collisional plasmas.** *J. Phys. D: Appl. Phys.*, **36**, 2859, (2003).
- [132] S. A. KHRAPAK, S. V. RATYNSKAIA, A. V. ZOBININ, A. D. USACHEV, V. V. YAROSHENKO, M. H. THOMA, M. KRETSCHMER, H. HÖFNER, G. E. MORFILL, O. F. PETROV, AND V. E. FORTOV. **Particle charge in the bulk of gas discharges.** *Phys. Rev. E*, **72**, 016406, (2005).
- [133] O. HAVNES, C. K. GOERTZ, G. E. MORFILL, E. GRÜN, AND W. IP. **Dust charges, cloud potential, and instabilities in a dust cloud embedded in a plasma.** *J. Geophys. Res. - Space*, **92**, 2281–2287, (1987).
- [134] I. GOERTZ, F. GREINER, AND A. PIEL. **Effects of charge depletion in dusty plasmas.** *Phys. Plasmas*, **18**, 013703, (2011).
- [135] I. GOERTZ. **Staub - Plasma Wechselwirkung in einer Doppelplasma-Anlage.** PhD thesis, Christian-Albrechts-Universität zu Kiel, (2011).

- [136] T. TROTTENBERG, A. MELZER, AND A. PIEL. **Measurement of the electric charge on particulates forming Coulomb crystals in the sheath of a radiofrequency plasma.** *Plasma Sources Sci. Technol.*, **4**, 450, (1995).
- [137] J. CARSTENSEN, H. JUNG, F. GREINER, AND A. PIEL. **Mass changes of microparticles in a plasma observed by a phase-resolved resonance method.** *Phys. Plasmas*, **18**, 033701, (2011).
- [138] S. RATYNSKAIA, S. KHRAPAK, A. ZOBIN, M. H. THOMA, M. KRETSCHMER, A. USACHEV, V. YAROSHENKO, R. A. QUINN, G. E. MORFILL, O. PETROV, AND V. FORTOV. **Experimental Determination of Dust-Particle Charge in a Discharge Plasma at Elevated Pressures.** *Phys. Rev. Lett.*, **93**, 085001, (2004).
- [139] U. KONOPKA, L. RATKE, AND H. M. THOMAS. **Central Collisions of Charged Dust Particles in a Plasma.** *Phys. Rev. Lett.*, **79**, 1269–1272, (1997).
- [140] A. BARKAN, N. D'ANGELO, AND R. L. MERLINO. **Charging of Dust Grains in a Plasma.** *Phys. Rev. Lett.*, **73**, 3093–3096, (1994).
- [141] J. CARSTENSEN, F. GREINER, AND A. PIEL. **Determination of dust grain charge and screening lengths in the plasma sheath by means of a controlled cluster rotation.** *Phys. Plasmas*, **17**, 083703, (2010).
- [142] P. S. EPSTEIN. **On the resistance experienced by spheres in their motion through gases.** *Phys. Rev.*, **23**, 710–733, (1924).
- [143] J. CARSTENSEN, F. HAASE, H. JUNG, B. TADSEN, S. GROTH, F. GREINER, AND A. PIEL. **Probing the Plasma Sheath by the Continuous Mass Loss of Microparticles.** *IEEE Trans. Plasma Phys.*, **41**, 764–768, (2013).
- [144] I. H. HUTCHINSON AND C. B. HAAKONSEN. **Collisional effects on nonlinear ion drag force for small grains.** *Phys. Plasmas*, **20**, 083701, (2013).
- [145] V. R. IKKURTHI, K. MATYASH, A. MELZER, AND R. SCHNEIDER. **Computation of charge and ion drag force on multiple static spherical dust grains immersed in rf discharges.** *Phys. Plasmas*, **17**, 103712, (2010).
- [146] I. H. HUTCHINSON. **Nonlinear collisionless plasma wakes of small particles.** *Phys. Plasmas*, **18**, 032111, (2011).
- [147] M. KROLL, J. SCHABLINSKI, D. BLOCK, AND A. PIEL. **On the influence of wakefields on three-dimensional particle arrangements.** *Phys. Plasmas*, **17**, 013702, (2010).
- [148] D. BLOCK, J. CARSTENSEN, P. LUDWIG, W. MILOCH, F. GREINER, A. PIEL, M. BONITZ, AND A. MELZER. **Wake Formation and Wake**

- Field Effects in Complex Plasmas.** *Contrib. Plasma Phys.*, **52**, 804–812, (2012).
- [149] A. MELZER, A. SCHELLA, AND M. MULSOW. **Nonequilibrium finite dust clusters: Connecting normal modes and wakefields.** *Phys. Rev. E*, **89**, 013109, (2014).
- [150] S. A. KHRAPAK, A. V. IVLEV, G. E. MORFILL, H. M. THOMAS, S. K. ZHDANOV, U. KONOPKA, M. H. THOMA, AND R. A. QUINN. **Comment on “Measurement of the ion drag force on falling dust particles and its relation to the void formation in complex (dusty) plasmas”** [Phys. Plasmas **10**, 1278 (2003)]. *Phys. Plasmas*, **10**, 4579–4581, (2003).
- [151] C. ZAFIU, A. MELZER, AND A. PIEL. **Response to “Comment on ‘Measurement of the ion drag force on falling dust particles and its relation to the void formation in complex (dusty) plasmas’ ”** [Phys. Plasmas **10**, 4579 (2003)]. *Phys. Plasmas*, **10**, 4582–4583, (2003).
- [152] S. A. KHRAPAK, A. V. IVLEV, G. E. MORFILL, AND S. K. ZHDANOV. **Scattering in the Attractive Yukawa Potential in the Limit of Strong Interaction.** *Phys. Rev. Lett.*, **90**, 225002, (2003).
- [153] A. PIEL AND A. MELZER. **Dynamical processes in complex plasmas.** *Plasma Phys. Control. Fusion*, **44**, R1, (2002).
- [154] S. CHANDRASEKHAR. **Dynamical friction I. General considerations: the coefficient of dynamical friction.** *Astrophys. J.*, **97**, 255, (1943).
- [155] T. REICHSTEIN. **Sondendiagnostik zur Analyse von Einschluss und Dynamik von Staub in magnetisierten Plasmen.** Diplomarbeit, Christian-Albrechts-Universität zu Kiel, (2008).
- [156] S. ROBERTSON AND Z. STERNOVSKY. **Monte Carlo model of ion mobility and diffusion for low and high electric fields.** *Phys. Rev. E*, **67**, 046405, (2003).
- [157] L. MALTER, E. O. JOHNSON, AND W. M. WEBSTER. **Studies Of Externally Heated Hot Cathode Arcs, Part I. – Modes Of The Discharge.** *RCA Rev.*, **12**, 415, (1951).
- [158] W. M. WEBSTER, E. O. JOHNSON, AND L. MALTER. **Studies Of Externally Heated Hot Cathode Arcs, Part II. – The Anode-Glow Mode.** *RCA Rev.*, **13**, 163, (1952).
- [159] E. O. JOHNSON AND W. M. WEBSTER. **Studies Of Externally Heated Hot Cathode Arcs, Part III. – Plasma Density Distributions In The Anode-Glow Mode.** *RCA Rev.*, **16**, 82, (1955).

- 
- [160] E. O. JOHNSON. **Studies Of Externally Heated Hot Cathode Arcs, Part IV. – The Low-Voltage Form Of The Ball-Of-Fire Mode.** *RCA Rev.*, **16**, 498, (1955).
- [161] B. SONG, N. D'ANGELO, AND R. L. MERLINO. **On anode spots, double layers and plasma contactors.** *J. Phys. D: Appl. Phys.*, **24**, 1789–1795, (1991).
- [162] T. AN, R. L. MERLINO, AND N. D'ANGELO. **Cylindrical anode double layers ("firerods") produced in a uniform magnetic field.** *J. Phys. D: Appl. Phys.*, **27**, 1906–1913, (1994).
- [163] I. LANGMUIR. **The Interaction of Electron and Positive Ion Space Charges in Cathode Sheaths.** *Phys. Rev.*, **33**, 954–989, (1929).
- [164] L. P. BLOCK. **A double layer review.** *Astrophys. Space Sci.*, **55**, 59–83, (1978).
- [165] N. HERSHKOWITZ. **Review of recent laboratory double layer experiments.** *Space Sci. Rev.*, **41**, 351–391, (1985).
- [166] C. CHARLES. **A review of recent laboratory double layer experiments.** *Plasma Sources Sci. Technol.*, **16**, R1, (2007).
- [167] E. THOMAS, JR. **Dust Clouds in Dc-Generated Dusty Plasmas: Transport, Waves, and Three-Dimensional Effects.** *Contrib. Plasma Phys.*, **49**, 316–345, (2009).
- [168] T. TROTTEBERG. **Diagnostik mit Resonanzkegeln, Partikeleinschluss und staubakustische Wellen in magnetisierten komplexen Plasmen.** PhD thesis, Christian-Albrechts-Universität zu Kiel, (2006).
- [169] J. E. DAUGHERTY AND D. B. GRAVES. **Derivation and experimental verification of a particulate transport model for a glow discharge.** *J. Appl. Phys.*, **78**, 2279–2287, (1995).
- [170] NVIDIA CORPORATION, SANTA CLARA, CA.
- [171] NVIDIA. **NVIDIA CUDA C Programming Guide, Vers. 4.1.** NVIDIA Corporation, Santa Clara, CA, (2011).
- [172] I. PILCH. **Synchronization of Dust-Density Waves and Formation of Torus-Shaped Dust Clouds in a Magnetized Anodic Plasma.** PhD thesis, Christian-Albrechts-Universität zu Kiel, (2010).
- [173] F. CHEN. **Electric Probes.** in *Plasma Diagnostic Techniques*, edited by H. HUDDLESTONE, chapter 4, pages 113–200. Academic, New York, (1965).
- [174] L. SCHOTT. **Electric probes.** in *Plasma diagnostics*, edited by W. LOCHTE-HOLTGREVEN, chapter 11, pages 668–731. North-Holland Publishing Company, Amsterdam, (1968).

- [175] N. HERSHKOWITZ. **How Langmuir probes work.** in *Plasma diagnostics*, edited by D. F. O. AUCIELLO, chapter 3, pages 113–183. Academic, San Diego, (1989).
- [176] I. HUTCHINSON. **Principles of plasma diagnostics.** Cambridge Press, Cambridge, 2nd edition, (2002).
- [177] J. E. ALLEN. **Probe theory - the orbital motion approach.** *Phys. Scr.*, **45**, 497, (1992).
- [178] J. E. ALLEN, R. L. F. BOYD, AND P. REYNOLDS. **The Collection of Positive Ions by a Probe Immersed in a Plasma.** *Proc. Phys. Soc. B*, **70**, 297, (1957).
- [179] F. F. CHEN. **Numerical computations for ion probe characteristics in a collisionless plasma.** *Plasma Phys.*, **7**, 47, (1965).
- [180] I. B. BERNSTEIN AND I. N. RABINOWITZ. **Theory of Electrostatic Probes in a Low-Density Plasma.** *Phys. Fluids*, **2**, 112–121, (1959).
- [181] F. F. CHEN. **Langmuir probe analysis for high density plasmas.** *Phys. Plasmas*, **8**, 3029–3041, (2001).
- [182] P. BRYANT, A. DYSON, AND J. E. ALLEN. **Langmuir probe measurements of weakly collisional electropositive RF discharge plasmas.** *J. Phys. D: Appl. Phys.*, **34**, 1491, (2001).
- [183] B. BUTTENSCHÖN. **Parametrisierung des Ionenstroms der Radial-Motion-Theorie für eine schnelle Plasmadiagnostik mit Langmuirsonden.** Diplomarbeit, Christian-Albrechts-Universität zu Kiel, (2006).
- [184] V. I. DEMIDOV, S. V. RATYNSKAIA, AND K. RYPDAL. **Electric probes for plasmas: The link between theory and instrument.** *Rev. Sci. Instr.*, **73**, 3409–3439, (2002).
- [185] J. P. SHEEHAN AND N. HERSHKOWITZ. **Emissive probes.** *Plasma Sources Sci. Technol.*, **20**, 063001, (2011).
- [186] R. F. KEMP AND J. M. SELLEN. **Plasma Potential Measurements by Electron Emissive Probes.** *Rev. Sci. Instr.*, **37**, 455–461, (1966).
- [187] H. FUJITA, S. NOWAK, B. HOEGGER, AND H. SCHNEIDER. **Potential measurements by an emissive probe in a magnetized plasma.** *Phys. Lett. A*, **78**, 263 – 265, (1980).
- [188] M. R. AKDIM AND W. J. GOEDHEER. **Modeling the effect of dust on the plasma parameters in a dusty argon discharge under microgravity.** *Phys. Rev. E*, **67**, 066407, (2003).

- [189] L. PRANDTL. **Über Flüssigkeitsbewegung bei sehr kleiner Reibung.** In *Verhandlungen des III. Internationalen Mathematiker-Kongresses, Heidelberg*, pages 484–491, (1905).
- [190] S. TANEDA. **Experimental Investigation of the Wakes behind Cylinders and Plates at Low Reynolds Numbers.** *J. Phys. Soc. Japan*, **11**, 302–307, (1956).
- [191] H. WERLÉ. **Le Tunnel hydrodynamique au service de la recherche aérospatiale.** Publication - Office national d'études et de recherches aérospatiales. O.N.E.R.A, (1974).
- [192] M. VAN DYKE. **An Album of Fluid Motion.** The parabolic press, Stanford, CA, 7th edition, (1998).
- [193] R. MEYNART. **Instantaneous velocity field measurements in unsteady gas flow by speckle velocimetry.** *Appl. Opt.*, **22**, 535–540, (1983).
- [194] R. J. ADRIAN. **Particle-Imaging Techniques for Experimental Fluid Mechanics.** *Annu. Rev. Fluid Mech.*, **23**, 261–304, (1991).
- [195] A. K. PRASAD. **Particle image velocimetry.** *Curr. Sci. India*, **79**, 51–60, (2000).
- [196] R. ADRIAN. **Twenty years of particle image velocimetry.** *Exp. Fluids*, **39**, 159–169, (2005).
- [197] M. RAFFEL, C. WILLERT, AND J. KOMPENHAUS. **Particle image velocimetry.** Springer-Verlag Berlin Heidelberg, (1998).
- [198] J. K. SVEEN AND E. A. COWEN. **Quantitative Imaging Techniques and Their Application to Wavy Flows.** in *PIV and Water Waves*, edited by J. GRUE, P. L.-F. LIU, AND G. K. PEDERSEN, **9**, chapter 1, pages 1–50. World Scientific Publishing, Singapore, (2004).
- [199] R. J. ADRIAN AND J. WESTERWEEL. **Particle image velocimetry.** Cambridge University Press, Cambridge, (2011).
- [200] J. K. SVEEN. **"An introduction to MatPIV v. 1.6.1"**. University of Oslo, (2004). <http://folk.uio.no/jks/matpiv/index2.html>.
- [201] M. P. ARROYO AND C. A. GREATED. **Stereoscopic particle image velocimetry.** *Meas. Sci. Technol.*, **2**, 1181, (1991).
- [202] A. K. PRASAD. **Stereoscopic particle image velocimetry.** *Exp. Fluids*, **29**, 103–116, (2000).
- [203] K. D. HINSCH. **Three-dimensional particle velocimetry.** *Meas. Sci. Technol.*, **6**, 742, (1995).

- [204] D. H. BARNHART, R. J. ADRIAN, AND G. C. PAPAN. **Phase-conjugate holographic system for high-resolution particle-image velocimetry.** *Appl. Opt.*, **33**, 7159–7170, (1994).
- [205] G. ELSINGA, F. SCARANO, B. WIENEKE, AND B. OUDHEUSDEN. **Tomographic particle image velocimetry.** *Exp. Fluids*, **41**, 933–947, (2006).
- [206] E. THOMAS, JR. **Direct measurements of two-dimensional velocity profiles in direct current glow discharge dusty plasmas.** *Phys. Plasmas*, **6**, 2672–2675, (1999).
- [207] E. THOMAS, JR. **Direct measurements of particle transport in dc glow discharge dusty plasmas.** *Phys. Scr.*, **2001**, 20, (2001).
- [208] E. THOMAS, JR. AND R. MERLINO. **Dust particle motion in the vicinity of dust acoustic waves.** *IEEE Trans. Plasma Sci.*, **29**, 152–157, (2001).
- [209] R. FISHER AND E. THOMAS, JR. **Thermal Properties of a Dusty Plasma in the Presence of Driven Dust Acoustic Waves.** *IEEE Trans. Plasma Sci.*, **38**, 833–837, (2010).
- [210] J. D. WILLIAMS, E. THOMAS, JR., L. COUËDEL, A. V. IVLEV, S. K. ZHDANOV, V. NOSENKO, H. M. THOMAS, AND G. E. MORFILL. **Kinetics of the melting front in two-dimensional plasma crystals: Complementary analysis with the particle image and particle tracking velocimetry.** *Phys. Rev. E*, **86**, 046401, (2012).
- [211] E. THOMAS, JR., J. D. WILLIAMS, AND J. SILVER. **Application of stereoscopic particle image velocimetry to studies of transport in a dusty (complex) plasma.** *Phys. Plasmas*, **11**, L37–L40, (2004).
- [212] J. WILLIAMS AND E. THOMAS, JR. **Measurement of the Kinetic Dust Temperature of a Weakly Coupled Dusty Plasma.** *IEEE Trans. Plasma Sci.*, **35**, 303–308, (2007).
- [213] J. D. WILLIAMS. **Application of tomographic particle image velocimetry to studies of transport in complex (dusty) plasma.** *Phys. Plasmas*, **18**, 050702, (2011).
- [214] H. KÄHLERT AND M. BONITZ. **How Spherical Plasma Crystals Form.** *Phys. Rev. Lett.*, **104**, 015001, (2010).
- [215] H. KÄHLERT AND M. BONITZ. **Time Evolution from Weak to Strong Coupling in a Spherically Confined Dusty Plasma.** *Contrib. Plasma Phys.*, **51**, 519–523, (2011).
- [216] G. UCHIDA, U. KONOPKA, AND G. MORFILL. **Wave Dispersion Relation of Two-Dimensional Plasma Crystals in a Magnetic Field.** *Phys. Rev. Lett.*, **93**, 155002, (2004).

- [217] M. BONITZ, Z. DONKÓ, T. OTT, H. KÄHLERT, AND P. HARTMANN. **Non-linear Magnetoplasmons in Strongly Coupled Yukawa Plasmas.** *Phys. Rev. Lett.*, **105**, 055002, (2010).
- [218] C. K. BIRDSALL AND A. B. LANGDON. **Plasma physics via computer simulation.** IOP Publishing Ltd, Philadelphia, (1991).
- [219] M. P. ALLEN AND D. J. TILDESLEY. **Computer Simulation of Liquids.** Oxford Science Publications, Oxford, (1994).
- [220] M. R. AKDIM AND W. J. GOEDHEER. **Modeling of self-excited dust vortices in complex plasmas under microgravity.** *Phys. Rev. E*, **67**, 056405, (2003).
- [221] V. LAND AND W. J. GOEDHEER. **Effect of large-angle scattering, ion flow speed and ion-neutral collisions on dust transport under microgravity conditions.** *New J. Phys.*, **8**, 8, (2006).
- [222] W. J. MILOCH, H. L. PÉCSELI, AND J. TRULSEN. **Numerical simulations of the charging of dust particles by contact with hot plasmas.** *Nonlinear Proc. Geophys.*, **14**, 575–586, (2007).
- [223] K. MATYASH, R. SCHNEIDER, F. TACCOGNA, A. HATAYAMA, S. LONGO, M. CAPITELLI, D. TSKHAKAYA, AND F. X. BRONOLD. **Particle in Cell Simulation of Low Temperature Laboratory Plasmas.** *Contrib. Plasma Phys.*, **47**, 595–634, (2007).
- [224] V. R. IKKURTHI, K. MATYASH, A. MELZER, AND R. SCHNEIDER. **Computation of dust charge and potential on a static spherical dust grain immersed in rf discharges.** *Phys. Plasmas*, **15**, 123704, (2008).
- [225] L. S. FROST. **Effect of Variable Ionic Mobility on Ambipolar Diffusion.** *Phys. Rev.*, **105**, 354–356, (1957).
- [226] A. BARKAN, R. L. MERLINO, AND N. D'ANGELO. **Laboratory observation of the dust acoustic wave mode.** *Phys. Plasmas*, **2**, 3563–3565, (1995).
- [227] C. THOMPSON, A. BARKAN, N. D'ANGELO, AND R. L. MERLINO. **Dust acoustic waves in a direct current glow discharge.** *Phys. Plasmas*, **4**, 2331–2335, (1997).
- [228] I. PILCH, T. TROTTENBERG, A. PIEL, AND M. KOEPKE. **Dynamics of small dust clouds trapped in a magnetized anodic plasma.** *Phys. Plasmas*, **14**, 123704, (2007).
- [229] I. PILCH, T. REICHSTEIN, AND A. PIEL. **Synchronization of dust density waves in anodic plasmas.** *Phys. Plasmas*, **16**, 123709, (2009).



- [230] M. ROSENBERG. **A note on ion-dust streaming instability in a collisional dusty plasma.** *J. Plasma Phys.*, **67**, 235–242, (2002).
- [231] W. H. PRESS, B. P. FLANNERY, S. A. TEUKOLSKY, AND W. T. VETTERLING. **Numerical Recipes: The Art of Scientific Computing.** Cambridge University Press, Cambridge, (1992).
- [232] L. VERLET. **Computer “Experiments” on Classical Fluids. I. Thermodynamical Properties of Lennard-Jones Molecules.** *Phys. Rev.*, **159**, 98–103, (1967).
- [233] W. C. SWOPE, H. C. ANDERSEN, P. H. BERENS, AND K. R. WILSON. **A computer simulation method for the calculation of equilibrium constants for the formation of physical clusters of molecules: Application to small water clusters.** *J. Chem. Phys.*, **76**, 637–649, (1982).
- [234] S. CHANDRASEKHAR. **Stochastic Problems in Physics and Astronomy.** *Rev. Mod. Phys.*, **15**, 1–89, (1943).
- [235] L.-J. HOU, A. PIEL, AND P. K. SHUKLA. **Self-Diffusion in 2D Dusty-Plasma Liquids: Numerical-Simulation Results.** *Phys. Rev. Lett.*, **102**, 085002, (2009).
- [236] T. OTT AND M. BONITZ. **Is Diffusion Anomalous in Two-Dimensional Yukawa Liquids?** *Phys. Rev. Lett.*, **103**, 195001, (2009).
- [237] B. DÜNWEG AND K. KREMER. **Molecular dynamics simulation of a polymer chain in solution.** *J. Chem. Phys.*, **99**, 6983–6997, (1993).
- [238] W. EVANS, J. FISH, AND P. KEBLINSKI. **Role of Brownian motion hydrodynamics on nanofluid thermal conductivity.** *Appl. Phys. Lett.*, **88**, 093116, (2006).
- [239] E. HOLMBERG. **On the Clustering Tendencies among the Nebulae. II. a Study of Encounters Between Laboratory Models of Stellar Systems by a New Integration Procedure.** *Astrophys. J.*, **94**, 385, (1941).
- [240] S. F. P. ZWART, R. G. BELLEMAN, AND P. M. GELDOF. **High-performance direct gravitational N-body simulations on graphics processing units.** *New Astron.*, **12**, 641 – 650, (2007).
- [241] R. G. BELLEMAN, J. BDORF, AND S. F. P. ZWART. **High performance direct gravitational N-body simulations on graphics processing units II: An implementation in {CUDA}.** *New Astron.*, **13**, 103 – 112, (2008).
- [242] I. MOROZOV, A. KAZENNOV, R. BYSTRYI, G. NORMAN, V. PISAREV, AND V. STEGAILOV. **Molecular dynamics simulations of the relaxation processes in the condensed matter on {GPUs}.** *Computer Phys. Comm.*, **182**, 1974 – 1978, (2011).

- [243] H. BURAU, R. WIDERA, W. HONIG, G. JUCKELAND, A. DEBUS, T. KLUGE, U. SCHRAMM, T. COWAN, R. SAUERBREY, AND M. BUSSMANN. **PICongPU: A Fully Relativistic Particle-in-Cell Code for a GPU Cluster.** *IEEE Trans. Plasma Phys.*, **38**, 2831–2839, (2010).
- [244] P. MERTMANN, D. EREMIN, T. MUSSENBRÖCK, R. P. BRINKMANN, AND P. AWAKOWICZ. **Fine-sorting one-dimensional particle-in-cell algorithm with Monte-Carlo collisions on a graphics processing unit.** *Computer Phys. Comm.*, **182**, 2161 – 2167, (2011).
- [245] A. BUDEA, A. DERZSI, P. HARTMANN, AND Z. DONKÓ. **Shear Viscosity of Liquid-Phase Yukawa Plasmas from Molecular Dynamics Simulations on Graphics Processing Units.** *Contrib. Plasma Phys.*, **52**, 194–198, (2012).
- [246] L. NYLAND, M. HARRIS, AND J. PRINS. **Fast N-Body Simulation with CUDA.** in *GPU Gems 3*, edited by H. NGUYEN. Pearson Education, Inc., (2008).
- [247] J. HEINRICH, S.-H. KIM, AND R. L. MERLINO. **Laboratory Observations of Self-Excited Dust Acoustic Shocks.** *Phys. Rev. Lett.*, **103**, 115002, (2009).
- [248] R. L. MERLINO, J. R. HEINRICH, S.-H. HYUN, AND J. K. MEYER. **Non-linear dust acoustic waves and shocks.** *Phys. Plasmas*, **19**, 057301, (2012).
- [249] J. K. MEYER AND R. L. MERLINO. **Transient bow shock around a cylinder in a supersonic dusty plasma.** *Phys. Plasmas*, **20**, 074501, (2013).
- [250] J. K. MEYER, J. R. HEINRICH, S.-H. KIM, AND R. L. MERLINO. **Interaction of a biased cylinder with a flowing dusty plasma.** *J. Plasma Phys.*, **79**, 677–682, (2013).
- [251] O. VAULINA, A. SAMARIAN, O. PETROV, B. JAMES, AND F. MELANDSO. **Formation of vortex dust structures in inhomogeneous gas-discharge plasmas.** *Plasma Phys. Rep.*, **30**, 918–936, (2004).
- [252] W. E. AMATUCCI, D. N. WALKER, G. GATLING, AND E. E. SCIME. **Direct observation of microparticle gyromotion in a magnetized direct current glow discharge dusty plasma.** *Phys. Plasmas*, **11**, 2097–2105, (2004).
- [253] N. SATO, G. UCHIDA, T. KANEKO, S. SHIMIZU, AND S. IIZUKA. **Dynamics of fine particles in magnetized plasmas.** *Phys. Plasmas*, **8**, 1786–1790, (2001).
- [254] V. Y. KARASEV, E. S. DZLIEVA, A. Y. IVANOV, AND A. I. EIKHVALD. **Rotational motion of dusty structures in glow discharge in longitudinal magnetic field.** *Phys. Rev. E*, **74**, 066403, (2006).

- [255] G. GOZADINOS, A. V. IVLEV, AND J. P. BOEUF. **A fluid model for colloidal plasmas under microgravity conditions.** *New J. Phys.*, **5**, 32, (2003).
- [256] W. J. GOEDHEER, V. LAND, AND J. VENEMA. **Modelling of Voids in Complex Radio Frequency Plasmas.** *Contrib. Plasma Phys.*, **49**, 199–214, (2009).
- [257] W.-T. JUAN, Z.-H. HUANG, J.-W. HSU, Y.-J. LAI, AND L. I. **Observation of dust Coulomb clusters in a plasma trap.** *Phys. Rev. E*, **58**, R6947–R6950, (1998).
- [258] M. KLINDWORTH, A. MELZER, A. PIEL, AND V. A. SCHWEIGERT. **Laser-excited intershell rotation of finite Coulomb clusters in a dusty plasma.** *Phys. Rev. B*, **61**, 8404–8410, (2000).
- [259] A. RAHMAN AND J. P. SCHIFFER. **A Condensed State in a System of Stored and Cooled Ions.** *Phys. Scr.*, **1988**, 133, (1988).
- [260] G. BIRKL, S. KASSNER, AND H. WALTHER. **Multiple-shell structures of laser-cooled  $^{24}\text{Mg}^+$  ions in a quadrupole storage ring.** *Nature*, **357**, 310–313, (1992).
- [261] H. WALTHER. **From a single ion to a mesoscopic system - crystallization of ions in Paul traps.** *Phys. Scr.*, **1995**, 360, (1995).
- [262] H. BAUMGARTNER. **Structure and dynamics of Yukawa balls.** PhD thesis, Christian-Albrechts-Universität zu Kiel, (2009).
- [263] H. TOTSUJI AND C. TOTSUJI. **Structures of Yukawa and Coulomb particles in cylinders: Simulations for fine particle plasmas and colloidal suspensions.** *Phys. Rev. E*, **84**, 015401, (2011).
- [264] H. TOTSUJI, K. TAKAHASHI, S. ADACHI, C. TOTSUJI, AND M. TONOUCI. **Structures of fine particles in cylindrical plasmas: Theory, simulations, and experiments under gravity and microgravity.** *Europhys. Conf. Abstr.*, **36F**, O4.307, (2012).
- [265] L.-W. TENG, P.-S. TU, AND L. I. **Microscopic Observation of Confinement-Induced Layering and Slow Dynamics of Dusty-Plasma Liquids in Narrow Channels.** *Phys. Rev. Lett.*, **90**, 245004, (2003).
- [266] M. KÖPPL, P. HENSELER, A. ERBE, P. NIELABA, AND P. LEIDERER. **Layer Reduction in Driven 2D-Colloidal Systems through Microchannels.** *Phys. Rev. Lett.*, **97**, 208302, (2006).
- [267] P. HENSELER, A. ERBE, M. KÖPPL, P. LEIDERER, AND P. NIELABA. **Density reduction and diffusion in driven two-dimensional colloidal systems through microchannels.** *Phys. Rev. E*, **81**, 041402, (2010).

- [268] K. R. SÜTTERLIN, A. WY SOCKI, A. V. IVLEV, C. RÄTH, H. M. THOMAS, M. RUBIN-ZUZIC, W. J. GOEDHEER, V. E. FORTOV, A. M. LIPA EV, V. I. MOLOTKOV, O. F. PETROV, G. E. MORFILL, AND H. LÖWEN. **Dynamics of Lane Formation in Driven Binary Complex Plasmas.** *Phys. Rev. Lett.*, **102**, 085003, (2009).
- [269] K. SÜTTERLIN, H. THOMAS, A. IVLEV, G. MORFILL, V. FORTOV, A. LIPA EV, V. MOLOTKOV, O. PETROV, A. WY SOCKI, AND H. LÖWEN. **Lane Formation in Driven Binary Complex Plasmas on the International Space Station.** *IEEE Trans. Plasma Sci.*, **38**, 861–868, (2010).
- [270] A. SCHELLA, M. MULSOW, AND A. MELZER. **Correlation buildup during recrystallization in three-dimensional dusty plasma clusters.** *Phys. Plasmas*, **21**, 050701, (2014).
- [271] A. SCHELLA, T. MIKSCH, A. MELZER, J. SCHABLINSKI, D. BLOCK, A. PIEL, H. THOMSEN, P. LUDWIG, AND M. BONITZ. **Melting scenarios for three-dimensional dusty plasma clusters.** *Phys. Rev. E*, **84**, 056402, (2011).
- [272] S. A. KHRAPAK, B. A. KLUMOV, P. HUBER, V. I. MOLOTKOV, A. M. LIPA EV, V. N. NAUMKIN, H. M. THOMAS, A. V. IVLEV, G. E. MORFILL, O. F. PETROV, V. E. FORTOV, Y. MALENTSCHENKO, AND S. VOLKOV. **Freezing and Melting of 3D Complex Plasma Structures under Microgravity Conditions Driven by Neutral Gas Pressure Manipulation.** *Phys. Rev. Lett.*, **106**, 205001, (2011).
- [273] S. A. KHRAPAK, B. A. KLUMOV, P. HUBER, V. I. MOLOTKOV, A. M. LIPA EV, V. N. NAUMKIN, A. V. IVLEV, H. M. THOMAS, M. SCHWABE, G. E. MORFILL, O. F. PETROV, V. E. FORTOV, Y. MALENTSCHENKO, AND S. VOLKOV. **Fluid-solid phase transitions in three-dimensional complex plasmas under microgravity conditions.** *Phys. Rev. E*, **85**, 066407, (2012).
- [274] A. MELZER, A. SCHELLA, T. MIKSCH, J. SCHABLINSKI, D. BLOCK, A. PIEL, H. THOMSEN, H. KÄHLERT, AND M. BONITZ. **Phase Transitions of Finite Dust Clusters in Dusty Plasmas.** *Contrib. Plasma Phys.*, **52**, 795–803, (2012).
- [275] M. KROLL. **Strukturanalyse staubiger Plasmen mittels digitaler Holographie.** PhD thesis, Christian-Albrechts-Universität zu Kiel, (2010).
- [276] K. A. PACHA, J. R. HEINRICH, S.-H. KIM, AND R. L. MERLINO. **Observation of the Taylor instability in a dusty plasma.** *Phys. Plasmas*, **19**, 014501, (2012).
- [277] J. ASHWIN AND R. GANESH. **Kelvin Helmholtz Instability in Strongly Coupled Yukawa Liquids.** *Phys. Rev. Lett.*, **104**, 215003, (2010).

- [278] J. ASHWIN AND R. GANESH. **Coherent Vortices in Strongly Coupled Liquids.** *Phys. Rev. Lett.*, **106**, 135001, (2011).
- [279] Y. SAITOU, Y. NAKAMURA, T. KAMIMURA, AND O. ISHIHARA. **Bow Shock Formation in a Complex Plasma.** *Phys. Rev. Lett.*, **108**, 065004, (2012).
- [280] J. H. CHU, J.-B. DU, AND L. I. **Coulomb solids and low-frequency fluctuations in RF dusty plasmas.** *J. Phys. D: Appl. Phys.*, **27**, 296, (1994).
- [281] S.-H. KIM, J. R. HEINRICH, AND R. L. MERLINO. **Diffraction of dust acoustic waves by a circular cylinder.** *Phys. Plasmas*, **15**, 090701, (2008).
- [282] J. R. HEINRICH, S.-H. KIM, J. K. MEYER, AND R. L. MERLINO. **Experimental quiescent drifting dusty plasmas and temporal dust acoustic wave growth.** *Phys. Plasmas*, **18**, 113706, (2011).
- [283] M. J. STEVENS, M. O. ROBBINS, AND J. F. BELAK. **Shear melting of colloids: A nonequilibrium phase diagram.** *Phys. Rev. Lett.*, **66**, 3004–3007, (1991).
- [284] R. P. A. DULLENS AND C. BECHINGER. **Shear Thinning and Local Melting of Colloidal Crystals.** *Phys. Rev. Lett.*, **107**, 138301, (2011).
- [285] H. HASEGAWA, M. FUJIMOTO, T.-D. PHAN, H. REME, A. BALOGH, M. W. DUNLOP, C. HASHIMOTO, AND R. TANDOKORO. **Transport of solar wind into Earth’s magnetosphere through rolled-up Kelvin-Helmholtz vortices.** *Nature*, **430**, 755–758, (2004).
- [286] S.-I. AKASOFU. **Energy coupling between the solar wind and the magnetosphere.** *Space Sci. Rev.*, **28**, 121–190, (1981).
- [287] N. D’ANGELO. **Kelvin-Helmholtz Instability in a Fully Ionized Plasma in a Magnetic Field.** *Phys. Fluids*, **8**, 1748–1750, (1965).
- [288] N. D’ANGELO AND S. V. GOELER. **Investigation of the Kelvin-Helmholtz Instability in a Cesium Plasma.** *Phys. Fluids*, **9**, 309–313, (1966).
- [289] N. D’ANGELO AND B. SONG. **The Kelvin-Helmholtz instability in dusty plasmas.** *Planet. Space Sci.*, **38**, 1577 – 1579, (1990).
- [290] Q. Z. LUO, N. D’ANGELO, AND R. L. MERLINO. **The Kelvin-Helmholtz instability in a plasma with negatively charged dust.** *Phys. Plasmas*, **8**, 31–35, (2001).
- [291] G. T. BIRK AND H. WIECHEN. **Shear flow instabilities in magnetized partially ionized dense dusty plasmas.** *Phys. Plasmas*, **9**, 964–970, (2002).

- [292] H. M. WIECHEN. **Simulations of Kelvin-Helmholtz modes in partially ionized dusty plasmas comparing different charge numbers, charge polarities, and masses of the dust.** *Phys. Plasmas*, **13**, 062104, (2006).
- [293] J. ASHWIN AND R. GANESH. **Parallel shear flow instabilities in strongly coupled Yukawa liquids: A comparison of generalized hydrodynamic model and molecular dynamics results.** *Phys. Plasmas*, **17**, 103706, (2010).
- [294] Z. DONKÓ AND P. HARTMANN. **Shear viscosity of strongly coupled Yukawa liquids.** *Phys. Rev. E*, **78**, 026408, (2008).
- [295] J. W. BOND, K. M. WATSON, AND J. A. J. WELCH. **Atomic theory of gas dynamics.** Addison-Wesley Publishing Company, Inc., Reading, (1965).
- [296] R. J. TAYLOR, D. R. BAKER, AND H. IKEZI. **Observation of Collisionless Electrostatic Shocks.** *Phys. Rev. Lett.*, **24**, 206–209, (1970).
- [297] Y. NAKAMURA, H. BAILUNG, AND P. K. SHUKLA. **Observation of Ion-Acoustic Shocks in a Dusty Plasma.** *Phys. Rev. Lett.*, **83**, 1602–1605, (1999).
- [298] Q.-Z. LUO, N. D'ANGELO, AND R. L. MERLINO. **Experimental study of shock formation in a dusty plasma.** *Phys. Plasmas*, **6**, 3455–3458, (1999).
- [299] Y. NAKAMURA. **Experiments on ion-acoustic shock waves in a dusty plasma.** *Phys. Plasmas*, **9**, 440–445, (2002).
- [300] S. I. POPEL, T. V. LOSSEVA, A. P. GOLUB', R. L. MERLINO, AND S. N. ANDREEV. **Dust Ion-Acoustic Shocks in a Q Machine Device.** *Contrib. Plasma Phys.*, **45**, 461–475, (2005).
- [301] E. THOMAS, JR. AND J. WILLIAMS. **Applications of stereoscopic particle image velocimetry: Dust acoustic waves and velocity space distribution functions.** *Phys. Plasmas*, **13**, 055702, (2006).

# List of Publications

## Publications in peer-reviewed journals

### Part of this thesis

- [A.1] Torben Reichstein, Iris Pilch, Robert Große-Ahlert, and Alexander Piel,  
*Toroidal Dust Clouds and Voids in a Magnetized Anodic Plasma*,  
IEEE Transactions on Plasma Science, **38**, 814 (2010)
- [A.2] Torben Reichstein, Iris Pilch, and Alexander Piel,  
*Toroidal dust motion in magnetized plasmas*,  
Physics of Plasmas, **17**, 093701 (2010)
- [A.3] Torben Reichstein and Alexander Piel,  
*Simulation of dust streaming in toroidal traps: Stationary flows*,  
Physics of Plasmas, **18**, 083705 (2011)
- [A.4] Torben Reichstein, Jochen Wilms, Franko Greiner, Alexander Piel, and André Melzer,  
*Experiments and Simulations of Particle Flows in a Magnetized Dust Torus*,  
Contribution to Plasma Physics, **52**, 813 (2012)
- [A.5] Torben Reichstein, Jochen Wilms, and Alexander Piel,  
*Dust Streaming in Toroidal Traps*,  
IEEE Transactions on Plasma Science, **41**, 759 (2013)
- [A.6] Torben Reichstein, Jochen Wilms, and Alexander Piel,  
*Spontaneous symmetry breaking in magnetized dust flows*,  
Physics of Plasmas, **21**, 023705 (2014)

### Further publications

- [1] Iris Pilch, Torben Reichstein, and Alexander Piel,  
*Torus-shaped dust clouds trapped in a magnetized anodic plasma*,  
Physics of Plasmas, **15**, 103706 (2008)
- [2] Iris Pilch, Torben Reichstein, and Alexander Piel,  
*Synchronization of dust density waves in anodic plasmas*,  
Physics of Plasmas, **16**, 123709 (2009)

## Selected Contributions to International Conferences

- [B.1] T. Reichstein, I. Pilch, A. Piel,  
*Toroidal dust motion in magnetized plasmas,*  
Europhysics Conference Abstracts, **34A**, P1.305 (2010)
- [B.2] Torben Reichstein and Alexander Piel,  
*Dust streaming in toroidal traps,*  
AIP Conference Proceedings, **1397**, 429 (2011)



# Danksagung

An dieser Stelle möchte ich mich bei allen Personen bedanken, die zum Gelingen dieser Arbeit beigetragen haben. Als erstes gilt mein Dank Herrn Prof. Dr. Alexander Piel für die freundliche Aufnahme in die Arbeitsgruppe und die Möglichkeit diese Arbeit unter seiner Anleitung anfertigen zu können. Ohne die zahlreichen Diskussionen und Anregungen wäre die Arbeit in dieser Form nicht möglich gewesen. Ebenso möchte ich mich dafür bedanken, dass ich meine Ergebnisse auf Tagungen im In- und Ausland vorstellen konnte.

Als nächstes möchte ich mich bei Dr. Iris Pilch bedanken, die mir schon während meiner Diplomarbeit und in den ersten Jahren meiner Doktorarbeit mit Rat und Tat zur Seite gestanden hat und mich nicht nur im physikalischen Denken geprägt hat. Weiterhin gilt mein Dank Jochen Wilms für die zahlreichen Diskussionen rund um Physik und um Physik herum, ebenso für seinen unermüdlichen Einsatz, Matilda wieder ins Leben zurückzuholen. Allerdings wäre mancher musikalische Exkurs nicht nötig gewesen. Gleichfalls danke ich Christian Schmidt, der immer ein offenes Ohr für mich hatte und mich all die Jahre während des Studiums begleitet und ertragen hat. Für das Korrekturlesen dieser Arbeit danke ich Christian, Jochen und Rika Finck. Eure Anmerkungen und Kommentare haben sehr geholfen, die Arbeit verständlicher zu machen.

Stellvertretend für die gesamte Arbeitsgruppe möchte ich mich bei Prof. Dr. Dietmar Block und Dr. Franko Greiner bedanken. Bei ihnen, wie bei allen anderen Mitgliedern der AG, konnte man immer mit Hilfe und Unterstützung rechnen, unabhängig vom Anlass oder Zeitdruck des Problems. Für die Unterstützung in allen bürokratischen Angelegenheiten möchte ich mich bei Frau Seeger, Frau Sommer und Frau Thiedemann bedanken. Für die Hilfe bei der Umsetzung technischer Vorhaben gilt mein Dank Michael Poser, Volker Rohwer und Mario Knüppel. Für die Entwicklung und Erprobung der ITO-Anode im Rahmen seiner Diplomarbeit danke ich Robert Große-Ahlert. Bei der gesamten Arbeitsgruppe möchte ich mich für die unzähligen Kaffeerunden, Kuchenwetten und Diskussionen rund um wichtige, weniger wichtige und besonders wichtige Themen innerhalb und vor allem auch außerhalb der Physik danken.

Und bevor ich's vergesse: Danke NVIDIA...

Auch außerhalb der Universität haben eine Vielzahl von Personen ihren Anteil am Gelingen dieser Arbeit. Kathrin Bonn und den *seitotachi* danke ich dafür, den Kopf von *butsuri* zu befreien und bei *kudamono* nicht an Grafikkarten zu denken. Danke auch an Mike und Rieke für inzwischen 12 Jahre Freitagskicken und Tempoläufe.

Weiterhin danke ich Rika Finck für mehr als 25 Jahre echte Freundschaft, Spaß und für die Selbstverständlichkeit, mit der du mir zugehört hast, wenn es mal wieder nicht so lief, wie ich gern gehabt hätte. Auf die nächsten 25 Jahre! Für die Unterstützung und Ablenkung gleichermaßen in jeder Hinsicht während der Endphase dieser Arbeit gilt mein besonderer Dank Linda Kochniss.

Meiner Schwester Wiebke und den Haasen danke ich ebenfalls ganz herzlich für ihre Unterstützung und das Ertragen meiner Launen. Abschließend gebührt mein größter Dank meinen Eltern, die es mir ermöglicht haben, Physik zu studieren, mir immer den Rücken freigehalten und bei Gelegenheit auch mal in den Hintern getreten haben, wenn es sein musste. Dafür und für alles andere auch: DANKE!

# Lebenslauf

## Persönliche Daten

Name: Torben Reichstein  
Geburtsdatum: 14.04.1984  
Geburtsort: Preetz  
Staatsangehörigkeit: deutsch  
Familienstand: ledig

## Schulbildung

1990 - 1994 Grund- und Hauptschule Flintbek  
1994 - 2003 Humboldt-Schule Kiel  
Juni 2003 Abitur mit den Leistungskursen  
Mathematik und Physik

## Studium

April 2004 Immatrikulation im Fach Physik  
an der Christian-Albrechts-Universität zu Kiel  
März 2006 Vordiplom mit Nebenfach Chemie  
Dezember 2008 Beendigung des Studiums der Physik mit Abschluss  
Diplom  
Nebenfach: Astronomie  
Thema der Diplomarbeit:  
Sondendiagnostik zur Analyse von Einschluss und Dy-  
namik von Staub in magnetisierten Plasmen  
seit Dezember 2008 Promotion in der Arbeitsgruppe "Plasmadynamik"  
am Institut für Experimentelle und Angewandte Phy-  
sik der Christian-Albrechts-Universität zu Kiel



# Erklärung

Hiermit versichere ich, dass die vorliegende Dissertation - abgesehen von der Beratung durch meinen wissenschaftlichen Lehrer und der Verwendung der angegebenen Hilfsmittel - nach Inhalt und Form meine eigene ist. Sie hat weder ganz noch teilweise an einer anderen Stelle im Rahmen eines Prüfungsverfahrens vorgelegen. Die Arbeit ist unter Einhaltung der Regeln der guten wissenschaftlichen Praxis der Deutschen Forschungsgemeinschaft entstanden.

Kiel, den